Development and Evaluation of Experiments for Pure Shift Solution-State Magnetic Resonance Spectroscopy

Vom Fachbereich Chemie der Technischen Universität Darmstadt
zum Erlangen des akademischen Grades eines Doctor rerum naturalium (Dr. rer. nat.)
genehmigte Dissertation, vorgelegt von
Lukas Kaltschnee (M. Sc. Chemie) aus Frankfurt am Main
August 2016, Darmstadt, D17

TECHNISCHE
UNIVERSITÄT
DARMSTADT

Fachbereich Chemie
Clemens-Schöpf-Institut für
Organische Chemie und
Biochemie
Prof. Dr. C. M. Thiele

Titel in deutscher Sprache:
Entwicklung und Bewertung von Pure Shift Experimenten für die Magnetische Resonanzspektroskopie gelöster Moleküle

1. Gutachten: Prof. Dr. Christina M. Thiele (Technische Universität Darmstadt)
2. Gutachten: Prof. Dr. Michael Reggelin (Technische Universität Darmstadt)
3. Gutachten: Prof. Dr. Klaus Zangger (Universität Graz)

Tag der Einreichung: 28. Juni 2016
Tag der mündlichen Prüfung: 09. August 2016

Development and Evaluation of Experiments for Pure Shift Solution-State Magnetic Resonance Spectroscopy

Entwicklung und Bewertung von Pure Shift Experimenten für die Magnetische Resonanzspektroskopie gelöster Moleküle

genehmigte Dissertation von Lukas Kaltschnee aus Frankfurt am Main

1. Gutachten: Prof. Dr. Christina M. Thiele
2. Gutachten: Prof. Dr. Michael Reggelin
3. Gutachten: Prof. Dr. Klaus Zangger (Universität Graz)

Tag der Einreichung: 28. Juni 2016
Tag der mündlichen Prüfung: 09. August 2016

Darmstadt – D17

meiner Familie und den vielen lieben Menschen,
die mich ebenfalls durch diese Zeit begleiteten

Acknowledgements

For the supervision of this thesis I want to thank Christina Thiele, including the motivation and drive to follow this work, for making everything possible that serves my personal development, nice and sometimes also exhausting discussions, endless patience, the possibility to present my work to other people and the huge support – in particular in stressful situations.

There is a second (and in large parts even third, fourth and fifth) person that essentially also supervised this thesis and these are Gareth Morris and Katalin Kövér, Ralph Adams and Mathias Nilsson, who have been supportive wherever they could. You got to know me well through thousands of lengthy e-mails and a bit of personal contact and I'd be more than happy, if the close contact stayed intact in the future.

Strong support also came from the Merck KGaA (through the Merck'sche Gesellschaft für Kunst und Wissenschaft e.V.), which went beyond funding this work for two entire years. They have been very supportive in helping me to present my work at several conferences, which certainly was worth a lot – not only through promoting the work and by enabling me to get into contact with other people from the field. It also helped me a lot to get a broader knowledge of what is outside the small world of my own research.

For close collaboration, I first of all want to thank István Timári, who put a lot of effort into many of the projects contained in this work. Also I should mention Martin Koos here, for a very short, intense and fruitful collaboration.
This work has been blessed with many different collaborations, which clearly helped and pushed me a lot. In addition to the people named above, I should mention Volker Schmidts and Andreas Kolmer for their contributions to Projects A and B through their work, but also through the many discussions, guiding help, good ideas, criticism etc.. For his contributions to Project A, also for his calmness during the time I've been pushing him Kevin Knoll should also be mentioned here.
Contributions to Project B have also come from Felix Roth, who spent several interns with me and always has done a very reliable job, while being great company. Further contributions to project B came from Dušan Uhrín and Nicholle Bell, for which I want to thank a lot.
Project C was in collaboration with Yulia Moskalenko-Serra, Wolfgang Bermel, Karolina Pulka-Ziach and Timo Imhof, who all devoted their time and energy.
To Project D, further Burkhard Luy and Grit Kummerlöwe have contributed. I want to use this possibility to not only thank for the shared efforts, but also for the many discussions together with Burkhard.
For the shared work not appearing herein, but which still took a lot of effort, I also want to thank Jonas Kind and Martin Leyendecker at this point – in particular for the good working atmosphere. ☺

There are also a lot of people I should thank which does not have to be related to shared projects. This includes the entire Thielelab for the great group they are. You really have not been just the people populating the other desks, and you know that!
Also the Manchester Group needs mentioning here, who welcomed me for a little while.

With respect to the period in Manchester, a great thanks goes out to all who spent their time with me at the MIH. You really made my days back then!

Finally, my family and friends who carried me through a lot in the past years. As this is a thesis in first place just this much: You know how much you mean to me!

„Wir stehen neben einer modernen Litfaßsäule – eine Litfaßsäule, die sich um sich selber dreht. Eine Litfaßsäule, die es einem ermöglicht, ohne sich von der Stelle zu rühren, alle drei darauf angebrachten Plakate zu begutachten. Es ist dreimal das gleiche Plakat.
»Das muss dieser Fortschritt sein, von dem immer alle reden«, sage ich.“

aus „Das Känguru-Manifest“ von Marc-Uwe Kling

1. Table of Contents

2. List of Publications

No	Bibliographic information	Chapter No	Publication status
1	A. Kolmer, L. Kaltschnee, V. Schmidts, L. H. Peeck, H. Plenio, C. M. Thiele, "The influence of electronic modifications on rotational barriers of bis-NHC-complexes as observed by dynamic NMR spectroscopy", *Magn. Reson. Chem.* **2013**, *51*, 695–700. (DOI: 10.1002/mrc.4002) (Supporting Information)	not contained	published (3rd Sept. 2013)
2	I. Timári, L. Kaltschnee, A. Kolmer, R. W. Adams, M. Nilsson, C. M. Thiele, G. A. Morris, K. E. Kövér, "Accurate determination of one-bond heteronuclear coupling constants with "pure shift" broadband proton-decoupled CLIP/CLAP-HSQC experiments", *J. Magn. Reson.* **2014**, *239*, 130-138. (DOI: 10.1016/j.jmr.2013.10.023)	7.2	published (14th Nov. 2013)
3	L. Kaltschnee, A. Kolmer, I. Timári, V. Schmidts, R. W. Adams, M. Nilsson, K. E. Kövér, G. A. Morris, C. M. Thiele, „Perfecting" pure shift HSQC: full homodecoupling for accurate and precise determination of heteronuclear couplings, *Chem. Commun.* **2014**, *50*, 15702-15705. (DOI: 10.1039/C4CC04217D) (Supplementary Information)	7.3.2	published (16th Oct. 2014)
4	M. R. M. Koos, G. Kummerlöwe, L. Kaltschnee, C. M. Thiele, B. Luy, CLIP-COSY: A Clean Inphase Experiment for the Rapid Acquisition of COSY-type Correlations, *Angew. Chem. Int. Ed.* **2016**, *55*, 7655-7659. (DOI: 10.1002/anie.201510938) (Supporting Information)	9.3	published (19th May. 2016)
5	I. Timári, L. Kaltschnee, M. Raics, F. Roth, N. G. A. Bell, R. A. Adams, M. Nilsson, D. Uhrín, G. A. Morris, C. M. Thiele, K. E. Kövér, Real-time broadband proton-homodecoupled CLIP/CLAP-HSQC for automated measurement of heteronuclear one-bond coupling constants, *(submitted to RSC Advances)*	7.4	submitted (02nd June 2016)
6	L. Kaltschnee, K. Knoll, V. Schmidts, R. W. Adams, M. Nilsson, G. A. Morris, C. M. Thiele, Extraction of Distance Restraints from Pure Shift NOE experiments, *J. Magn. Reson.* **2016**, *in press – accepted manuscripts*, (DOI: 10.1016/j.jmr.2016.08.007)	6.2	accepted (16th Aug. 2016)

3. Introduction

Investigating matter at an atomic length scale, to characterize its structure and the dynamics of matter in a way that the relative positions of single atoms are resolved, is a central discipline of chemistry ever since tools to do this have been developed. This results from the fact, that molecular structure and dynamics are inherently linked to the properties of bulk matter (as e.g. used in LCDs [1]), to its reactivity in chemical reactions (e.g. controlling asymmetric synthesis[2]) and to its possibility to interact with living organisms which is a prerequisite for its use as drugs (e.g. to form protein-ligand interaction[3]).
The past century has drastically changed our understanding of the structure and dynamics of matter at the atomic length scale through a number of methods that emerged and now give us the possibility to answer the question from different points of view – with the complete picture of molecular structure that we are interested in certainly only arising from combinations of different methods[4].
X-ray scattering methods give us important insights how atoms are arranged inside crystalline solids – a source of structural knowledge from which structural conclusions are often also transferred to other states of matter. Mass spectrometry has evolved to a highly sensitive and discriminative "balance", which enables structural conclusion to be drawn e.g. from dissociation processes. Computational methods provide tools for modelling interactions at the atomic level, and to derive from that models for solution structure and for its dynamics (amongst other information). Furthermore, spectroscopic methods enable the investigation of energies associated with various atomic interactions, from which structural knowledge can be derived.
This enumeration clearly does not represent all sources of structural information available to the practicing chemist, which cover an essential part of the typical 10 years studies in chemistry.

It is at the heart of this work to add to the development of Nuclear Magnetic Resonance (NMR) spectroscopy, which, for the investigation of solution state samples, has emerged to a truly versatile and indispensable source of structural and dynamic information to physics, chemistry and biology[5-10].
For studying organic molecules by high resolution liquid state NMR[11], the field of pure shift NMR has recently, mainly during the time-course of this work, attracted much interest[12-15], because it significantly pushes the limits of signal resolution in liquid state proton-detected NMR.
More than being a mean to save money during instrument purchase - which is fair-enough by itself -, the new experimental abilities that are brought to liquid state NMR by pure shift methods were source of my excitement to explore this field. It is an essential advantage of pure shift NMR that it enables efficient filtration of the multitude of structural information that can be extracted from NMR spectra to the one information, the user actually is interested in. Figuratively speaking, it is a method to pick-out of the pool of nuclear spin interactions that could be probed just the ones desired, while effectively masking the other ones.
The nuclear spin interactions we were interested in are measured through structural parameters that can be interpreted in terms of molecular structure and dynamics. The development and testing of new experimental pure shift NMR techniques enabling structural parameters to be measured with high accuracy and precision was thereby the main goal of this work.

As the field of pure shift NMR was rapidly emerging by the time I first got into contact with it, I was not quite aware of, where my interest in this field would all lead me to…

4. State of the Art

The introduction describes various different techniques for looking at structure and dynamics of condensed matter at atomic resolution, to provide us with images of how matter looks like and how it behaves at the atomic level. The emphasis of this thesis application of the techniques described in this work is the determination of molecular solution structure and of its dynamics, which is a major field of application of NMR spectroscopy.
For the start it is briefly summarized in section 4.1, which nuclear spin interactions are used throughout this work to derive structural information. This section is intended to cover only the most important aspects for this work and the reader interested in a more complete discussion is referred e.g. to the textbooks by RICHARD ERNST[16], MALCOLM LEVITT[17], JAMES KEELER[18] or the concise work of PETER HORE[19].
In the following it is first described, what sorts of information NMR spectroscopy can offer to solution structure elucidation (section 4.2). The focus hereby is on the structural information that can be used to elucidate the structure of small organic molecules. Methods are described to study the connectivity of atoms within a molecule, i.e. the constitution of the molecule. Furthermore, sources of information of the spatial structure of molecules (their relative configuration and their conformation), intrinsically also containing information about solution dynamics, are described. Methods for data measurement and analysis are described for the nuclear Overhauser effect (NOE) and residual dipolar couplings (RDCs).
Subsequently methods are outlined in section 4.3, which are required for understanding the way modern NMR experiments work. It is the design of multi pulse Fourier-transform NMR experiments[16, 20], which allows quite selectively to measure different interactions of spins with their environment, and thus to emphasize selected structural information in different experiments. Approaches are outlined, which can be used to analyse the (ensemble average) time evolution of the spin systems studied and thus to understand the working principles of multi-pulse sequences.
These concepts are used to highlight developments in the field of pure shift NMR in section 4.4, which is the major field of this work. The field of pure shift NMR is a collection of different experimental techniques masking of homonuclear spin-spin interactions and thus leading to homonuclear decoupled spectra. Techniques are described which can be used for homonuclear decoupling and experiments are summarized, which are designed for solution structure elucidation. As this field has evolved significantly in the past few years (in particular since the start of my doctorate in 2012), this section contains many aspects that were not described at the start of my own investigations.

4.1. Nuclear Spin Interactions in NMR – Setting the Scene

The summary in this section follows the lines of the chapters 2 in refs. [16, 21].

Nuclear spins are described in the literature as properties of atomic nuclei, which can be described in the framework of quantum mechanics. This formalism describes the state of the system by so-called state functions $|\psi\rangle$ and operators for probing physical properties of these state functions. For spectroscopy, which measures differences between different energy levels, it is the Hamilton operator $\hat{\mathcal{H}}$, which is of central importance. This operator probes the energy levels of a system and governs the time evolution of its state, according to the time-dependent Schrödinger equation,

$$\frac{d}{dt}|\psi(t)\rangle = -i\hbar\hat{\mathcal{H}}(t)|\psi(t)\rangle\,. \tag{4.1}$$

The description of NMR experiments in a quantum mechanical framework much benefits from the fact that for interpretation of the results, it is not required to know or to use the complete Hamiltonian $\hat{\mathcal{H}}_{full}$ of the system studied, but that it is rather sufficient to only consider a few terms sometimes called the *nuclear spin* Hamiltonian[16] for NMR $\hat{\mathcal{H}}_{NMR}$. For discussions contained in this work, it is sufficient to consider only three basic terms

$$\hat{\mathcal{H}}_{NMR} = \hat{\mathcal{H}}_Z + \hat{\mathcal{H}}_J + \hat{\mathcal{H}}_{DD} + \dots\,, \tag{4.2}$$

namely the ZEEMAN term $\hat{\mathcal{H}}_Z$, describing interactions between the nuclear magnetic dipole moments with external magnetic fields, the so-called *indirect spin-spin coupling* term $\hat{\mathcal{H}}_J$ and the *direct dipolar coupling* between pairs of nuclear spins, as expressed by $\hat{\mathcal{H}}_{DD}$.
These terms can be expressed in different operator bases (will be introduced later in chapter 4.3.2), such as a Cartesian basis of spin angular momentum operators (e.g. $\hat{I}_{k,x}$, $\hat{I}_{k,y}$, $\hat{I}_{k,z}$, $\hat{I}_{k,x}\hat{I}_{l,x}$, …; k and l are indices for the nuclei considered) and/or a set of raising lowering and polarization operators (e.g. $\hat{I}_k^+$, $\hat{I}_k^-$, $\hat{I}_k^\alpha$, $\hat{I}_k^\beta$, $\hat{I}_k^+\hat{I}_l^+$, …). The construction of these product operator bases, as dependent on the choice of spin system and on the choice of spin basis set they are expressed in, is summarized in refs. [16, 17].
Throughout most discussions, isotopes with the *nuclear spin angular momentum* quantum number $I = ½$ (e.g. ^{1}H, ^{13}C, ^{15}N), often referred to as spin-½ nuclei, will be considered, for which nuclear magnetic quadrupole moments are zero and do not need to be considered in equation (4.2).

4.1.1. Zeeman interaction

The ZEEMAN term describes the interaction of the nuclear spins k with the effective magnetic field $\vec{B}_{\text{eff}}$, at the individual nuclear positions

$$\hat{\mathcal{H}}_Z = -\sum_k \gamma_k \hat{I}_k \vec{B}_{\text{eff},k}(t), \tag{4.3}$$

where γ_k is the gyromagnetic ratio of nucleus k and $\hat{I}_k = \left(\hat{I}_{k,x};\quad \hat{I}_{k,y};\quad \hat{I}_{k,z}\right)$. Note that for convenience, all terms of the nuclear spin Hamiltonian $\hat{\mathcal{H}}_{NMR}$ are reported here in angular frequency units [rad s^{-1}], and that energies can be obtained by multiplication with $\hbar$ (the Planck constant divided by 2π).
The effective magnetic field, $\vec{B}_{\text{eff},k}$ contains a dominant contribution from the static magnetic field $\vec{B}_0$ oriented in the z-direction of the laboratory frame, time dependent contributions from radio-frequency pulses acting as sources of effective additional fields with components in the transverse (x and y) plane, and contributions from the site and orientation dependent chemical shielding σ_k. The structural information contained in the orientation dependence of the chemical shielding[17, 22-28] is not used throughout this work and thus it suffices to say here that for measurements in isotropic solution, and that for describing free evolution of a system under ZEEMAN-interaction, the form

$$\hat{\mathcal{H}}_Z = -\sum_k \omega_{0,k}\hat{I}_{k,z} \tag{4.4}$$

with the site-dependent Larmor frequency

$$\omega_{0,k} = -\gamma_k(1-\sigma_{iso})B_0 \tag{4.5}$$

will be used. For signal assignment purpose in solution, it is common to report *chemical shifts* δ_k instead of Larmor frequencies, which are measured with respect to a given reference frequency:

$$\delta_k = \frac{\omega_{0,k}-\omega_{0,\text{ref}}}{\omega_{0,\text{ref}}} + \delta_{\text{ref}}; \text{ usually in [ppm]} \tag{4.6}$$

Computation of spin system evolution will be performed in a coordinate system rotating around the z-axis at the frequency ω_{rf} where radio-frequency pulses are applied (which usually is close to the Larmor frequency of one specific nucleus). This facilitates the analysis of spin system evolution caused by ZEEMAN interactions through their segmentation into a term $\hat{\mathcal{H}}_{CS}$ describing the evolution through offset from ω_{rf} and a term describing the action of radio frequency pulses $\hat{\mathcal{H}}_{RF}(t)$. In the rotating reference frame, the radio frequency pulses are *de facto* experienced as static additional magnetic fields acting on the spins leading to the form of the ZEEMAN contribution that will be used later:

$$\hat{\mathcal{H}}_Z^{rot}(t) = \hat{\mathcal{H}}_{CS}^{rot} + \hat{\mathcal{H}}_{RF}^{rot}(t), \tag{4.7}$$

with

$$\hat{\mathcal{H}}_{CS}^{rot} = -\sum_k (\omega_{0,k}-\omega_{\text{rf}})\hat{I}_{k,z} = -\sum_k \Omega_k \hat{I}_{k,z} \tag{4.8}$$

and

$$\hat{\mathcal{H}}_{RF}^{rot}(t) = -B_1(t)\sum_k \gamma_k\{\hat{I}_{k,x}\cos(\phi(t)) + \hat{I}_{k,y}\sin(\phi(t))\}. \tag{4.9}$$

In these expressions, Ω_k was introduced as the offset of $\omega_{0,k}$ from the transmitter frequency, the amplitude of the radio frequency pulses is expressed as an effective time-dependent magnetic field $B_1(t)$ they induce at the sample position and $\phi(t)$, referred to as the pulse phase, describes the angle between the effective field $\vec{B}_1$ (which is applied perpendicular to the z-axis) and the arbitrarily chosen x-axis of the rotating frame.

4.1.2. Indirect Spin-Spin Coupling (also: "Scalar Coupling" or "J Coupling")

In the context of this work, it is also sufficient to neglect anisotropic interactions ($\hat{\mathcal{H}}_J^{iso}$) to the indirect spin-spin coupling term $\hat{\mathcal{H}}_J$, for which effective contribution under fast isotropic tumbling is given by

$$\hat{\mathcal{H}}_J^{iso} = 2\pi\sum_{k<l} J_{k,l}\hat{I}_k\hat{I}_l = 2\pi\sum_{k<l} J_{k,l}\left(\hat{I}_{k,x}\hat{I}_{l,x} + \hat{I}_{k,y}\hat{I}_{l,y} + \hat{I}_{k,z}\hat{I}_{l,z}\right). \tag{4.10}$$

The summation herein runs over all coupling pairs of spins k and l and the strength of their coupling is expressed by the isotropic scalar coupling constant $J_{k,l}$. Note that the presence of a non-zero effective coupling even for rapidly and isotropically tumbling molecules has led to the term *scalar coupling* as synonym for the isotropic contribution to indirect spin-spin interaction, which will be used throughout the rest of this work.
Quite frequently, the approximation will be used, that spin coupling evolution by the terms $\hat{I}_{k,x}\hat{I}_{l,x}$ and $\hat{I}_{k,y}\hat{I}_{l,y}$ is averaged to zero effectively by the difference in Larmor precession of spins k and l (*"secular" or "weak-coupling" approximation*). This approximation is good, if the two spins that are coupling with each other have a difference in Larmor frequency that is much bigger than their effective scalar coupling constant $J_{k,l}$. The weak-coupling approximation

$$\hat{\mathcal{H}}_J^{iso} \approx \hat{\mathcal{H}}_J^{iso,weak} = 2\pi\sum_{k<l} J_{k,l}\hat{I}_{k,z}\hat{I}_{l,z} \tag{4.11}$$

normally is considered to be valid, if $2\pi|J_{k,l}| * 10 < |\omega_{0,k} - \omega_{0,l}|$. For heteronuclear scalar coupling interactions, it is fair to assume a validity of the weak coupling approximation for the measurement conditions chosen in this work, while for homonuclear couplings, it may be required to consider the case of strong coupling described by (4.10).

4.1.3. Direct Spin-Spin Couplings (also "Dipolar Couplings")

Whereas for chemical shielding and for scalar couplings it is not essential to describe the anisotropy of the interaction for what is outlined in this work, we cannot do without in the case of direct dipole-dipole interactions. In fact, when considering molecules that rapidly and randomly reorient in isotropic solution, the time average of the direct dipole-dipole contribution to $\hat{\mathcal{H}}_{NMR}$ cancels out.

$$\langle\hat{\mathcal{H}}_{DD}^{iso}(t)\rangle = 0 \tag{4.12}$$

For this reason, direct dipole-dipole couplings are only apparent in studies in isotropic solution through their contribution to relaxation phenomena.
Studies of *residual dipolar couplings* (RDCs) contained in this work however utilize the orientation-dependence of the direct dipole-dipole coupling, for which the Hamiltonian is usually expressed as

$$\hat{\mathcal{H}}_{DD}(t) = \sum_{k<l} b_{k,l}\left\{\hat{I}_k\hat{I}_l - 3\frac{1}{r_{k,l}^2}\left(\hat{I}_k\vec{r}_{k,l}\right)\left(\hat{I}_l\vec{r}_{k,l}\right)\right\}, \text{with } b_{k,l} = \frac{\mu_0\gamma_k\gamma_l\hbar}{4\pi r_{k,l}^3} \tag{4.13}$$

and μ_0 as the vacuum permeability. The time dependence is caused by a possible change of the orientation of the vector $\vec{r}_{k,l}$ connecting the two spins or of its length $r_{k,l}$, through all possible sorts of molecular motions, such as molecular rotation, vibration, changes in conformation and so forth.

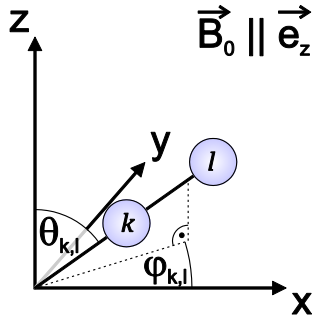

Figure 4.1: Definition of the polar and the azimuthal angles $\theta_{k,l}$ and $\varphi_{k,l}$ between the internuclear vector and the external magnetic field, which is parallel to the static magnetic field. The angular definition is shown for the laboratory coordinate system.

Expression of the orientation of the internuclear vector $\vec{r}_{k,l}$ in terms of polar coordinates (for definition, see Figure 4.1) and using the interrelation between Cartesian operators and raising and lowering operators

$$\hat{I}_k^+ = \left(\hat{I}_{k,x} + i\hat{I}_{k,y}\right) \text{ and } \hat{I}_k^- = \left(\hat{I}_{k,x} - i\hat{I}_{k,y}\right) \tag{4.14}$$

the spin part and the angular part can be factorized out[29], to obtain

$$\hat{\mathcal{H}}_{DD}(t) = \sum_{k<l} b_{k,l}\{A + B + C + D + E + F\} \tag{4.15}$$

with

$$A = \left(1 - 3\cos^2\theta_{k,l}\right)\hat{I}_{k,z}\hat{I}_{l,z} \tag{4.16}$$

$$B = -\frac{1}{4}\left(1 - 3\cos^2\theta_{k,l}\right)\left(\hat{I}_k^+\hat{I}_l^- + \hat{I}_k^-\hat{I}_l^+\right) \tag{4.17}$$

$$C = -\frac{3}{2}\sin\theta_{k,l}\cos\theta_{k,l}\exp\left(-i\varphi_{k,l}\right)\left(\hat{I}_k^+\hat{I}_{l,z} + \hat{I}_{k,z}\hat{I}_l^+\right) \tag{4.18}$$

$$D = -\frac{3}{2}\sin\theta_{k,l}\cos\theta_{k,l}\exp\left(+i\varphi_{k,l}\right)\left(\hat{I}_k^-\hat{I}_{l,z} + \hat{I}_{k,z}\hat{I}_l^-\right) \tag{4.19}$$

$$E = -\frac{3}{4}\sin^2\theta_{k,l}\exp\left(-i2\varphi_{k,l}\right)\hat{I}_k^+\hat{I}_l^+ \tag{4.20}$$

$$F = -\frac{3}{4}\sin^2\theta_{k,l}\exp\left(+i2\varphi_{k,l}\right)\hat{I}_k^-\hat{I}_l^-, \tag{4.21}$$

which is usually called the *dipolar alphabet*.
Very direct use is made of the time average of term A in the analysis of residual dipolar couplings (RDCs) that will be discussed in section 4.2.4. The measurement of RDCs we later use refers to the measurement of time averaged dipolar couplings, which, in comparison to their static counterparts, are largely scaled (typically by a factor of $\sim 10^{-4}$)[30] due to rapid but not fully isotropic molecular reorientation in solution. In this context we predominately measure RDCs between different nuclei, where use of $\langle A(t)\rangle$ is sufficient. However, if RDCs are measured between spins of the same nuclei terms $\langle A(t)\rangle$ and $\langle B(t)\rangle$ need to be considered. The analogy to the case of weak and strong coupling for indirect spin-spin coupling should be noted (equations (4.10) and (4.11)).
Even though it is less apparent from what is outlined below, all terms are used in the description of the nuclear Overhauser effect (NOE) used for distance determination in this work. In the picture of SOLOMON[31], the terms A and B and the terms E and F are the basis for the two opposing mechanisms of two-spin transitions causing the NOE, whereas terms C and D lead to magnetization dissipation from the

system studied. A brief introduction into the use of this effect for interatomic distance measurement in solution is provided in section 4.2.3.

4.2. NMR-based Solution Structure Elucidation of Organic Molecules

When discussing molecular solution structure, the level of detail the structure is reported in, widely varies across the literature. Thus the very different amount of structural information available. It is therefore useful to classify different levels of structural information according to the structural details they contain[32]. A coarse graphical summary is given in Figure 4.2.
Questions of molecular composition, namely what sorts of and how many atoms are contained in one molecule of the substance studied, are most conveniently approached nowadays by mass spectrometry, though other analytical techniques, including NMR, can also provide useful information[33].
Solving the constitutional problem means tracing out which atom is connected to which via chemical bonds (also determining the bond order). This clearly demands knowledge about which atoms are contained in the molecule, at least for those parts of the molecule subjected to constitutional analysis. Constitutional models by themselves do not explicitly contain geometrical information about the geometry of the molecule itself, though for many possible molecular subunits there is good prior knowledge about the geometry they typically adopt in solution.
The configuration of a molecule further distinguishes stereoisomers, namely molecules of identical constitution, which cannot be interconverted without breaking of bonds (including the change of bond order). This includes the relative or absolute orientation of stereogenic elements. Depending on the ability to assign molecules with mirror image relation (enantiomers) or not, the question of absolute configuration can be addressed.
Questions of molecular conformation finally are related to the actual three dimensional structure of the molecule, including the description of bond lengths and of angles between bonds. As molecules are generally flexible, the description of molecular conformation always requires a description of the dynamics of the system. When trying to describe experimental data this most often is tackled by classing molecular motions into those that are fast enough that the observable quantities average over contributions from the different conformations and into those that are so slow, so that the observable quantities yield different values for the different conformations contributing. The question of what is fast and what is slow herein is governed by the method of observation – in our case NMR-spectroscopy.
The strength of solution state NMR is in the determination of molecular constitution, relative configuration and conformation. In terms of the methods used, it is sensible to classify the stages of NMR-based solution structure elucidation into questions of constitution determination and into studies of configuration conformation and of molecular dynamics.

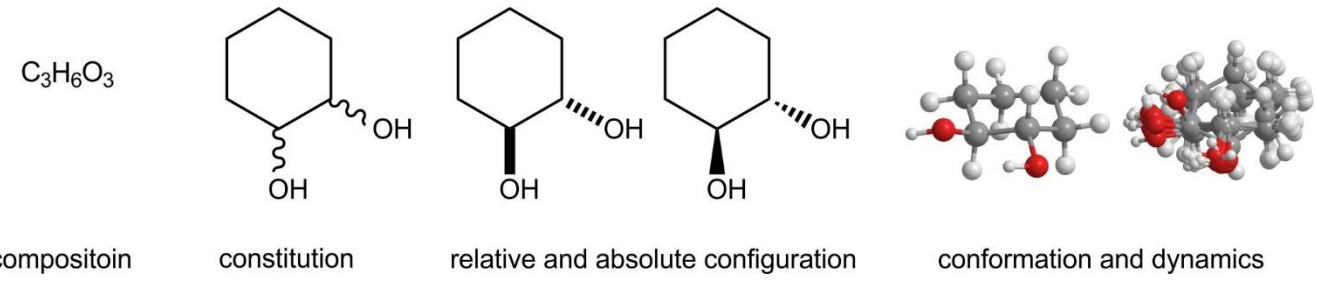

Figure 4.2: Graphical summary of the different stages of describing molecular solution structure, as exemplified for (1S,2S)-cyclohexane-1,2-diol. Models for conformation and dynamics are added only for illustrative purpose, and it is not claimed that these represent the actual solution structure and dynamics of the molecule.

4.2.1. Determination of Connectivity (Constitution)

For determining the connectivity of atoms inside a molecule, it is required to have some observable for different positions inside the molecule, and it is necessary to give direct proof for the existence of a bond between pairs of nuclei. NMR offers a rich toolbox of experiments that can be used for these purposes, which mainly (but not uniquely) use the chemical shift and the scalar *J*-coupling as reporters.

As an identifier for different nuclei k, the ZEEMAN interaction (see equations (4.4) and (4.5)) with the strong static field $\vec{B}_0$ is used, which usually leads to a grouping of the NMR signals into characteristic frequency regions for different isotopes according to γ_k, where within these frequency regions the exact Larmor frequency depends – amongst other factors - on the shielding, which normally is expressed as the chemical shift δ_k. The chemical shifts observed depends on the local electronic environment of the nucleus and thus carries information about the chemical environment of the nucleus. The signal frequencies observed in NMR spectra thus are the major basis for distinguishing different nuclei.
In addition to the signal position in the frequency spectrum, also the signal integral can be used as an important observable. In some experiments, most prominent being the single-scan ^{1}H-spectrum, the signal integral usually reflects the relative number of nuclei contributing to the signals. This provides useful information for constitution determination, possibly revealing (chemical or magnetic) equivalence of nuclei and molecular symmetry.
Bonding networks between nuclei are most often traced out through the (electron-mediated) *J*-coupling, which is regarded as a direct proof for the existence of a network of chemical bonds connecting the two nuclei. *J*-coupling constants also cluster around characteristic values for different bonding situations.
The signal splitting (signal multiplicity) caused by *J*-couplings can be used to identify pairs of spins that share the same coupling constant, as an indication for chemical bonds between the two.
The mightiest methods to trace out bonding networks come through the methods of multidimensional correlation experiments[20] on which I want to expand here:

The appeal of multidimensional correlation experiments[34], as opposed to their one-dimensional counterparts[35], comes through their ability to directly map out interactions in multidimensional fashion, as nicely summarized from the perspective of organic structure determination by TIMOTHY CLARIDGE[11]. The field can roughly be subdivided into methods that correlate nuclei of the same isotope (homonuclear correlation) and those that correlate nuclei of different isotopes (heteronuclear correlations). A graphical overview over the most important techniques is given in Figure 4.2. As in the context of NMR of small organic molecules, homonuclear correlations via COSY, TOCSY, NOESY, ROESY and EXSY are mostly measured for ^{1}H, whereas heteronuclear correlations via HSQC, HMQC, HMBC and HSQMBC experiments are mostly measured between ^{1}H and ^{13}C, explicit statement of the nuclei prefixes "^{1}H-^{1}H" and "^{1}H-^{13}C" will largely be omitted. Other nuclei are also regularly employed in studies of constitution, in particular ^{15}N, ^{19}F and ^{31}P, though not be discussed here.
The most essential correlation experiments for establishing the constitution of small organic molecules most probably are ^{1}H-^{1}H COSY[34, 36] experiments and the combination of ^{1}H-^{13}C HMQC[37, 38] or ^{1}H-^{13}C HSQC[39] with the ^{1}H-^{13}C HMBC[40]. In the simplest case, the COSY experiment enables tracing out the proton skeleton for protonated compartments of the molecule, from which the assignment can be transferred to ^{13}C via HSQC or HMQC experiments. If this assignment strategy fails due to the presence of links inside the molecule that do not carry protons (e.g. quaternary carbon atoms) or because of ambiguities in the assignment, the HMBC experiments helps out with long-range carbon assignments, which can be used to fuse assigned molecular parts or to cross-validate ^{1}H assignments.
When proton spectra become complex, because large molecules are studied it is often very useful to use ^{1}H-^{1}H TOCSY[41, 42] spectra in addition or as alternative to COSY spectra. This experiment enables the

mapping of complete uninterrupted proton *J*-coupling networks, and thus to correlate spins that are part of the same ^{1}H coupling network, even if not significantly coupled to each other. The experiment enables simple grouping of spins into coupling networks, facilitating the signal assignment, and can be used to carry coupling information over sites that are heavily overlapped (e.g. with the solvent signal). Extensive use is made of this experiment for the assignment of peptides.

Where proton coupling networks are interrupted over longer distances, it might be required to use ADEQUATE[43] or INADEQUATE[44] experiments to directly obtain ^{13}C-^{13}C correlation information. Both experiments can be tuned to only show ^{13}C-^{13}C one-bond correlations or to emphasize long-range correlations. These experiments enable the elucidation of the carbon skeleton even for very complex hydrogen-deficient molecules, but suffer from the low ^{13}C natural abundance (1.1%), leading to very low sensitivity if the solutes are not isotopically enriched. These techniques therefore mainly are applied if they are indispensable or if isotopically enriched samples are studied.

Finally, in addition to correlation experiments that map out the *J*-coupling network, important information for constitution determination is often also taken from the nuclear Overhauser effect (NOE)[45, 46] or from chemical exchange.

The physical exchange of nuclei, termed chemical exchange, can be observed e.g. in ^{1}H-^{1}H EXSY spectra[47, 48], if exchange happens between two positions in the molecule or its surrounding leading to different signals in the spectra. Typical cases are aromatic rings flipping slowly between two states[49] or the exchange of labile protons with the solvent. Awareness of these phenomena can be helpful when trying to establish molecular constitution, in particular if the presence of slowly interconverting conformations leads to multiple sets of signals for a single solute[6, 50, 51].

The NOE, as observed e.g. in ^{1}H-^{1}H-NOESY[47, 52-54] or ^{1}H-^{1}H-ROESY[55, 56] experiments is a spin-spin interaction transmitted through space, if the two spins involved are in spatial proximity (normally < 5 Å). It therefore is not a direct evidence for chemical bonding, but can be used as additional source of information. It however is the most frequently used source of information for determinations of configuration and conformation, covered in the following section.

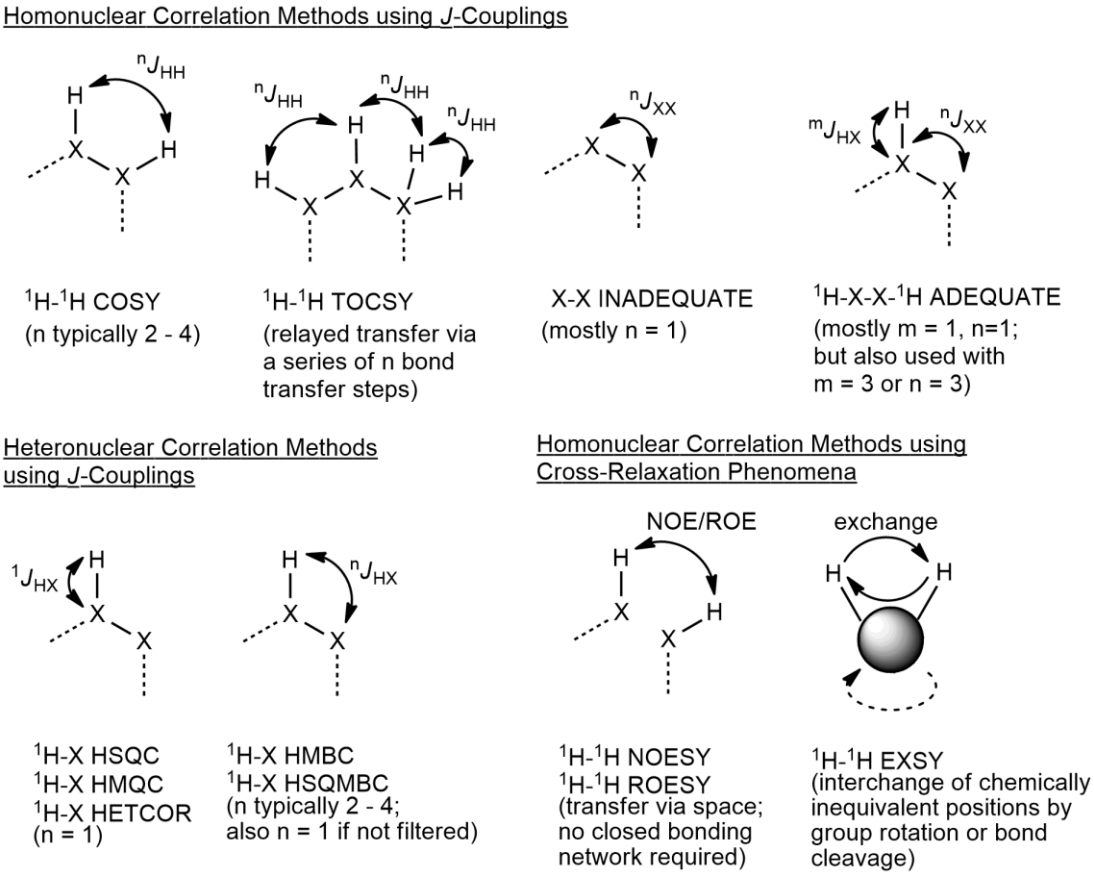

Figure 4.3: Overview of the two-dimensional correlation experiments of most frequent used in constitution determination of small molecules. The content of this figure is adopted from ref. [11].

4.2.2. Methods for Elucidating Spatial Structure by NMR (Relative Configuration and Solution Conformation and Dynamics)

For determining relative configuration or molecular conformation, in general a measurement of interatomic distances and a measurement of angles between sets of atoms is required.
In the previous section, it was already mentioned, that the nuclear Overhauser effect[46] can be used to probe spatial proximity. If measurement conditions are chosen appropriately, this effect can even be used for quantitative measurement of interatomic distances, thus providing a very valuable source of information for determining both relative configuration and molecular conformation[5, 52, 57-60].
The most prominent source of angular information is by the dependence of the $^{3}J_{HH}$ coupling constant on the dihedral angle as described in the model of KARPLUS[61, 62]. Other scalar coupling constants, such as $^{2}J_{H,C}$ and $^{3}J_{C,H}$ couplings can further provide angular information, if suitable parametrization accounts for the effect of different chemical environments[63-65].
Dipolar couplings finally depend on both interatomic distances and angles (see equation (4.13)) and thus provide a parameter that can be used for accessing both sources of information. In the context of solution state NMR, however, dipolar coupling uses the angular information that can be extracted for pairs of nuclei with comparably well-known (average) distance. Major parts of this work will be devoted to the measurement of residual dipolar couplings (RDCs), which emerged as a rich source of structural information for studies of small molecules[66, 67] and biomacromolecules[30, 68]. Measurement of cross-correlated relaxation phenomena in addition can be used as a direct access to projection angle information relating two bonds[69, 70], though applications thus far have been mainly limited to studies using isotopic enrichment. Furthermore, the analysis of the residual chemical shift anisotropy can also be used in small molecule studies[24, 28].

Methods for measuring and interpreting NOE and RDC data, later used in this work, are summarized below.

All of these techniques are probes for molecular geometry in solution. As, however, the geometry of molecules in solution is not fixed, but constantly changes due to molecular motion all of these probes for molecular geometry have in common that for interpretation of the values measured, in principle a picture for molecular structure representing the geometry and its dynamics has to be used.
Many aspects of molecular dynamics e.g. molecular vibration, happen on a timescale that is too fast for NMR to resolve the motion. For such cases, the observables obtained will represent some sort of average value containing contributions from all conformations rapidly interconverting[60, 70-77]. Comparably simple interpretation in the framework of a static average solution structure can be possible, if the molecule is rigid enough to not undergo large amplitude conformational changes. If however, the molecule studied is flexible, structure modelling has to find representations of the solution structure representing these average quantities[9, 46, 60, 71, 74, 75, 78-83]. The challenges inherent in finding good representations of the average solution structure, e.g. by means of simulated annealing protocols[84, 85], can be considerable, and further ambiguities in data interpretation can easily arise, as only average quantities are experimentally available.

4.2.3. Interatomic Distance Measurement in Solution using the Nuclear Overhauser Effect (NOE)

Explanation in this section follows the lines of chapter 9 in ref. [18] and of chapters 2 - 4 in ref. [46].

The interaction of an isolated spin-½ nucleus with an external magnetic field via the ZEEMAN-interaction leads to a splitting in the energy level diagram of the system. The corresponding eigenvalues, termed α and β here, which are separated by an energy difference

$$E_\alpha - E_\beta \approx \hbar\gamma_k B_0, \tag{4.22}$$

if the small contribution from the chemical shielding is neglected. The energy level diagram is illustrated in Figure 4.4 A). When probing, the system, there is a preference of finding the system in the energetically lower state of the two, in accordance to the Boltzmann's distribution. In NMR we are usually inspecting a big number N of identical spin systems, and it is common to speak of the populations n_α and n_β, as the number of systems being found in either of the two states.
The higher population of one of the states at equilibrium results in a non-zero sample magnetization along field axis, which (assuming $|E_\alpha - E_\beta| \ll k_B T$) given by

$$M_z^0 = \frac{1}{2}\hbar\gamma_k\left(n_\alpha^0 - n_\beta^0\right) = \frac{\hbar^2\gamma_k^2 N B_0}{4k_B T}. \tag{4.23}$$

Coupling to a thermal bath (the "lattice") enables transitions of the individual spins. This allows the populations to return to thermal equilibrium values n_α^0 and n_β^0, as described by a first order rate law.

$$\frac{d}{dt}n_\alpha = -\frac{d}{dt}n_\beta = -W_1(n_\alpha - n_\alpha^0) + W_1\left(n_\beta - n_\beta^0\right) \tag{4.24}$$

For the rate constant W_1 I use the subscript 1 to indicate, that the transition is associated with a net change of spin angular momentum by $1 * \hbar$, to be consistent with what follows.

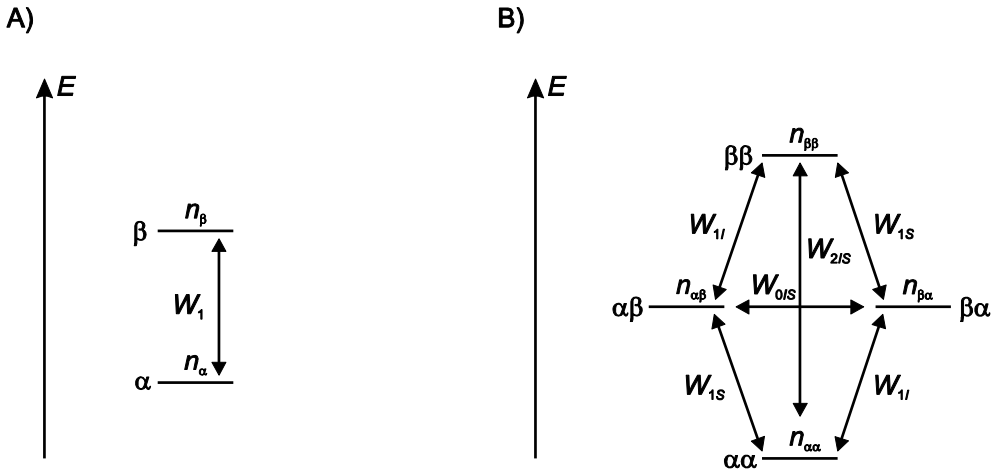

Figure 4.4: Energy level diagrams for A) a one-spin-½ and B) a homonuclear two-spin-½ system. Both diagrams only show contributions from the Zeeman interaction and neglecting chemical shielding. The diagrams are drawn for a nucleus with positive gyromagnetic ratio. The populations *n* are only physically meaningful, when considering large ensembles of identical spin systems.

In complete analogy, for a homonuclear two-spin-½ system, the energy level diagram representing pure ZEEMAN-interaction with the external field is shown in Figure 4.4 B). It should be noted that the effects of chemical shielding, indirect and direct spin-spin couplings are not represented in the energy level diagram.
In addition to transitions of only one of the spins called I and S, also simultaneous transitions for both of the spins are possible. Rate constants for transitions of only one spin are called W_{1I} and W_{1S} and rate constants for simultaneous transition of both spins are called W_{0IS} and W_{2IS}.
If again considering a large ensemble of spin systems, rather than a single one, rate laws for the net magnetic moments $\bar{I}_z$ and $\bar{S}_z$ of each of the spins can be found, known as the Solomon equations[31].

$$\frac{d}{dt}\bar{I}_z = -(W_{0IS} + 2W_{1I} + W_{2IS})(\bar{I}_z - \bar{I}_z^0) - (W_{2IS} - W_{0IS})(\bar{S}_z - \bar{S}_z^0) \tag{4.25}$$

$$\frac{d}{dt}\bar{S}_z = -(W_{0IS} + 2W_{1S} + W_{2IS})(\bar{S}_z - \bar{S}_z^0) - (W_{2IS} - W_{0IS})(\bar{I}_z - \bar{I}_z^0) \tag{4.26}$$

$\bar{I}_z^0$ and $\bar{S}_z^0$ hereby represent the thermal equilibrium values of $\bar{I}_z$ and $\bar{S}_z$ respectively. The net magnetic moments $\bar{I}_z$ and $\bar{S}_z$ thus depend on each other, if the so-called cross-relaxation rate $\sigma_{IS} = W_{2IS} - W_{0IS}$ is non-zero. Similar equations can be found, which describe the relaxation processes in a direction orthogonal to the static magnetic field, leading to the rotating frame nuclear Overhauser effect (ROE), which can also be used for distance measurements[41, 55, 56, 86-88]. This sort of mixing can be advantageous for studies of systems, where the NOE cancels out because of $W_2 = W_0$, but the ROE does not. It further can be useful for distinguishing dipole-dipole cross relaxation from other sources of cross-relaxation, such as chemical exchange.
For arbitrarily large spin-systems, the Solomon equations can be generalized to sets of coupled first order differential equations, as outlined e.g. in refs. [16, 53, 89].

The most commonly used model which is used to interpret interatomic cross-relaxation in terms of the nuclear Overhauser effect is to assume that only direct dipole-dipole couplings contribute to the transition rates W. As shown in section 4.1.3, dipole-dipole interactions are orientation-dependent and thus change upon reorientation of the molecule in space. Molecular tumbling in solution thus induces a fluctuation of the energy eigenvalues, which can induce transitions.
When assuming fully random isotropic reorientation of a rigid molecule in a strong static field and the sole contribution of direct dipole-dipole couplings[90]

$$W_{1I} = \frac{3}{40} b_{IS}^2 j(\omega_{0,I}) \tag{4.27}$$

$$W_{1S} = \frac{1}{20} b_{IS}^2 j(\omega_{0,S}) \tag{4.28}$$

$$W_{0IS} = \frac{1}{20} b_{IS}^2 j(\omega_{0,I} - \omega_{0,S}) \tag{4.29}$$

$$W_{2IS} = \frac{3}{10} b_{IS}^2 j(\omega_{0,I} + \omega_{0,S}), \tag{4.30}$$

where again

$$b_{k,l} = \frac{\mu_0 \gamma_k \gamma_l \hbar}{4\pi r_{k,l}^3}, \tag{4.31}$$

As previously defined in equation (4.13). The term $j(\omega)$ is the reduced spectral density, which in for the case of isotropic tumbling of a rigid molecule is given by

$$j(\omega) = \frac{2\tau_c}{1 + \omega^2 \tau_c^2}. \tag{4.32}$$

For this case, the spectra density only depends on the correlation time τ_c, characterizing how rapidly the molecule typically tumbles in solution. If required, it is also possible to use different motional models, to describe conformational flexibility inside the molecule, or anisotropic tumbling of the molecule.[46, 70, 71].

As can be seen, for the rigid molecule we are considering, the cross relaxation rate σ_{IS} directly depends on b_{IS}^2, from which

$$\sigma_{IS} \propto r_{IS}^{-6}. \tag{4.33}$$

This dependency can be used to calculate interatomic distances, from a known calibration distance, inside of rigid molecules or molecular fragments.

Quantitative measurement of cross-relaxation rates in complex spin systems can be achieved in transient NOE or ROE measurements, which generate a non-equilibrium state of longitudinal or transverse magnetization and monitor its kinetics of relaxation back to equilibrium.
Generation of the non-equilibrium state of magnetization was traditionally achieved through saturation of one spin by continuous irradiation at its Larmor frequency[91], though this method has been largely replaced by techniques using selective inversion of spins or using frequency labelling in an indirect spectral dimension for creation of the non-equilibrium state.
The phase-sensitive NOESY experiment[47, 52, 92, 93] (see Figure 4.5 A)) is amongst the most widely used techniques for measurement of cross-relaxation. It uses a frequency labelling in the indirect spectral dimension to generate the state of non-equilibrium magnetization and thus provides access to 2D spectra directly showing peaks from longitudinal magnetization transferred from one frequency to another via cross-relaxation processes. Peaks that end up on the frequency diagonal will be referred to as *diagonal peaks*. Peaks that are found off the frequency diagonal are caused by magnetization transfer via at least one magnetization transfer step and will be termed *cross peaks*. The time evolution of longitudinal relaxation can be traced over a variable time period, called the mixing time τ_m, by extraction of signal integrals from a 2D spectrum. Possible interference from COSY-type cross-peaks, often referred to as zero-quantum artefacts in the context of NOE measurement, can be counteracted by methods of z-filtration[94-96].
The technique can be extended to higher dimensionalities[97] and can be used with frequency encoding using a heteronucleus e.g. in HMQC-NOESY experiments[98, 99] to improve signal dispersion in different frequency dimensions.
The generation of non-equilibrium states by frequency labelling is also used in ROESY techniques[55, 56], which use spin-locking pulses for mixing to trap transverse magnetization along a fixed axis. It is possible

to counteract the inherent problems of using spin-locking pulses for mixing, namely the simultaneous evolution of TOCSY-like coherence transfer and a chemical-shift dependent variation of the spin-lock strength, by off-resonance spin-locking at different frequencies[87, 88]. These techniques enable direct use of ROESY experiments for quantitative measurements of cross-relaxation rates.
In contrast to NOESY and ROESY techniques which map out the full cross-relaxation network in the chosen multidimensional spectral range, 1D selective NOE and ROE techniques can be used to probe individual cross-relaxation pathways in devoted 1D spectra[35], which can bring time-savings if the number of NOEs/ROEs to be measured is small. Of particular note should be gradient filtered variants[100] using the *double pulse field gradient spin echo* (DPFGSE) for selective inversion of one particular frequency[101, 102] (see Figure 4.5 B)). This selective inversion element effectively suppresses signals not selectively inverted, and thus provides high quality spectra with very little interference from subtraction artefacts (the counterpart to t_1-noise in 2D NOESY) that previously was interfering with the detection of very weak NOE cross-peaks. In contrast to 2D NOESY, only magnetization transfer from the selectively inverted spin can be traced. In the case of 1D selective NOE experiments, the terms *selectively inverted peak* and *NOE peak* will be used as the respective counterparts to *diagonal peak* and *cross peak* used in NOESY.

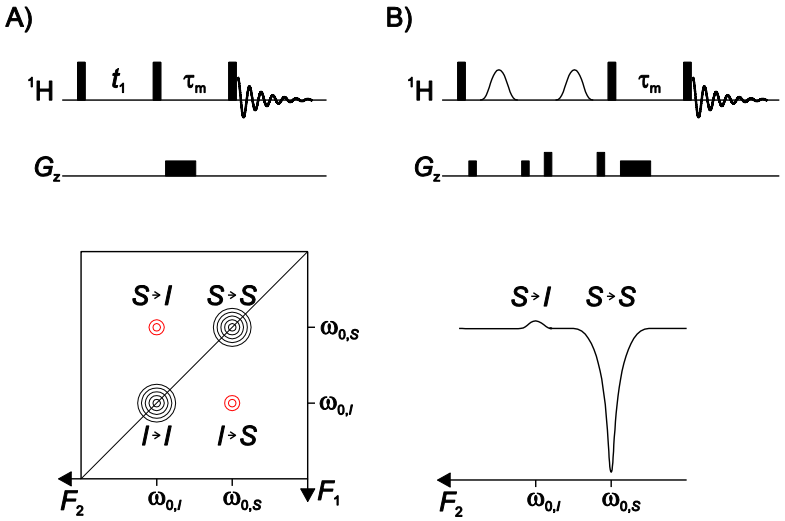

Figure 4.5: Typical gradient selected NOE experiments as simplified pulse sequence schemes and a schematic representation of the spectra obtained. A) ^{1}H-^{1}H NOESY with the corresponding 2D-NOESY, B) DPFGSE-NOE experiment with the corresponding 1D NOE spectrum that may be obtained by inversion of *S*. For simplification, no pulse phases are given and possible inversion pulses during τ_m are omitted.

Quantitative extraction of cross-relaxation rates from transient NOE and ROE experiments in this thesis is performed using measurements with small mixing time τ_m. This is a very common choice, even though for small mixing times the intensity of the *cross* or *NOE peaks* containing distance information is small. The advantage of this approach is, that for small mixing times, the kinetics of magnetization transfer occurring in complex spin systems still follow the rate-laws (4.25) and (4.26) to good approximation[53]. The aim is to exclude magnetization transfer steps involving more than two spins, referred to in the literature as *spin diffusion*, to sufficient extent to obtain unbiased results from the simpler two spin analysis. In this limit one simply obtains

$$\frac{d}{d\tau_m}\bar{I}_z(\tau_m)\Big|_{\tau_m\to 0} = \sigma_{IS}\bar{S}_z^0, \tag{4.34}$$

where $\bar{I}_z(\tau_m)$ is measured from the integral of the *cross peak* or *NOE peak* respectively and $\bar{S}_z^0$ is the integral for the *diagonal peak* or *selectively inverted peak* in a reference experiment with $\tau_m = 0$. The range of mixing times where a simplified analysis can be performed can be significantly extended to larger τ_m by normalization with the integrals from *diagonal peak* or *selectively inverted peak* measured at the same mixing time[103, 104], an approach used later in Project A.

An alternative approach would be to extract the desired cross relaxation rates from a truncated[53, 105] or from a full relaxation matrix analysis[81, 106, 107], which allows to fit even later points during the relaxation process. For experiments measured in fast succession, also the effect of truncated relaxation may be considered[108, 109].

4.2.4. Residual Dipolar Couplings (RDCs) in Solution Structure Elucidation of Small Molecules

As described in section 4.1.3, the direct dipole-dipole coupling is dependent on both the distance between two spins interacting and on the orientation of the internuclear vector with respect to the external magnetic field. This interaction therefore contains a wealth of structural information, if it can be measured and interpreted. This has been recognized since the early days of NMR spectroscopy[110].
As stated before, in isotropic solution, dipolar couplings very effectively average to zero, due to fast isotropic molecular tumbling. They are however a dominant interaction in the solid state and in liquid phases with a preferential molecular orientation, due to the large dipole-dipole coupling constant $b_{k,l}$ (see equation (4.13)), which can easily exceed 10kHz for pairs of protons.
In terms of high-resolution solution structure elucidation, measurements of dipolar couplings that appear largely scaled (typically by a factor of $\sim 10^{-4}$)[30], called *residual dipolar couplings*, have evoked large interest[66, 67, 111-113]. In these studies, the RDCs are ideally just large enough (say not exceeding a range of -20 Hz to +10 Hz for $^1D_{CH}$ in small molecules; measurement uncertainties are normally around ± 1 Hz for these systems) to provide the angular solution structure information desired, while keeping the spectral quality at an acceptable level for high resolution structure analysis of complex molecules.
In the following it will be reviewed how experimental RDC data can be used to derive structural information, I will summarize how for small molecules RDCs can be rendered observable through the use of suitable *alignment media* and I will summarize important experimental techniques for the measurement of RDCs and.

4.2.4.1. A model for describing and interpreting RDCs in the framework of a rigid molecular structure.

The discussion outlined will be restricted to the case of a rigid molecule, tumbling fast in solution, but having a preferential spatial orientation. From equation (4.15) we recall that

$$\hat{\mathcal{H}}_{DD}(t) = \sum_{k<l} b_{k,l}\left(1 - 3\cos^2\theta_{k,l}\right)\left(\hat{I}_{k,z}\hat{I}_{l,z} - \frac{1}{4}\left(\hat{I}_k^+\hat{I}_l^- + \hat{I}_k^-\hat{I}_l^+\right)\right), \tag{4.35}$$

when not considering terms $C - F$, which is appropriate for describing direct dipole-dipole coupling evolution, but not the relaxation phenomena associated with it, under the effect of a strong external magnetic field $\vec{B}_0$[21]. When considering the case of a molecule tumbling fast in solution (with the smallest correlation time about the principal axes of molecular reorientation being much smaller than ${b_{k,l}}^{-1}$), it is the time average of the interaction that is governing the direct dipole-dipole coupling evolution. We therefore try to evaluate

$$\langle\hat{\mathcal{H}}_{DD}(t)\rangle = \sum_{k<l}\langle b_{k,l}\left(1 - 3\cos^2\theta_{k,l}\right)\rangle\left(\hat{I}_{k,z}\hat{I}_{l,z} - \frac{1}{4}\left(\hat{I}_k^+\hat{I}_l^- + \hat{I}_k^-\hat{I}_l^+\right)\right), \tag{4.36}$$

Where angular brackets indicate the time average quantities. Considering a rigid molecular structure, the time dependency of $b_{k,l}$ vanishes, so we are left with the challenge to describe the time average angle the molecular bonds takes with respect to the magnetic field. When discussing this average orientation, it is convenient to perform a coordinate transformation from the laboratory frame within which equation (4.15) is described, into a coordinate system, which tightly follows the tumbling of the molecule in solution, the so-called *molecular frame of reference*. In the molecular frame of reference, the coordinates of the atoms remain fixed, while the orientation of the magnetic field is tumbling as a consequence of molecular reorientation, as illustrated in Figure 4.6.

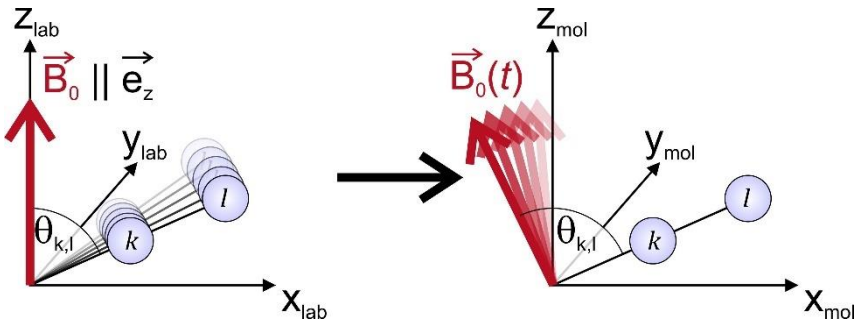

Figure 4.6: Schematic representation of the coordinate transformation from the laboratory frame of reference to the molecular frame of reference for a single selected pair of nuclei.

For expressing the average orientation of $\vec{B}_0$ in the molecular fixed frame we evaluate $\langle\cos^2\theta_{k,l}\rangle$ by

$$\begin{aligned}\langle\cos^2\theta_{k,l}\rangle &= \langle\left(\vec{e}_b(t)\vec{e}_{k,l}\right)^2\rangle = \langle\left(\vec{e}_b{}^T(t)\vec{e}_{k,l}\right)\left(\vec{e}_b{}^T(t)\vec{e}_{k,l}\right)\rangle = \langle\left(\vec{e}_{k,l}{}^T\vec{e}_b(t)\right)\left(\vec{e}_b{}^T(t)\vec{e}_{k,l}\right)\rangle \\ &= \vec{e}_{k,l}{}^T\langle\vec{e}_b(t)\vec{e}_b{}^T(t)\rangle\vec{e}_{k,l},\end{aligned} \tag{4.37}$$

where the time dependence of the magnetic field orientation can be separated out through commutation in the first scalar product[114]. The vectors $\vec{e}_b$ and $\vec{e}_{k,l}$ are unit vectors which are parallel to the magnetic field orientation and the bond orientation, respectively. The matrix $\boldsymbol{P} = \langle\vec{e}_b(t)\vec{e}_b{}^T(t)\rangle$ thereby is describing the probability distribution describing the orientation of $\vec{B}_0$ in the molecular reference frame. Caused by normalization ($\mathrm{tr}\{\boldsymbol{P}\} = 1$) and symmetry ($P_{xy} = P_{yx};\ P_{xz} = P_{zx}; P_{yz} = P_{zy}$) of $\boldsymbol{P}$, it can be described by five independent variables.
In the context of NMR, it is common to use the alignment tensor $\boldsymbol{A}$ for describing molecular alignment, which is[114]

$$\boldsymbol{A} = \boldsymbol{P} - \frac{1}{3}\mathbf{1}, \tag{4.38}$$

so that for a given internuclear orientation (as expressed in the molecular reference frame)

$$\vec{e}_{k,l}{}^T\boldsymbol{A}\vec{e}_{k,l} = \vec{e}_{k,l}{}^T\boldsymbol{P}\vec{e}_{k,l} - \frac{1}{3}\mathbf{1}\vec{e}_{k,l}{}^T\vec{e}_{k,l} = -\frac{1}{3}\langle\left(1 - 3\cos^2\theta_{k,l}\right)\rangle. \tag{4.39}$$

With knowledge of the alignment tensor, the residual dipolar splitting, expressed by the effective dipolar coupling constant (expressed here in [rad s^{-1}])

$$D_{k,l} = \frac{1}{2}\langle b_{k,l}\left(1 - 3\cos^2\theta_{k,l}\right)\rangle = -\frac{3}{2}b_{k,l}\vec{e}_{k,l}{}^T\boldsymbol{A}\vec{e}_{k,l}, \tag{4.40}$$

can therefore be computed and the average Hamiltonian for describing spin system evolution neglecting relaxation processes can be written in the form

$$\langle\hat{\mathcal{H}}_{DD}(t)\rangle = \sum_{k<l} 2D_{k,l}\left(\hat{I}_{k,z}\hat{I}_{l,z} - \frac{1}{4}\left(\hat{I}_k^+\hat{I}_l^- + \hat{I}_k^-\hat{I}_l^+\right)\right). \tag{4.41}$$

The question now arises, how to determine $\boldsymbol{A}$.

Determination of the alignment tensor $\boldsymbol{A}$ in most cases is performed from the set of RDCs measured for structure elucidation and a best fit solution of $\boldsymbol{A}$ is determined during the process of determining consistency of the structural proposal with the experimental data. This is because direct prediction of $\boldsymbol{A}$ for small molecules still is not a routine tool[115].
Therefore, the typical method for analysing RDCs of small molecules is to measure a set of RDCs experimentally and uses a structural proposal previously generated to determine the alignment tensor that describes the experimental values best $\boldsymbol{A}_{opt}$ by singular value decomposition[116] (note that in ref. [116], the symbol $\boldsymbol{A}$ has a different meaning and that the Saupe tensor is used instead).

From $\boldsymbol{A_{opt}}$ and the structure proposal, a set of back-calculated RDCs is obtained, which can be checked for consistency with the experimental RDCs. A lack of consistency can be used to falsify structural proposals.
It should be noted, that this approach to RDC-based structure analysis requires that the system of equations describing the alignment tensor is overdetermined during the singular value decomposition, resulting in the requirement that a minimum number or experimental RDCs needs to be measured. This poses challenges to NMR methods development, because it is desirable to extract as many RDCs as possible from the rigid molecular fragments for good definition of the alignment tensor. Using various different sorts of RDCs[117] can be valuable for restricting the analysis to small molecular fragments that can be assumed to be rigid (or described by an appropriate motional model), and to avoid carrying out an analysis in the presence of high conformational flexibility[77].
For expressing the agreement between experimental RDCs and back-calculated RDCs, typically plots comparing the two sets of RDCs are shown[118] and quality factors[76, 119] with different effects of error-weighting are used.

In the framework of the model outlined, rigid molecular fragments of molecules can be analysed. For models describing molecular flexibility in the models, the reader is referred to the literature[74, 75, 80, 120-128]. Suffice to say, that in particular when trying to describe conformational flexibility, generally there is an increased requirement for measuring as many RDCs as possible with the maximum obtainable accuracy. This is a major challenge for both the development of suitable alignment media and for the development of NMR techniques for RDC measurement.

4.2.4.2. Alignment Media for Small Molecule RDC Studies

For introducing the weak preferential orientation of small molecules suitable for RDC measurement, it is common to use oriented media[66, 112]. These induce, by virtue of molecular interactions a preferential orientation onto the molecules dissolved therein. Two main strategies have emerged, namely the use of lyotropic liquid crystalling phases (LLCs) which orient themselves with respect to the external magnetic field of the spectrometer, and the use of cross-linked polymer gels, which are swollen with different degrees of swelling in different spatial directions (SAG; *strain-induced alignment in a gel*). Further alignment media are also grouped into water based media and media compatible with organic solvents. A full review is out of the scope of this work and I will focus on only a few selected media. The reader is referred to refs. [112, 129] for a joint discussion of water based alignment media and media compatible with organic solvents or to ref. [130] for the sole discussion of water based media.

Liquid lyotropic phases (LLCs), formed by a phase builder with large anisotropy of shape and a solvent, can introduce suitable alignment for RDC measurements. Characteristic features of this class of alignment media are comparably easy and rapid preparation of the alignment medium (provided the phase builder is available) and the ability to tune the strength of the alignment by both temperature and the concentration of the phase builder. Changes of the concentration of the phase builder however are limited by its solubility in the solvent and by the lower critical concentration for forming the liquid crystalline phase[131]. The latter can be interfering with the desire to create alignment media which induce only a weak alignment. If degrees of alignment are too large, the RDCs may be scaled by variable-angle sample spinning[132]. Many LLC-based alignment media alignment media use chiral phase builder, which leads to the advantage of the possible enantiodifferentiation in these media.
Prominent water based LLC alignment media use phospholipid bicelles[133-135], bacteriophage virus particles with rod-like shape[136, 137] and so-called Otting-phases[138]. In aqueous solution, it is particularly important to consider the compatibility of the molecule to be studied with the surface charge of the phase builder. Some phase builder, a notable case being bacteriophage virus particles, carry high surface charge which can induce too strong alignment, if the molecule studied is stuck to the phase builder by coulomb interaction. Also limitations in the pH-regimes may be necessary to consider.

The biggest class of LLC phases compatible with organic solvents is that of homopolypeptides, including Poly-γ-benzyl-L/D-glutamate (PBLG and PBDG)[131, 139, 140], Poly-γ-ethyl-L-glutamate (PELG)[141, 142] and Poly-ε-carbobenzyloxy-L-lysin (PCBLL)[141]. They form stable alignment media with many apolar organic solvents, such as $CDCl_3$, CD_2Cl_2 and THF, and can be used to study a broad range of apolar solutes. Helically chiral polyacetylene-based alignment media[143] have been synthesized, which enable the measurement of high quality spectra in $CDCl_3$-based media. Furthermore, an LLC based alignment medium being compatible with DMSO was recently presented, which uses dispersions of graphene oxide particles that are stabilized by grafting of polymer brushes[144, 145].

Lower-bound limits of the degree of alignment can be circumvented when using the SAG approach[146, 147]. This approach uses a cross-linked polymer gel, which is swollen in a way that cavities with anisotropic shape are created. The anticipated mode of action is that solutes that permeated the gel by diffusion interact with the polymer network of anisotropic shape and thus orient with respect to the anisotropy.
The clear advantages of this approach is the scalability of the alignment to very low degrees of orientation. For tuning the degree of alignment in such gels, devices for compressing and stretching the gels are available[148-150]. Another method for scaling the strength of the alignment is to use different orientations of the gel with respect to the magnetic field[28]. Also combinations of alignment media are possible by trapping of field-oriented LLCs inside gel matrices[151, 152].
Disadvantages inherent in the SAG approach mainly are related to their sample preparation. Swelling of the gels may be time consuming and even more importantly, diffusion of the solute into the gel may require long equilibration periods. Furthermore, the gels may show inhomogeneity of the swelling due to friction and may even break as a consequence of mechanical stress.
The most prominent water based gel-matrix used for weak alignment is poly(acrylamide) and partially charged polymer matrices thereof[147, 153-155]. Gels with inherent handedness could be obtained for example using stretched gelatine gels[156].
Compatibility with polar aprotic solvents is much less problematic than it is for LLCs and alignment media are available which show compatibility with a large variety of solvents, e.g. poly(acroylonitrile)[157] or crosslinked gelatine[156], though the availability of gels cross-linked by accelerated electrons may be limited. Chemically cross-linked polymer gels e.g. poly(styrene) cross-linked with divinylbenzene[158] are viable alternatives.

4.2.4.3. Experiments for Measurement of RDCs in Small Molecules

As stated previously, when using RDCs for structure analysis, it is essential to measure as many experimental RDCs as possible with the best accuracy available. Sample preparation is an essential step for obtaining large sets of experimental data, because inappropriate alignment conditions can easily lead to quite severe degradation of the spectral quality. The facts that sample preparation often is laborious whereas it is generally not possible to predict which alignment media are suitable for a given solute result in the desire to figuratively “squeeze” as many RDCs as possible out of a sample that has been prepared.

In the limit of weak alignment, which the discussions in this thesis is limited to, RDCs arise as an apparent additional contribution to the total coupling constant $T_{k,l}$. We will use in the heteronuclear case

$$T_{k,l} = J_{k,l} + 2D_{k,l}. \text{ (all coupling constants expressed in [Hz])} . \qquad (4.42)$$

Separation of the two contributions to $T_{k,l}$ is normally achieved by performing two different sets of measurements. First measurement in an isotropic medium provides $J_{k,l}$ and subsequent measurement of $T_{k,l}$ in anisotropic solution then enables the extraction of the RDC by simple subtraction. The inherent assumption that the molecular conformation does not change by change of the medium may not always be valid.
For small molecules, measurement of RDCs is solely based on measuring frequency differences between signal multiplet features, though in principle also intensity-based extraction methods, as used in studies of biomacromolecules[159], could in principle be employed. In the following, methods are grouped

according to the dipolar couplings that can be probed. Even though methods derived for *J*-coupling constant extraction are often also suitable for RDC extraction, I will restrict the discussion to methods that have already proven suitable in practical tests.

Heteronuclear one-bond RDCs (e.g. $^1D_{CH}$, $^1D_{NH}$*)* are the most easily accessible RDCs, because (in absolute value) they are often the biggest RDCs. In most cases, they are measured as a small additional contribution to the apparent heteronuclear splitting already present due to the scalar *J*-coupling. Keeping them smaller than the *J*-coupling (with additional knowledge of the sign of one-bond couplings) has the nice effect that their sign, which is informative in RDC analysis, can be extracted from equation (4.42) even in sign-insensitive measurements.
In the small molecule context, heteronuclear one-bond RDCs are mostly measured from gradient-selected HSQC variants, acquired without heteronuclear decoupling in one of the spectral dimensions. Methods are described for measurement of $^1T_{XH}$ along the (indirect) X-dimension and along the (direct) ^{1}H-dimension. For example, simply removing the ^{1}H-decoupling from the X-dimension[160] can be used for $^1T_{XH}$ measurement. The inherent problem of these techniques to require very long measurement times for obtaining sufficient signal resolution can be counteracted by *J*-scaling[118, 161]. The inherent loss in resolution impaired by the doubling of the resonances can be efficiently counteracted by the so-called IPAP principle[162], which later found ample use, because it enables coupling constant measurements when doublet components are not resolved.
Unfortunately, these approaches suffers from the additional observation of long-range interactions ($^nT_{XH}$) in the X-dimension, leading to the broadening of lines in that spectral dimension. It was soon recognized, that this line broadening is limiting the accessible accuracy of the measurement, a problem that could be reduced through the introduction of a BIRD-filter, which leads to suppression of long-range couplings between ^{1}H and the X-nucleus[163]. A problem that persisted in all F_1-coupled HSQC experiments is their inherent disability to provide separate values for chemically inequivalent ^{1}H, bound to the same X-nucleus. This could be solved using an HMQC-like *J*-scaling period in these experiments[164].
The inherent problem of these methods, that the couplings are measured along the X-dimension, where achieving a high resolution is a time-consuming task can be counteracted by non-uniform sampling methods[165], yet for small molecules, there is another good alternative:
Of particular use nowadays are the CLIP- and the CLAP-HSQC experiment[166], which enable rapid and accurate measurement of $^1T_{XH}$, by measurement of the coupling along the high-resolution direct dimension. The particular benefit of these experiments is, that heteronuclear anti-phase contributions to the signal are effectively suppressed. The disadvantage of these methods however is, that again long-range couplings (this time $^nT_{HH}$) broaden the signals, which again can be limiting experimental accuracy. Much of the following work directly is related to the circumvention of this problem, with the aim to restore the ability of extracting $^1T_{XH}$ coupling constants from narrow signals.
Though not related to signal narrowing, it should be noted, that recently an F_2-coupled HSQC experiment with efficient filtration of both homo- and heteronuclear antiphase contribution, the PIP-HSQC was presented[167]. As in the original CLIP/CLAP-HSQC, the signals appear broadened by long-range couplings in the spectra. The application to RDC measurement has not been demonstrated for this experiment.

One-bond homonuclear RDCs for heteronuclei (e.g. $^1D_{CC}$*)* have rarely been measured in the context of small-molecule NMR due to the inherent low sensitivity of the measurement. If required however, $^1D_{CC}$-couplings can be extracted from INADEQUATE experiments[168, 169]. Alternatively, *J*-modulated ADEQUATE experiments can be used[170-172].

Long-range homonuclear RDCs for protons (i.e. $^nD_{HH}$*)* are not as frequently used in small-molecule RDC analysis as might be anticipated from their omnipresence and from the high sensitivity offered in ^{1}H-^{1}H correlation experiments. This can be attributed to the fact that their extraction may be challenging and by the fact that a sign-sensitive measurement of these coupling constants is desirable, which is not offered by all methods. The following discussion, is separated into the measurement of $^2D_{HH}$ and of $^nD_{HH}$ with n>2.

$^2D_{HH}$ are comparably easy to access through existing methods. For methylene groups, the SPITZE-HSQC[173], the closely related CH_2-S^{3}E HSQC[117] and the P.E.HSQC[174] should be emphasized, because of their ability to provide sign-sensitive measurements. Furthermore, $^2D_{HH}$ can be accessed by the methods described for $^nD_{HH}$-measurement. For methyl groups, the DiM ("dipolar couplings in methyls") experiment[175] should be mentioned. Though these couplings certainly can be used in structural calculations, there is the disadvantage that these coupling constants can easily be derived from the corresponding $^1J_{CH}$ couplings if a geometric model for the corresponding group is assumed.
$^nD_{HH}$ with n>2 are a delicate task, because of the multitude of ^{1}H-^{1}H dipolar couplings present in organic molecules and, again, because of the desire to measure their sign. If the alignment is weak enough, this task can be tackled by the E.COSY[176]. An improved separation of the multiplet components can be achieved via filtration with a heteronucleus, as achieved in XLOC experiments[177, 178]. Recently the SJS-HSQC[179] was added to the techniques available, which enables simultaneous $^nD_{HH}$ and $^nD_{XH}$ measurement at a selected proton frequency, including their relative signs.
If the sign information is compromised, CT-COSY experiments can provide $|^nD_{HH}|$ via intensity based measurements[180].

Long-range heteronuclear RDCs ($^nD_{XH}$) are accessible via a number of methods, though their small size often renders the extraction inaccurate. A recent survey of methods designed for $^nJ_{XH}$ measurement is given in ref. [181]. Herein, just a few representative techniques are mentioned, all of which in principle should enabling sign sensitive measurements of $^nD_{XH}$.
A first class of experiments that can be exploited is that of F_1-BIRD-filtered TOCSY derivatives, namely the HETLOC[182] experiment and the HECADE[183] experiment, as its variant with frequency encoding on the heteronucleus in the indirect dimension. Both experiments extract the sign of $^nD_{XH}$ relative to the $^1D_{XH}$ coupling constant from E.COSY-type signal patterns.
A drawback of these experiment is that they cannot be used to measure $^nD_{XH}$-couplings to quaternary carbon atoms. To avoid this problem, it can be resorted to HSQMBC-based techniques, out of which the HSQMBC-COSY-IPAP technique[184], the selHSQMBC technique[185] should be mentioned here.

A major part of this work will be devoted to the design of new pulse sequences for $^1D_{CH}$ extraction, which requires a knowledge of how NMR experiments can be described. The description of NMR experiments from the dynamic perspective that is required is described in the next section.

4.3. NMR Experiments from a Dynamic Perspective – Tools for Describing Modern Solution State Techniques

A short intermezzo (along the lines of refs. [19, 186] and of chapters 2 and 4 of ref. [16]):

NMR makes excessive use of manipulating the time-evolution of nuclear spin systems in their non-equilibrium state. For understanding the design of NMR pulse sequences an understanding (or at least a coarse picture) of these processes is required, which can come through different approaches of analysing spin dynamics. Rather than providing a full description, I try to give an abstract of the field with extension on the product operator formalism[186] here.

4.3.1. An Overview of Approaches to Describe the Dynamic of NMR Experiments

The aim of all the techniques described herein is to describe the bulk dynamics of nuclear magnetization of liquid samples. Though talking about small spin systems, this usually means that one tries to describe the behaviour of a large number of identical spin systems, the sample is normally composed of.

Many NMR experiments can be understood in the classical picture of the *Bloch equations*, describing the motion of a magnetization vector $\vec{M}$ under the action of a time dependent external magnetic field $\vec{B}(t)$, according to

$$\frac{d}{dt}\vec{M}(t) = \gamma_k \vec{M}(t) \times \vec{B}(t) - \boldsymbol{R}\{\vec{M}(t) - \vec{M}_0\}. \tag{4.43}$$

$\vec{M}(t)$ hereby has the thermal equilibrium value $\vec{M}_0 = (0; 0; M_Z^0)^T$ (see equation (4.32)) and the relaxation matrix is given by

$$\boldsymbol{R} = \begin{pmatrix} 1/T_2 & 0 & 0 \\ 0 & 1/T_2 & 0 \\ 0 & 0 & 1/T_1 \end{pmatrix}. \tag{4.44}$$

The analysis is typically carried out after transformation from the laboratory frame into a rotating frame of reference, where

$$\overrightarrow{B^r}(t) = \begin{pmatrix} B_1(t)\cos\phi \\ B_1(t)\sin\phi \\ \Omega_k/\gamma_k \end{pmatrix} \tag{4.45}$$

if all radio frequency pulses are directly applied at the frequency of rotation of the reference frame (compare to equation (4.9)).
This picture can be used, whenever spins can be treated as isolated, i.e. when they are not interacting via spin-spin couplings or quadrupolar couplings. Use of this picture is made in various situations, e.g. when analysing the effects of radio-frequency pulses on isolated spins[187, 188]. As the next section will cover the dynamics of coupled spin-systems, however we have to resort to a quantum-mechanical description of the time-evolution of nuclear magnetization.

Quantum-mechanical description of NMR experiments is usually performed via the *density operator approach*. If relaxation phenomena do not have to be considered, this usually means solving the Liouville-von Neumann equation

$$\frac{d}{dt}\hat{\rho}(t) = -i\left[\hat{\mathcal{H}}(t), \hat{\rho}(t)\right], \tag{4.46}$$

which describes the time evolution of the density operator $\hat{\rho}$. The quantity $\left[\hat{\mathcal{H}}(t), \hat{\rho}(t)\right]$ thereby is the commutator of the Hamiltonian describing the spin system dynamics (see equation (4.2)) and the density operator $\hat{\rho}$. The time evolution of $\hat{\rho}$ is mostly performed during time intervals, where $\hat{\mathcal{H}}$ is constant in the rotating reference frame, where

$$\hat{\rho}(t) = e^{-i\hat{\mathcal{H}}t}\hat{\rho}(0)e^{+i\hat{\mathcal{H}}t} \tag{4.47}$$

can be applied to describe the time evolution of the density operator from its initial state $\hat{\rho}(0)$ to a later stage $\hat{\rho}(t)$. The evolution of the density operator through complex pulse sequences can be performed by sequential application of such transformations. This requires that small pulse sequence segments (e.g. a single hard r.f. pulse) are chosen, where one can assume $\hat{\mathcal{H}}_i = const.$.

$$\hat{\rho}(\tau_1 + \tau_2 + \tau_3) = e^{-i\hat{\mathcal{H}}_3\tau_3}e^{-i\hat{\mathcal{H}}_2\tau_2}e^{-i\hat{\mathcal{H}}_1\tau_1}\hat{\rho}(0)e^{+i\hat{\mathcal{H}}_1\tau_1}e^{+i\hat{\mathcal{H}}_2\tau_2}e^{+i\hat{\mathcal{H}}_3\tau_3} \tag{4.48}$$

Time ordering hereby has to be respected, if operators in the exponentials do not commute. For rapid changes of the Hamiltonian that cannot be followed by the spin system, the individual $\hat{\mathcal{H}}_i$ can also be replaced by their time-average values.
Expectation values $\langle A \rangle$ for observables can be computed by

$$\langle A \rangle = \mathrm{tr}\{\hat{A}\hat{\rho}(t)\} \tag{4.49}$$

using their respective operators $\hat{A}$, so that e.g. the observable magnetization components in x and y, caused by a large ensemble of N_{ens} identical spin systems are obtained by

$$M_x(t) = N_{ens}\sum_k \gamma_k \hbar\, \mathrm{tr}\{\hat{I}_{k,x}\hat{\rho}(t)\} \text{ and } M_y(t) = N_{ens}\sum_k \gamma_k \hbar\, \mathrm{tr}\{\hat{I}_{k,y}\hat{\rho}(t)\}\ , \tag{4.50}$$

where the summation runs over all nuclei contained in one of the spin systems.
Explicitly solving the time-evolution of the density operator in suitable matrix representations, possibly also including effects of relaxation to an external lattice, is a task normally performed in quantum-mechanical simulation software developed for the analysis of NMR pulse sequences[189, 190].
The density operator approach is well suitable for machines to be solved, but is very little intuitive for people trying to understand what happens during the pulse sequence. For analysis of pulse sequences, it is therefore often resorted to the product operator formalism, which is derived from the density operator formalism, but is way more intuitive.

4.3.2. The product operator formalism – in brief

The product operator formalism can be regarded as a collection of rules of thumb – albeit with quantum-mechanical background – that give a pictorial description of what happens during NMR experiments.

For describing the state of the spin system, the density operator $\hat{\rho}$ is expressed as a linear combination of product operators

$$\hat{\rho} = \sum_s b_s(t)\, B_s \tag{4.51}$$

out of which normally only those of interest are analysed. B_s thereby are the product operators as for example listed below and $b_s(t)$ are the time dependent coefficients describing the time evolution of the density operator.

The product operators are constructed from a set of single-spin operators, which can be combined to two-spin, three-spin and higher operators through multiplication. There is a nomenclature relating the different product operators to the signal shape that is associated with their observation.
In a Cartesian basis for a two-spin-½ system, there are six *one-spin product-operators* which are named as follows:

$I_{1,x}$ and $I_{2,x}$: "in-phase x-magnetization on spin 1 or 2"
$I_{1,y}$ and $I_{2,y}$: "in-phase y-magnetization on spin 1 or 2"
$I_{1,z}$ and $I_{2,z}$: "longitudinal magnetization on spin 1 or 2" (also: "y-magnetization")

Further a set of nine *two-spin product-operators* is obtained, which can be grouped into:

$2I_{1,x}I_{2,z}$: “antiphase x-magnetization on spin 1 (with respect to spin 2)”
$2I_{1,y}I_{2,z}$: “antiphase y-magnetization on spin 1 (with respect to spin 2)”
$2I_{1,z}I_{2,x}$: “antiphase x-magnetization on spin 2 (with respect to spin 1)”
$2I_{1,z}I_{2,y}$: “antiphase y-magnetization on spin 2 (with respect to spin 1)”
$2I_{1,z}I_{2,z}$: “longitudinal two-spin order on spins 1 and 2”
$2I_{1,x}I_{2,x}$, $2I_{1,x}I_{2,y}$, $2I_{1,y}I_{2,x}$ and $2I_{1,y}I_{2,y}$: “two-spin coherences”

(Note that the circumflex is omitted for convenience.)

The raising and lowering operators frequently used to express Hamilton operators throughout this introduction can be constructed by

$$\hat{I}_k^+ = \hat{I}_{k,x} + i\hat{I}_{k,y} \; and \; \hat{I}_k^- = \hat{I}_{k,x} - i\hat{I}_{k,y} \tag{4.52}$$

The analysis of pulse sequences typically proceeds through successive steps where the Hamiltonian is constant, just as in the density operator treatment, according to (4.47), but with the advantage, that the evolution of individual product operators can be analysed separately. Suppose $\hat{\rho}_a = I_{1,x} + 0.3I_{2,z}$, then

$$\hat{\rho}_a(t) = e^{-i\hat{\mathcal{H}}t}\hat{\rho}_a(0)e^{+i\hat{\mathcal{H}}t} = e^{-i\hat{\mathcal{H}}_1 t}I_{1,x}e^{+i\hat{\mathcal{H}}_1 t} + 0.3e^{-i\hat{\mathcal{H}}_2 t}I_{2,z}e^{+i\hat{\mathcal{H}}_2 t}, \tag{4.53}$$

where $\hat{\mathcal{H}}_1$ and $\hat{\mathcal{H}}_2$ denote only those parts of the Hamiltonian acting on spin 1 and 2 respectively.

Rather than solving the product of matrix exponentials explicitly every time the calculation is performed, it is sufficient to provide the solutions in the form of transformations, which can be applied successively.

A particularly simple picture arises, if we perform the analysis in the weak coupling approximation, using (4.8) for describing chemical shift evolution, (4.9) for radio frequency pulses, (4.11) for scalar couplings and not considering the effective evolution of RDCs.
Results obtained under this assumption are listed below. Under the assumption of this simplified Hamiltonian, they are valid irrespective of other product operators in the unspecified multiplier L.

The effect of free evolution under a frequency offset (see (4.8)):

$$LI_{k,x} \xrightarrow{\Omega_k \tau I_{k,z}} L\left(I_{k,x}\cos\Omega_k\tau + I_{k,y}\sin\Omega_k\tau\right) \tag{4.54}$$

$$LI_{k,y} \xrightarrow{\Omega_k \tau I_{k,z}} L\left(I_{k,y}\cos\Omega_k\tau - I_{k,x}\sin\Omega_k\tau\right) \tag{4.55}$$

$$LI_{k,z} \xrightarrow{\Omega_k \tau I_{k,z}} LI_{k,z}, \tag{4.56}$$

For radio-frequency pulses, it is common to use the assumption of perfect instantaneous flips and thus to express $\gamma_K B_1 \tau$ as an effective flip angle ϑ:

$$LI_{k,x} \xrightarrow{\vartheta I_{k,x}} LI_{k,x} \tag{4.57}$$

$$LI_{k,y} \xrightarrow{\vartheta I_{k,x}} L\left(I_{k,y}\cos\vartheta + I_{k,z}\sin\vartheta\right) \tag{4.58}$$

$$LI_{k,z} \xrightarrow{\vartheta I_{k,x}} L\left(I_{k,z}\cos\vartheta - I_{k,y}\sin\vartheta\right), \tag{4.59}$$

and similarly

$$LI_{k,x} \xrightarrow{\vartheta I_{k,y}} L\left(I_{k,x}\cos\vartheta - I_{k,z}\sin\vartheta\right) \tag{4.60}$$

$$LI_{k,y} \xrightarrow{\vartheta I_{k,y}} LI_{k,y} \tag{4.61}$$

$$LI_{k,z} \xrightarrow{\vartheta I_{k,y}} L\left(I_{k,z}\cos\vartheta + I_{k,x}\sin\vartheta\right), \tag{4.62}$$

The effect of weak scalar coupling:

$$LI_{k,x} \xrightarrow{\pi J_{k,l}\tau I_{k,z}I_{l,z}} L\left(I_{k,x}\cos\left(\pi J_{k,l}\tau\right) + 2I_{k,y}I_{l,z}\sin\left(\pi J_{k,l}\tau\right)\right) \tag{4.63}$$

$$LI_{k,y} \xrightarrow{\pi J_{k,l}\tau I_{k,z}I_{l,z}} L\left(I_{k,y}\cos\left(\pi J_{k,l}\tau\right) - 2I_{k,x}I_{l,z}\sin\left(\pi J_{k,l}\tau\right)\right) \tag{4.64}$$

$$LI_{k,z} \xrightarrow{\Omega_k\tau I_{k,z}} LI_{k,z}, \tag{4.65}$$

$$L2I_{k,x}I_{l,z} \xrightarrow{\pi J_{k,l}\tau I_{k,z}I_{l,z}} L\left(2I_{k,x}I_{l,z}\cos\left(\pi J_{k,l}\tau\right) + I_{k,y}\sin\left(\pi J_{k,l}\tau\right)\right) \tag{4.66}$$

$$L2I_{k,y}I_{l,z} \xrightarrow{\pi J_{k,l}\tau I_{k,z}I_{l,z}} L\left(2I_{k,y}I_{l,z}\cos\left(\pi J_{k,l}\tau\right) - I_{k,x}\sin\left(\pi J_{k,l}\tau\right)\right) \tag{4.67}$$

$$LI_{k,z} \xrightarrow{\Omega_k\tau I_{k,z}} LI_{k,z}, \tag{4.68}$$

Linking product operators to the observable time-domain NMR signal and in consequence to the signal shape obtained is possible through equations (4.50). The complex signal $S(t)$ that is measured in NMR combines the two magnetization components, which are both measured during the acquisition period.

$$S(t) \propto \left(M_x(t)\cos\phi_{rec} + iM_y(t)\sin\phi_{rec}\right) \tag{4.69}$$

The quantity ϕ_{rec} is the receiver phase, which we will deliberately set to zero for the discussion that follows.
From equations (4.50), it follows that observable signal only is obtained from the product operators $I_{k,x}$ and $I_{k,y}$. All other product operators are not directly observed. I will now try to link the product operators to time domain signals and further to its appearance after Fourier transformation.

Starting with an isolated spin ($J_{1,2} = 0$), time evolution out of e.g. $I_{1,x}$ leads to an interconversion of magnetization between the two in-phase components $I_{1,x}$ and $I_{1,y}$, which is described by a simple oscillating function. An in-phase absorptive singlet is obtained.

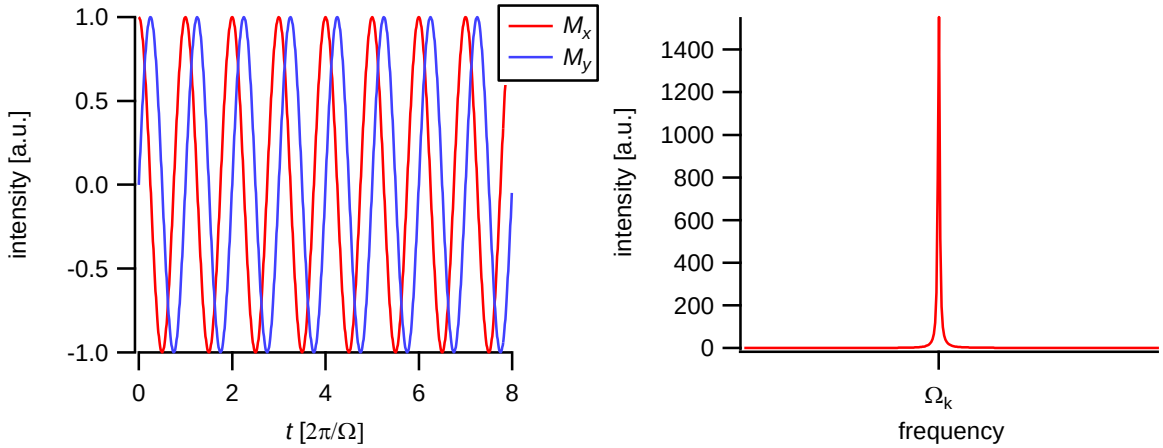

Figure 4.7: FID (left) and spectrum (right) for a single spin. (Note for FFT more time point were used than shown in the left plot and that an apodization function was used.)

In contrast, if a two spin system is considered ($J_{1,2} \neq 0$) , still only analysing the evolution out of $I_{1,x}$, not only do the tow in-phase components interconvert: The signal disappears and reappears, as a consequence of signal evolution into the antiphase terms $2I_{1,x}I_{2,z}$ and $2I_{1,y}I_{2,z}$ and back into the in-phase terms $I_{1,x}$ and $I_{1,y}$. This leads to an apparent splitting of the signal. The signal is said to be in-phase, because both components have the same sign.

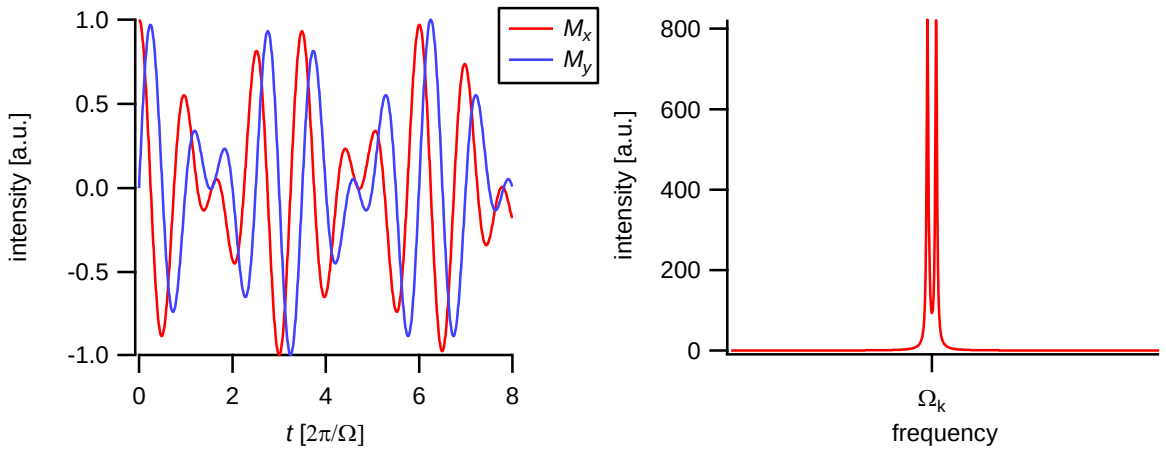

Figure 4.8: FID (left) and Spectum (right) for a single spin. (Note for FFT more time point were used than shown in the left plot and that an apodization function was used.)

In contrast, if we are performing the analysis out of the product operator $2I_{1,y}I_{2,z}$, we obtain a doublet where both signal components point in opposite direction. This is called an anti-phase signal appearance. It is stated above, that only the in-phase components are observable, but still we are obtaining a signal here. This is not in contradiction, because $2I_{1,y}I_{2,z}$ evolves into the in-phase operator $I_{1,x}$ during the acquisition. In fact, all product operators with a single transverse component can evolve into observable magnetization during acquisition, with just a small caveat: In addition to what is considered in this product operator analysis, the signal disappears through the action of transverse relaxation and possibly also through exchange processes that are in-between the slow- and the fast exchange regime. If the signal disappears faster through the action of these processes than it builds-up through coupling evolution, the total signal intensity may become too small as to be detectable. We will meet this particular disadvantage of anti-phase signals in Project D.

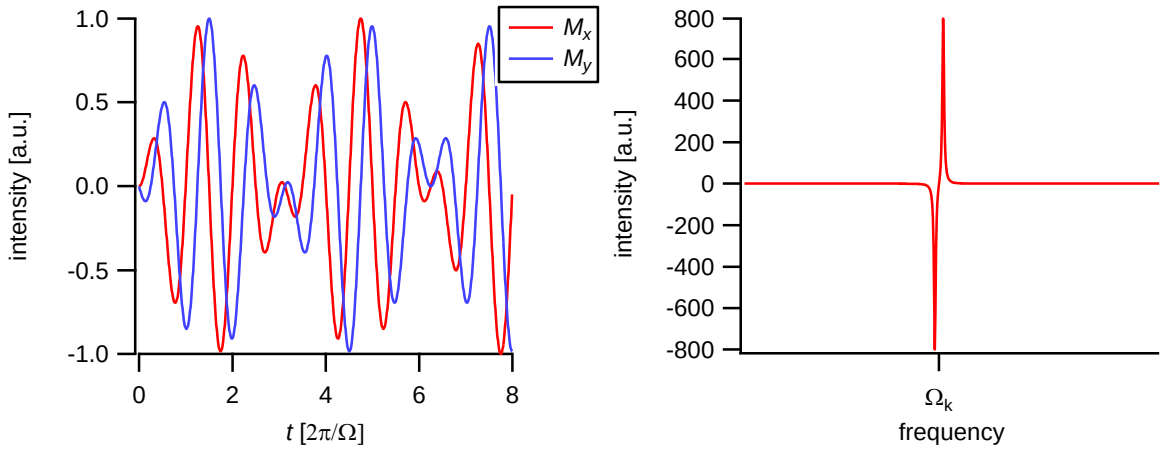

Figure 4.9: FID (left) and Spectum (right) for a single spin. (Note for FFT more time point were used than shown in the left plot and that an apodization function was used.)

In Projects A, B and C, the main focus will be to suppress homonuclear splitting of NMR-signals in the spectra. The challenge hereby is to suppress the disappearance of the FID through transfer of magnetization from in-phase into anti-phase terms to achieve signal evolutions resembling that shown in Figure 4.7, even if investigating multi-spin systems. The aim is thus to keep the in-phase terms throughout the entire FID accumulation period, to obtain spectra that – in the homodecoupled dimension - look as if there were no homonuclear coupling partners present.

One further note: Suppressing the in-phase to anti-phase interconversion also counteracts the conversion from (unobservable) anti-phase terms into (observable) in-phase terms. I will use this special feature of homodecoupled methods e.g. during Project A (chapter 6) to suppress unwanted signals, dubbed “artefacts”.

4.4. Methods for Homonuclear Decoupling in ^{1}H-dimensions – The Dawn of Pure Shift NMR

As just mentioned, the idea of homonuclear decoupling in NMR is to suppress signal splitting arising from homonuclear spin-spin interactions. Even though methods that achieve suppression of homonuclear couplings have been around for many decades, the recent development of new experimental approaches to achieve homonuclear decoupling for protons have generated substantial interest in this field. Since 2007, this field of research is mostly referred to as *pure shift NMR*. Recent reviews describe the developments in the field[12-15, 191, 192], yet I intend to provide a survey from my own perspective in the following pages.

Methods for spin-spin decoupling are ubiquitous in NMR, and many fields critically rely on the ability to introduce spin-spin decoupling. This is particularly apparent in the field of solid-state NMR, which (amongst other decoupling techniques) heavily relies on Magic-Angle Sample spinning as a tool to remove direct spin-spin couplings and the anisotropies of chemical shift and *J*-coupling[193]. The isotropic part of the *J*-coupling, which leads to the couplings visible in liquid state spectra, cannot be removed by methods that use fast sample rotation or that mimic its effect.

For the discussion of techniques that can provide spectra without signal multiplicity due to scalar couplings, I will roughly subdivide the methods existing into three groups:

The first group achieves homonuclear decoupling by 180° degree rotations of all spins from the isotope to decouple. These are based on the concepts of the classical Hahn-echo (shown in Figure 4.10 A)), which, for weakly coupled systems leads to a refocusing of chemical shift evolution. When consulting text-books, as nicely summarized in Appendix A.10 in ref. [17], it can be found that the classical Hahn echo leads to an accumulation of homonuclear coupling evolution during the full period, while fully refocusing chemical shift evolution (assumptions made: only weak homonuclear coupling, an infinitely short 180° rotation). It is this refocusing of the chemical shift during continuous evolution of the *J*-coupling, which is exploited in this method.

The second group of experiments solves the problem of homonuclear decoupling by turning the problem of homonuclear decoupling into a problem that resembles the heteronuclear decoupling case. For the heteronuclear case it is long known, that the heteronuclear echo element shown in Figure 4.10 B) is able to refocus heteronuclear coupling evolution over the period τ (again described in Appendix A.10 in ref. [17]). For isotope 1, the element introduces a chemical shift labelling during τ which will later be used for frequency-encoding in the FID. It should be noted at this point, that coupling between nuclei both belonging to isotope 1 evolve unperturbedly.
Treating a homonuclear case just like a heteronuclear one requires a method of separating the entire ensemble of homonuclear spins into two groups (described later as *spin-subset selection*): one that is observed (the *active* spins; would be isotope 1 in Figure 4.10 B)) and one that is manipulated to achieve the decoupling (the *passive* spins). Methods for achieving this will be explained later.

The third group of experiments also uses a pulse in the middle of an evolution period, but as shown in Figure 4.10 C) not necessarily a 180° rotation. Rather than forming an echo during which either chemical shift evolution or *J*-coupling evolution are refocused, these experiments use coherence mixing to achieve an addition of magnetization not showing modulation by couplings, while magnetization terms reflecting the effect of accumulated couplings add up to zero.
Interestingly, the sole experiment belonging to this third group that to my personal knowledge was used thus far is the "time-reversal" approach[194] described by SØRENSEN, GRIESINGER and ERNST. The homonuclear decoupling approach used is further not adopted in current work.

In addition to the possible use of the "time-reversal" decoupling by itself, the reader should note that the "perfect echo"-block[195] achieves a virtual cancellation of signal antiphase by a principle, that can also be understood in the general picture of Figure 4.10 C) and therefore attracted research interest, because it enables time-intervals of no net *J*-coupling evolution **and** no net chemical shift evolution to be introduced[167, 196-204].
In this work, I extended this principle to also be used for broadband homonuclear decoupling of pairs of protons, while introducing chemical shift evolution for the latter, adding a second experiment to this class of experiments.

The experiments using Hahn-echo based decoupling and the concept of spin-subset selection will be described in the following.

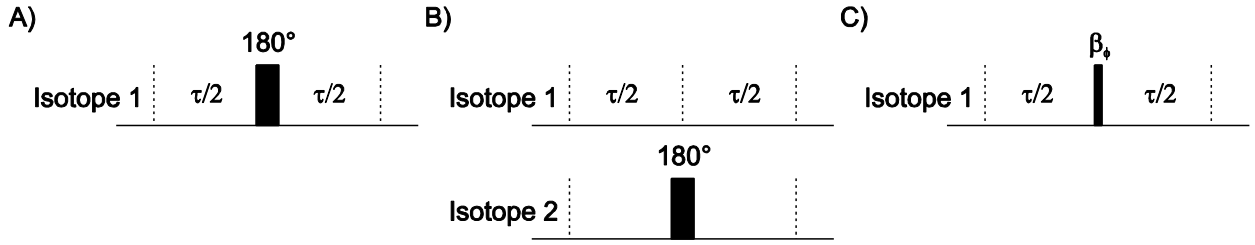

Figure 4.10: Different basic building blocks that are used to group the homonuclear decoupling techniques discussed. A) The homonuclear Hahn-echo sequence. B) The heteronuclear echo. C) An evolution period with coherence mixing in the middle.

4.4.1. Hahn-Echo Based *J*-Resolved Experiments

Homonuclear broadband decoupling was first achieved by AUE, KARHAN and ERNST through projection of a *J*-resolved spectrum they first described[205]. This was one of the first applications of two-dimensional spectroscopy, described just shortly after the introduction of two-dimensional spectroscopy[34].
The experiment uses a simple Hahn-echo with incremented duration as the t_1-element, which refocuses net chemical shift evolution for weakly coupled spins at the end of the t_1-peroid. The signal is thus only modulated by *J*-couplings in t_1, while both *J*-couplings and chemical shifts freely evolve during t_2. This leads to an appearance of the signal multiplicity tilted by 45° away from the F_2-direction where chemical shift is encoded. It is the appearance of these two effects along two different frequency axes that can be used to separate the two effects, by projection of the spectrum along the axis where signal multiplicity appears. *J*-resolved experiments provide high sensitivity and can be measured rapidly, because only small spectral widths need to be used in the indirect time domain.

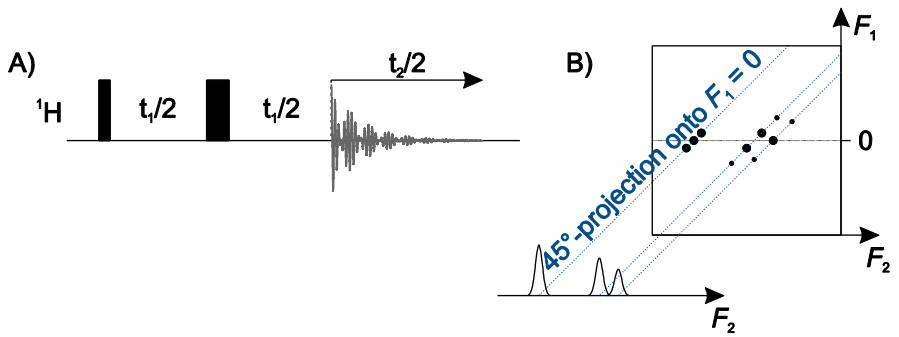

Figure 4.11: Schematic representation of the basic *J*-resolved experiment. A) Pulse sequence used in the original works[205]. B) Schematic representation of the magnitude-mode spectrum obtained and the pictorial description of how a pure shift spectrum is constructed.

A drawback of this method however is that the mixed phase appearance of the signals, which leads to cancellation of the signals during the projection, when using phase-sensitive processing of the spectra[206]. This enforces the use of magnitude calculation during Fourier transformation. Projection in spectra obtained with magnitude processing however leads to very broad dispersion-mode, which counteracts the original aim of broadband decoupling to achieve good signal resolution in the resulting spectra.
There are different approaches that try to solve the problems of the phase-twist lineshape. The multitude of methods existing indicates that none has been commonly accepted as the uncontestably best solution to the problem of the phase-twist signal appearance in *J*-resolved experiments.
Before describing these different methods to deal with phase-twist lineshapes let me state that these disappear when building up *J*-resolved spectral dimensions using the strategy of spin-subset selection described in section 4.4.3. The realization of this fact les to the field of SERF methods[279]. Because of the different principle of action, I will make that clear distinction throughout the document and come back to SERF-methods in section 4.4.3.5..
Let me also mention, that *J*-resolved methods have led to the only HMBC experiment described to my knowledge with broadband homonuclear decoupling in the proton[207] or carbon[208] dimension.

4.4.1.1. Strong Apodization to form a "Pseudo Echo"

Dispersion-mode contributions can be cancelled out of the spectra by using strong apodization functions that produce a time-symmetrical appearance of the FID, which is described as the "Pseudo Echo" technique[209]. The large first-order phase error produced in the spectra can be counteracted again by using magnitude mode processing, however this time leading to peaks with absorptive appearance. Whereas leading to narrow signal shapes, strong apodization at the beginning of the FID obviously leads to a strong signal attenuation, reducing effective sensitivity, in particular if long FIDs (the prerequisite for a high resolution) are processed. The strong differences of signal intensity after "Pseudo Echo" apodization render signal integrals unusable for determining for example relative concentrations of different solutes from the broadband decoupled spectra obtained. Nevertheless, the use of strong time-symmetrical apodization has found widespread application to remove dispersive signal components, not only in *J*-resolved experiments[210], but also e.g. in COSY techniques for rapid acquisition[211].

4.4.1.2. A 90°-Rotation Prior to Acquisition

Cancellation of the mixed phase appearance of peaks in *J*-resolved spectra is further possible by adding spectra of two different *J*-resolved experiments, one to which a 90°-pulse has been added just prior to acquisition[212]. The technique is mentioned here because of its close relation to the perfect-echo[195] based decoupling[213] that is used in Projects B and C of this work. Unfortunately, in analogy to the perfect-echo based decoupling approach, the technique is limited to cancel out the phase-twist lineshape only for two-spin systems, and thus is of little use in practice. Also the close analogy of this approach to the procedure of adding *J*- and anti-*J*-spectra, as proposed by PELL and KEELER[214], should be noted.

4.4.1.3. Magnetization Filtration prior to acquisition

Unlike most 2D experiments, the original *J*-resolved experiment does not have a classical mixing block separating t_1 and t_2, and as such no element purging anti-phase magnetization prior to acquisition. If a magnetization filter is used in between the two incremented time periods, dispersive magnetization components can be suppressed[215-217]. This leads to favourable line shapes, but unfortunately, the methods described loose the effect of quadrature detection, so that all peaks appear with mirror images around $F_1 = 1$. The presence of these mirror images brings back multiplet structure into the projection of the spectrum, so peak-pattern recognition algorithms are used to construct the pure shift spectrum.
Recently, it was however realised that when combining this technique with one of the strategies for pure shift acquisition in F_2 (described below), this again collapses pairs of signals, leading to spectra that can be projected along F_1[218].

4.4.1.4. Alternative Data Processing

A series of data processing methods have emerged that further can be used for obtaining pure chemical shift information from the classical *J*-resolved experiment. These include a peak search algorithm[219], use of the filter-diagonalization method (FDM)[220, 221] instead of Fourier transformation or the use of linear prediction to eliminate dispersion mode signal components [222, 223].

4.4.2. Constant Time Experiments

Constant-time experiments use an alternative strategy for Hahn-echo based homonuclear broadband decoupling. The technique was first introduced shortly after the description of the original *J*-resolved technique[224]. The technique can be implemented into the indirect dimension of multidimensional experiments, as first used in the constant-time COSY experiment (CT-COSY)[36, 180, 225, 226].

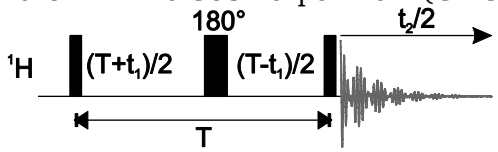

Figure 4.12: Pulse sequence of a constant-time COSY experiment

The technique does accept that there is non-zero *J*-coupling evolution at time point *T*, but collapses signal multiplet structure in F_1 by using the same amount of coupling evolution for all t_1-points. The effect of coupling evolution in the constant-time dimension is thus translated from a frequency modulation of the signal into an intensity-modulation of the signal. Signal loss due to relaxation and coupling evolution is traded for the decoupling, but collapse of the signals can counteract this and lead to signal gains. The choice of *T* thereby requires a good compromise between the resolution that is achieved in the homonuclear decoupled dimension, which increases with *T*, and between signal loss due to relaxation and coupling evolution during *T*. If the magnitude of the homonuclear decoupling is uniform, *T* can be adjusted to provide comparably small signal loss by coupling evolution, loss by relaxation however remains.
Frequent use was made of constant-time decoupling in HETCOR experiments, where protons are detected in the indirect dimension[177, 227-231].
While in today's library of small molecule NMR, constant-time decoupling is not met too frequently, it is an indispensable tool for ^{13}C-^{13}C homonuclear decoupling in triple resonance experiments of labelled proteins[232].

4.4.3. *J*-Refocusing with Spin-Subset Selection Techniques

4.4.3.1. The Principle of Spin-Subset Selection

The homonuclear decoupling techniques that are described in the following are closely related to heteronuclear decoupling methods from a conceptual perspective. For introducing their mode of action, it is instructive to start off with heteronuclear decoupling:

In liquid state NMR frequent use is made of heteronuclear decoupling techniques[187, 233-241], which normally are used as broadband approaches in the sense that they cover the entire spectral width of one nucleus, while observing the other one. The large frequency separation between nuclei of different species hereby enables continuous pulsing on the nucleus not observed, because it avoids disruption of signals at the frequency band, where acquisition is performed (see illustration in Figure 4.13).

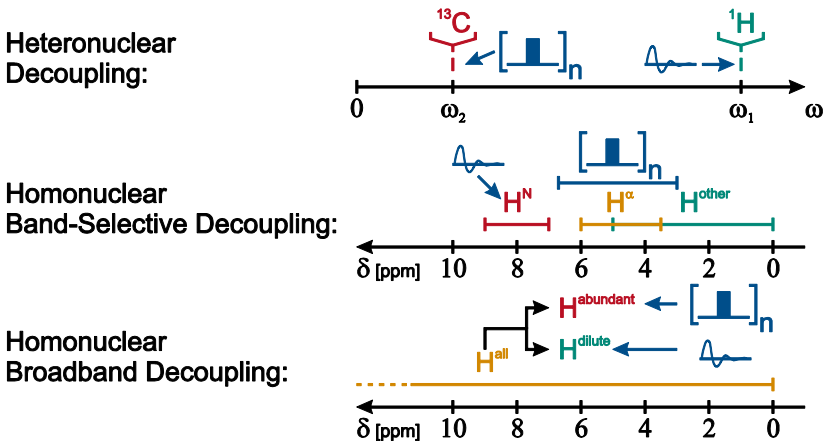

Figure 4.13: Illustration of the conceptual link between heteronuclear decoupled experiment, homonuclear band-selective decoupled experiments and homonuclear broadband decoupled experiments using spin-subset selection. All three kinds of experiments use 180° pulses applied to the nuclei the observed nuclei shall be decoupled from.

In the homonuclear case, techniques performing a decoupling at specific frequencies in the spectrum spread-out by the chemical shift can also be used. They can easily be implemented in indirect spectral dimensions, where it suffices to insert a frequency-selective pulse half-way through the chemical shift evolution period[242-247]. For band selective irradiation of decoupling pulses in the direct acquisition dimension, there is the problem that simultaneous pulsing and irradiation is not possible on the same channel. However during parts of the acquisition dwell-time, the receiver shutter can be closed to enable pulsing in regular acquisition-synchronized intervals[248]. Not only does this allow to perform the Fourier-transform NMR-analogue to double resonance experiments[91] (which correlate spins through partial homonuclear decoupling), if further can be used with adiabatic decoupling, which allows the application of decoupling sequences in well-defined frequency bands[249, 250].

In contrast to the two cases discussed above, in broadband homonuclear decoupling experiments one tries to measure the whole spectrum, while at the same time decoupling over the same spectral range. This causes a problem, because applying trains of inversion pulses to those nuclei that shall be observed suppresses their chemical shift evolution and further does in general not lead to decoupling within the region where pulsing is performed.

The experiments, which attracted most attention in the past years, solve this problem by dividing the spins into two groups and pulse on one of the groups of spins, called the *passive* spins, while observing the signal of the *active* spins that, in effect, do not experience the rotation by the decoupling sequence[12-15]. Making sure, that the active spin is very dilute in the spin system, meaning that no active spins are coupling with each other, for the nuclei observed an effective decoupling of all homonuclear couplings is achieved.

This approach is analogous to the above-mentioned techniques of heteronuclear decoupling and band-selective homonuclear decoupling in the sense that the coupling spins are divided into two groups, where pulsing is performed on one of the groups, while observation is performed of the (ideally unperturbed) other group.

This time however, the distinction between the two groups of nuclei cannot come from frequency selection alone, and other methods are sought for discrimination. Irrespective of the mode of selectively manipulating the active and passive spins, these methods therefore translate the problem of broadband homonuclear decoupling into the “pseudo-heteronuclear decoupling” situation of the heteronuclear spin-echo (see Figure 4.10 B)), just like band-selective homonuclear decoupling methods do.

As compared to known methods of homonuclear decoupling that do not use spin-subset selection, this brings a true refocusing of scalar coupling evolution by reversing the sense of coupling evolution. The common concept is that the *“bilinear”* $2I_{k,z}I_{l,z}$ terms of the Hamiltonian reverse sign through inversion of only one of the spins[251], say l, being the passive spin. If this is performed half-way through a chemical

shift evolution period (as illustrated in Figure 4.15), refocusing of homonuclear *J*-evolution is achieved (the reason why these methods are also called "*J*-refocusing methods"). As no net inversion is performed on the active spins *k*, their chemical shift evolution proceeds seemingly unperturbed under the action of the *"linear"* $I_{k,z}$ terms of the Hamiltonian. For the interested reader, a density operator treatment of these effects is provided in ref. [12] for an inversion block under successive action of a broadband inversion pulse on *k* and *l*, followed by a selective inversion of only *k*, which is what will be used later.

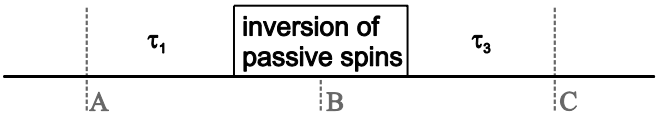

Figure 4.14: Basic building block of *J*-refocussing methods for homonuclear decoupling. In the idealized case, *J*-refocusing to the level present at time A is achieved at time C for active spins, if $\tau_1 = \tau_3$.

It is unnecessary at this point to carry the reader though a product operator treatment of the element shown in Figure 4.14. This can be taken in analogy from Appendix A.10 in ref. [17], assuming that the period inverting the passive spins does nothing else than this (e.g. does not introduce net chemical shift evolution), and can be summarized as follows:
In the weak coupling limit, the *active* spins *k* experience

- net chemical shift evolution during $\tau_3 + \tau_1$
- net coupling evolution to all *passive* spins during $\tau_3 - \tau_1$
- net coupling evolution to all *active* spins during $\tau_3 + \tau_1$

If we manage to choose experimental situations that prevent couplings between active spins, which is done by "diluting *active* spins in the bath of *passive* spins", we can thus refocus all coupling evolution for these spins. This restores in-phase magnetization for active spins after the period of one *J*-refocusing element, if we stated off with in-phase magnetization. This allows us to introduce chemical shift evolution for active spins, while refocusing *J*-coupling evolution for them at a single instant of time.

4.4.3.2. Construction of a full FID

It was outlined in the previous section, that when using spin-subset selection, refocusing of homonuclear *J*-coupling evolution is possible at one instant of time. When not being exactly at the point of *J*-refocusing however coupling evolution continues. Homonuclear decoupling, in the sense of collecting an FID which evolves in time, resembling the motion of isolated spins (as illustrated for one isolated spin in (4.7)), in contrast needs to come through continuous *J*-refocusing over the longer period of an FID. Three approaches have been used to collect FIDs of useful length for high-resolution NMR:

1) The *J*-refocusing method can be used in an indirect dimension of an experiment, with setting the evolution times equal to half the incremented time-evolution period in the indirect dimension ($\tau_1 = \tau_3 = t_1/2$)[242, 251]. This introduces homonuclear decoupling in the indirect dimension. Optimal *J*-refocusing in terms of collecting all data at $\tau_1 = \tau_3$ can be achieved by this approach, avoiding so-called chunking artefacts present in other techniques.

2) The *J*-refocusing block can be used in pseudo-indirect dimensions (see Figure 4.15 A)), as first presented by ZANGGER and STERK[252]. These approaches are collected under the name *interferogram-based* experiments. They realized that when collecting data in a short time interval around the point of full coupling refocusing, coupling evolution has only little effect. For the maximum length of this time interval Δ_{max}, it needs to be satisfied, that $\Delta_{max} \ll (1/|J_{HH,max}|)$, where $|J_{HH,max}|$ is the biggest splitting that needs to be suppressed. For typical $|J_{HH,max}|$ below

20 Hz, it proved to be sufficiently conservative to use data block lengths of 10ms to 30ms. To sample the full FID, the experiment needs to be repeated, with different evolution periods t_i in the pseudo-indirect dimension, to vary the amounts of chemical shift evolution accumulated. With a comparably low number of time-points in the pseudo-indirect dimension (e.g. 16 - 32) FIDs of sufficient length can thus be sampled. In consequence, a much shorter overall experiment duration is required than in the case of an indirect dimension with full spectral width. For collecting and processing of the data from pseudo-indirect dimensions, different strategies have been developed:

a. Data is sampled with increments in the indirect dimension Δ_i amounting to the maximum length allowed by the coupling network in the sample $\Delta_i = \Delta_{max}$ (the concept used in ref. [252]). This is used to sample the FID as quickly as possible, a process that is particularly efficient if refocusing happens in the middle of the block of data collected [253]. These blocks of data, typically called *data chunks*, are then assembled together to provide a continuous time signal in the pseudo-direct dimension. The time position t_i^* of the data points in the pseudo-direct acquisition-dimension, with $i = 1$ in the case of a pseudo-2D dataset, amounts to $t_i^* = t_i + t_{i+1}$, providing apparently continuous evolution of the FID. For a pseudo-2D dataset, this is illustrated in Figure 4.15 A), while for a pseudo-3D dataset, this is illustrated in Figure 4.16 (left).
b. Data is sampled with $\Delta_i < \Delta_{max}$ and subjected to addition with data from other t_1-increments during processing. This method, presented as RESET-processing[254], achieves an averaging of data during FID construction, which has been sampled for different t_2. Linear back-prediction is used to reconstruct points at the beginning of the FID that are not experimentally accessible.
c. Data can be subjected to Fourier-transformation and a pattern recognition algorithm can be used for constructing a synthetic homodecoupled spectrum[255]. The pseudo-indirect dimension in this case is collected with extensive spectral folding. The pattern recognition algorithm not only creates a synthetic broadband homodecoupled spectrum, but further extracts coupling constant from the direct acquisition dimension, even for multiplets normally heavily overlapped.

3) The *J*-refocusing block can be applied in rapid succession during a loop to continuously refocus *J*-coupling evolution while acquisition is performed in between the *J*-refocusing blocks[256, 257], as illustrated in Figure 4.15 B). This "*real-time*" or "*instant*" decoupling strategy comes with the benefit of being able to collect a full FID with sufficient length in a single scan. The FID is hereby assembled on-the-fly interrupting the data writing process during the homonuclear decoupling elements. Relaxation during application of the homonuclear decoupling blocks leads to sudden jumps in intensity in the constructed FID. This limits the maximum length of the usable *J*-refocusing elements to normally below 15 ms.

While all *J*-refocusing elements presented thus-far are compatible with the use in indirect spectral dimensions and in pseudo-indirect dimensions, not under all circumstances can real-time decoupling be used. In fact, the choice of the *J*-refocuing element determines the most important properties of the homonuclear decoupling scheme and its compatibility to a target application.
In the following, I will give an overview of the different methods for spin-subset selection that have been established, before reporting on the different applications that pure shift NMR using spin-subset selection has found.

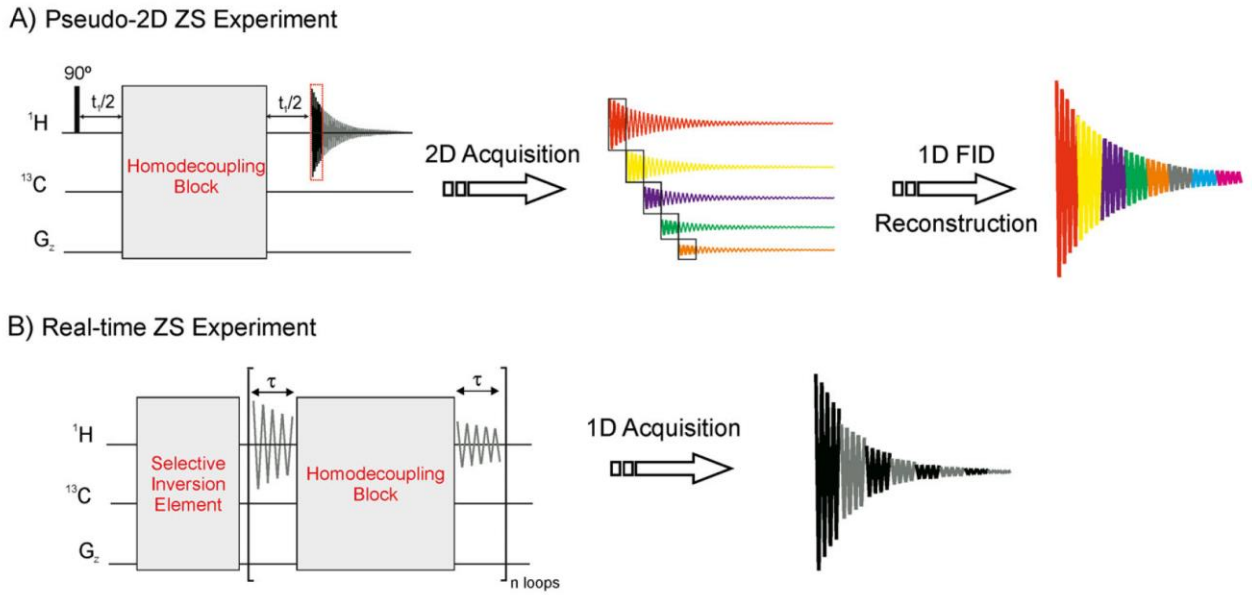

Figure 4.15: Sampling schemes and data assembly for acquisition of data from J-refocusing experiments along A) a pseudo-direct dimension and B) along a real-time acquisition dimension. Reproduced with permission from reference [14].

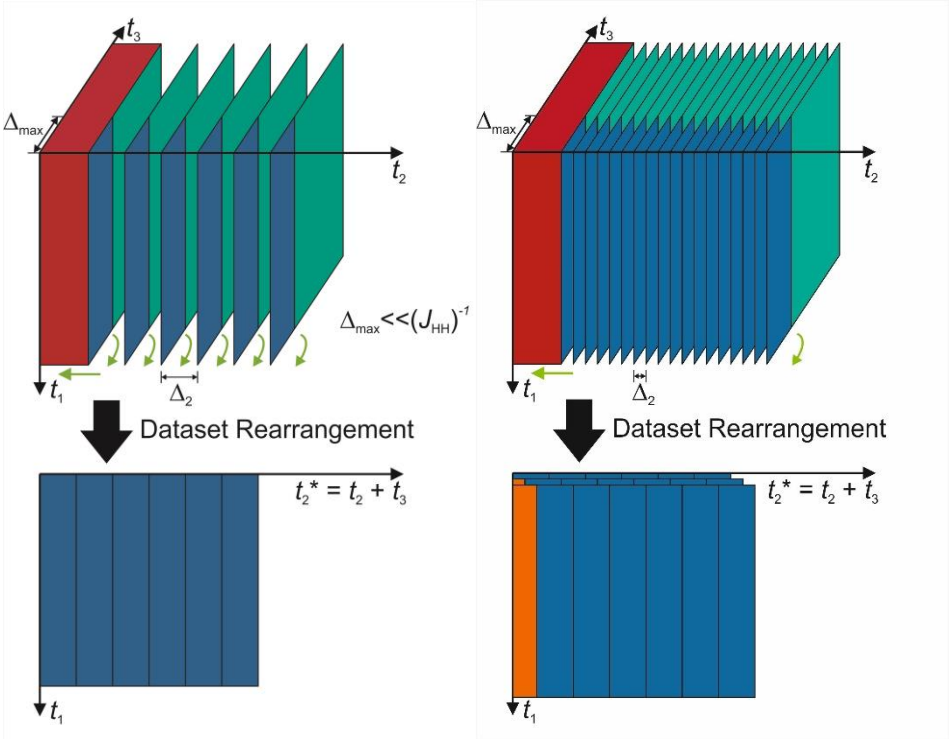

Figure 4.16: Data rearrangement for pseudo-3D dataset acquired with J-refocusing. Left: Data rearrangement, if using $\Delta_2 = \Delta_{max}$ for sampling. Right: Data rearrangement, if using $\Delta_2 < \Delta_{max}$ for sampling[254]. The data is colour coded. During the sampling, continuous planes with separations of the data points by the respective dwell times of the dimensions are measured in t_1 and t_3. In t_2, the data planes are separated by Δ_2, which is an entire multiple of the dwell time in t_3. The data is tilted onto the t_2*-axis to provide a continuous time domain signal for Fourier transformation. If data is sampled with maximum step-width in t_2 ($\Delta_2 = \Delta_{max}$; left), data does not overlap in t_2*. An overlapping of data from different t_2-increments however is obtained if smaller step-widths Δ_2 are used (right). For overlapping data, the time-domain signals are added up. The data is colour-coded for illustration: Blue: The data that is directly used for FID-construction. Green: Data possibly used in linear back-prediction. Orange: Data that is linearly back-predicted. Red: Data that is experimentally inaccessible due to the finite length of the homonuclear decoupling element.

4.4.3.3. Modes of Spin-Subset Selection for *J*-refocusing

The challenge of spin-subset selection to pick out only a few spins of a given nuclide, and to manipulate them differently from their surrounding spins has been succeeded through three main strategies: Through frequency selection, possibly combined with spatial encoding, by filtration with a directly bond nucleus of a different isotope and by statistical methods.
The mode of action of most experiments thereby is not actually selectively invert the *passive*, but the *active* spins. Using the subsequent application of a broadband 180°-pulse and the selective inversion of the *active* spins, as illustrated in Figure 4.17 (top) not only facilitates the selection process but also counteracts BLOCH-SIEGERT-like shifts[258] of the signal frequencies that arise in homonuclear decoupling methods that only invert the passive spins[91, 248, 249]. As in all cases signal detection is (ideally) limited to *active* spins, with most spins being *passive* ones, when standing on their own, all of these methods require compromises in the sensitivity to be made. Fortunate combinations with NMR techniques already choosing spin subsets by themselves, will be presented though, which prevent additional signal loss due to this common problem of pure shift methods based on spin-subset selection.

This setting of *J*-refocusing elements was already used in the original report of Bilinear Rotation Decoupling (BIRD)[251], which first described broadband homonuclear decoupling by *J*-refocusing. By GARBOW *et al.* it was shown, that the simple four-pulse cascade shown in Figure 4.17 can invert the magnetization of only those protons bound to a ^{13}C-nucleus, restoring the magnetization of all other protons. A very clean discrimination between *active* and *passive* spins thereby is achieved, because the heteronuclear one-bond coupling used for selection is very large (mostly 120 – 160 Hz for $^{1}J_{CH}$), as compared to long-bond couplings (normally below 20 Hz). With an overall length of $1/^{1}J_{CH}$ of about 8 ms, the BIRD rotation is a relatively fast slice-selective inversion element. The technique is used for broadband homonuclear decoupling on natural abundance samples, where the low natural abundance of ^{13}C gives a good separation of active spins from one-another, however it also sets an upper limit to the experiment sensitivity. One distinct disadvantage of the BIRD element is, that is cannot discriminate between two nuclei that are bound to the same heteronucleus, a fact that will be intensely discussed in Projects B and C.

Frequency selective pulses are a very versatile tool for homonuclear decoupling, because their properties can be tuned over a wide range[188, 259-261] so that an optimization of pure shift experiments for individual samples becomes possible. For single- and multiple frequency selective *J*-refocusing they have been used since the introduction of “soft” decoupling experiments[242], with the band-selective decoupling schemes derived soon becoming an important tool for studying biomacromolecules[243, 262]. Their frequency-selective nature however also brings inherent challenges: Firstly, they require spatial selection to enable broadband homonuclear decoupling, a combination commonly known as Zangger-Sterk decoupling[252] (see Figure 4.17 E-G)), which comes with a sensitivity penalty increasing with bandwidth as well as with the selectivity of the pulse for a given bandwidth. Secondly, and for Zangger-Sterk decoupling critically linked to the question of sensitivity, they introduce a lower limit of frequency separation that is needed for enabling homonuclear decoupling. Signals that are inverted by the same pulse will continue to evolve homonuclear couplings within the group on inverted spins. So ultimately they cannot decouple signals that are very close in frequency. The problem of strong losses of signal intensity in the case of Zangger-Sterk methods can however be counteracted, in particular for very selective pulses, through the use of multiple-frequency selective pulses[255].

Finally, the use of small flip-angle pulses, as used to the field by PELL, EDDEN and KEELER[263] selects active spins on a purely statistical basis. With two small angle flips of typically 10° - 20°, detecting only signals

that underwent both flips, clean statistical selection of the active spins can be achieved. However it is this statistical nature, which renders them impossible to use for real-time decoupling methods. An additional challenge comes through the z-COSY-type mixing introduced by the two pulses, namely that they introduce many unwanted signals that need to be efficiently suppressed. The very successful implementation by MOHAMMADALI FOROOZANDEH achieves filtering by a pair of small flip-angle frequency-swept pulses that use the spatial dispersion[264] of magnetization by action of a field gradient is shown in Figure 4.17 H). This inversion element shows very uniform performance over the entire spectral range. A problem that is inherent in the magnetization filtration approach used however is, that this selective inversion element typically is implemented with a 30 ms duration, which already leads to appreciable relaxation losses.

Having introduced the general building concepts of experiments with spin-subset selection for homonuclear decoupling, I will now discuss the different applications that pure shift experiments have been applied to, starting with homodecoupled 1D experiments, mentioning methods designed for signal assignment and ending with experiments dedicated to the quantitative extraction of structural parameters.

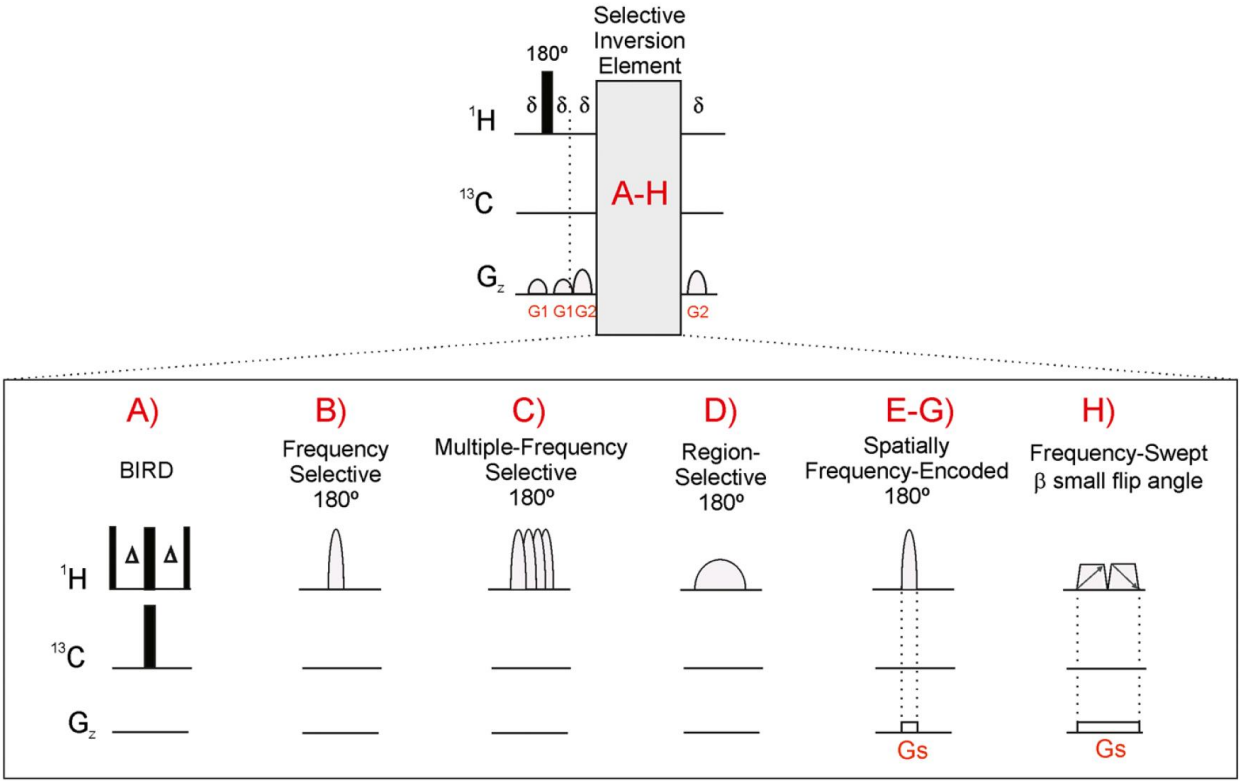

Figure 4.17: Top: Double-echo setup of a *J*-refocusing element. The gradients at either side of the inversions are omitted in many applications. The timing is shown for an experiment with real-time homonuclear decoupling. For experiments with decoupling along indirect or pseudo-decoupling dimensions, other timings[253] may be preferred. Bottom: Overview of different spin-subset selection techniques, which are used for band-selective or broadband homonuclear decoupling. Reproduced with permission from reference [14].

4.4.3.4. Applications I: Broadband Homodecoupled 1D-spectra

Many of the recent developments in pure shift NMR clearly are inspired by the seminal work by KLAUS ZANGGER and HEINZ STERK[252], who presented two developments inside their paper describing broadband homonuclear decoupled experiments that much influenced the field. They introduced the frequency and spatially selective decoupling method shown in Figure 4.17 E-G) which combines the use of a frequency-selective pulse for band-selective decoupling with a weak field-gradient, which disperses the frequency selection to the pulse over the spectral bandwidth at different positions inside the sample. This technique still is amongst the most effective techniques to create a broadband spin-subset selection partially because it is adjustable to a wide range of situations. In addition, the paper describes collection of the homodecoupled time-domain signal in a pseudo-homonuclear decoupling dimension, an approach which could be extended to all methods of spin subset selection. Ironically, this work remained largely unnoticed for ten years, until Mathias Nilsson and Gareth Morris adopted it for ^{1}H and DOSY experiments with broadband homonuclear decoupling[253]. Just a month prior to that, a contribution from ANDREW PELL and JAMES KEELER was published which describes in detail a fundamentally different approach for the extraction of broadband homonuclear decoupled spectra[263]. The anti z-COSY is introduced, which uses two successive low flip-angle pulses, to obtain pure shift spectra. This approach provides good integral reproducibility for weakly coupled signals. Further, it is demonstrated that the anti z-COSY approach can be used for homonuclear decoupling in DOSY spectra, for T_1-analysis and for the analysis of complex mixtures.

The anti z-COSY method was complemented the same year by ANDREW PELL and JAMES KEELER by a method to produce *J*-resolved spectra with full absorption mode lineshape[214]. They introduce the Zangger-Sterk decoupling element into two separate *J*-coupled experiments, which after addition lead to a cancellation of the dispersive signal components.

The group from Manchester then drew further attention to the field by their works on pure shift spectra[265-267] for high-resolution applications. To increase the sensitivity of interferogram-based Zangger-Sterk experiments, approaches were presented that make use of multiple frequency selection[268-270], though the true breakthrough came through the introduction of the real-time decoupling approach depicted in Figure 4.15 B).

The first implementation of real-time homonuclear decoupling[256] was presented by the group of LUCIO FRYDMAN, which used a train of BIRD elements for real-time homonuclear decoupling. Soon after, HELGE MEYER and KLAUS ZANGGER first demonstrated that high-quality homonuclear broadband decoupled spectra can be recorded[257], using the Zangger-Sterk homonuclear decoupling element. The method was soon complemented by LAURA CASTAÑAR, PAU NOLIS, ALBERT VIRGILI and THEODOR PARELLA by the band-selective variant of the experiment[271], which restricts the observation to a small frequency band, but enables the experiment to be measured at full sensitivity, for many signals in the observed region often even higher than in a ^{1}H-experiment without homonuclear decoupling.

For real-time acquisition of broadband decoupled ^{1}H-experiments, two further methods were presented, the use of ASAP-mixing of magnetization[272] and, very interestingly the combination with hyperpolarization methods[273].

As not only the sensitivity, but also the spectral quality of real-time decoupled experiments can be a limiting issue to real-time decoupling techniques, approaches were designed to flatten-out signal sidebands in a first report also testing the robustness of signal integral quantification[274]. Steps towards the application of real-time homodecoupled experiments for the analysis of complex mixtures have further been reported[275].

While real-time decoupling methods provide fast access to pure shift ^{1}H-spectra, which is particularly important for applications to multidimensional experiments, the two most notable compromises between

experimental duration, sensitivity per unit time and spectral quality possibly are the NemoZS-DIAG experiment and the PSYCHE experiment.
The NemoZS-DIAG experiment[255] makes excessive use of multiple-frequency inversion pulses to boost the intensity of the interferogram-based Zangger-Sterk experiment it is derived from. For processing, instead of time-domain data rearrangement, a peak-search algorithm is applied to the spectrum obtained from Fourier transformation of the interferogram, which is able to analyse the multiplet pattern in the spectra to report pure shift signals and the respective *J*-couplings of the peaks.
PSYCHE decoupling[264] was introduced by MOHAMMADALI FOROOZANDEH as a technique using the statistical approach from the anti z-COSY experiment to perform the spin-subset selective inversion. The experiment requires a good suppression of unwanted coherence paths, which is achieved through the simultaneous action of frequency-swept pulses and a weak field gradient. Equipped with these, the PSYCHE experiment is able to provide high-quality ^{1}H-spectra for a variety of different experimental conditions, possibly making it the most useful pure shift ^{1}H experiment currently available.

4.4.3.5. Applications II: Coupling constant extraction

As already mentioned, the NemoZS-DIAG experiment[255] provides convenient access to chemical shifts and to *J*-coupling constants (their magnitudes). In fact, a number of pure shift techniques have been developed explicitly for coupling constant extraction. The great spectral simplification that comes with pure shift methods has led to a number of interesting attempts towards a convenient analysis of signal multiplicity that is normally masked by signal overlap.
Current developments of the PSYCHE experiment reflect this development[276]. Further manipulations of *J*-coupling evolution in single scan real-time techniques are interesting for homonuclear coupling constant extraction, with the possibility to both up- and downscale homonuclear couplings during acquisition with respect to *J*-coupling evolution[277-279].
The fact that echoes using spin-subset selection could be a useful counterpart to *J*-refocused methods, in particular for resolving complicated and overlapping spin-systems is not a new idea, as is documented by the development of SERF methods[280-282], which are a useful tool for structure elucidation even though being tedious for bigger molecules. It appears that the concepts that have been introduced as pure shift NMR have taken away the major limitations of these techniques, namely that of only being able to probe a single frequency per spectrum. This lead to a reinvention of these techniques, which now are able to probe multiple spin-spin interactions couplings in a single experiment with the same ease of interpretation as the singly selective experiments[272, 283-285]. This illustrates how the field of NMR in general can profit from the new concepts brought by pure shift NMR.
Also the field of heteronuclear coupling constant extraction much benefits from pure shift acquisition techniques. In addition to the developments outlined in this thesis, in particular the measurement of long-range heteronuclear coupling constants clearly experienced new possibilities. A number of experiments uses the ability to completely remove the homonuclear coupling pattern from peaks, which normally masks the desired long-range heteronuclear couplings. Major efforts have been devoted to the development of HSQMBC variants enabling long-range coupling constant meausrements[286] featuring a full suppression of homonuclear couplings in the dimension of coupling constant measurement[287-289]. Further, highly simplified E.COSY-like signal patterns facilitating the extraction of long-range RDCs can be obtained through the action of homonuclear decoupling[290].

4.4.3.6. Applications III: Correlation Experiments for Structure Elucidation

The ease of being compatible with many different multidimensional correlation experiments also drew much attention to the field of pure shift NMR. The broadband homodecoupled methods now available offer very interesting alternatives to and combinations with existing methods for homo- and heteronuclear correlation spectroscopy.

TOCSY has been the most frequently modified homonuclear correlation experiment. Already in their early publication, ZANGGER and STERK reported F_1-broadband homonuclear decoupling in TOCSY[252]. Transfer of the homonuclear decoupling into the direct spectral dimension via an interferogram-based approach was subsequently demonstrated[266, 291] and found application in solution structure elucidation[292]. Real-time homonuclear broadband and band-selective decoupling schemes have been used to decoupled the direct dimension of TOCSY spectra, now offering pure shift TOCSY experiments with essentially no additional cost in experiment duration[257, 271]. The combination of F_1 and F_2-decoupling found application in studies requiring very high resolution for protons[293].
Because of their high robustness towards situations of strong coupling, PSYCHE-TOCSY combinations[294, 295] are particularly suitable for studies of complex systems[296].

The advantages of using homonuclear decoupling by spin-subset selection in NOESY spectra are documented since the introduction of "soft-NOESY"[242] experiments. They lead to important simplifications in the spectra, featuring the benefits of both significant signal narrowing and simultaneous suppression of zero-quantum artefacts[243], and thus were soon used for solution structure investigations[262].
The recent extension by Zangger-Sterk decoupling to achieve broadband decoupling in NOESY[297] may be particularly interesting for studies of small molecules, which often lack the clear frequency discrimination between groups of coupling spins. Extensions of NOESY spectra with real-time band-selective decoupling in the direct dimension have also been reported with the emphasis to study biomacromolecules[298, 299], there are however indications that the extraction of interatomic distances from real-time decoupled experiments may be problematic[299].
In a similar way for ROESY techniques the extension of existing band-selective experiments[247, 300] to the real-time band-selective decoupling method introduced by CASTAÑAR *et al.* has been reported[301], though again a discussion of the quantitative features of these experiments is largely lacking.

While TOCSY, NOESY and ROESY spectra are readily extended to the novel concepts of pure shift NMR, it is striking to see, that COSY as one of the most frequently used homonuclear correlation techniques has for a long time not been extended with pure shift acquisition techniques.
The sole COSY experiment that was reported for long is the constant-time COSY[36, 292, 297], which suffers from the inherent signal loss at high resolutions, as was already described in 4.4.2. For this very essential homonuclear correlation experiment, there is thus the evident need for extension to the recent concepts of homonuclear broadband decoupling, which enable high resolutions to be obtained in the decoupled dimensions.

When discussing heteronuclear correlations, it is in particular the HETCOR experiments, which made extensive use of homonuclear decoupling in the (indirect) proton dimension[227, 230, 231, 302-304]. However, HMQC and HSQC techniques are nowadays almost completely replacing HETCOR experiments due to their bigger inherent sensitivity.
As was the case for HETCOR, it was soon shown by SAKHAII and BERMEL[254], how nicely BIRD decoupling complements HSQC experiments, when applied in the proton dimension.

Amongst the most useful techniques that emerged during the development of pure shift NMR certainly is the real-time decoupled BIRD HSQC experiment[305] described by PAUDEL *et al.*, which introduces homonuclear decoupling without a severe signal intensity penalty, often even increasing signal-to-noise ratio through the collapse of multiplet structure. Through these combined advantages, the experiment is being evaluated for routine analytics[306] as well as for the study of proteins[307]. Expanding the field of broadband homonuclear BIRD decoupling certainly is a promising field.
A very nice example, how rethinking existing concepts can lead to key improvements is the extension of ADEQUATE experiments with pure shift BIRD acquisition[308, 309], which very generally leads to sensitivity improvements in a technique which most of all requires high sensitivity.

For heteronuclear correlations, a number of studies also documents the use of real-time band-selective techniques, focusing on the development of assignment strategies in casts of challenging instances of signal assignment. Combinations of real-time homonuclear band-selective HSQC[271, 310] and selHSQMBC[287, 311] are explored by the group of THEODOR PARELLA, with the aim of increasing both signal separation and signal intensity to facilitate assignment processes. The interest in heteronuclear correlation experiments with high resolution certainly extend the interest of every-day analytics and may easily also find application in studies of biomacromolecules[208, 312, 313].

4.4.3.7. Applications IV: Quantitative Extraction of Integrals from Pure Shift Spectra

Finally, it is intriguing to see, if pure shift techniques can be found that feature the favourable line-shape homonuclear decoupling can lead to, while at the same time retaining the ability of signal integration. In general measurement of relative signal integrals, or alternatively signal intensities from signals with narrowed lines may reduce ambiguity in many situations.
When realizing that a relatively small number of reports actually discusses the possibilities and limitations of signal integral quantification from pure shift NMR[263, 269, 274, 314], the impression may arise that this is a fundamental problem to pure shift NMR.
On the other hand, initial interest for these techniques largely arose in the context of diffusion ordered spectroscopy (DOSY)[253, 263], which further remains to be an important field of application[315-317]. Also reports of relaxation rate measurements[263, 318] have been presented and even the determinations of diastereomeric ratios[319, 320] have been attempted.
These techniques have in common that the require an accurate representation of signal integrals to avoid possible misinterpretation. A critical evaluation of the capabilities and the limits of pure shift techniques with respect to signal integral quantification therefore seems to be of general interest.

5. Motivation and Research Goals

As described in section 4.4.3, Experiments with homonuclear decoupling through spin-subset selection have recently evolved into a very vital field of research. We were intrigued by the idea of using such techniques for quantitative measurements of structural parameters for small molecules.

The aim of this thesis is thus, to present contributions to the development of pure shift NMR methods that provide access to solution structure information from high resolution spectra. These techniques are intended to be used for studies of natural products and synthetic organic molecules, which typically are obtained without specific isotope labelling and which can feature a large variety of chemical building blocks. For such cases the experiments to be developed shall provide high resolution alternatives to existing techniques.
The narrowing of signal widths offered by pure shift methods shall be used for deriving high resolution methods that guide signal assignments and structure elucidation even in very crowded spectral regions. As opposed to band-selective homonuclear decoupling techniques[242, 249, 271, 321], the recent advances in the design of broadband decoupling techniques[252, 254, 267, 297] shall be used here in techniques that are suitable for studying a broad range of substances.

5.1. Quantitative Measurement of Solution Structure Parameters from Pure Shift Experiments

To assess the solution structure of the above-mentioned substances, a particular emphasis is put on the measurement of the nuclear Overhauser effect[46] (NOE) and on the measurement of residual dipolar couplings[66] (RDCs) as key structural parameters that can be used for studying the relative configuration and the molecular conformation of the above-mentioned types of molecules in solution. For these parameters it shall be investigated, if the use of pure shift acquisition techniques can be helpful during the extraction procedure.
Projects A and B describe the development and the characterization of pure shift NMR experiments specifically designed for the measurement of the NOE or of RDCs respectively form experiments with pure shift acquisition. The primary aim in both cases is to evaluate the accuracy and the precision with which the experimental techniques that have been derived for the quantitative measurement of these interactions are able to provide these structural parameters. The motivation for this evaluation is twofold:

- It is interesting to use pure shift methods wherever signal overlap interferes with the extraction of NOEs or RDCs. The idea is to enable the use of these methods in solution structure studies of solutes that are otherwise hard to investigate due to an unfavourable signal dispersion.
- Pure shift techniques used may influence both the accuracy and the precision with which the structure parameters may be determined. Potentially the simpler apparent lineshape observed in pure shift experiments is able to mask effects interfering with the extraction of NOEs and RDCs and thus facilitates the unbiased extraction of these parameters. The aim therefore is to investigate if pure shift techniques can be used for measurement of these parameters and to evaluate the achievable precision and accuracy.

The combination of these two projects is stimulated by the complementary information content that can be obtained from NOEs and RDCs favouring a combined use of these parameters[172, 322-327].
Also from a conceptual point of view the direct comparison of these two projects may yield interesting insights into the characteristics of pure shift experiments with respect to quantitative data interpretation, because the mode of extraction of NOEs and RDCs is fundamentally different in the experiments studied. In the case of NOE measurements, the distance information is obtained from relative signal integrals, while the RDC extraction procedure uses frequency differences between pairs of peaks. The discussion

of these two projects therefore covers the question if pure shift experiments are able to reliably reproduce peak positions (as detailed in Project B), and the question if signal integrals can be measured from these spectra (discussed in Project A).
In these projects, therefore two different questions of the robustness of pure shift techniques in terms of quantitative data interpretation therefore are addressed.

5.2. Design and Testing of Novel High-Resolution NMR Techniques with Favourable Signal Shapes

The advances in pulse sequence design presented in Project B directly stimulated developments of the NMR experiments described in Project C and D. We chose to pursue both of these experiments because of their potential use to solution structure elucidation. The close methodologic relationship to the techniques described in Project B provides a common base for these experiments and their joint discussion is used to illustrate various aspects of the perfect echo[195, 196] building block that is the common basis of these experiments.

As discussed, when summarising different pure shift correlation experiments that have emerged in section 4.4.3.6, a number HSQC and HSQMBC experiments were described using pure shift acquisition in the proton dimension, all based on either BIRD decoupling or on homonuclear band-selective methods. By the time we started to pursue Project C, the sole pure shift HSQC experiment that was described is the BIRD-based RESET HSQC[254]. This experiment was able to generate high quality C-H one-bond correlation maps with broadband character and significant improvements of the signal resolution, as shown in Figure 5 of the publication, which is reproduced below (Figure 5.1). Also the real-time BIRD decoupled HSQC[305] experiment later published in 2013 is able to generate broadband homonuclear decoupling with high levels of spectral quality. As however apparent from expansions g) and h) in Figure 5.1, proton splitting from $^{2}J_{HH}$ remains visible in these spectra, if methylene protons are diastereotopic. Realizing, that this problem could potentially be solved with the perfectBIRD extension of HSQC experiments (described in Project B, section 7.3.1), retaining the broadband decoupling character of the HSQC experiment, we were excited to see, if a F_2-perfectBIRD decoupled HSQC experiment would be a good solution to obtain HSQC correlation information with full suppression of all signal splittings (both of homo- and of heteronuclear nature). The obvious advantages over band-selective decoupling schemes that were also applied to HSQC experiment after we started working on the topic[310] are the retention of the broadband character of the experiment and the ability to decouple signals with only small frequency separation in the ^{1}H-dimension.

Insights into the working mechanism of the perfect echo[195, 196], used in the perfectBIRD decoupling scheme, also led to the idea of using the perfect echo as basic mixing element in a COSY-type experiment. It was perceived, that this could lead to spectra featuring the favourable absorptive and in-phase signal shape required for the application of pure shift acquisition schemes based on the principles of spin-subset selection (discussed in section 4.4.3). As stated in section 4.4.3.6, pure shift acquisition was at that time not reported for the direct acquisition dimension of COSY-type, so reports were limited to the application of constant-time decoupling in the indirect dimension of the spectra[36, 297].
We figured, that it would be highly interesting to follow this new idea, leading to a new class of COSY-type correlation experiments. After initial investigations, it was found, that the group of BURKHARD LUY followed the same approach with very alike motivation, which led to a collaborative work on this project. As it turned out that the access to COSY-type correlations that was chosen is highly interesting even without homodecoupling, the work that is reported in project D focuses on the basic CLIP-COSY experiment[328], showing pure shift applications only in a proof-of-principle.

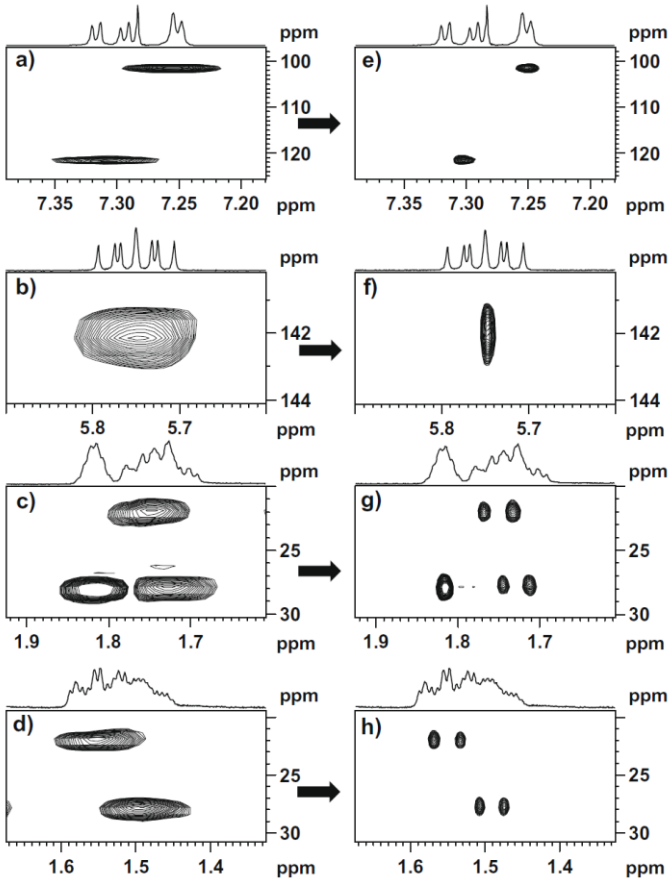

Figure 5.1: Expansions from HSQC spectra of quinine (90 mM in $CDCl_3$) measured without proton-proton decoupling (left) and with the BIRD-based RESET decoupling method (right). For experimental details, the reader is referred to the original work[254]. Figure reproduced with permission from Elsevier. Copyright © 2009 Elsevier Inc. All rights reserved.

6. Project A: Quantification of Cross-Relaxation using Pure Shift Experiments

Content of this chapter have been accepted for publication in *J. Magn. Reson.*:
L. Kaltschnee, K. Knoll, V. Schmidts, R. W. Adams, M. Nilsson, G. A. Morris, C. M. Thiele, "Extraction of Distance Restraints from Pure Shift NOE experiments", *J. Magn. Reson.* **2016**, *in press – accepted manuscripts*,
DOI: 10.1016/j.jmr.2016.08.007

6.1. Motivation

Initial studies of pure shift experiments in this work were centred around the question, to what extent spectra with ZANGGER-STERK homonuclear decoupling[252, 253] provide useful quantitative information from *relative* signal integrals. Signal integrals measured in different established solution-state NMR techniques can provide a variety of very valuable information and its use to the interatomic distance measurement from the NOE, as introduced in section 4.2.3, for the determination of solution structure[57, 60, 105, 262, 329, 330] is only one possible application (another application may be e.g. reaction monitoring[331-334]).
The interest in using pure shift techniques when measuring signal integrals comes from the possible avoidance of signal overlap, were signal are not separated in experiments without homonuclear decoupling. To illustrate, how pronounced this effect can be in crowded spectral regions, sections of NOESY spectra are compared in Figure 6.1. In the spectrum shown on the right ZANGGER-STERK homonuclear decoupling has been applied in the F_2-dimension of the NOESY spectrum[297]. In contrast the left spectrum features fully coupled multiplets in both spectral dimensions. The signal separation that is achieved in the pure shift experiment is improved. Thus in consequence an analysis is possible for more signals without interference from overlap with other signals. The possible benefit of pure shift techniques, when it comes to signal integral quantification, would therefore be to enable a simple analysis of signals that previously could not be analysed, or that required sophisticated multi-component fitting for analysis, and thus to obtain the structural information contained in these peaks that previously was not or not readily accessible.
For NOESY experiments, soon-after the introduction of the basic NOESY technique[47, 52-54, 92], experimental techniques have been described, that introduce homonuclear decoupling in the F_1-dimension of the experiment[194, 242, 243, 262]. These achieve improved signal separation by homonuclear decoupling if the F_1-resolution of these experiments is sufficient. Literature precedence also indicates, that in addition to offering an improved signal dispersion, homonuclear decoupling also eliminates zero-quantum artefacts from NOESY spectra[243], which is a very favourable feature.
With band-selective techniques[242, 243, 247, 249, 262, 298-300, 335], however homonuclear decoupling can only be used efficiently, if peaks within the observed frequency band are not mutually coupled to each other. Band-selective techniques are therefore well suited for solution structure determinations of proteins[262, 336], while for many substances the lack of a clear separation of coupling spins into distinct frequency regions renders these techniques inefficient.
For studying substances where band-selective methods become ineffective, AGUILAR *et al.*[297] presented a method, which provides full homonuclear decoupling over an arbitrarily adjustable chemical shift range through the introduction of Zangger-Sterk homonuclear decoupling[252] into the F_2-dimension of NOESY spectra. The authors however limit discussions in the paper to the qualitative features of the experiment, in particular the very favourable improvement in signal dispersion. An evaluation, if the integrals of the cross-peaks contained can directly be used for a quantitative analysis of cross-relaxation phenomena is not provided. However, for using this technique for the quantitative analysis of chemical exchange

phenomena or the interatomic distance measurement this information is essential. Evaluation of a possible quantitative analysis of the resulting spectra therefore was the initial motivation for this project. The experimental convenience of using a simpler and faster experiment and the fact that no reports on possible relative integral measurements existed at the start of the project prompted us towards first examining the Zangger-Sterk decoupled ^{1}H-experiment, to characterize the influence the homonuclear decoupling technique used can have on apparent relative integrals in the resulting spectra, before turning to the NOESY experiment. In addition, if relative integral measurement was possible directly from this technique, this could also be exploited in various other applications.
In the following chapter, the possibility of determining relative signal integrals in pure shift spectra acquired with the method proposed by ZANGGER and STERK[252] is evaluated. With respect to NOE distance determination, it is illustrated, that precise relative integrals and distance restraints can be obtained with this pure shift method during small molecule studies and it is outlined what the limits to the accuracy of relative integral measurements are in these spectra.

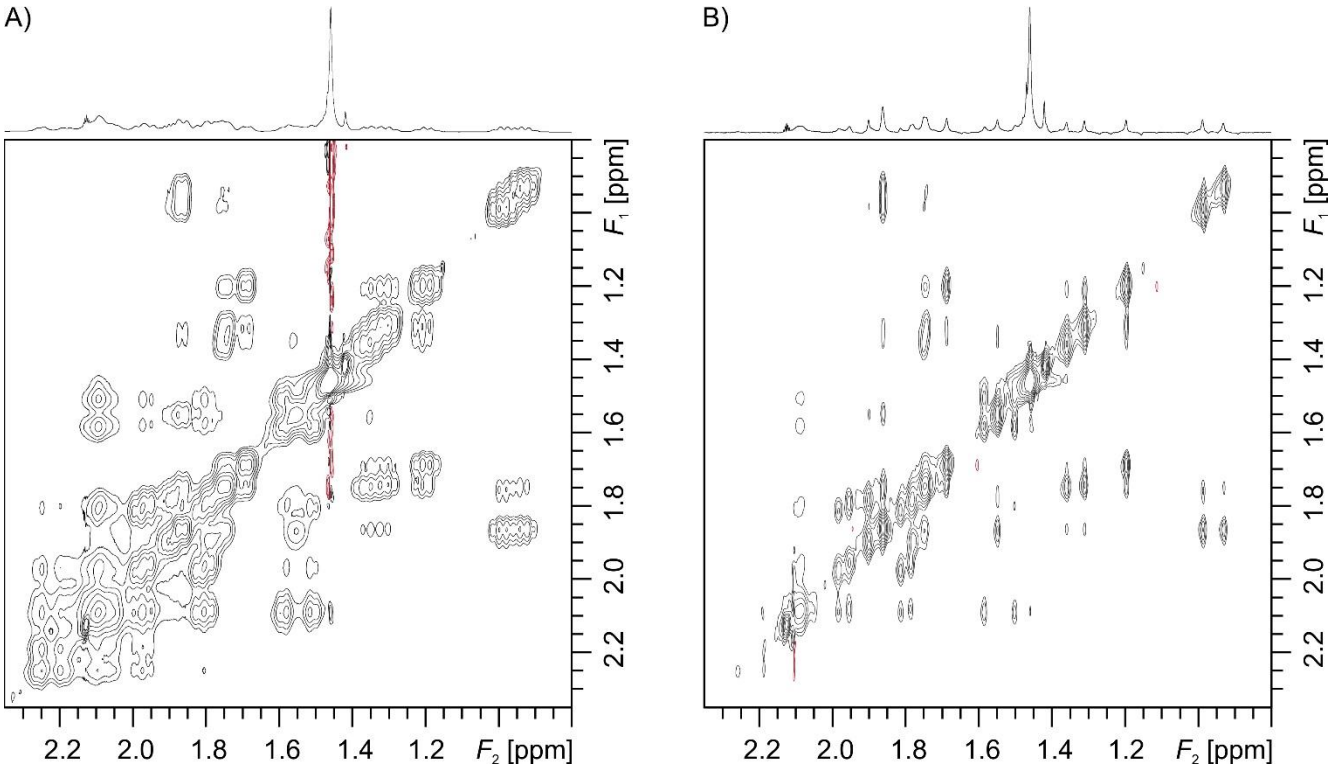

Figure 6.1: Comparison between sections from NOESY spectra with A) normal acquisition and B) Zangger-Sterk homonuclear decoupling in the F_2-dimension. A 55 mM sample of a synthetic tetrapeptide organocatalyst[337] dissolved in toluene-d_8 was used. Experiment durations are 1 h with traditional acquisition and 49.5 h with interferogram-based Zangger-Sterk decoupling. Atop the spectra, ^{1}H spectra are shown A) from a conventional ^{1}H-experiment and B) from a ^{1}H-experiment using the pure shift approach also used for the NOESY spectrum shown. For experimental information, see 14.1.1.

6.2. Outline of the results

For evaluation of the quantitative features of experiments with Zangger-Sterk homonuclear decoupling, data measured for strychnine **1**, as a representative small organic compound, is shown. The structure and numbering used throughout is shown in Figure 6.2. This substance is used to illustrate, that in ^{1}H spectra with Zangger-Sterk homonuclear decoupling[252, 265, 266], relative signal integrals provide a measure for the corresponding number of protons only with a limited accuracy (~ 25%). The relative integrals measured in ^{1}H-ZANGGER-STERK experiments were used to compensate for the limited accuracy during the NOE experiments performed. As this very practical approach, however, is not able to provide insights

into the sources of the errors introduced, some of the factors leading to systematic deviations of relative integrals are briefly discussed. It is illustrated that major contributions come from differential relaxation and from signal dissipation into decoupling sidebands.

In the following, I introduce a selective 1D NOE experiment with pure shift acquisition. With support from KEVIN KNOLL, who joined for his bachelor thesis, I was able to show that these spectra provide accurate distance restraints, when using them in a high sensitivity band-selective acquisition scheme. We used these experiments to show that pure shift NOE experiments can provide NOE derived distances restraints with accuracies better than 0.1 Å, if the distances probed are below 3.4 Å. This illustrates, that the pure shift technique used can be employed in solution structure investigations of small molecules, in cases where signal overlap normally is prohibitive. In addition, in his bachelor thesis[338] KEVIN KNOLL was able to show that also the experiment with broadband homonuclear decoupling provides precise distance restraints, if signal-to-noise is not limiting. For the high signal-to-noise data measured with the band-selective experiment, normalization of NOE peak intensities with relative integrals from ^{1}H-ZANGGER-STERK spectra lead to an improvement of the accuracy of distance determination, while this was not apparent for the broadband decoupled data. In the latter case, the low signal-to-noise ratio of the data seems to mask effects of limited accuracy.

Finally, it is illustrated, that in complete analogy, the NOESY experiment with Zangger-Sterk decoupling[297] enables interatomic distance measurements with accuracies comparable to those that are achieved in NOESY spectra without homonuclear decoupling[47, 52, 53], with the upper limit for distances that can be measured again being limited by sensitivity.

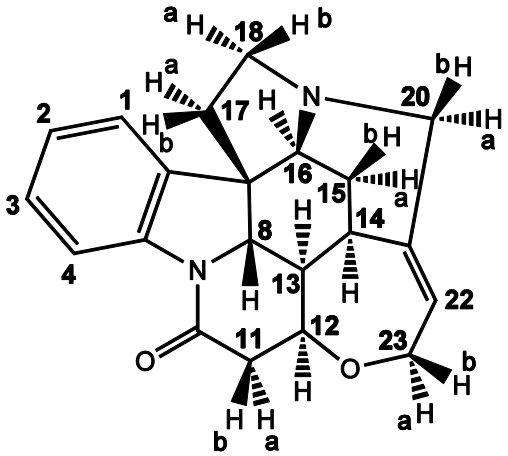

1

Figure 6.2: Structure of strychnine **1** and atom numbering used throughout this work. N.B.: In my Master thesis, I adopted the signal assignment reported in the book by BERGER and SICKER[339], which reports a wrong signal assignment for signals H20a and H20b (the signals are interchanged). The corrected numbering of signals is used in this work, which therefore differs from the numbering used in my master thesis.

Content of this chapter have been accepted for publication in *J. Magn. Reson.*:

L. Kaltschnee, K. Knoll, V. Schmidts, R. W. Adams, M. Nilsson, G. A. Morris, C. M. Thiele, "Extraction of Distance Restraints from Pure Shift NOE experiments", *J. Magn. Reson.* **2016**, *in press – accepted manuscripts*,
DOI: 10.1016/j.jmr.2016.08.007

The Supporting information is not printed in full length: The pulse sequences & the AU contained in the Supporting information are provided in the electronic material only.

Extraction of Distance Restraints from Pure Shift NOE experiments

Lukas Kaltschnee[1], Kevin Knoll[1], Volker Schmidts[1], Ralph W. Adams[2], Mathias Nilsson[2], Gareth A. Morris[2], Christina M. Thiele[1]

1: Clemens-Schöpf-Institut für Organische Chemie und Biochemie, Technische Universität Darmstadt, Alarich-Weiss-Straße 16, D-64287 Darmstadt, Germany, cthiele@thielelab.de

2: School of Chemistry, University of Manchester, Oxford Road, Manchester M13 9PL, UK.

1 Abstract

NMR techniques incorporating pure shift methods to improve signal resolution have recently attracted much attention, owing to their potential use in studies of increasingly complex molecular systems. Extraction of frequencies from these simplified spectra enables easier structure determination, but only a few of the methods presented provide structural parameters derived from signal integral measurements. In particular, for quantification of the nuclear Overhauser effect (NOE) it is highly desirable to utilize pure shift techniques where signal overlap normally prevents accurate signal integration, to enable measurement of a larger number of interatomic distances. However, robust methods for the measurement of interatomic distances using the recently developed pure shift techniques have not been reported to date.

In this work we discuss some of the factors determining the accuracy of measurements of signal integrals in interferogram-based Zangger-Sterk (ZS) pure shift NMR experiments. The ZS broadband homodecoupling technique is used in different experiments designed for quantitative NOE determination from pure shift spectra. It is shown that the techniques studied can be used for quantitative extraction of NOE-derived distance restraints, as exemplified for the test case of strychnine.

2 Introduction

Rational design of catalysts and drugs generally requires models for molecular structure and motion, in order to understand the different modes of action involved. When it comes to the study of molecules in the liquid state, structural parameters available from nuclear magnetic resonance spectroscopy have become indispensable tools, the most prominent being vicinal couplings[1, 2], nuclear Overhauser enhancements[3-5] and residual dipolar couplings[6, 7]. In the case of small molecules, support or rejection of a given structural model is often based on the limited number of structural restraints that are experimentally available, making such decisions prone to ambiguity unless ways of complementing the existing information are found.

In particular, for signals participating in complicated scalar coupling networks, the extraction of NOE enhancements is likely to be corrupted by signal overlap either with other multiplets, or with zero quantum responses. Approaches to reducing problems related to signal overlap are commonly based on the dispersal of signals into multiple spectral dimensions[8-11], while interference from zero quantum artefacts can be reduced by using a zero quantum suppression filter[12-15].

If the compound in question provides favourable signal dispersion, as is the case for the backbone signals of proteins, both improved spectral separation and suppression of zero quantum artefacts can be achieved for limited spectral regions by using band-selective homonuclear decoupling techniques[13, 16-23]. These not only reduce the widths of the resulting signals, reducing the risk of signal overlap, but also refocus the evolution of (weak) homonuclear coupling evolution along the band-selectively decoupled dimension, cancelling (antiphase) zero quantum artefacts.

These desirable effects of homonuclear decoupling have also been reported for NOESY experiments using Zangger-Sterk decoupling[24], which enable homonuclear decoupled signals to be collected over the entire spectral width within a single experiment (broadband decoupling). Broadband decoupling is particularly helpful when band-selective experiments become inefficient, for example due to the lack of repetitive structural motifs within the target species, as is typically the case in small molecules.

Even though the improved signal resolution and the suppression of zero-quantum artefacts inherent in pure shift NOESY and ROESY experiments could be very beneficial in the context of quantitative evaluation of the resulting spectra, recent reports have focused on the qualitative features of these spectra[20, 21, 24]. McKenna and Parkinson made an initial investigation of quantitative analysis of real-time band-selective (HOBS) pure shift NOESY, but encountered difficulties in obtaining reliable data[21]. It could be argued that, while the precise measurement of signal positions and peak separations can be readily achieved by modern pure shift techniques[25-32], the robust measurement of relative signal intensities or integrals using pure shift methods has yet to be demonstrated.

In principle, quantification using signal intensity/integral should not be an issue for pure shift methods. Indeed, comparing peak intensities or integrals for a given chemical site works well, as in the case of T_1, T_2, and DOSY measurements[33-36]. Direct comparison of peak integrals in the case of proton sites in similar chemical environments also works well, as in determinations of diastereoisomeric and enantiomeric excesses[37-39]. However, a problem when comparing the signal intensities/integrals for chemically distinct nuclei is that the responsivity for different signals varies to some extent in all existing methods, due to differences in relaxation rates and to the different spin-spin couplings present. Where absolute signal intensities are required, it is shown here, *inter alia,* that it is helpful to normalise measured integrals against those obtained in the equivalent 1D pure shift experiment, in order to cancel out the effects of site-dependent responsivity. Such normalisation would not, however, protect against the potential effects of overlap between the small artefacts generally present in pure shift spectra and signals of interest.

We will show here that under appropriate conditions, NOESY and PFGSE NOE experiments with broadband homodecoupling using the ZS method can indeed yield interatomic distance restraints suitable for structural analysis. Such experiments can be used as alternative sources of NOE-derived distance restraints in cases where classical methods are biased, either by signal overlap or by residual zero quantum artefacts. We will also illustrate the use of signal normalisation to correct for site-dependent responsivity, and assess the relative contributions to such effects from different sources.

3 Methods

The development of pure shift NMR experiments, providing full homonuclear decoupling for proton signals either over a narrow frequency band (band-selective methods) or over the full spectral width (broadband methods), has evolved of late into a lively field of research[40-42]. In particular, decoupling schemes achieving refocusing of coupling evolution for a chosen subset of spins (the active spins) have been used to improve signal separation in a wide variety of one- and multidimensional spectra, including 1D ^{1}H[43-50], TOCSY[43, 51, 52], DOSY[33], HSQC[27-30, 53-55], NOESY[20, 21, 24], ROESY[23] and HSQMBC[31] experiments.

For experiments based on this principle, the mode of spin subset selection largely determines how well a particular homodecoupling method is suited to the application in question. Spin subset selection can be achieved by using the selection of limited frequency bands (soft-pulse experiments such as HOBS)[16, 50], by simultaneous spatially and frequency-dependent selection (ZS decoupling)[43, 46], by filtration using a dilute spin isotope (BIRD)[44, 56] and by statistical selection (the Pell-Keeler anti-z-COSY method and PSYCHE)[34, 47].

Here we employ the method of spatially-dependent frequency selection, as proposed by Zangger and Sterk[43], in which a selective pulse is applied under a weak field gradient (Figure 1a) in order to

invert the active spins independently of the passive ones. In this case, the field gradient makes the frequency range for which the selective pulse causes signal inversion to vary systematically with position along the long axis of the sample. The field gradient spreads out the frequency range affected by the selective 180° pulse to cover the whole spectrum, but each chemical shift is excited in a different thin slice of the sample so the high bandwidth comes at a high cost in sensitivity.

Accumulation of a time domain signal – a FID – with negligible modulation from homonuclear coupling requires a decoupling block to be applied more frequently than the frequency of the coupling evolution. Two approaches have been presented to achieve this. In the first, a single homodecoupling element is inserted into an incremented evolution time t_1 so that homonuclear couplings refocus at the end of t_1. This allows the collection of a single homodecoupled time point per time increment (if the decoupling is applied in an indirect dimension), or the collection of a block of data points either side of the instant of full refocusing (interferogram-based decoupling in a pseudo-direct acquisition dimension)[43]. The second approach, collection of the entire time domain signal within a single scan in the direct dimension, as in instant or real-time homodecoupling methods, avoids the need for time-consuming data collection in indirect or pseudo-direct dimensions. However it requires repeated application of the homodecoupling element during acquisition, causing the unwanted effects of relaxation and pulse imperfections to accumulate and leading to line broadening and spectral artefacts[46].

Here we use NOESY[57] and 1D PFGSE NOE[58, 59] experiments with interferogram-based ZS decoupling. The interferogram approach requires a pseudo-direct homodecoupling dimension, but does not require repeated application of the homodecoupling element and hence limits spectral artefacts and enables the acquisition of comparatively clean spectra. In addition, long frequency-selective pulses, which are needed to decouple signals separated by only a few tens of hertz, can be used. Because experimental imperfections such as incomplete signal inversion by the selective pulses do not accumulate as the homodecoupling element is repeated, the spectral artefacts caused by such loss mechanisms are avoided. Thus these advantages in terms of spectral quality, signal integral quantification, and experimental versatility are traded for an increased experiment duration compared to real-time decoupling experiments.

For the NOESY experiment, we use an implementation providing ZS homodecoupling in a pseudo-direct dimension, which has previously been shown to provide high quality NOESY spectra[44] (see Figure 1c)). In addition, we introduce the ZS-homodecoupled 1D PFGSE NOE experiment[59, 60] shown in Figure 1b). This 1D PFGSE NOE experiment uses the same homodecoupling sequence as the 2D NOESY method, in each case replacing the acquisition block in the conventional experiment.

From the direct time domain data, acquired for different increments of the pseudo-direct decoupling dimension, time domain signals are constructed in which weak coupling contributions are largely suppressed and which, after Fourier transformation, provide the homodecoupled spectra. The data

rearrangement process is performed conveniently using an AU program, which can be downloaded from http://nmr.chemistry.manchester.ac.uk/sites/default/files/pshift.

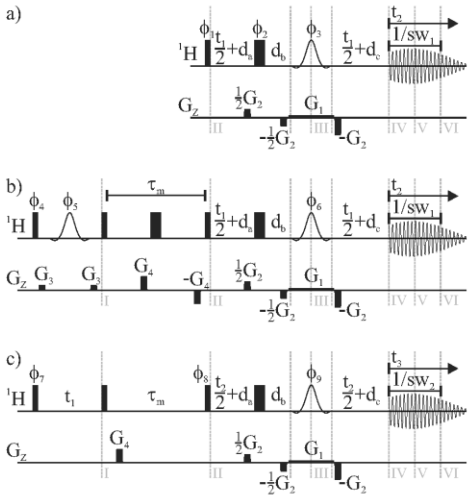

Figure 1: Pulse sequence schemes for the ^{1}H (a), the PFGSE NOE (b) and the NOESY (c) experiment, in each case using a ZS element for homodecoupling in the pseudo-direct acquisition dimension[24]. Narrow bars and wide bars indicate hard 90° and 180° pulses respectively, with phase x unless stated explicitly. Selective pulses are indicated by unfilled shapes. The duration of the data acquisition chunk (1/sw$_i$) is equal to the time increment of t_i in the homodecoupling dimension, which also determines the delays d_a = (1/(4*sw$_i$)), d_b = (1/(2*sw$_i$)) and d_c = (1/(4*sw$_i$)). To avoid signal distortion introduced by digital filtration, acquisition is started before the end of d_c and the data points acquired before the end of d_c are discarded. The pulse phases used are $\Phi_1 = (x\ -x)_2\ (y\ -y)_2$, $\Phi_2 = (x)_{16}\ (y)_{16}\ (-x)_{16}\ (-y)_{16}$, $\Phi_3 = ((x)_2\ (y)_2)_2\ ((-x)_2\ (-y)_2)_2$ and $\Phi_{rec} = x\ -x\ -x\ x\ y\ -y\ -y\ y$ for the ^{1}H experiment, $\Phi_4 = x\ -x$, $\Phi_5 = (x)_2\ (y)_2\ (-x)_2\ (-y)_2$, $\Phi_6 = (x)_8\ (y)_8\ (-x)_8\ (-y)_8$ and $\Phi_{rec} = (x\ -x\ -x\ x)_2\ (-x\ x\ x\ -x)_2$ for the PFGSE NOE experiment and $\Phi_7 = x\ -x$, $\Phi_8 = (x)_2\ (-x)_2$, $\Phi_9 = (x)_4\ (y)_4$ and $\Phi_{rec} = x\ -x\ -x\ x\ -x\ x\ x\ -x$ for the NOESY experiment.

The ability of interferogram-based ZS techniques to improve signal resolution has been demonstrated previously[24, 33, 43, 48, 51, 61], but there has been only limited discussion of quantitation. Resolution of overlapped signals is clearly beneficial for NOE quantification in crowded spectral regions, and here we investigate the quantitative interpretation of signal integrals from spectra acquired using ZS-based techniques. We chose a test system with well-dispersed proton signals; at first sight, this is a strange choice, since such a system has no need of improved resolution, but it allows us to make direct comparisons between pure shift and conventional measurements for the majority of signal integrals. In addition, we required that the compound of choice be well characterized in previous NOE studies, and that an appropriate structural model be available for comparison. We therefore used strychnine, for which the structural model has recently been reinvestigated[62-65] using high accuracy measurements of NOEs and J-couplings, as test substance for these studies. The structural restraints determined here are compared to the two-conformer model

proposed by Butts *et al.*[63]. NOE data analysis is performed assuming the validity of the initial rate approximation, using the method of internal normalization described by Macura *et al.*[66] for 2D NOESY data and using the PANIC analysis described by Hu and Krishnamurthy[67], with a slight modification, for 1D selective NOE data (for data analysis details, see section 1.1 in the SI). As discussed in detail below, the data analysis for homodecoupled experiments is carried out here in two different ways: the integrals measured are either used directly in the analysis, or they are first normalised with respect to the integrals in a 1D homodecoupled ^{1}H spectrum, measured with the same parameters, in order to correct for differential signal losses caused by the decoupling.

4 Experimental

4.1 Sample preparation

Samples were prepared by dissolving strychnine in $CDCl_3$, degassing by the freeze-pump-thaw method, and sealing under vacuum. Selective NOE experiments were performed with a 120 mM sample; all other experiments were performed using a 267 mM sample.

4.2 Experimental setups

1D PFGSE NOE experiments were performed on a Bruker Avance III HD spectrometer operating at 400.13 MHz ^{1}H base frequency, equipped with a 5 mm triple-resonance broadband direct probe with z-gradient. Sample temperature was regulated at 300 K using a BCU II -80/60 unit and the 90° ^{1}H pulse duration was 10 µs.

For all other experiments, a Bruker Avance III spectrometer operating at 600.4 MHz proton base frequency was used, equipped with a 5 mm triple-resonance broadband inverse probe with z-gradient. Sample temperature was regulated at 300 K using a BCU-Xtreme unit and the 90° ^{1}H pulse duration was 9.35 µs.

4.3 ^{1}H experiment with Zangger-Sterk decoupling

For acquisition, we used the pulse sequence freely available at http://nmr.chemistry.manchester.ac.uk/sites/default/files/push1dzs (added to section 6.1 in the SI). The spectrum was collected using a proton spectral width of 10 ppm (166.4 µs dwell time) with the carrier positioned at 5 ppm. A single transient was collected for each increment in the homodecoupling dimension. We used a relaxation delay of 24 s (highest T_1: 4.8 s; see Table S1 in the SI) and no dummy scans. An rSNOB[68] pulse of 93.6 ms duration was used for homodecoupling, applied under a nominal pulsed field gradient, G_1, of 1.05 G/cm. Coherence selection gradient pulses were of duration 0.5 ms and had a smoothed square shape (SMSQ) with a nominal strength, G_2, of 12.5 G/cm.

16 increments were collected in the homodecoupling dimension and chunks of duration 21.3 ms were used (d_c was shortened by 16 complex points for pre-collection of data). The data chunks were concatenated to produce a FID of 340.8 ms with 2048 complex data points; the constructed FID was zero-filled to 4096 complex data points and exponential apodization (1 Hz line broadening) was applied. Automatic baseline correction was applied to the spectrum before manual integration of the peaks.

4.4 Selective NOE experiments

For PFGSE NOE experiments without homodecoupling, Bruker pulse program library implementations were used. (Topspin 3.2 patchlevel 6). The selective NOE experiment without Thrippleton-Keeler zero-quantum filtration[14] used the implementation described in ref. [59], with the modification that a single gradient-filtered selective inversion was used in the preparatory phase (PFGSE instead of DPFGSE for selective inversion; *selnogp* in the Bruker pulse program library). The experiment with zero-quantum filtration used a uniaxial Thrippleton-Keeler filter[14] at the end of the second half of the mixing period (the filter is executed during $\tau_m/2$; *selnogpzs* in the Bruker pulse program library). In both cases, phase cycling for the first hard pulse and the selective inversion pulse followed ϕ_4 and ϕ_5 as reported in Figure 1 and the receiver phase cycle was ϕ_{rec} = x -x -x x. All other phases were x. The pulse sequence used for homodecoupled experiments is provided in section 6.2 in the SI.

For all selective NOE experiments the carrier frequency was 2.79 ppm in the proton spectrum and the spectral width 5000 Hz (12.5 ppm; 200 µs dwell time). In all cases, 4 dummy scans, an 8 scan phase cycle, and a recovery delay of 10 s were used. NOE build-up was monitored for a series of eight mixing times from 50 to 500 ms (500, 270, 120, 400, 50, 180, 300 and 90 ms) in all cases. For experiments with band-selective decoupling, 40 ms rSNOB[68] selective pulses were used. In experiments both without homodecoupling and with broadband homodecoupling, selective inversion before NOE mixing was performed using RE-BURP[69] pulses of different lengths (90 ms for H12, 40 ms for H13, 80 ms for H15a and 50 ms for H15b). Broadband decoupling was achieved using 20 ms rSNOB pulses applied at the transmitter frequency under a constant z-gradient of nominal amplitude G_1 = 0.25 G/cm. G_2, G_3 and G_4 were shaped gradient pulses (SMSQ) of 1 ms duration. Maximum amplitudes used were G_2 = 7.5 G/cm, G_3 = 20 G/cm and G_4 = 25 G/cm respectively. All pulsed field gradients were followed by a 200 µs recovery delay. Experiments with Thrippleton-Keeler filtration used a 20 ms smoothed chirp pulse with a frequency sweep over 60 kHz, applied under a z-gradient of 4.5 G/cm.

In experiments without homodecoupling, the time domain signal was acquired with 32768 complex data points (6.6 s acquisition time). Exponential apodization (line broadening of 0.3 Hz) was applied before Fourier transformation, and manual phasing and automated baseline correction were used.

The time domain signal in homodecoupled selective NOE experiments was collected in 16 data chunks of 20 ms (except for data acquired with 10 ms and 25 ms data chunk durations to illustrate relative sideband intensities in section 5.2; these were acquired in 32 and in 13 data blocks respectively, with similar numbers of time domain data points used for processing in all cases). Concatenated FIDs were zero-filled to 2048 complex data points and exponential apodization (3 Hz line broadening) was applied before Fourier transformation. Automated baseline correction was used before integration.

For normalisation of pure shift NOE data with relative integrals from ^{1}H ZS experiments, ^{1}H ZS spectra were measured under identical conditions to the homodecoupled selective NOE experiments. For normalisation of data with broadband ZS decoupling, a single ^{1}H ZS experiment was performed, with the eight-step phase cycle also used for NOE measurements. In the case of band-selective experiments, a series of band-selective ^{1}H ZS spectra was measured, with the irradiation frequency of the selective pulse shifted to the frequencies also used for homodecoupling in band-selective homodecoupled NOE experiments. Relative integrals were calculated from this series of spectra. A single scan per t_1-increment was used for the band-selective ^{1}H ZS series for convenience, while eight scans were used for the broadband decoupled reference spectrum. Data processing was identical to that used in the pure shift selective NOE measurements.

4.5 NOESY experiments

Gradient-selected NOESY experiments without decoupling used the pulse sequence codes supplied by the manufacturer (*noesygpph* for experiments without, and *noesygpphzs* for experiments with, Thrippleton-Keeler filtration during mixing, TopSpin 3.1 patchlevel 7)). The two-step phase cycle used was that of the homodecoupled experiment shown in Figure 1c. For experiments with uniaxial Thrippleton-Keeler filtration[14], the filter element was incorporated into the mixing time 50 µs after its beginning, followed by the coherence selection gradient pulse. For acquisition of the homodecoupled data, we used the pulse sequence given in section 6.2 of the SI. All NOESY experiments were collected with a proton spectral width of 10 ppm (166.4 µs dwell time) in both dimensions. In the indirect dimension, 512 data points were collected in all cases, using States-TPPI phase encoding[70]. All NOESY data were collected with 16 dummy scans and two scans per increment in the indirect dimension(s). All pulsed field gradients were followed by a 200 µs recovery delay. Experiments without homodecoupling were measured in two mixing time series (a shorter and a longer one), whereas a single mixing time was used for the pure shift experiment.

The longer mixing time series, acquired with Thrippleton-Keeler filtration (*noesygpphzs*), was collected with 16384 complex data points in the direct dimension (2.7 s of acquisition) and a relaxation delay of 25 s. Mixing times from 50 to 500 ms were used (50, 300, 150, 500, 100, 400, 200

and 250 ms). During mixing, a spoil gradient pulse of 5 ms duration with smoothed square shape (SMSQ) and an amplitude of $G_4 = 20$ G/cm was used. For Thrippleton-Keeler filtration, a 20 ms smoothed chirp pulse with a frequency sweep of 60 kHz and a 6 G/cm z-gradient was used.

The shorter mixing time series was acquired using NOESY experiments without zero-quantum filtration (*noesygpph*). These spectra were collected with 2048 complex points in the direct dimension (0.34 s acquisition time) and a relaxation delay of 7 s. Mixing times from 100 to 400 ms were used (100, 200, 300, and 400 ms). During mixing, a spoil gradient pulse of 1 ms duration and 20 G/cm amplitude with smoothed square shape (SMSQ) was used.

For NOESY spectra with F_2-ZS decoupling, the time-domain signal in the pure shift dimension was constructed from 16 data chunks of 21.3 ms duration. The resulting time domain signals contained 2048 complex points (0.34 s acquisition). The experiment was collected with a mixing time of 400 ms and a relaxation delay of 7 s. The selective pulse used for homodecoupling was a 93.6 ms rSNOB[68] pulse applied under a z-gradient $G_1 = 1.05$ G/cm. During the mixing time a purging gradient pulse G_3 of 0.5 ms duration with a maximum amplitude of 10 G/cm and smoothed square shape (SMSQ) was used. The slice selection gradient pulse G_1 proved sufficient for coherence selection and $G_2 = 0$ was used.

All NOESY data were zero filled twice in each dimension. The 2D FIDs were processed using exponential apodization (line broadening of 0.5 Hz for the long mixing time series and of 3 Hz for the short mixing time series and the pure shift NOESY) in the direct dimension and cosine squared in the indirect dimension. In all cases, automatic baseline correction was applied first along the indirect and then along the direct spectral dimension. Integration regions were manually defined. For normalisation of NOESY data with ZS decoupling, the relative integrals measured from the ^{1}H ZS experiment described in section 4.3 were used (as shown in Figure 2).

5 Results

We show first that that under suitably chosen experimental conditions, ZS homodecoupling using the interferogram based acquisition approach[43] leads only to minor changes in the relative signal integrals measured. Results obtained using the broadband homodecoupled ^{1}H-experiment shown in Figure 1a are presented, the sources of systematic errors introduced by the homodecoupling are discussed, and a simple method to correct for those errors is described. Full raw experimental data, pulse sequence code, and the pshift interferogram assembly software can be downloaded from DOI: 10.15127/1.303031 and DOI: 10.15127/1.303032.

5.1 Signal amplitude quantification in ^{1}H-experiments with interferogram-based Zangger-Sterk decoupling

ZS decoupled experiments can in general use a wide range of experimental parameters, with the optimal settings depending on the sample studied. The example shown in Figure 2 illustrates a typical situation for a small organic molecule for which homodecoupling can be achieved for almost all signals studied (signals for H17a and H17b are isochronous by chance and cannot be decoupled by the method used, so signals involving these protons will be excluded from analysis that follows).

Comparison of the relative integrals shown in Figure 2 illustrates directly that, as compared to the normal single scan proton experiment, the relative numbers of protons contributing to the integrals are represented less accurately, with deviations of up to 25% (between H4 and H11a) from their ideal values. In each case H22 was arbitrarily assigned an integral of 1. While the variation in measured integral could be attributed in part to the lower signal-to-noise (S/N) ratio obtained in the homodecoupled experiment, clear systematic deviations can be observed. In particular, it is evident that all protons from methylene groups (shown in red) show reduced integrals relative to the arbitrarily chosen reference of H22, while all other relative integrals deviate by less than 7% (between H4 and H1). We now discuss the factors responsible for the discrepancies, and hence for the desirability of normalization. A full analysis can be found in section 9.2 of the SI.

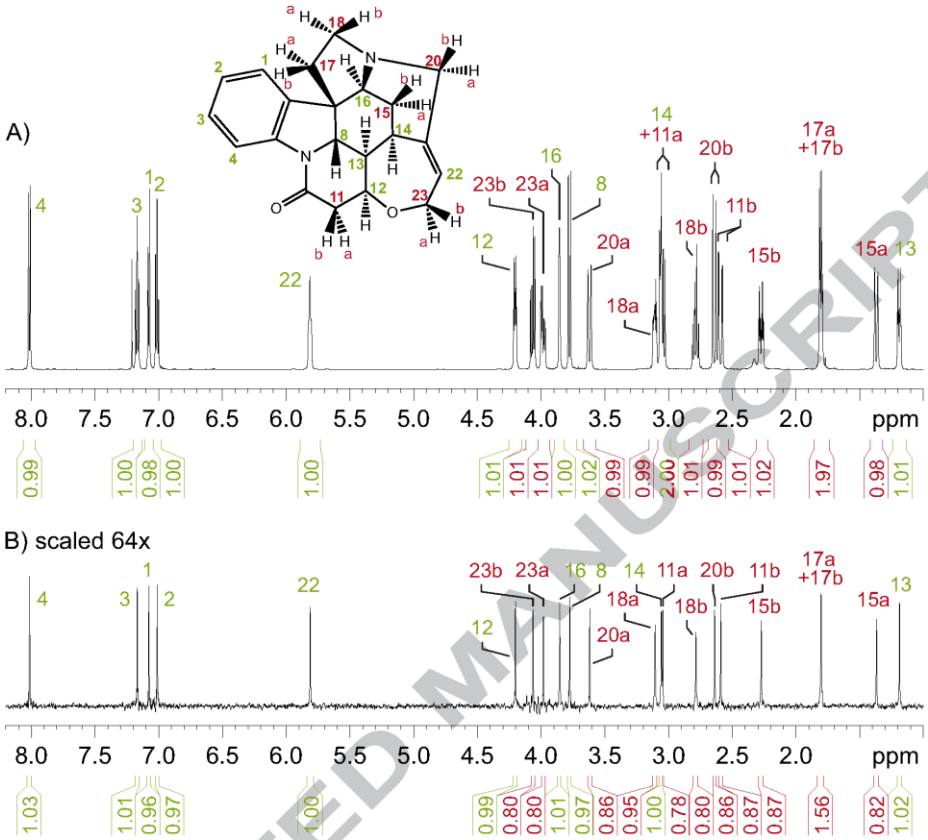

Figure 2: Relative signal integrals, with respect to H22, obtained in an interferogram-based 1D ZS experiment and a single scan ^{1}H experiment. A) Normal single-scan ^{1}H spectrum. B) ZS homodecoupled spectrum. Integrals and atom numbers are color coded, with CH groups green and CH_2 groups red.

5.1.1 Signal attenuation by relaxation

The most important factor distorting the relative signal integrals measured in ZS experiments is generally relaxation during the homodecoupling pulse sequence element. For the experiments studied here, the relaxation that matters is that seen between time points II and IV in Figure 1, i.e. the relaxation that happens in every increment during the homodecoupling element. In particular, if decoupling of signals with small frequency separations (< 100 Hz) is desired, the selective pulse required is sufficiently long (e.g. 36 ms for a pulse with Gaussian shape and a 100 Hz width at the 5% inversion level) that significant signal decay can occur even for small molecules. In the case of strychnine, the pairs of coupled spins with the lowest frequency separations that we aim to decouple are the H1-H2 pair ($\Delta\Omega$ = 38.5 Hz at 11.4 T, $^{3}J_{HH}$ = 7.5 Hz) and the H23a-H23b pair ($\Delta\Omega$ = 46.9 Hz at 11.4 T, $^{2}J_{HH}$ = -13.8 Hz). These require a selective pulse with a maximum bandwidth of ~ 40 Hz. For the spectrum shown in Figure 2, we chose to use an rSNOB pulse of 93.6 ms duration because of the

steep cut-off of the refocusing profile obtained (~ 27 Hz and 40 Hz bandwidths at the 50% and 1% levels, respectively). Together with the additional evolution delays d_a, d_b and d_c this results in quite a substantial duration for the homodecoupling block (115 ms), rendering relaxation during this period significant.

5.1.2 Signal amplitude changes introduced by data chunking

An additional source of signal intensity loss in the homodecoupled data collected, whether using interferogram-based[43] or real-time acquisition[45], is the recording of data chunks of finite length Δ_{ZS}, rather than just single data points. Since couplings are fully refocused only at the midpoint of each chunk, J evolution causes a reduction in signal towards the edges of chunks, diverting a small fraction of the available signal intensity into decoupling sidebands. These sidebands lead both to a reduction in the intensity of the central peak, and to the possibility of overlap between parent signals and the decoupling sidebands of other signals. We show in the SI how, given the values of the principal coupling constants responsible, the intensity losses caused by chunking, which can approach 7% in the case studied, may be estimated.

5.1.3 Impact of field inhomogeneities

Spectra acquired with ZS decoupling feature a pronounced loss of overall signal intensity compared to spectra without decoupling, mainly as a necessary consequence of the use of spatial selection. In this experiment, signals are collected from small slices within the sample located at different z-positions

$$z_m = \frac{2\pi(\nu_m - \nu_{sel})}{\gamma_m G_z} \quad (1)$$

relative to the centre of the gradient coil, governed by the difference between the resonance frequencies ν_m of the individual signals and the frequency ν_{sel} of the selective pulse (γ_m is the gyromagnetic ratio of spin m and G_z is the field gradient applied). As signals are collected from different sample positions, the relative signal intensities observed in the ZS decoupled experiment will depend on the B_1 field strength at the different z-positions at which different signals are measured. In the setup used here this effect is small, as the B_1-field in the probe varies only around 2% over the ~ 1 cm sample length used to collect this spectrum (see Figure S6 in the SI), as should be the case for most modern probes. A second, and sometimes much larger, source of systematic variation in signal intensity with offset is non-uniformity of the z field gradient used[71, 72]. If desired, corrections can be applied to compensate for both sources of amplitude error[73, 74].

5.2 NOE-based distance determinations in pure shift spectra

The previous section shows that interferogram-based ZS homodecoupling can reproduce relative 1D integrals in strychnine with a worst case error of ~ 25%, and summarises the reasons for the site-specific differences in responsivity. In the analysis that follows, we compare the results of NOE-based interatomic distance measurements with and without normalisation to correct for differences in responsivity, and show that NOE experiments with interferogram-based Zangger-Sterk homodecoupling, whether with or without normalization, can indeed be used to determine NOE-based distances in small molecule applications.

5.2.1 PFGSE NOE experiments with band-selective decoupling

Before discussing the possibility of extracting quantitative distance information from ZS homodecoupled NOE spectra, we first discuss the case of band-selective decoupling, using the selective 1D NOE experiment shown in Figure 1b) which has the slice-selective gradient set to zero. The band-selective decoupling scheme that results, retains many of the features of the two ZS decoupled experiments discussed below, while providing better signal-to-noise ratio. This experiment is used here to investigate possible adverse effects of the second selective inversion block on the quantitative information contained in the spectra. However, due to the high S/N ratio it offers, this band-selective variant of the 1D NOE experiment can be of substantial use in its own right if homodecoupling is only required for a limited range of resonances.

As is illustrated in Figure 3, the results obtained with this technique feature good spectral quality, due to the interferogram based acquisition scheme chosen. The traces shown in Figure 3 c), d) and e) show that close to ideal spectra, with flat baselines, can be obtained for spectra containing NOE peaks. These features are very favourable for signal integration or lineshape fitting, in particular if quantification of signals that are very close in frequency is desired. This is illustrated for the signals from H14 and H11a, for which baseline separation is achieved in the band-selectively decoupled experiment, while these signals overlap partially in the spectrum without homodecoupling (compare Figure 3a) and e)).

The band-selective acquisition scheme chosen may require a set of different spectral regions of interest to be sampled in separate spectra, unlike spectra acquired without homodecoupling or with broadband homodecoupling techniques. This also means that a separate set of mixing time series may be required to collect spectra of the inverted signal before mixing, for internal referencing according to equation (S3) (see paragraph 1.1 in the SI). These sets need to be acquired under the same experimental conditions as those for the NOE peaks, with only the offset of the band-selective pulse for decoupling being varied.

For the intense signals of the protons selectively inverted before mixing, *J*-modulation sidebands are visible around the central signal (see Figure 3b)).

While the amplitudes of these sidebands can be comparable to the cross-peaks that need to be quantified later, they are only a minor hindrance to cross peak integration, for two reasons. First, their positions may easily be predicted and altered, as the sidebands appear at integer multiples of the inverse data chunk duration. Second, if the peak selectively inverted before mixing is not part of the band observed (see e.g. trace Figure 3 d)), both the intense inverted signal and its sidebands are absent from the spectra containing the weak cross-peaks. This second feature is a particular advantage of the band-selective experiment discussed.

A very effective way to reduce *J*-modulation sideband intensities, if needed, is to reduce the chunk duration (an alternative approach is to average results over different chunk durations [75]). We illustrate the effect of reducing the chunk length here using the high S/N-ratio data obtained in band-selectively decoupled experiments. In spectra with H15a as the selectively inverted peak, we determined sideband intensities for different chunk lengths by lineshape fitting. For H15a, the total integral intensity of all sidebands, as a fraction of the central peak intensity, amounted to -3.1% for 10 ms chunk duration, -6.8% for 20 ms and -11.2% for 25 ms (from theory, as described by equations (S8) and (S9) in the SI, we expect -1.7%, -7.1% and -11.4% respectively). This illustrates how *J*-modulation sidebands can be scaled down by using shorter chunk lengths. In practice, a compromise has to be made between lower sideband intensities and the longer experiment durations resulting from acquiring larger numbers of shorter data chunks. In the context of distance determination, a signal loss of ~10% will have hardly any influence on the accuracies of the distances determined, and even with chunk lengths of 25 ms, signal loss due to coupling evolution is very unlikely to be the dominant source of error.

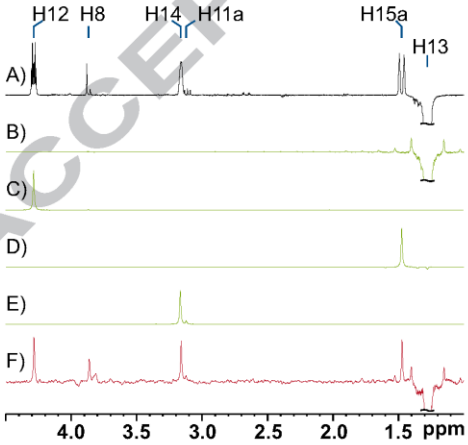

Figure 3: 1D-NOE spectra obtained with selective inversion of H13 and a mixing time of 500 ms. A) Spectrum acquired without homodecoupling, using zero-quantum filtration (3.5 min). The four middle traces B) to E) show the

band-selectively decoupled spectra acquired with observation of B) H13, C) H12, D) H15a and E) H14 & H11a (24 min each). F) Spectrum acquired with broadband ZS homodecoupling (24 min). S/N-ratios measured for H12 are 90 in A), 377 in C) and 28 in F).

To test the distance quantification in 1D NOE experiments, NOE buildup was measured for the set of spin pairs listed given in Table 1. We used two experiments without homodecoupling, one with and one without Thrippleton-Keeler zero quantum coherence suppression during the mixing time. Distance estimation from modified selective NOE experiments was tested without normalization. In most cases in which pure shift techniques are potentially interesting, selective inversion will only be possible for one of the sites involved, due to signal overlap. Therefore, the majority of the distances shown were determined using inversion of only one proton site.

The values listed in Table 1 show that the experiment with band-selective homodecoupling is able to provide cross-relaxation rates from NOE transfer with high fidelity, and therefore only small deviations are seen in the distances determined. Even without normalization, the distance restraints derived from these integrals are in good agreement with the structural model used for comparison. The root mean squared deviation of the distances found amounts to 0.07 Å (2.7%) for the experiment with band-selective decoupling (where distances up to 3.4 Å have been probed), and 0.05 Å for both the experiments without homodecoupling. Normalization of the NOE peak integrals measured using the relative integrals measured in a 1D ^{1}H-ZS experiment reduces the rms deviation (0.05 Å; 2.2%). This suggests that the simple normalization procedure should indeed be used, wherever relative integrals can be measured in the corresponding pure shift ^{1}H experiments. In the case studied, conventional selective NOE experiments without homodecoupling and band-selectively decoupled experiments with normalization yielded distance restraints that were in equally good agreement with the structural model used. We therefore conclude that for high S/N data, the homodecoupling does not interfere with NOE distance determination.

While the molecule studied here is comparatively rigid, for molecules which undergo larger amplitude structural dynamics it is rare for root mean squared deviations of NOE distances from structural models to be less than 0.1 Å. Thus even if normalization is not used, and a small compromise in experimental accuracy has therefore to be made owing to the additional sources of errors discussed above, the penalty in accuracy is negligible in the context of typical NOE analyses (and in the context of the interpretation of these distances using structural models, which in themselves carry many potential sources of error [5, 76]). We therefore conclude that the experiment with band-selective homodecoupling is well suited to NOE analysis.

Table 1: Cross relaxation rates (σ_{jk}) at 9.4 T and interatomic distances ($r_{experimental}$) determined using selective NOE experiments with and without homodecoupling. Selective experiments without homodecoupling were performed

without (PFGSE NOE) and with Thrippleton-Keeler filtration (PFGSE NOE ZQF) during the mixing period; the homodecoupled experiments were band-selective (PFGSE NOE BS) and broadband (PFGSE NOE ZS). In all cases, selective inversion was performed using a single pulse-field gradient selected echo (PFGSE).

nuclei	σ_{jk} (measured at 9.4 T) / s^{-1}						r_{model} / Å	$r_{experimental}$ / Å					
	PFGSE NOE	PFGSE NOE ZQF	PFGSE NOE BS	PFGSE NOE BS normalized with 1H-ZS	PFGSE NOE ZS	PFGSE NOE ZS normalized with 1H-ZS		PFGSE NOE	PFGSE NOE ZQF	PFGSE NOE BS	PFGSE NOE BS normalized with 1H-ZS	PFGSE NOE ZS	PFGSE NOE ZS normalized with 1H-ZS
H15a, H15b	-0.377	-0.381	-0.373	-0.374	-0.370	-0.369	1.757‡						
H13, H12	-0.070	-0.070	-0.068	-0.068	-0.066	-0.066	2.350	2.328	2.329	2.332	2.332	2.342	2.341
H13, H15a	-0.093	-0.092	-0.095	-0.094	-0.078	-0.076	2.260	2.219	2.225	2.205	2.211	2.278	2.287
H12, H14*			-0.030	-0.033	-0.033	-0.031	2.738			2.676	2.626	2.625	2.655
H12, H11a*			-0.052	-0.060	-0.070	-0.069	2.352			2.441	2.383	2.318	2.326
H13, H14*	-0.069	-0.07	-0.059	-0.060	-0.063	-0.058	2.414	2.335	2.333	2.391	2.386	2.359	2.395
H13, H11a*			-0.006	-0.006	-0.012	-0.011	3.401			3.483	3.456	3.131	3.153
H15a, H14*	-0.046	-0.045	-0.047	-0.045	-0.060	-0.046	2.550	2.495	2.507	2.480	2.503	2.380	2.486
H15b, H14*	-0.056	-0.056	-0.059	-0.054	-0.053	-0.042	2.485	2.418	2.420	2.392	2.425	2.426	2.524
H15b, H20a#	-0.106	-0.104	-0.111	-0.109	-0.089	-0.081	2.241	2.171	2.183	2.151	2.157	2.227	2.263
H15b, H16#	-0.054	-0.051	-0.058	-0.056	-0.047	-0.040	2.476	2.428	2.454	2.399	2.410	2.482	2.546
H15a, H16#	-0.049	-0.051	-0.054	-0.051	-0.043	-0.037	2.478	2.469	2.454	2.425	2.447	2.515	2.572
Maximum deviation from model [Å] (all distances)								0.079	0.081	0.093	0.111	0.270	0.248
RMSD from model [Å] (only distances listed for all experiments)								0.054	0.048	0.065	0.052	0.068	0.051
RMSD from model [%] (only distances listed for all experiments)								2.2	2.0	2.7	2.2	2.7	2.1

‡: reference distance, *: can only be quantified unidirectionally, as selective excitation is not possible in one of the spectral regions (selectively inverted spins are H12, H13, H15a or H15b), #: While these distances could have been measured bidirectionally, we only collected data after selective inversion of H15a or H15b.

5.2.2 PFGSE NOE experiments with broadband homodecoupling

In addition to the spectra already discussed, Figure 3 f) shows a spectrum collected with ZS broadband homodecoupling, using the pulse sequence shown in Figure 1(b) with a spatially- and frequency selective pulse rather than just a frequency-selective pulse. It is apparent that the spectral quality deteriorates due to low S/N, but that this is compensated for by the ability to acquire the full homodecoupled spectrum in a single experiment. The ZS signal-to-noise ratio penalty can vary widely depending on the desired bandwidth of the broadband decoupling and the minimum shift difference between coupled spins.

Given the very similar experiment setup of the band-selective and the ZS broadband decoupled experiments, we expect the two experiments to behave very similarly in terms of quantification, apart from the effects of spatial selection. The results reported in Table 1 show that the broadband

decoupled experiment is indeed suitable for NOE-based distance determination, despite the much reduced S/N-ratio.

On average, the uncorrected cross-relaxation rates deviate by 13% from the values obtained with the zero-quantum filtered experiment without homodecoupling, and the normalized values by 16%. This is substantially more in both cases than the 6.5% found for the experiment with band-selective decoupling, reflecting the significant signal-to-noise ratio penalty of the ZS method. All these differences in cross-relaxation rate are sufficiently small that the impact on the distances obtained (which depend on the inverse sixth power) is small, and they remain in good agreement with the structural model used. The largest deviation observed is for the distance between H13 and H11a; from Figure 3 f) it is apparent that the signal of H11a is barely above the noise level (S/N ≈ 4), so integration is of very limited precision in this case. As expected, the poorer sensitivity of the broadband ZS method sets an upper limit on the distances that can be determined reliably using it; the limit depends on the system studied and the experimental settings chosen. The data show that below that upper limit, NOE distance measurements using interferogram-based ZS experiments are sufficiently precise for use in solution structure investigations.

5.2.3 Quantitative interpretation of 2D NOESY with Zangger-Sterk decoupling in the pseudo-direct dimension

The one-dimensional NOE techniques discussed thus far are mainly of interest in cases where the number of NOE contacts to be studied is limited. They will therefore mainly be of interest for determining individual NOE contacts that cannot normally be studied due to signal overlap. If the number of signals to be studied is larger, the F_2-ZS-NOESY[24] experiment shown in Figure 1 may be a more time-efficient approach. In addition to being less time-consuming for complex systems, this approach may also be useful in cases where the signals of both the spins of interest overlap with other spins to which they are not coupled, and hence it is not possible to achieve clean selective inversion. Which of the two alternative approaches, pure shift selective 1D NOE measurement or pure shift 2D NOESY, is the more appropriate clearly depends on the system to be studied.

Because of the low intensities of NOE cross-peaks in molecules in the fast tumbling regime, the intensities of the homodecoupling sidebands seen on either side of the diagonal in the homodecoupled dimension can be comparable to those of the cross-peaks (see Figure 4). This possibility clearly has to be taken into account when making signal assignments in these spectra, to avoid confusion between cross peaks and homodecoupling artefacts. Since the homodecoupling sidebands appear at regular frequency intervals, this is straightforward in most cases. Clearly, the symmetry of cross-peaks about the diagonal helps in the case of remaining doubts.

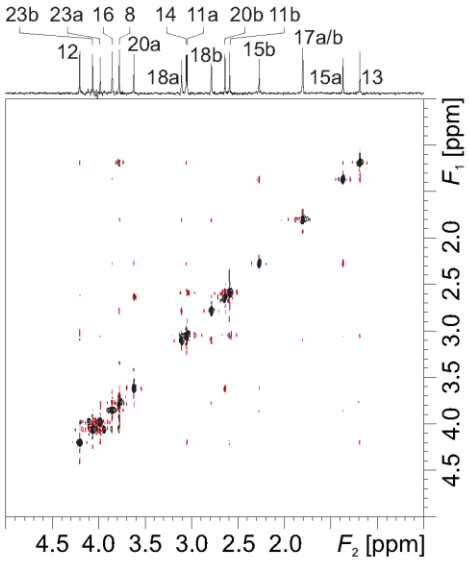

Figure 4: Section of a NOESY spectrum of strychnine, collected with F_2-ZS homodecoupling (experiment duration: 35.3 h).

Again, we tested the ability of this experiment to provide quantitative distance information via the NOE using strychnine as a test sample. As collection of multiple 2D spectra can be very time-consuming (the current experiment required 35.3 h of measurement time), it is unlikely in practice that a series of such spectra will be collected. In contrast to the 1D experiments shown above, we therefore used a single NOESY experiment with ZS homodecoupling, measured with a 400 ms mixing time, to assess the precision that can be achieved using such a single-point-measurement. For comparison with this "compromised precision" measurement, we provide data from different conventional NOESY measurements for comparison: an exhaustive mixing time series (eight mixing times from 50 to 500 ms) of NOESY experiments with Thrippleton-Keeler filtration during the mixing period and a relaxation delay of $5*T_{1,max}$ (total duration of the 8 experiments: 64.9 h), and a reduced mixing time series (four mixing times from 100 to 400 ms) of NOESY experiments using the same compromise relaxation delay as used for the homodecoupled experiment ($1.5*T_{1,max}$, total duration of the 4 experiments: 8.9 h).

For these measurement series, the cross-relaxation rates measured and the distances derived from the latter are given in Table 2. The corresponding scatter plot for distances, obtained without normalization, is given in Figure 5; as with the 1D ZS experiment, the poor signal-to-noise ratio meant that normalization did not produce any significant improvement. Despite the fact that we are using a single mixing time point for the homodecoupled experiment, again the homodecoupled experiment is able to yield cross relaxation rates and interatomic distance estimates of sufficient precision to allow the use of this experiment in solution structure investigations. The risks inherent in using a single

mixing time for distance determinations, in particular if strong coupling is present, should however be noted[60, 64].

As with the selective NOE experiment with ZS homodecoupling, the range of distances that can be determined using F_2-ZS NOESY is limited by the signal-to-noise ratio of the experiment. In the present case, distances of up 2.55 Å could be sampled, though this upper limit will depend strongly on the experimental parameters chosen. Within this distance range, the distances measured are in equally good agreement with the structural model as the data from the reduced mixing time series (acquired without homodecoupling), while only a minor reduction in measurement accuracy is seen compared to the data from the exhaustive mixing time series. It is noteworthy that this high accuracy has been achieved in the pure shift experiment despite its comparatively low S/N-ratio and despite the fact that only a single mixing time was used. It can be concluded that NOESY spectra with interferogram-based ZS homodecoupling and ZS homodecoupled selective NOE experiments are both able to provide internuclear distances with sufficient accuracy for use in solution structure elucidation in future studies.

Table 2: Cross relaxation rates (σ_{jk}) at 14.1 T and interatomic distances ($r_{experimental}$) determined using selective 2D NOESY experiments with and without homodecoupling. Experiments were performed without homodecoupling without (NOESY) and with Thrippleton-Keeler filtration (NOESY ZQF) during the mixing period, and with broadband homodecoupling (NOESY ZS). For values reported in parentheses, interference from zero-quantum artefacts (either between the two spins or through overlap with other cross-peaks) is clearly visible even for mixing times exceeding 200 ms. For the calculation of maximum and root-mean-squared deviations from the distances in the model, only values where the model distance does not exceed 2.55 Å are considered.

nuclei	σ_{jk} (measured at 14.1 T) / s^{-1}				r_{model} / Å	$r_{experimental}$ / Å			
	NOESY	NOESY ZQF	NOESY ZS	NOESY ZS normalized with 1H-ZS		NOESY	NOESY ZQF	NOESY ZS	NOESY ZS normalized with 1H-ZS
15a, 15b	(-0.267)	-0.281	-0.241	-0.241	1.757‡				
H13, H15a	-0.032	-0.047	-0.057	-0.054	2.260	2.498	2.366	2.234	2.253
H13, H14	-0.031	-0.038	-0.025	-0.025	2.414	2.514	2.457	2.556	2.556
H13, H12	-0.035	-0.040	-0.030	-0.030	2.350	2.462	2.429	2.486	2.486
H15a, H14	(-0.023)	-0.026	-0.014	-0.014	2.550	(2.648)	2.606	2.814	2.822
H15a, H16	(-0.028)	-0.029	-0.026	-0.027	2.478	(2.565)	2.562	2.543	2.537
H15b, H14	(-0.025)	-0.031	-0.017	-0.017	2.485	(2.599)	2.533	2.730	2.730
H15b, H20a	-0.068	-0.074	-0.065	-0.065	2.241	2.205	2.195	2.189	2.189
H15b, H16	(-0.023)	-0.038	-0.016	-0.016	2.476	(2.638)	2.556	2.751	2.777
H11b, H8	-0.0126	-0.016			2.632	2.922	2.827		
H20b, H18a		-0.011			2.822		3.020		
H20b, H18b	-0.019				2.456	2.734			
H20b, H20a	(-0.211)	(-0.229)	-0.261	-0.261	1.801	(1.827)	(1.819)	1.733	1.734
H20b, H22	-0.031	-0.035	-0.046	-0.047	2.391	2.518	2.493	2.312	2.305
H18b, H18a	(-0.180)	(-0.203)	-0.195	-0.197	1.771	(1.876)	(1.855)	1.821	1.818
H18b, H8	-0.051	-0.055	-0.046	-0.046	2.371	2.311	2.308	2.315	2.312
H18b, H22	-0.065	-0.005			3.157	3.260	3.419		
H11a, H12	(-0.043)		-0.055	-0.053	2.352	(2.381)		2.247	2.263
H14, H23a	-0.030	-0.035			2.617	2.530	2.491		
H16, H1		-0.041	-0.035	-0.035	2.385		2.426	2.428	2.427
H23a, H12	-0.049	-0.058	-0.034	-0.038	2.303	2.330	2.283	2.439	2.390
H23a, H22	(-0.004)	(-0.007)			2.956	(3.483)	(3.232)		
H23b, H22	(-0.023)	(-0.029)	-0.031	-0.031	2.392	(2.649)	(2.571)	2.479	2.476
RMSD from model [Å] (for distances up to 2.55 Å)						0.14	0.08	0.14	0.14
Maximum deviation from model [Å] (for distances up to 2.55 Å)						0.28	0.18	0.28	0.30

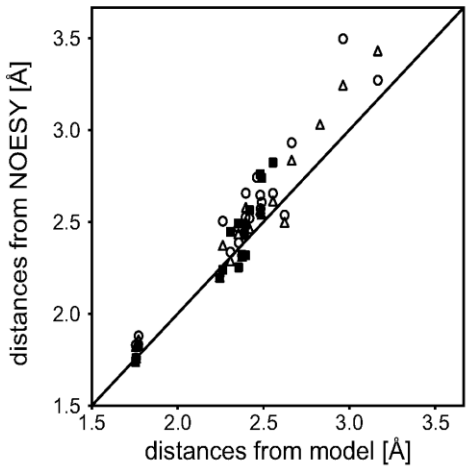

Figure 5: Scatter plot showing the distances determined experimentally, using unnormalized data, versus the averaged distances derived from the two-conformer model described by Butts *et al.*[63], with averaging performed according to a two-site jump model[77] assuming fast molecular tumbling (see equation (S6) in the SI). Results from the pure shift NOESY experiment are given as filled boxes, open circles show the results from the short mixing time series (NOESY) and open triangles show the results from the long mixing time series acquired with Thrippleton-Keeler filtration during mixing (NOESY ZQF). The (very similar) plot for normalized data is shown in the supporting information.

6 Discussion

The results shown illustrate that signal amplitude quantification in pure shift NMR spectra can achieve comparable accuracy to conventional methods, but that careful choice of experimental parameters is required. Signal amplitude quantification characteristics are expected to vary significantly between different homodecoupling methods, as both the signal attenuations introduced by the decoupling technique and the sidebands introduced will be different. Different applications of quantitation require different levels of accuracy. While the experiments outlined here may well be suitable for NOE-based distance determination, they are not likely to be appropriate for applications where signal integrals need to be determined to accuracies higher than 10% - 20% unless appropriate normalization is used.

We have only tested interferogram-based ZS experiments in this work; while other pure shift methods have different characteristics, it is likely some other factors will be relevant in addition to those identified here. Relaxation losses and data chunking will also affect the signal amplitude quantification characteristics of experiments with real-time decoupling. We expect that their effects will be different (e.g. losses due to relaxation or incomplete signal inversion during the homodecoupling elements will cause additional signal sidebands and signal broadening, rather than just signal amplitude reduction).

The relatively good capability to reproduce relative signal intensities that was demonstrated for pure shift spectra derived from anti z-COSY spectra[34] potentially translates into PSYCHE-based pure shift experiments[47], as both experiments use small flip-angle pulses for homodecoupling, but the latter introduces some unwanted T_2 weighting and offset dependence. Both methods may be of interest for pure shift NOESY. In the case of constant-time experiments[78], it should be noted that the strong J modulation of the signal intensities as a function of the constant time used causes severe distortion of relative integrals.

In terms of the precision of signal amplitude quantification, pure shift NMR experiments to date fall well short of the standards achievable with conventional experiments where signals are well separated. However, where conventional spectra show overlap, the extra errors, both random and systematic, introduced by adopting pure shift methods may be a very small price to pay for the ability to make site-specific measurements without the complications of overlapping multiplets.

The broadband-ZS pure shift NOESY approach is clearly of limited use where signal-to-noise ratio is insufficient for precise signal integration. Methods for increasing S/N ratio in ZS based experiments may potentially reduce such problems[48, 79], though such techniques introduce further sources of systematic error and may require a separate evaluation of signal integral accuracy. It should also be noted that we have used a relatively small test molecule here, and that the conclusions drawn may not all apply to larger molecules in which transverse relaxation is much faster. The analysis used here also assumes that full homodecoupling is achieved for the signals studied, which will not be the case for strongly coupled signals.

Our intention here has been to show that careful choice of experimental settings can enable accurate signal integral quantification when increasingly popular ZS homodecoupling methods are used, but also to stimulate critical discussion of the limits of emerging pure shift techniques in terms of signal integral determination.

7 Conclusion

In this paper, we have discussed the quantitative aspects of selected interferogram-based ZS ^{1}H pure shift NMR experiments. For the example of ZS ^{1}H spectra, limitations on direct signal integration are discussed and the influences of different signal loss mechanisms are described for the representative case of a small organic molecule, and a simple correction method is described. Based on this analysis it is concluded that with or without such correction, typical proton-site-dependent systematic errors do not significantly perturb NOE-based interatomic distance determinations. This is corroborated by the results of selective NOE experiments with band-selective and broadband homodecoupling, and a NOESY experiment with broadband homodecoupling, all showing good agreement with a structural model.

While a recent study testing the feasibility of interatomic distance measurements when using a real-time homodecoupling approach reported some results for individual distances that deviated significantly from those obtained without homodecoupling (and other results that showed similar discrepancies between 2D and 1D NOESY methods)[21], such problems were not observed in this study. This may be partly a consequence of the higher spectral quality that can be achieved with interferogram-based, as compared to real-time, homodecoupling. Despite interferogram-based approaches being more demanding in experiment time, for critical applications they may well be the better choice because of the higher spectral quality that can be obtained.

8 Acknowledgements

This work was supported by the ERC (grant number 257041 to C.M.T.), by the Engineering and Physical Sciences Research Council (grant numbers EP/I007989/1 and EP/L018500/1) and by the Merck Foundation for Arts and Science (Ph.D. scholarship to L.K.). Helpful discussions with Drs. Adam Colbourne and Juan Aguilar are gratefully acknowledged.

9 References

[1] M. Karplus, Contact Electron-Spin Coupling of Nuclear Magnetic Moments, J. Chem. Phys., 30 (1959) 11-15.
[2] G. Bifulco, P. Dambruoso, L. Gomez-Paloma, R. Riccio, Determination of Relative Configuration in Organic Compounds by NMR Spectroscopy and Computational Methods, Chem. Rev., 107 (2007) 3744-3779.
[3] A.W. Overhauser, Paramagnetic Relaxation in Metals, Phys. Rev., 89 (1953) 689-700.
[4] I. Solomon, Relaxation Processes in a System of Two Spins, Phys. Rev., 99 (1955) 559-565.
[5] D. Neuhaus, M.P. Williamson, The Nuclear Overhauser Effect in Structural and Conformational Analysis, Second ed., John Wiley & Sons, New York, 2000.
[6] J.R. Tolman, J.M. Flanagan, M.A. Kennedy, J.H. Prestegard, Nuclear magnetic dipole interactions in field-oriented proteins: information for structure determination in solution, Proc. Natl. Acad. Sci., 92 (1995) 9279-9283.
[7] C.M. Thiele, Residual Dipolar Couplings (RDCs) in Organic Structure Determination, Eur. J. Org. Chem., 2008 (2008) 5673-5685.
[8] J. Jeener, B.H. Meier, P. Bachmann, R.R. Ernst, Investigation of exchange processes by two-dimensional NMR spectroscopy, J. Chem. Phys., 71 (1979) 4546-4553.
[9] A. Kumar, R.R. Ernst, K. Wüthrich, A two-dimensional nuclear Overhauser enhancement (2D NOE) experiment for the elucidation of complete proton-proton cross-relaxation networks in biological macromolecules, Biochem. Biophys. Res. Commun., 95 (1980) 1-6.
[10] R.C. Crouch, R.B. McFadyen, S.M. Daluge, G.E. Martin, Disentangling coupling and NOE pathways involving poorly resolved proton signals: HMQC-TOCSY and HMQC-NOESY, Magn. Reson. Chem., 28 (1990) 792-796.
[11] J. Kawabata, E. Fukushi, J. Mizutani, 2D 13C-coupled HMQC-ROESY: a probe for NOEs between equivalent protons, J. Am. Chem. Soc., 114 (1992) 1115-1117.
[12] O.W. Sørensen, M. Rance, R.R. Ernst, z Filters for purging phase- or multiplet-distorted spectra, J. Magn. Reson., 56 (1984) 527-534.

[13] G. Otting, L.P.M. Orbons, K. Wüthrich, Suppression of zero-quantum coherence in NOESY and soft NOESY, J. Magn. Reson., 89 (1990) 423-430.
[14] M.J. Thrippleton, J. Keeler, Elimination of Zero-Quantum Interference in Two-Dimensional NMR Spectra, Angew. Chem. Int. Ed., 42 (2003) 3938-3941.
[15] K.E. Cano, M.J. Thrippleton, J. Keeler, A.J. Shaka, Cascaded z-filters for efficient single-scan suppression of zero-quantum coherence, J. Magn. Reson., 167 (2004) 291-297.
[16] R. Brüschweiler, C. Griesinger, O.W. Sørensen, R.R. Ernst, Combined use of hard and soft pulses for ω1 decoupling in two-dimensional NMR spectroscopy, J. Magn. Reson., 78 (1988) 178-185.
[17] M. Billeter, Y.-q. Qian, G. Otting, M. Müller, W.J. Gehring, K. Wüthrich, Determination of the three-dimensional structure of theAntennapedia homeodomain fromDrosophila in solution by1H nuclear magnetic resonance spectroscopy, J. Mol. Biol., 214 (1990) 183-197.
[18] A. Kaerner, D.L. Rabenstein, An ω1-band-selective, ω1-homonuclear decoupled ROESY experiment: application to the assignment of 1H NMR spectra of difficult-to-assign peptide sequences, Magn. Reson. Chem., 36 (1998) 601-607.
[19] J. Wang, D. Borchardt, D.L. Rabenstein, Improved resolution in two-dimensional 1H NMR spectra of peptides by band-selective, homonuclear decoupling during both the evolution and acquisition periods: application to characterization of the binding of peptides by heparin, Magn. Reson. Chem., 44 (2006) 744-752.
[20] J. Ying, J. Roche, A. Bax, Homonuclear decoupling for enhancing resolution and sensitivity in NOE and RDC measurements of peptides and proteins, J. Magn. Reson., 241 (2014) 97-102.
[21] J.M. McKenna, J.A. Parkinson, HOBS methods for enhancing resolution and sensitivity in small DNA oligonucleotide NMR studies, Magn. Reson. Chem., 53 (2015) 249-255.
[22] A. Hammarstroem, G. Otting, Improved Spectral Resolution in 1H NMR Spectroscopy by Homonuclear Semiselective Shaped Pulse Decoupling during Acquisition, J. Am. Chem. Soc., 116 (1994) 8847-8848.
[23] V.M.R. Kakita, J. Bharatam, Real-time homonuclear broadband and band-selective decoupled pure-shift ROESY, Magn. Reson. Chem., 52 (2014) 389-394.
[24] J.A. Aguilar, A.A. Colbourne, J. Cassani, M. Nilsson, G.A. Morris, Decoupling Two-Dimensional NMR Spectroscopy in Both Dimensions: Pure Shift NOESY and COSY, Angew. Chem. Int. Ed., 51 (2012) 6460-6463.
[25] A. Couffin, O. Thillaye du Boullay, M. Vedrenne, C. Navarro, B. Martin-Vaca, D. Bourissou, Enantio-differentiation of O-heterocycles using a binol-derived disulfonimide as a chiral solvating agent, Chem. Commun., 50 (2014) 5997-6000.
[26] D. Sinnaeve, M. Foroozandeh, M. Nilsson, G.A. Morris, A General Method for Extracting Individual Coupling Constants from Crowded 1H NMR Spectra, Angew. Chem. Int. Ed., 55 (2016) 1090-1093.
[27] L. Kaltschnee, A. Kolmer, I. Timari, V. Schmidts, R.W. Adams, M. Nilsson, K.E. Kövér, G.A. Morris, C.M. Thiele, "Perfecting" pure shift HSQC: full homodecoupling for accurate and precise determination of heteronuclear couplings, Chem. Commun., 50 (2014) 15702-15705.
[28] N. Helge Meyer, K. Zangger, Enhancing the resolution of multi-dimensional heteronuclear NMR spectra of intrinsically disordered proteins by homonuclear broadband decoupling, Chem. Commun., 50 (2014) 1488-1490.
[29] T. Reinsperger, B. Luy, Homonuclear BIRD-decoupled spectra for measuring one-bond couplings with highest resolution: CLIP/CLAP-RESET and constant-time-CLIP/CLAP-RESET, J. Magn. Reson., 239 (2014) 110-120.
[30] I. Timári, L. Kaltschnee, A. Kolmer, R.W. Adams, M. Nilsson, C.M. Thiele, G.A. Morris, K.E. Kövér, Accurate determination of one-bond heteronuclear coupling constants with “pure shift” broadband proton-decoupled CLIP/CLAP-HSQC experiments, J. Magn. Reson., 239 (2014) 130-138.
[31] L. Castañar, J. Saurí, P. Nolis, A. Virgili, T. Parella, Implementing homo- and heterodecoupling in region-selective HSQMBC experiments, J. Magn. Reson., 238 (2014) 63-69.
[32] S. Glanzer, K. Zangger, Visualizing Unresolved Scalar Couplings by Real-Time J-Upscaled NMR, J. Am. Chem. Soc., 137 (2015) 5163-5169.
[33] M. Nilsson, G.A. Morris, Pure shift proton DOSY: diffusion-ordered 1H spectra without multiplet structure, Chem. Commun., (2007) 933-935.
[34] A.J. Pell, R.A.E. Edden, J. Keeler, Broadband proton-decoupled proton spectra, Magn. Reson. Chem., 45 (2007) 296-316.

[35] L. Castañar, P. Nolis, A. Virgili, T. Parella, Measurement of T1/T2 relaxation times in overlapped regions from homodecoupled 1H singlet signals, J. Magn. Reson., 244 (2014) 30-35.
[36] S. Glanzer, K. Zangger, Directly Decoupled Diffusion-Ordered NMR Spectroscopy for the Analysis of Compound Mixtures, Chem. Eur. J., 20 (2014) 11171-11175.
[37] L. Castañar, M. Pérez-Trujillo, P. Nolis, E. Monteagudo, A. Virgili, T. Parella, Enantiodifferentiation through Frequency-Selective Pure-Shift 1H Nuclear Magnetic Resonance Spectroscopy, ChemPhysChem, 15 (2014) 854-857.
[38] K. Rachineni, V.M.R. Kakita, S. Dayaka, S.P.B. Vemulapalli, J. Bharatam, Precise Determination of Enantiomeric Excess by a Sensitivity Enhanced Two-Dimensional Band-Selective Pure-Shift NMR, Anal. Chem., 87 (2015) 7258-7266.
[39] R.W. Adams, L. Byrne, P. Kiraly, M. Foroozandeh, L. Paudel, M. Nilsson, J. Clayden, G.A. Morris, Diastereomeric ratio determination by high sensitivity band-selective pure shift NMR spectroscopy, Chem. Commun., 50 (2014) 2512-2514.
[40] R.W. Adams, Pure Shift NMR Spectroscopy, in: eMagRes, John Wiley & Sons, Ltd, 2014, pp. 295 - 309.
[41] K. Zangger, Pure shift NMR, Prog. Nucl. Magn. Reson. Spectrosc., 86–87 (2015) 1-20.
[42] L. Castañar, T. Parella, Broadband 1H homodecoupled NMR experiments: recent developments, methods and applications, Magn. Reson. Chem., 53 (2015) 399-426.
[43] K. Zangger, H. Sterk, Homonuclear Broadband-Decoupled NMR Spectra, Journal of Magnetic Resonance, 124 (1997) 486-489.
[44] J.A. Aguilar, M. Nilsson, G.A. Morris, Simple Proton Spectra from Complex Spin Systems: Pure Shift NMR Spectroscopy Using BIRD, Angew. Chem. Int. Ed., 50 (2011) 9716-9717.
[45] A. Lupulescu, G.L. Olsen, L. Frydman, Toward single-shot pure-shift solution 1H NMR by trains of BIRD-based homonuclear decoupling, J. Magn. Reson., 218 (2012) 141-146.
[46] N.H. Meyer, K. Zangger, Simplifying Proton NMR Spectra by Instant Homonuclear Broadband Decoupling, Angew. Chem. Int. Ed., 52 (2013) 7143-7146.
[47] M. Foroozandeh, R.W. Adams, N.J. Meharry, D. Jeannerat, M. Nilsson, G.A. Morris, Ultrahigh-Resolution NMR Spectroscopy, Angew. Chem. Int. Ed., 53 (2014) 6990-6992.
[48] A. Cotte, D. Jeannerat, 1D NMR Homodecoupled 1H Spectra with Scalar Coupling Constants from 2D NemoZS-DIAG Experiments, Angew. Chem. Int. Ed., 54 (2015) 6016-6018.
[49] K.J. Donovan, L. Frydman, HyperBIRD: A Sensitivity-Enhanced Approach to Collecting Homonuclear-Decoupled Proton NMR Spectra, Angew. Chem. Int. Ed., 54 (2015) 594-598.
[50] L. Castañar, P. Nolis, A. Virgili, T. Parella, Full Sensitivity and Enhanced Resolution in Homodecoupled Band-Selective NMR Experiments, Chem. Eur. J., 19 (2013) 17283-17286.
[51] G.A. Morris, J.A. Aguilar, R. Evans, S. Haiber, M. Nilsson, True Chemical Shift Correlation Maps: A TOCSY Experiment with Pure Shifts in Both Dimensions, J. Am. Chem. Soc., 132 (2010) 12770-12772.
[52] M. Foroozandeh, R.W. Adams, M. Nilsson, G.A. Morris, Ultrahigh-Resolution Total Correlation NMR Spectroscopy, J. Am. Chem. Soc., 136 (2014) 11867-11869.
[53] P. Sakhaii, B. Haase, W. Bermel, Experimental access to HSQC spectra decoupled in all frequency dimensions, J. Magn. Reson., 199 (2009) 192-198.
[54] L. Paudel, R.W. Adams, P. Király, J.A. Aguilar, M. Foroozandeh, M.J. Cliff, M. Nilsson, P. Sándor, J.P. Waltho, G.A. Morris, Simultaneously Enhancing Spectral Resolution and Sensitivity in Heteronuclear Correlation NMR Spectroscopy, Angew. Chem. Int. Ed., 52 (2013) 11616-11619.
[55] P. Kiraly, R.W. Adams, L. Paudel, M. Foroozandeh, J.A. Aguilar, I. Timari, M.J. Cliff, M. Nilsson, P. Sandor, G. Batta, J.P. Waltho, K.E. Kövér, G.A. Morris, Real-time pure shift 15N HSQC of proteins: a real improvement in resolution and sensitivity, J. Biomol. NMR, 62 (2015) 43-52.
[56] J.R. Garbow, D.P. Weitekamp, A. Pines, Bilinear rotation decoupling of homonuclear scalar interactions, Chem. Phys. Lett., 93 (1982) 504-509.
[57] S. Macura, R.R. Ernst, Elucidation of cross relaxation in liquids by two-dimensional N.M.R. spectroscopy, Mol. Phys., 41 (1980) 95-117.
[58] J. Stonehouse, P. Adell, J. Keeler, A.J. Shaka, Ultrahigh-Quality NOE Spectra, J. Am. Chem. Soc., 116 (1994) 6037-6038.
[59] K. Stott, J. Stonehouse, J. Keeler, T.-L. Hwang, A.J. Shaka, Excitation Sculpting in High-Resolution Nuclear Magnetic Resonance Spectroscopy: Application to Selective NOE Experiments, J. Am. Chem. Soc., 117 (1995) 4199-4200.

[60] K. Stott, J. Keeler, Q.N. Van, A.J. Shaka, One-Dimensional NOE Experiments Using Pulsed Field Gradients, J. Magn. Reson., 125 (1997) 302-324.
[61] G. Hamdoun, M. Sebban, E. Cossoul, A. Harrison-Marchand, J. Maddaluno, H. Oulyadi, 1H Pure Shift DOSY: a handy tool to evaluate the aggregation and solvation of organolithium derivatives, Chem. Commun., 50 (2014) 4073-4075.
[62] C.P. Butts, C.R. Jones, E.C. Towers, J.L. Flynn, L. Appleby, N.J. Barron, Interproton distance determinations by NOE - surprising accuracy and precision in a rigid organic molecule, Org. Biomol. Chem., 9 (2011) 177-184.
[63] C.P. Butts, C.R. Jones, J.N. Harvey, High precision NOEs as a probe for low level conformers-a second conformation of strychnine, Chem. Commun., 47 (2011) 1193-1195.
[64] A. Kolmer, L.J. Edwards, I. Kuprov, C.M. Thiele, Conformational analysis of small organic molecules using NOE and RDC data: A discussion of strychnine and α-methylene-γ-butyrolactone, J. Magn. Reson., 261 (2015) 101-109.
[65] M. Schmidt, F. Reinscheid, H. Sun, H. Abromeit, G.K.E. Scriba, F.D. Sönnichsen, M. John, U.M. Reinscheid, Hidden Flexibility of Strychnine, Eur. J. Org. Chem., 2014 (2014) 1147-1150.
[66] S. Macura, B.T. Farmer Ii, L.R. Brown, An improved method for the determination of cross-relaxation rates from NOE data, J. Magn. Reson., 70 (1986) 493-499.
[67] H. Hu, K. Krishnamurthy, Revisiting the initial rate approximation in kinetic NOE measurements, J. Magn. Reson., 182 (2006) 173-177.
[68] Ē. Kupče, J. Boyd, I.D. Campbell, Short Selective Pulses for Biochemical Applications, J. Magn. Reson. B, 106 (1995) 300-303.
[69] H. Geen, R. Freeman, Band-selective radiofrequency pulses, J. Magn. Reson., 93 (1991) 93-141.
[70] D. Marion, M. Ikura, R. Tschudin, A. Bax, Rapid recording of 2D NMR spectra without phase cycling. Application to the study of hydrogen exchange in proteins, J. Magn. Reson., 85 (1989) 393-399.
[71] P. Damberg, J. Jarvet, A. Gräslund, Accurate Measurement of Translational Diffusion Coefficients: A Practical Method to Account for Nonlinear Gradients, J. Magn. Reson., 148 (2001) 343-348.
[72] M.A. Connell, P.J. Bowyer, P. Adam Bone, A.L. Davis, A.G. Swanson, M. Nilsson, G.A. Morris, Improving the accuracy of pulsed field gradient NMR diffusion experiments: Correction for gradient non-uniformity, J. Magn. Reson., 198 (2009) 121-131.
[73] J. Murphy-Boesch, G.J. So, T.L. James, Precision mapping of the B1 field using the rotating-frame experiment, J. Magn. Reson., 73 (1987) 293-303.
[74] S. Vashaee, B. Newling, B. MacMillan, B.J. Balcom, B1 mapping with a pure phase encode approach: Quantitative density profiling, J. Magn. Reson., 232 (2013) 68-75.
[75] J. Mauhart, S. Glanzer, P. Sakhaii, W. Bermel, K. Zangger, Faster and cleaner real-time pure shift NMR experiments, J. Magn. Reson., 259 (2015) 207-215.
[76] C.M. Thiele, A. Kolmer, Response to "Comment on "Conformational analysis of small organic molecules using NOE and RDC data: A discussion of strychnine and α-methylene-γ-butyrolactone" by I.A. Khodov, M.G. Kiselev, V.V. Klochkov, S.V. Efimov [http://dx.doi.org/10.1016/j.jmr.2016.02.009]" - Or Life is about compromises, J. Magn. Reson., 266 (2016) 69-72.
[77] P.F. Yip, D.A. Case, Incorporation of Internal Motion in NMR Refinements Based on NOESY Data, in: J.C. Hoch, F.M. Poulsen, C. Redfield (Eds.) Computational Aspects of the Study of Biological Macromolecules by Nuclear Magnetic Resonance Spectroscopy, Plenium Press, New York, 1991, pp. 317 - 330.
[78] A. Bax, A.F. Mehlkopf, J. Smidt, Homonuclear broadband-decoupled absorption spectra, with linewidths which are independent of the transverse relaxation rate, J. Magn. Reson., 35 (1979) 167-169.
[79] L. Castañar, P. Nolis, A. Virgili, T. Parella, Simultaneous Multi-Slice Excitation in Spatially Encoded NMR Experiments, Chem. Eur. J., 19 (2013) 15472-15475.

Supporting Information for: Extraction of Distance Restraints from Pure Shift NOE experiments

Lukas Kaltschnee, Kevin Knoll, Volker Schmidts, Ralph W. Adams, Mathias Nilsson, Gareth A. Morris, Christina M. Thiele

Table of Contents

1 NOE Data Analysis

1.1 Extraction of Cross-Relaxation-Rates

For quantitative evaluation of signal intensities in transient NOE spectra, we use the well-described method of extracting longitudinal cross relaxation rates σ_{jk} from the initial magnetization build-up regime for the NOE cross peaks[1]. Following the approach described by Macura *et al.*[2] for the analysis of 2D NOESY spectra using internal calibration of the cross-peak integrals $I_{jk}(\tau_m)$ by the diagonal peak integrals $I_{jj}(\tau_m)$ and $I_{kk}(\tau_m)$, for 2D-NOESY spectra cross relaxation rates are determined from

$$a_2(\tau_m) = \frac{I_{jk}(\tau_m)}{\frac{1}{2}n_k I_{jj}(\tau_m) + \frac{1}{2}n_j I_{kk}(\tau_m)} \approx -\sigma_{jk}\tau_m, \tag{S1}$$

if both diagonal signals can be used for internal calibration, or from

$$a_1(\tau_m) = \frac{I_{jk}(\tau_m)}{n_j I_{kk}(\tau_m)} \approx -\sigma_{jk}\tau_m, \tag{S2}$$

if only one diagonal peak can be used, due to signal overlap. τ_m here is the mixing time, while n_j is the number of equivalent positions contributing to signal j (for strychnine n_j equals 1 all cases). The cross relaxation rate is extracted from the slopes of the normalized signal amplitudes a_1 and a_2 with respect to mixing time.

For selective NOE experiments, data evaluation was performed according to the PANIC approach of Hu and Krishnamurthy[3], paralleling the analysis using normalization to one cross-peak only (a_1). Even though in PANIC analysis it is normally assumed that fitting to a straight line without intercept is appropriate for selective NOE data, we repeatedly observed that this was not necessarily the case (see plots in Figure S1). For selective NOE data, measured cross-peak intensities may not be zero at mixing time zero, for reasons outlined below.

Performing the analysis for a two spin system as described by Hu and Krishnamurthy, but assuming the magnetizations of the first and the second spin to be –κ and –γ for the first and κ and γ for the second phase cycling step respectively, provides the rate law we used for analysis of PFGSE NOE data:

$$a_1^{selective}(\tau_m) = \frac{I_{jk}(\tau_m)}{n_j I_{kk}(\tau_m)} \approx \left(\frac{\gamma}{\kappa}\right) - \sigma_{jk}\tau_m\left(1 - \left(\frac{\gamma}{\kappa}\right)^2\right) \tag{S3}$$

For fitting, instead we used

$$a_1^{selective}(\tau_m) = \frac{I_{jk}(\tau_m)}{n_j I_{kk}(\tau_m)} \approx \left(\frac{\gamma}{\kappa}\right) - \sigma_{jk}\tau_m, \text{ for } \gamma/\kappa \ll 1, \quad \text{(S4)}$$

which requires that $\gamma/\kappa << 1$, a condition that was satisfied in all cases. (n.b.: $\gamma/\kappa < 7.2\%$, throughout this entire study; in most cases this ratio did not exceed 1%). In the limiting case of $\gamma = 0$, this is the initial rate law described by Hu and Krishnamurthy

There are several scenarios that may lead to non-zero cross peaks for zero mixing time. Insufficient selectivity of the 180°pulse - a scenario the experimentalist should try to avoid – may be the most trivial cause. For signals close to the inverted peak, overlap with the broad base of the very intense inverted peak can also be an issue. Strong coupling between the inverted spin and that causing the cross peak can cause magnetization transfer between the two spins during the selective pulse, in a coherence pathway that is not suppressed by gradient selection or phase cycling. Chemical exchange that is in the slow exchange limit but is non-negligible during the selective 180° pulse may be another issue, though not in the present study. Finally, TOCSY/ROESY-like magnetization transfer may take place during selective pulses, in particular if shaped pulses with high peak intensities are used. Evaluation of the extent of these contributions to the measured values is beyond the scope of this article. It should be noted here that the characteristics of the single selective gradient echo, used here, and a double selective gradient echo (excitation sculpting)[4] may differ with respect to these contributions.

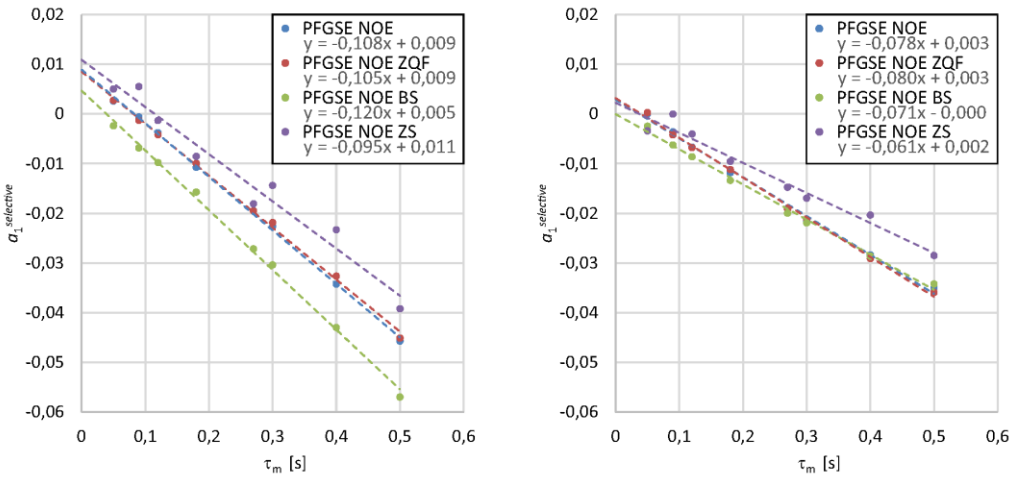

Figure S1: PANIC plots[3] illustrating the occurrence of non-zero intercepts in 1D PFGSE NOE experiments. Left: Normalized signal integrals at the H13 position, after inversion of H15a, right: normalized signal integrals at the H15a position after inversion of H13. The results are shown for 1D PFGSE NOE experiments without homodecoupling (PFGSE NOE), for 1D PFGSE NOE experiments without homodecoupling but with Thrippleton-Keeler filtration (PFGSE NOE ZQF), for 1D PFGSE NOE experiments with band-selective homodecoupling (PFGSE NOE BS) and for 1D PFGSE NOE experiments with ZS homodecoupling (PFGSE NOE ZS). Slopes and intercepts measured are listed in the legends.

1.2 Distance Determination

Estimation of interatomic distances here is based on the assumption that only isotropic molecular tumbling contributes to the spectral density function determining longitudinal relaxation, so that a single reference distance can be used independent of the chemical entity studied. Based on this assumption, unknown distances are estimated from the equation

$$\langle r_{jk} \rangle = \langle r_{ref} \rangle \left(\frac{\sigma_{jk}}{\sigma_{ref}} \right)^{-\frac{1}{6}}, \tag{S5}$$

where the reference distance $<r_{ref}>$ was extracted from the structural model used, as described below[5]. Following Butts *et al.*[6] the distances in the two conformer model used for strychnine were averaged according to

$$\langle r_{jk} \rangle = \left(\sum_{\mu} p_{\mu} r_{jk,\mu}^{-6} \right)^{-\frac{1}{6}}, \tag{S6}$$

assuming a jump model for conformational interconversion, with conformational interconversion being uncoupled from external molecular motion and with the rate of interconversion being much smaller than the molecular tumbling rate[7, 8]. In all cases, we used the cross relaxation rate measured for the proton pair $H_{15a} - H_{15b}$ in the respective experimental technique for calibration. The reference distance thus derived from the given model is $<r_{ref}> = 1.757$ Å.

2 A T_1 inversion recovery experiment with ZS homodecoupling

The inversion recovery experiment[9] with ZS homodecoupling[10] described here can be used in cases where signal overlap in proton spectra prohibits direct T_1 measurement. Using other homodecoupling methods, it has previously been shown that precise measurement of T_1 and T_2 is possible with pure shift techniques[11, 12]. The results shown in Table S1 confirm that the inversion recovery experiment given in Figure S2 enables robust T_1 measurement.

For comparison, inversion recovery experiments with and without ZS homodecoupling were performed on a strychnine sample. After data rearrangement using the pshift script (available from: http://nmr.chemistry.manchester.ac.uk/sites/default/files/pshift), both inversion recovery datasets could be analysed in the same way. The data were Fourier transformed along the direct dimension, manually phased, subjected to automated baseline correction, and fitted using the T_1/T_2 analysis tool implemented in TopSpin™ (Bruker BioSpin™ GmbH, version 3.1). For comparison, results are listed for the data analysis using both intensities and integrals for fitting, according to the equation $I(t) = I(0) + P*\exp(-t/T_1)$. The T_1 values obtained are given in Table S1. The values determined with the

conventional experiment are nicely reproduced by the pure shift experiment (differences are below 4%, when comparing to the area fit analysis of the reference experiment, excluding H14 and H11a), even if the broadband homodecoupling approach used demands large compromises in S/N ratio to be made. The errors reported are those provided by the fitting routine; these tend to underestimate the true uncertainty of the measurement, as bias from systematic errors during the measurement, such as partial overlap of different signals or non-optimal baseline correction, is not taken into account.

In the case of H14 and H11a, where signals overlap severely in the experiment without homodecoupling, the pure shift approach is able to provide improved separation of the two signals (see Figure S3). In this case, the experiment without homodecoupling only allows either an intensity fit at signal positions showing little signal overlap, or a total integral fit to give an average relaxation rate. The pure shift experiment, on the other hand, allows facile measurement of both relaxation rates in either mode of operation.

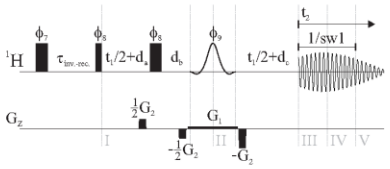

Figure S2: Pulse sequence of the homonuclear broadband decoupled inversion recovery experiment. For inversion recovery measurements, a series of experiments is performed with differing variable delays $\tau_{inv.-rec.}$. Dummy scans are executed at the beginning of the experiment and after changing $\tau_{inv.-rec.}$. As for the homonuclear decoupled NOE experiments discussed in the main article, the time domain signals are constructed from an interferogram created by making successive measurements with t_1 incremented. ($1/sw_i$), τ_a, τ_b and τ_c and defined in the caption of Figure 1 of the main text. Pulse phases are $\Phi_7 = x\ -x$, $\Phi_8 = (x)_2\ (-x)_2\ (y)_2\ (-y)_2$, $\Phi_9 = (x)_2\ (-x)_2\ (y)_2\ (-y)_2\ (y)_2\ (-y)_2\ (-x)_2\ (x)_2\ (-x)_2\ (x)_2\ (-y)_2\ (y)_2\ (-y)_2\ (y)_2\ (x)_2\ (-x)_2$ and $\Phi_{rec} = (x)_2\ (-x)_2\ (y)_2\ (-y)_2$.

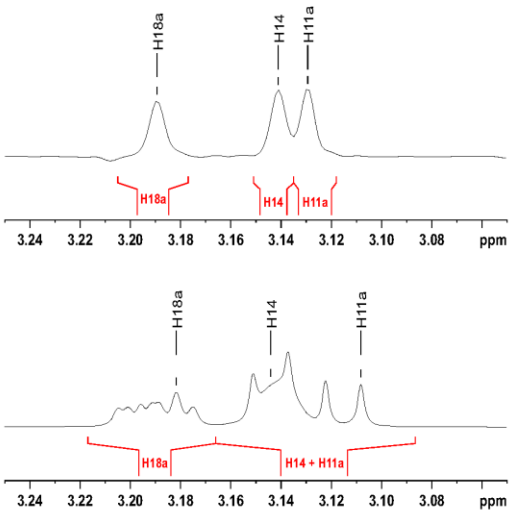

Figure S3: Spectral region containing the signals of H18, H14 and H11a for the inversion recovery measurement with the longest relaxation period ($\tau_{inv-rec} = 30$ s). The frequencies used for intensity measurement in intensity-based fitting and the integral regions used for area-based fitting are shown. Top: Experiment with interferogram-based ZS homodecoupling, bottom: experiment without homodecoupling.

Table S1: Summary of the T_1 relaxation times obtained from inversion recovery measurements with and without ZS homodecoupling. Results are from two different fitting methods (peak area and peak intensity) available in the TopSpin™ T_1/T_2-relaxation module are given. Eight different values for $\tau_{inv.-rec.}$ were used (5 ms, 10 ms, 50 ms, 0.5 s, 1.25 s, 4 s, 10 s and 30 s). For all steps in $\tau_{inv.-rec.}$ 4 dummy scans and 8 scans per increment were performed. A preparatory delay of 30 s was chosen. For broadband decoupling 16 chunks, each 21.3 ms, were collected in the homodecoupling dimension. During the selective inversion using an rSNOB shaped pulse of 93.6 ms length a field-gradient of G_1 = 1.05 G/cm was applied. For coherence transfer selection, gradient pulses of 500 µs duration, followed by a 200 µs recovery delay, were used, with G_2 = 12.5 G/cm. The value given in red was determined by integrating over the entire region of the overlapping signals 14 and 11a.

Signal	normal inversion recovery experiment		ZS inversion recovery experiment	
	T_1 (area fit) / s	T_1 (intensity fit) / s	T_1 (area fit) / s	T_1 (intensity fit) / s
4	4.794 ± 0.007	4.763 ± 0.008	4.782 ± 0.007	4.684 ± 0.016
3	2.984 ± 0.005	3.007 ± 0.007	3.088 ± 0.013	3.032 ± 0.013
1	1.954 ± 0.002	1.999 ± 0.003	1.927 ± 0.008	1.942 ± 0.009
2	2.821 ± 0.005	2.867 ± 0.007	2.844 ± 0.007	2.857 ± 0.012
22	2.007 ± 0.006	2.010 ± 0.005	2.017 ± 0.008	1.992 ± 0.007
12	1.166 ± 0.005	1.151 ± 0.010	1.127 ± 0.011	1.153 ± 0.008
23b	0.838 ± 0.004	0.802 ± 0.011	0.859 ± 0.012	0.856 ± 0.010
23a	0.672 ± 0.006	0.686 ± 0.005	0.659 ± 0.012	0.667 ± 0.011
16	1.392 ± 0.004	1.402 ± 0.004	1.382 ± 0.011	1.387 ± 0.008
8	1.447 ± 0.009	1.451 ± 0.011	1.459 ± 0.011	1.453 ± 0.010
20a	0.695 ± 0.006	0.695 ± 0.006	0.714 ± 0.012	0.702 ± 0.008
18a	0.748 ± 0.008	0.766 ± 0.007	0.742 ± 0.007	0.739 ± 0.010
14	1.058 ± 0.008	(0.995 ± 0.009)*	1.290 ± 0.013	1.300 ± 0.017
11a		0.841 ± 0.010	0.868 ± 0.013	0.840 ± 0.008
18b	0.558 ± 0.008	0.556 ± 0.010	0.579 ± 0.013	0.558 ± 0.010
20b	0.665 ± 0.003	0.683 ± 0.006	0.664 ± 0.010	0.657 ± 0.012
11b	0.892 ± 0.006	0.881 ± 0.008	0.885 ± 0.004	0.879 ± 0.011
15b	0.543 ± 0.004	0.536 ± 0.005	0.530 ± 0.006	0.523 ± 0.011
17a/b	0.694 ± 0.002	0.685 ± 0.007	0.693 ± 0.011	0.690 ± 0.022
15a	0.555 ± 0.004	0.552 ± 0.005	0.560 ± 0.008	0.551 ± 0.015
13	1.262 ± 0.005	1.248 ± 0.006	1.274 ± 0.007	1.264 ± 0.012
TMS	3.285 ± 0.006	3.236 ± 0.016	3.359 ± 0.005	3.339 ± 0.006

*** : The T_1/T_2 relaxation analysis module used did not fit this peak properly, instead analysing the pronounced maxima close by the signal position, which are caused by H11a (see Figure S3). The value reported was obtained by manually reading off signal intensities at the position of H14 and subsequently fitting these in an analysis software package.**

3 Estimation of contributions to signal amplitude modulations in interferogram-based Zangger-Sterk homodecoupling

This section considers the extent to which differential relaxation, non-negligible coupling evolution during acquisition, and B_1 field inhomogeneity can cause relative integrals to deviate systematically from their ideal values when interferogram-based Zangger-Sterk pure shift acquisition is used in the pseudo-direct dimension.

To compensate for systematic deviations of NOE cross-peak integrals, we discuss in the main article the method of normalizing the integrals measured with pure shift NOE experiments with the relative integrals measured in a pure shift ^{1}H experiment acquired with identical settings for homodecoupling. This method is easy to apply in practice as it requires no prior knowledge of the sources of relative integral loss and we suggest using this method wherever possible.

The idea of this section, in contrast, is to illustrate the relative impact of different sources of systematic deviations of the pure shift integrals, an insight that cannot be obtained with the empirical method above. We use approximate formulae for the evaluation of the contributions from relaxation and weak coupling evolution during the experiment to signal integral loss. While the simplified descriptions are of limited practical applicability, they provide useful insights into the origins and significance of the different loss mechanisms.

3.1 Signal attenuation by relaxation during the homonuclear decoupling element

In the interferogram-based pure shift experiments shown in Figure 1 of the main article, relaxation occurring during the homonuclear decoupling element leads to site-dependent signal intensity reductions. For a rough estimate of the bias on relative integrals measured, the signal intensity reduction for a given spin m can be approximated by

$$I'_{0,m} \approx I_{0,m} exp\left(-\frac{(d_a + d_b + d_c + p_{sel})}{T_{2,m}}\right), \quad \text{(S7)}$$

where p_{sel} is the duration of the selective 180° pulse used, d_a, d_b and d_c are as shown in Figure 1 of the main article, $I_{0,m}$ is the signal intensity for spin m in the absence of relaxation, and $I_{0,m}$' is the signal intensity in the presence of relaxation. The element of approximation lies in the assumption that the signal attenuation during the 180° pulse is determined by T_2; if $T_1 > T_2$ this will overestimate the signal loss to an extent that depends on the details of the selective pulse used (for the case of a rectangular 180° pulse on resonance, the effect relaxation time constant is $2T_1 T_2/(T_1 + T_2)$[13]).

A lower limit on the attenuation caused by relaxation in the strychnine system can be estimated using equation (S7) by taking the measured $T_{1,m}$ values (see Table S1) as upper limits on $T_{2,m}$. In practice T_2

is normally significantly less than T_1 in proton multiplets in small molecules[14]. Table S3 lists the relative integrals for the two spectra of Figure 2 in the main text, and the estimated minimum attenuation factors $F_{A,\,relax}$ caused by relaxation. The (conservatively) estimated relaxation losses are of up to ~20% in the present case, causing a variation of up to 14% in relative integral (see Table S2; the largest deviations are those seen for the H15b-H16 pair). In the case of NOESY applications, using referencing to both diagonal peaks in NOESY experiments, according to equation (S1), reduces bias from differential relaxation.

Where pure shift techniques are required for signal separation, both T_1 and T_2 measurement may be performed by pure shift techniques[11, 12]. An inversion recovery experiment with ZS homodecoupling is described in section 2 (see page S4).

Table S2: Estimates of the lower limit of changes of apparent cross relaxation rates σ_{jk} by relaxation during the homodecoupling element. The analysis is carried out using equation (S7) for a homodecoupling element of 115 ms length (rSNOB pulse of 93.6 ms, chunk length: 21.3 ms), assuming $T_2 = T_1$ and using the T_1 values listed in Table S1 (values from area fitting from the experiment without homodecoupling – for H14 and H11a the rates determined in the pure shift experiment were used). For the internal calibration method via a_2, only one value is reported, as the change of apparent σ_{jk} amounts to the negative change of apparent σ_{kj}, in this case.

pair of coupling protons		percentage change in apparent σ_{jk}			
H_a	H_b	a_2		a_1 or $a_1^{selective}$	
		a=j, b=k	a=k, b=j	a=j, b=k	a=k, b=j
15a	15b	0.2	For a_2-data analysis, the change in apparent σ_{jk} is equal and opposite to the change in apparent σ_{kj}.	0.5	-0.5
13	12	0.4		0.8	-0.7
13	15a	5.8		12.3	-11.0
12	14	-0.5		-0.9	1.0
12	11a	1.7		3.4	-3.3
13	14	-0.1		-0.2	0.2
13	11a	2.1		4.2	-4.1
15a	14	-5.9		-11.1	12.5
15b	14	-6.1		-11.5	13.0
15b	20a	-2.3		-4.5	4.7
15b	16	-6.4		-12.1	13.8
15a	16	-6.2		-11.7	13.3
20b	20a	-0.4		-0.7	0.7
20b	22	-5.8		-10.9	12.2
18a	18b	2.6		5.4	-5.1
18b	8	-6.3		-11.9	13.5
11a	12	-1.7		-3.3	3.4
16	1	-1.2		-2.3	2.4
23a	12	-3.6		-7.0	7.5
23b	22	-4.0		-7.7	8.3

3.2 Estimation of signal attenuation due to data chunking for weakly coupled spins

A second source of signal integral loss which is site-dependent, and thus causes bias in relative integrals measured, is the small signal attenuation caused by non-negligible coupling evolution during the data chunks collected. This small attenuation is the price paid for the very large saving in data collection time. Here we quantify the effect for the limiting case of weakly coupled spins with frequency separations much larger than the bandwidth of the selective pulse used.

For this limiting case, it is shown below that the intensity of a central signal $I_{0,m}$', already attenuated by relaxation as discussed in the previous section, is further reduced to

$$I''_{0,m} \approx I'_{0,m}\left(1-\tfrac{1}{3}\Delta_A\right), \text{ with } \quad \Delta_A = \tfrac{1}{2}\Sigma_j^{N_j}\left[\left(\pi J_{mj}\tfrac{\Delta_{ZS}}{2}\right)^2\right], \tag{S8}$$

if interferogram-based acquisition is used, in which coupling evolution is refocused at the midpoints of data chunks of duration Δ_{ZS}. For convenience, we introduce Δ_A as an approximate measure of the maximum fractional signal attenuation caused by coupling evolution at the edges of the data chunks. In principle, computation of Δ_A requires knowledge of all the coupling constants J_{mj} to the observed spin m from all N_j coupling partners j. However a good estimate of Δ_A can be obtained simply by summing the largest coupling constants J_{mj} to the spin concerned. For the case studied, the attenuation factors $F_{A,0}$ estimated are summarized in Table S3, with losses of up to 7% in signal intensity being estimated.

Diversion of signal intensity into sidebands also leads to the risk of signal overlap with sidebands from other signals. For the weak coupling case these sidebands appear evenly spaced around the frequency of the central band ν_m, at frequencies $\left(\nu_m \pm \frac{k}{\Delta_{ZS}}\right)$, with $k \in \mathbb{N}$. The intensity of the k'th sideband pair

$$I''_{k,m} \approx I'_{0,m}\left(-\frac{2}{k^2\pi^2}\Delta_A\right) \tag{S9}$$

decreases rapidly with k. For spectra with relatively uniform signal intensities, the impact of this source is relatively small. In the present case, accidental overlap with the first sidebands (k = 1) from a neighbouring signal should reduce signal integrals by 3% or less (see Table S3). The impact of higher order sidebands is much smaller. It should be noted, however, that the effect of overlap with sidebands can be much more pronounced in spectra with high dynamic range; thus a sideband of the inverted signal in an NOE difference spectrum could easily be of comparable magnitude to an NOE signal.

In the case of strong coupling, additional signals appear, the effect of which is not described by equations (S8) and (S9), further complicating the situation. It can be seen from the last column of Table S3 that even after approximate correction for relaxation and for weak coupling modulation of the signal, some pronounced deviations of signal integrals from their ideal values occur.

It can be concluded, that even when estimating only lower-bound values for signal loss by relaxation and by non-negligible coupling evolution during data chunks, both effects can have a marked influence on the relative integrals measured.

3.2.1 Derivation of equations (S8) and (S9)

For estimating the signal loss caused by using a finite chunk duration in interferogram-based ZS experiments, we explicitly derive a general approximation to the idealized signal shape obtained for such signals. This follows the analysis of sidebands in spectra with heteronuclear decoupling outlined in chapter 7.20 of the text-book by Slichter[15], with a modification to enable the analysis of systems with more than one coupling partner. The results derived below only apply to experiments in which refocusing of the coupling evolution is achieved at the midpoint of the chunk, as in most recent experiments, rather than at the start of the chunk, as in the original ZS experiment.

The effect we want to quantify here is the extent of signal loss caused by the incomplete refocusing of coupling evolution towards the edges of the data chunks acquired. In data chunks of finite duration Δ_{ZS}, the signal acquired is reduced by the combined effect of all N_j coupling partners j to which the spin m observed is coupled, with coupling constants J_{mj}. We assume that after chunk concatenation, the signal produced by a single spin can be described by the following functional form:

$$S_m(t)_{(M-1)\Delta_{ZS}\leq t\leq M\Delta_{ZS}} = I'_{0,m} exp\left(\left(i\omega_m - \frac{1}{T^*_{2,m}}\right)t\right)\prod_j^{N_j}\cos\left(\pi J_{mj}\left(t - \Delta_{ZS}\left(M - \tfrac{1}{2}\right)\right)\right) \qquad \text{(S10)}$$

where M is the number of the data chunk from which the data are taken ($M \in \mathbb{N}$). The initial magnetization $I'_{0,m}$ contains terms taking into account signal attenuation caused by slice selection and by relaxation, according to equation (S7). As usual, ω_m is the offset of the Larmor frequency of spin m from the carrier frequency and $T^*_{2,m}$ is the apparent transverse relaxation rate. This idealized signal shape assumes full refocusing of all couplings to m at the midpoint of each data chunk.

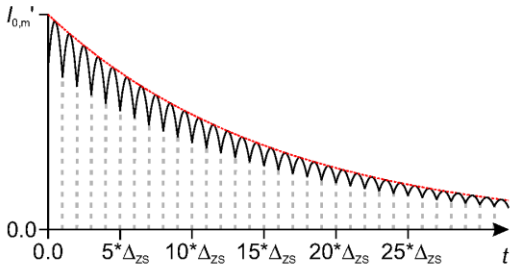

Figure S4: Figure illustrating the assumed ideal signal shape, for a single on-resonance signal ($\omega_m = 0$), constructed from an interferogram (black). In the absence of couplings, a simple exponential decay (red, dotted) would be expected instead.

As the experiment itself requires that $\Delta_{ZS} \ll 1/J_{mj}$ for all couplings, it is possible to approximate all cosines in terms of Taylor expansions, discarding all terms in fourth or higher power of t. We obtain:

$$S_m(t)_{(M-1)\Delta_{ZS}\leq t\leq M\Delta_{ZS}}$$

$$\approx I'_{0,m}exp\left(\left(i\omega_m-\frac{1}{T^*_{2,m}}\right)t\right)\left\{1-\sum_j^{N_j}\left[\frac{\left(\pi J_{mj}\left(t-\Delta_{ZS}\left(M-\frac{1}{2}\right)\right)\right)^2}{2}\right]\right\} \quad \text{(S11)}$$

Instead of describing the signal shape for discrete data chunks M only, we express the periodicity of the function introduced by data chunking using the following Fourier series[16]:

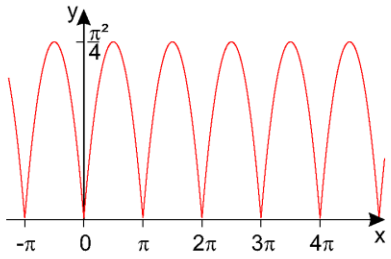

$$y=x(\pi-x)\text{ for }0\leq x\leq\pi \quad \text{(S12)}$$

$$y=\frac{\pi^2}{6}-\sum_{k=1}^{\infty}\frac{\cos(2kx)}{k^2} \quad \text{(S13)}$$

To this end, we offset y by the signal amplitude expected at the edges of the chunks for the limiting case $\frac{1}{T^*_{2,m}}=0$, which amounts to

$$\lim_{\frac{1}{T^*_{2,m}}\to 0}\left(S_m(t=n*\Delta_{ZS})\right)\approx\left\{1-\frac{1}{2}\sum_j^{N_j}\left[\left(\pi J_{mj}\frac{\Delta_{ZS}}{2}\right)^2\right]\right\}, \quad \text{(S14)}$$

and we scale the depth of the modulations according to

$$\lim_{\frac{1}{T^*_{2,m}}\to 0}\left(S_m\left(t=n*\Delta_{ZS};all\,J_{mj}=0\right)-S_m(t=n*\Delta_{ZS})\right)\approx\frac{1}{2}\sum_j^{N_j}\left[\left(\pi J_{mj}\frac{\Delta_{ZS}}{2}\right)^2\right]. \quad \text{(S15)}$$

Further introducing

$$x=\frac{t\pi}{\Delta_{ZS}}, \quad \text{(S16)}$$

we obtain

$$y'=\left\{1-\frac{1}{2}\sum_j^{N_j}\left[\left(\pi J_{IS_j}\frac{\Delta_{ZS}}{2}\right)^2\right]\right\}+\frac{4}{\pi^2}\left\{\frac{1}{2}\sum_j^{N_j}\left[\left(\pi J_{IS_j}\frac{\Delta_{ZS}}{2}\right)^2\right]\right\}\left\{\frac{\pi^2}{6}-\sum_{k=1}^{\infty}\frac{\cos\left(2k\frac{t\pi}{\Delta_{ZS}}\right)}{k^2}\right\}, \quad \text{(S17)}$$

which can be used to express $S_m(t)$, by setting

$$\left\{1-\sum_j^{N_j}\left[\frac{\left(\pi J_{mj}\left(t-\Delta_{ZS}\left(M-\frac{1}{2}\right)\right)\right)^2}{2}\right]\right\}_{(M-1)\Delta_{ZS}\leq t\leq M\Delta_{ZS}}=y'. \quad \text{(S18)}$$

For convenience, we introduce

$$\Delta_A = \frac{1}{2}\sum_j^{N_j}\left[\left(\pi J_{mj}\frac{\Delta_{ZS}}{2}\right)^2\right]. \tag{S19}$$

Conversion of the signal into the frequency domain is achieved by Fourier transformation.

$$\mathcal{F}\left(S_m(t)\right) = \int_0^\infty S_m(t)exp(-i\omega t)dt \tag{S20}$$

$$\approx I'_{0,m}\int_0^\infty exp\left(\left(i(\omega_m-\omega)-\frac{1}{T^*_{2,m}}\right)t\right)\left\{1-\frac{1}{3}\Delta_A-\frac{4}{\pi^2}\Delta_A\sum_{k=1}^{\infty}\frac{\cos\left(2k\frac{t\pi}{\Delta_{ZS}}\right)}{k^2}\right\}dt \tag{S21}$$

$$\begin{aligned}\approx I'_{0,m}\Bigg[&\left(1-\frac{1}{3}\Delta_A\right)\left\{\frac{1}{\frac{1}{T^*_{2,m}}+i(\omega-\omega_m)}\right\}\\ &-\frac{2}{\pi^2}\Delta_A\sum_{k=1}^{\infty}\frac{1}{k^2}\left\{\frac{1}{\frac{1}{T^*_{2,m}}+i\left(\omega-\omega_m-\frac{2k\pi}{\Delta_{ZS}}\right)}+\frac{1}{\frac{1}{T^*_{2,m}}+i\left(\omega-\omega_m+\frac{2k\pi}{\Delta_{ZS}}\right)}\right\}\Bigg]\end{aligned} \tag{S22}$$

The real part of this function, later used to display the spectrum, consists only of Lorentzian lines. The central line is positioned at ω_m and is attenuated by a factor $\left(1-\frac{1}{3}\Delta_A\right)$, due to the non-negligible coupling evolution during the finite data chunk duration. Sidebands appear with opposite sign to the central peak at frequencies $\left(\nu_m \pm \frac{k}{\Delta_{ZS}}\right)$ Hz, with the k^{th} pair of sidebands having a relative intensity of $I'_{0,m}\left(-\frac{2}{k^2\pi^2}\Delta_A\right)$.

To illustrate how well the experimental signal shape is reproduced by equation (S22), we show a sample plot of the real and imaginary parts of the function in Figure S5. The spectral features from the measured spectrum are well reproduced when using the coupling constants and the signal frequency measured in a ^{1}H spectrum as input.

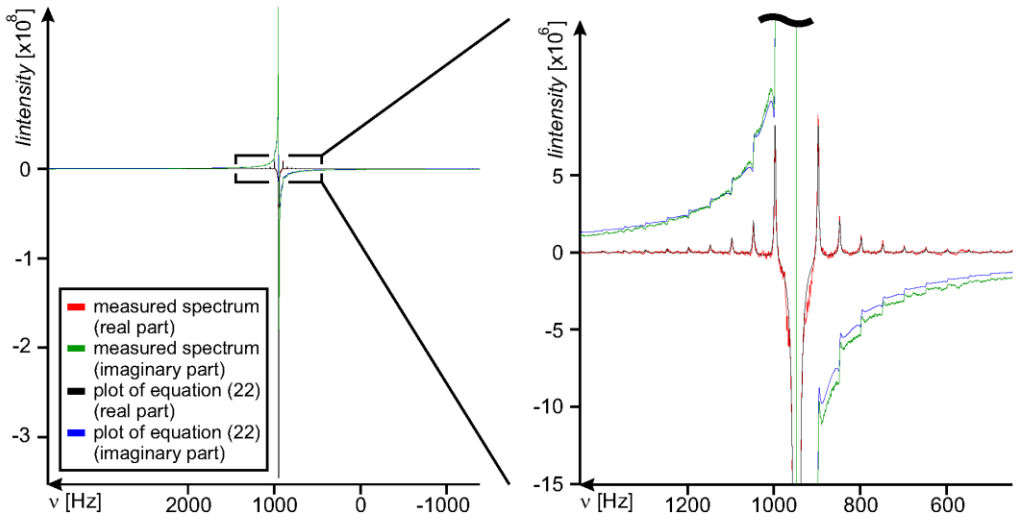

Figure S5: Comparison of the signal shape described by equation (S22) with experimental data. The left plot shows the full spectrum, while the right plot show an expansion of the region containing sidebands. Real (red) and imaginary (green) parts of the experimental band-selectively decoupled PFGSE NOE spectrum of H15b are shown (selective inversion before mixing at H15b frequency, band-selective acquisition at H15b frequency, 500 ms mixing time, Δ_{ZS} = 20 ms). For equation (S22), the real (black) and imaginary (blue) parts are plotted for comparison. For plotting equation (S22) we used ν(H15b) = 947.5 Hz (measured at 9.4 T), $^2J_{H15a,H15b}$ = -14.35 Hz, $^3J_{H16,H15b}$ = 4.33 Hz and $^3J_{H18,H15b}$ = 4.33 Hz, as measured in a normal ^{1}H experiment. The intensity used for plotting ($I_{0,H15b}$' = -7.2*10^8) and T_2* used ($T_{2,H15b}$* = 0.5 s) were manually adjusted, to roughly match the experimental spectrum.

As can be seen, sidebands caused by weak coupling are well separated in frequency from the central line (in most cases $\frac{1}{\Delta_{ZS}} > 40Hz$), so integration of the central line is possible without interference provided that overlap with the sidebands from other signals is absent. The relative attenuation of the integral which is caused by weak coupling evolution during the data chunks is given by $\left(1 - \frac{1}{3}\Delta_A\right)$. Knowledge of Δ_A and of the chemical shifts of all signals close to the spectral region analysed would therefore in principle allow correction of the relative integrals measured for losses introduced by weak coupling evolution during the finite chunk length used. It might appear that a lot of prior knowledge of the substance analyzed would be required; however, good estimates of Δ_A can be obtained if the coupling constants J_{mj} of largest amplitude are known, and overlap with sidebands of second or higher order would only have to be considered in high dynamic range spectra. In practice, the need to estimate corrections from first principles is short-circuited if integrals from corresponding pure shift 1D spectra are available, which is almost always the case, to use for normalization.

3.2.2 Illustration of approximate contributions to bias in signal integrals from relaxation and non-negligible weak coupling evolution

Table S3: Comparison of the relative integrals measured in strychnine, using a single scan ^{1}H experiment, and using a ^{1}H experiment with interferogram-based ZS homodecoupling. In all cases, signal integrals are referenced to the integral of H22. For the homodecoupled experiment, three stages for integral correction are applied, successively. First, compensation of relaxation losses according to equation (S7) is applied, then in addition corrections according to equation (S8) and (S9) are applied to the previously corrected value. In all cases, attenuation factors F_A are also reported, which are used for correction according to $I_{corrected} = I_{uncorrected} / F_A$. Maximum ($\Delta_{max}$) and root mean squared deviations (RMSD) from the value expected in the ideal case (1 or 2, depending on the number of protons in the respective integration region) are also reported. Further, the relative deviation between the extreme values is reported ($\Delta_{extreme} = (I_{max}-I_{min})/I_{max}$).

	^{1}H (no dec.)	^{1}H ZS homodecoupling						
	no correction	no correction	correction for relaxation (equation(S7), assumption $T_2 \approx T_1$)		additional correction for reduction of central band intensity (equation (S8))		additional correction for overlap with first set of sidebands (equation (S9))	
Signal	I [rel.]	I [rel.]	$F_{A,relax}$ [-]	I [rel.]	$F_{A,0}$ [-]	I [rel.]	$F_{A,1}$ [-]	I [rel.]
13	1.006	1.025	0.913	1.060	0.976	1.068	1	1.068
15a	0.985	0.820	0.813	0.953	0.960	0.976	1	0.976
17a+b	1.975	1.559	0.847	1.738	0.943	1.812	1	1.812
15b	1.025	0.874	0.809	1.020	0.958	1.047	1	1.047
11b	1.013	0.874	0.879	0.939	0.942	0.980	1	0.980
20b	0.992	0.857	0.841	0.962	0.959	0.986	1	0.986
18b	1.008	0.804	0.814	0.933	0.933	0.984	1	0.984
11a	1.998	0.775	0.876	0.835	0.931	0.883	1	0.883
14		1.000	0.915	1.032	0.994	1.021	1	1.021
18a	0.991	0.945	0.858	1.041	0.956	1.071	1	1.071
20a	0.992	0.865	0.848	0.963	0.958	0.989	1	0.989
8	1.017	0.969	0.924	0.991	0.980	0.995	0.997	0.997
16	1.001	1.006	0.921	1.032	0.995	1.019	0.988	1.032
23a	1.013	0.799	0.843	0.895	0.957	0.919	0.974	0.944
23b	1.011	0.799	0.872	0.864	0.955	0.890	0.973	0.914
12	1.006	0.993	0.906	1.035	0.983	1.036	1	1.036
22	1.000*	1.000*	0.944	1.000*	0.984	1.000*	1	1.000*
2	0.995	0.972	0.960	0.956	0.979	0.960	0.994	0.966
1	0.980	0.956	0.943	0.958	0.989	0.952	0.973	0.979
3	0.997	1.010	0.962	0.991	0.977	0.997	0.994	1.003
4	0.990	1.032	0.976	0.998	0.988	0.994	1	0.994
Δ_{max}	2.5%	22.5%		16.5%		11.7%		11.7%
RMSD	1.3%	15.1%		8.5%		6.4%		6.1%
$\Delta_{extreme}$	4.3%	24.9%		21.2%		17.5%		17.5%

3.3 The effect of B_1 field inhomogeneity

Because the ZS method measures each chemical shift from a slightly different horizontal slice of the sample, any variation in B_1 along the sample will cause systematic changes in the measured signal intensity as a function of shift. The experimental map of B_1 as a function of z in the inverse probe used shows that in this case the variation in B_1 with z is too small (*ca.* 2%) to be significant in the range of ± 5 mm around the centre of the gradient coil. The slice selection gradient was adjusted to fit the signal dispersion in strychnine (6.9 ppm, 4.1 kHz); for the gradient amplitude of 1.05 G/cm used, the ± 5 mm range spans 7.5 ppm (4.5 kHz).

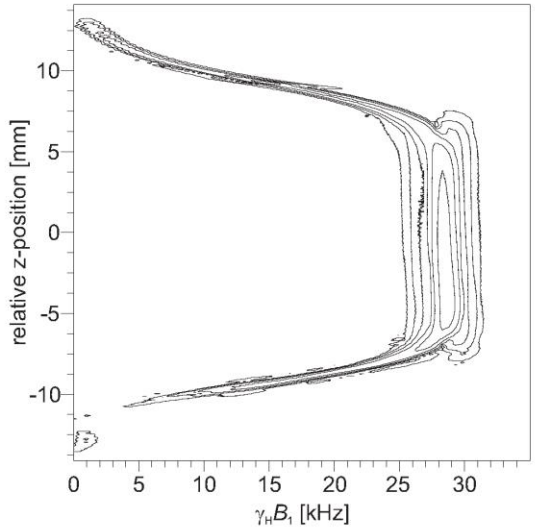

Figure S6: B_1 field map for the probe utilized in the 600 MHz instrument throughout this study. The field map was collected for a doped water sample using a simple gradient echo experiment for which the excitation pulse length was incremented in succeeding scans. Fourier transformation was applied to the data, which were then displayed in absolute value mode. The experiment produces a 2D spectrum symmetrical about $B_1 = 0$, of which only the positive half is shown.

4 Scatter plot for F_2-Zangger-Sterk NOESY-derived distances obtained with normalization

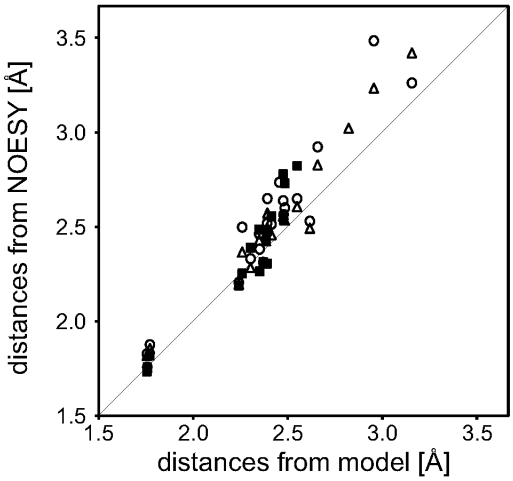

Figure S7: Scatter plot showing the distances determined experimentally versus the distances derived from the two-conformer model described by Butts *et al.*[6]. Open circles show the results from the small mixing time series (NOESY) and open triangles show the results from the extensive mixing time series acquired with Thrippleton-Keeler filtration during mixing (NOESY ZQF). Results from the pure shift NOESY are given as filled boxes, as obtained when normalizing the integrals to those from a ^{1}H ZS spectrum. Compare with Figure 5 in the main article, which shows the data without normalization.

5 References

[1] S. Macura, R.R. Ernst, Elucidation of cross relaxation in liquids by two-dimensional N.M.R. spectroscopy, Mol. Phys., 41 (1980) 95-117.

[2] S. Macura, B.T. Farmer Ii, L.R. Brown, An improved method for the determination of cross-relaxation rates from NOE data, J. Magn. Reson., 70 (1986) 493-499.

[3] H. Hu, K. Krishnamurthy, Revisiting the initial rate approximation in kinetic NOE measurements, J. Magn. Reson., 182 (2006) 173-177.

[4] K. Stott, J. Stonehouse, J. Keeler, T.-L. Hwang, A.J. Shaka, Excitation Sculpting in High-Resolution Nuclear Magnetic Resonance Spectroscopy: Application to Selective NOE Experiments, J. Am. Chem. Soc., 117 (1995) 4199-4200.

[5] B.A. Borgias, M. Gochin, D.J. Kerwood, T.L. James, Relaxation matrix analysis of 2D NMR data, Prog. Nucl. Magn. Reson. Spectrosc., 22 (1990) 83-100.

[6] C.P. Butts, C.R. Jones, J.N. Harvey, High precision NOEs as a probe for low level conformers-a second conformation of strychnine, Chem. Commun., 47 (2011) 1193-1195.

[7] J. Tropp, Dipolar relaxation and nuclear Overhauser effects in nonrigid molecules: The effect of fluctuating internuclear distances, J. Chem. Phys., 72 (1980) 6035-6043.

[8] P.F. Yip, D.A. Case, Incorporation of Internal Motion in NMR Refinements Based on NOESY Data, in: J.C. Hoch, F.M. Poulsen, C. Redfield (Eds.) Computational Aspects of the Study of Biological Macromolecules by Nuclear Magnetic Resonance Spectroscopy, Plenium Press, New York, 1991, pp. 317 - 330.

[9] R.L. Vold, J.S. Waugh, M.P. Klein, D.E. Phelps, Measurement of Spin Relaxation in Complex Systems, J. Chem. Phys., 48 (1968) 3831-3832.

[10] K. Zangger, H. Sterk, Homonuclear Broadband-Decoupled NMR Spectra, J. Magn. Reson., 124 (1997) 486-489.

[11] A.J. Pell, R.A.E. Edden, J. Keeler, Broadband proton-decoupled proton spectra, Magn. Reson. Chem., 45 (2007) 296-316.

[12] L. Castañar, P. Nolis, A. Virgili, T. Parella, Measurement of T1/T2 relaxation times in overlapped regions from homodecoupled 1H singlet signals, J. Magn. Reson., 244 (2014) 30-35.

[13] H.C. Torrey, Transient Nutations in Nuclear Magnetic Resonance, Phys. Rev., 76 (1949) 1059-1068.

[14] G. Navon, M. Polak, T1 Spin decoupling effects on the lineshapes of NMR spin—spin multiplets, Chem. Phys. Lett., 25 (1974) 239-242.

[15] C.P. Slichter, Principles of Magnetic Resonance, Third ed., Springer Verlag, Berlin, 1996.

[16] I.N. Bornstein, K.A. Semendjajew, G. Musiol, H. Mühlig, Taschenbuch der Mathematik, 6. ed., Wissenschaftlicher Verlag Harri Deutsch, Frankfurt a.M., 2005.

6.3. Conclusion on Project A

In Project A a comprehensive discussion of factors determining the robustness of relative integral measurements in interferogram-based Zangger-Sterk experiments is provided. It is described, which factors may limit the accuracy of relative integrals measured with this method and a simple method is presented for correcting for systematic bias of the pure shift method, that is applicable if peaks are well separated in the pure shift spectra. These works therefore pave the way for applications of relative integral measurements using pure shift spectra, a field that, with a few exceptions[263, 269, 274], was mostly avoided in the literature.

As it was found, that, even if an interferogram-based acquisition scheme is used, the accuracy that can be achieved is limited and that signal intensity dissipation into sidebands can adversely affect the accuracy of the relative integral measurement, applications of such relative integral measurements should be limited to cases, where only rough estimates of the relative integral is required (i.e.: where errors of up to ~ 25% are not adversely limiting the application), or to cases where the simple correction of integrals measured with the relative integrals observed in ^{1}H Zangger-Sterk experiments can be applied.

Noteworthy, applications such as T_1[263, 318], T_2[263, 318] and DOSY[253, 263, 315-317] measurements, where the height/integral of each signal is analysed independently for the intensity attenuation introduced by a preparatory phase in the experiment may be less affected by systematic errors introduced by pure shift techniques. In such cases, effects of differential relaxation and effects of differing *J*-coupling networks do contribute to an intensity attenuation which may differ from signal to signal, but this attenuation remains unaffected by the preparatory phase of the experiment. These applications may therefore be less critical in terms of bias of the homodecoupling method on the results, though it should be mentioned, that signal cross-talk by overlap of signals with decoupling sidebands of neighbouring signals may remain a critical issue in pure shift techniques.

It is demonstrated that for NOE-based interatomic distance measurements, such accuracies are sufficient to derive useful restraints for solution structure studies. On the experimental side, NOE-based structure analysis very often relies on comparably drastic simplifications for data analysis, such as analysing NOE build-up using the isolated-spin-pair approximation[53, 103, 105] and neglecting effects of differential relaxation. Additionally, considering the challenges inherent in generating models accurately describing the conformational flexibility of molecules in solution, it is likely that the small decrease in measurement precision that is introduced by using pure shift techniques for NOE quantification is compensated by the bigger number of structural restraints available, when complementing existing data with pure shift data. The results therefore enable future applications of pure shift NOE experiments to the solution structural analysis of small molecules.

6.4. Apportionment from the contents of my master thesis

Whether or not ^{1}H and 2D-NOESY pure shift spectra with Zangger-Sterk homonuclear decoupling[252, 253, 265, 266, 297, 340] would be suitable for direct quantification of relative signal integrals already was the central question of my Master thesis[341]. At that time, reports on Zangger-Sterk techniques were limited discussions to the qualitative features of these spectra, in particular the improved signal dispersion that could be obtained. The only discussion covering quantitative features of these spectra was the use of signal intensities in diffusion-attenuated pure shift ^{1}H-spectra for the construction of DOSY spectra[253].

To a big extent, my master thesis therefore was centred around the question, how experimental settings of Zangger-Sterk ^{1}H-spectra could be chosen to obtain optimal spectral quality and to enable direct measurement of relative signal integrals. Alike content later was also covered in the Ph.D. thesis of ARD KOLKMAN[269], albeit no publication of these results occurred in peer-review journals to date, so these are

largely unnoticed. For the investigations in my master thesis, I mostly used strychnine **1** for experiment benchmarking. I was able to show, that Zangger-Sterk ^{1}H-spectra can reproduce relative signal integrals to the accuracy of ~ 25% for the test substances studied. All investigations thereby followed the empirical approach of measuring relative signal integrals of known ideal value without making attempts to explain the pathways of signal losses in these spectra.

During my Ph.D. thesis I added a discussion of the factors limiting measurement accuracy (as outlined in chapter 3 of the SI). Noteworthy, a model is presented describing on a quantitative basis the signal shape observed in the resulting pure shift spectra including its sidebands, for weakly coupled systems. It is illustrated that this model is able to describe some of the major factors governing relative signal intensity loss caused by the homonuclear decoupling element. Albeit for practical applications, the simple method of using relative integrals form ^{1}H-Zangger-Sterk spectra is a better choice, the description of the underlying mechanisms of signal loss may contribute to the understanding of the fundamental challenges inherent in the measurement of quantitative signal integrals from Zangger-Sterk experiments.

In my master thesis, I subsequently tested, if NOESY experiments with F_2-Zangger-Sterk decoupling[297] would provide unbiased cross-relaxation rates for quantitative measurement chemical exchange rates[51] for a system enabling measurements with high signal-to-noise ratio. This was chosen initially to identify potential systematic bias on the results by the measurement technique. For cross-relaxation caused by NOE[46], the data reported in my master thesis is very promising, showing that measured cross-relaxation rates in strychnine agree well with those measured from 1D selective NOE experiments[35, 101, 102]. However, no detailed studies enabling evaluation of the errors introduced by the method were possible in the limited amount of time available.

In particular, the lack of high signal-to-noise data in the case of NOE measurements was problematic at that time, in terms of evaluation of the potential use of the pure shift data for NOE-based distance measurements. We therefore decided to reinvestigate the possibility of determining interatomic distances with pure shift NOE experiments in my Ph.D. thesis. The data should be supported by measurements from 1D selective NOE experiments with Zangger-Sterk decoupling, an experiment I developed in direct analogy to the NOESY with Zangger-Sterk decoupling. A very interesting feature of these selective NOE experiments is that, when using the homonuclear decoupling block only for band-selective decoupling, high signal-to-noise data can be collected in reasonable amounts of time. This enabled the measurement of high signal-to-noise data for benchmarking the band-selective version of the experiment for a number of NOE contacts and mixing times. The combination of Zangger-Sterk homonuclear decoupling with 1D selective experiments, as introduced in this work, can be particularly suitable in practice, as for many applications, experiments without homonuclear decoupling will be able to provide a majority of distance information, while only for a few selected distances resorting to pure shift techniques will be advisable. The ability of collecting band selective experiments in relatively little time further sidesteps the limited sensitivity inherent in broadband Zangger-Sterk decoupled experiments.

While clear indications that Zangger-Sterk homodecoupled NOE experiments can provide NOE derived distance restraints were already given in my master thesis, continued efforts during in this work not only provide a more solid data basis for this statement, they also significantly add to the project from a methodological point by the introduction of a new experimental technique with potentially higher practical use.

An additional aspect covered in this chapter, which is not contained in my master thesis, is the implementation and testing of a Zangger-Sterk inversion-recovery experiment suitable for measuring T_1-relaxation rates in crowded spectral regions (see chapter 2 of the SI).

7. Project B: Measurement of One-Bond Couplings from Pure Shift HSQC Spectra

The contents of sections 7.2 and 7.3 of this chapter have been published in

I. Timári, L. Kaltschnee, A. Kolmer, R. W. Adams, M. Nilsson, C. M. Thiele, G. A. Morris, K. E. Kövér, "Accurate determination of one-bond heteronuclear coupling constants with "pure shift" broadband proton-decoupled CLIP/CLAP-HSQC experiments", *J. Magn. Reson.* **2014**, 239, 130 – 139, DOI: 10.1016/j.jmr.2013.10.023

and in

L. Kaltschnee, A. Kolmer, I. Timári, V. Schmidts, R. W. Adams, M. Nilsson,K. E. Kövér, G. A. Morris, C. M. Thiele, ""Perfecting" pure shift HSQC: full homodecoupling for accurate and precise determination of heteronuclear couplings", *Chem. Commun.* **2014**, *50*, 15702 – 15705, DOI: 10.1039/C4CC04217D. – Published by the Royal Society of Chemistry.

The contents contained in section 7.4 are submitted for publication to *RSC Advances*:

I. Timári, L. Kaltschnee, M. Raics, F. Roth, N. G. A. Bell, R. W. Adams, M. Nilsson, D. Uhrín, G. A. Morris, C. M. Thiele and K. E. Kövér, "Real-time broadband proton-homodecoupled CLIP/CLAP-HSQC for automated measurement of heteronuclear one-bond coupling constants", *submitted the 2nd of June 2016*.

7.1. Motivation

In the previous chapter, pure shift NMR experiments are described and characterized, that predominantly provide structural information through signal integrals. The main motivation of using pure shift spectra providing signals with reduced widths was to reduce spectral overlap and thus to enable an extraction of the desired signal integrals, where this normally is hampered.

Throughout projects B, C and D, the focus will be towards precise measurement of signal positions and the structural information contained therein. For relative signal integral measurements, pure shift techniques required compromises to be made in terms of measurement accuracy and precision. It is shown here, that when signal positions are measured, even if signal overlap is absent, these techniques can provide improved accuracy and precision, as compared to experiments without homonuclear decoupling. The ability of pure shift techniques to narrow signals to single lines, which normally appear broad and featureless, and thus to facilitate peak position measurement, is illustrated in Figure 7.1. This was our initial motivation to explore possible benefits pure shift techniques could have on the measurement of residual dipolar couplings (RDCs), a structural parameter that is measured from differences of signal positions.

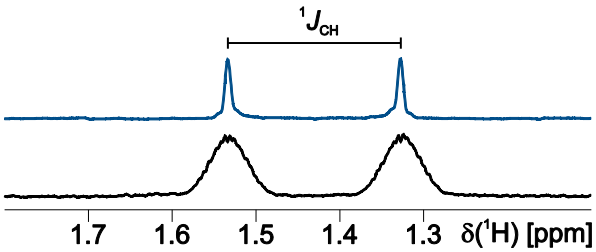

Figure 7.1: Illustration of the improvement in peak position definition, which can be achieved in an F_2-decoupled BIRD CLIP-HSQC[342, 343] (top), as compared to a CLIP-HSQC[166] without homonuclear decoupling in the proton dimension (bottom). Shown is a 1D-trace extracted at the H5-position of menthol. Full experimental details, the structure and the numbering are given in the manuscript added to chapter 7.3.2.

7.2. RDC measurements in interferogram-based F_2-BIRD decoupled CLIP-HSQCs

During the last three decades, methods for solution structure elucidation both for bio macromolecules[7, 30, 344] and for small molecules[66, 67, 112] have benefited significantly from the introduction of RDCs as an additional NMR-derived structure parameter. In structure calculations[84], the angular information contained in RDCs nicely complements information from *J*-couplings[61, 62, 64] and NOE[54, 60, 345], enabling very challenging systems to be studied.

As opposed to dipolar splittings observed in solids, RDCs appear strongly scaled, enabling their measurement in high resolution liquid-state NMR techniques, as a small additional contribution to signal splittings[130, 181, 346].

At the time of the introduction of RDCs it was already known, that the BIRD[251] method can introduce simplifications and sensitivity improvements to heteronuclear correlation spectra[302], when used for homonuclear decoupling in the indirect dimension of these experiments. Use of this technique for decoupling the indirect dimension in F_1-coupled HSQCs from long-range interactions as subsequently shown to increase the accuracy of the coupling constant measurement[163, 347-349] if lines are broadened by long-range couplings.

For small molecule applications in particular, but not exclusively, the use of F_1-coupled HSQC-based experiments for coupling constants extraction however has two notable disadvantages: First, for precise coupling constant extraction, the resolution along the coupled dimension has to be sufficient, leading to long experiment durations. This motivated the extension to experiments with upscaling of the apparent coupling[161] and the acquisition of data with non-uniform-sampling (NUS) schemes[165]. Second, in the case of methylene groups, F_1-coupled methods only allow the sum of the two one-bond couplings ($^1T_{CH}$) to be measured. This stimulated the development of dedicated F_1-coupled HMQC-HSQC-hybrids[164, 165]. Both of these problems do not arise in F_2-coupled HSQC experiments, such as the CLIP-HSQC experiment[166], because high resolution along F_2 is easily achieved and because separate peaks are observed for both protons in methylene groups.

The introduction of high resolution pure shift acquisition into the F_2-dimension of two-dimensional experiments[254, 266, 297] simultaneously stimulated KATALIN KÖVÉR, BURKHARD LUY and CHRISTINA THIELE to follow the idea of developing of F_2-heterocoupled-F_2-BIRD-homodecoupled CLIP-HSQC experiments. Through the persisting contact with the group of GARETH MORRIS, we were informed that KATALIN KÖVÉR intended to pursue the same developments as we intended, so the groups of GARETH MORRIS, KATALIN KÖVÉR and CHRISTINA THIELE decided to join forces and to work on this project in cooperation. We only found out much later, that the exact same development also took place in the group of BURKHARD LUY, which then lead to a back-to-back publication of the results[342, 343].

The shared interest of different groups to follow this development illustrates the high potential use of this technique to the field of research. It could be shown that F_2-BIRD-homodecoupled-CLIP/CLAP-HSQC experiments (also termed CLIP-RESET-HSQC experiments) can introduce considerable simplifications to one-bond coupling constant measurements in both isotropic and anisotropic solution for small molecules[342, 343]. In particular, for molecules that are weakly aligned in anisotropic media, the spectral simplification is very advantageous when it comes to coupling constant extraction. In addition to F_2-heterocoupled experiments, also variants were presented with broadband heteronuclear decoupling in the F_2-dimension and applications were shown for small organic molecules as well as for a small protein[343].

In the case of our work, the initial implementation of the experiment was performed by KATALIN KÖVER. The experiment was subsequently tested experimentally by ISTVÁN TIMÁRI with water-soluble substances, and by ANDREAS KOLMER and myself with small organic compounds. Support of the results through spin simulations was provided by RALPH ADAMS.

In the light of the invention of the perfectBIRD decoupling scheme[213], with which I was able to solve the problem of persisting $^{2}J_{HH}$-couplings inherent in BIRD decoupled experiments (see chapter 7.3), and the urgency of publishing results in parallel with REINSPERGER and LUY we opted for publishing the F_2-BIRD decoupled experiment in a first paper[343], and to provide a thorough comparison of the different CLIP-/CLAP-HSQC experiments together with the description of the perfectBIRD technique[213].
The first paper therefore describes the F_2-BIRD homodecoupled CLIP/CLAP-HSQC, which is optimized for one-bond heteronuclear coupling constant measurement and the F_2-BIRD homodecoupled HSQC with broadband heteronuclear decoupling, providing high resolution HSQC spectra.
ISTVÁN TIMÁRI first showed that the heterocoupled experiment is robust with respect to a wide range of settings for the BIRD- and INEPT transfer delays in a sense that offsetting of these delays from their optimum values does not introduce any peak distortions or additional peaks, but only leads to a reduction of the signal intensities observed. A ^{13}C-labeled substance was used in this case for convenience (structure **2**, shown in Figure 6.1)
In the following he showed, that high quality spectra can be obtained for a synthetically modified sugar (structure **3**, shown in Figure 7.2:) in both isotropic aqueous solution and under weak alignment induced by lipid bicells[138] (Otting-medium). Drastic simplifications can be observed for signals at tertiary carbon positions (positions 1 - 5). For the methylene groups (positions 6 and 7), strong signal distortions however are observed. Tests, that ANDREAS KOLMER and I performed on this experiment gave strong support for these results, they however were moved to the subsequent publication[213], to facilitate direct comparison with the results obtained with the F_2-perfectBIRD decoupled experiments described later.
For the experiment with F_2-BIRD homodecoupled HSQC with broadband heteronuclear decoupling it is shown that a significant narrowing is obtained for the signals though homonuclear decoupling, which in addition sidesteps resolution limits in the direct dimension, imposed by heteronuclear decoupling. In spectra of sucrose **4** it is shown that, in analogy to the suppression of zero-quantum interference in NOESY spectra, the pure shift approach is able to significantly attenuate anti-phase signals originating from long-range cross-peaks. A direct comparison with the RESET-HSQC[254] presented by SAKHAII *et al*. is also provided.
The work is concluded by showing that the experiment also provides high resolution ^{1}H-^{15}N-HSQC spectra for proteins, as illustrated for the 55-residue penicillium anti-fungal protein (PAF) uniformly labelled in ^{15}N.
Summarizing, the work reports on an experiment which is able to introduce BIRD decoupling into the F_2-dimension of HSQC spectra. One bond coupling constant extraction can directly profit from the simplified line shape for signals at tertiary carbon positions. As compared to F_1-BIRD decoupled experiments[163, 347-349], the interferogram-based homonuclear decoupling approach offers high resolution to be achieved in the dimension of coupling constant extraction within reduced experiment duration, without resorting to *J*-upscaling. In terms of overall experiment duration, however, the experiment still lacks behind the CLIP-HSQC experiment without homonuclear decoupling[166]. A practical solution to this will be presented in section 7.4. Furthermore, the BIRD technique is unable to fully decouple methylene groups, which feature signal distortions in the spectra, a problem to which a solution is presented in the next section.

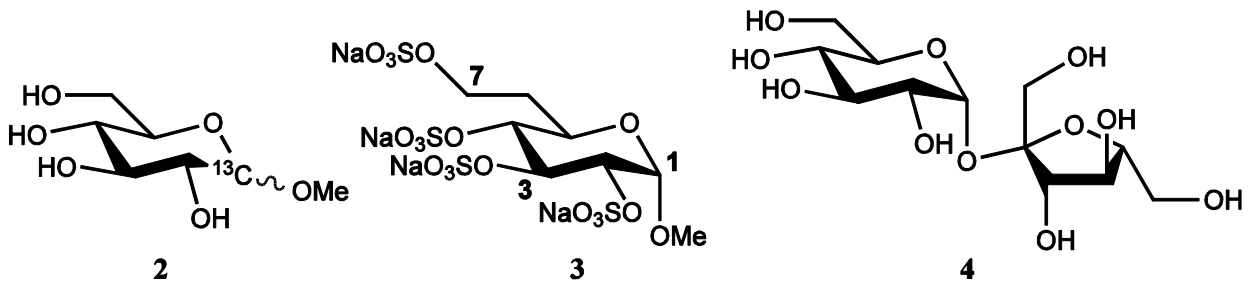

Figure 7.2: Small molecule compounds used by TIMÁRI during tests of F_2-BIRD decoupled HSQC experiments. **2**: uniformly ^{13}C-labeled [C-1]-methyl-α,β-D-glucopyranoside, **3**: tetra-sodium-(1-methyl-2,3,4-tri-O-sulfonato-6-deoxy-6-C-sulfonatomethyl-α-D-glucopyranoside) and **4**: D-sucrose.

I. Timári, L. Kaltschnee, A. Kolmer, R. W. Adams, M. Nilsson, C. M. Thiele, G. A. Morris, K. E. Kövér, "Accurate determination of one-bond heteronuclear coupling constants with "pure shift" broadband proton-decoupled CLIP/CLAP-HSQC experiments", *J. Magn. Reson.* **2014**, 239, 130 – 139,
DOI: 10.1016/j.jmr.2013.10.023

Journal of Magnetic Resonance 239 (2014) 130–138

Contents lists available at ScienceDirect

Journal of Magnetic Resonance

journal homepage: www.elsevier.com/locate/jmr

Accurate determination of one-bond heteronuclear coupling constants with "pure shift" broadband proton-decoupled CLIP/CLAP-HSQC experiments ☆

István Timári [a], Lukas Kaltschnee [b], Andreas Kolmer [b], Ralph W. Adams [c], Mathias Nilsson [c,d], Christina M. Thiele [b], Gareth A. Morris [c], Katalin E. Kövér [a,*]

[a] Department of Inorganic and Analytical Chemistry, University of Debrecen, Egyetem tér 1, H-4032 Debrecen, Hungary
[b] Clemens-Schöpf-Institut für Organische Chemie und Biochemie, Technische Universität Darmstadt, Alarich-Weiss-Straße 4, D-64287 Darmstadt, Germany
[c] School of Chemistry, University of Manchester, Oxford Road, Manchester M13 9PL, United Kingdom
[d] Department of Food Science, University of Copenhagen, Rolighedsvej 30, DK-1958 Frederiksberg C, Denmark

ARTICLE INFO

Article history:
Received 7 October 2013
Available online 14 November 2013

Keywords:
Broadband proton decoupling
F_2-coupled HSQC
Pure absorption
IPAP
RDC

ABSTRACT

We report broadband proton-decoupled CLIP/CLAP-HSQC experiments for the accurate determination of one-bond heteronuclear couplings and, by extension, for the reliable measurement of small residual dipolar coupling constants. The combination of an isotope-selective BIRD$^{(d)}$ filter module with a non-selective ^{1}H inversion pulse is employed to refocus proton–proton coupling evolution prior to the acquisition of brief chunks of free induction decay that are subsequently assembled to reconstruct the fully-decoupled signal evolution. As a result, the cross-peaks obtained are split only by the heteronuclear one-bond coupling along the F_2 dimension, allowing coupling constants to be extracted by measuring simple frequency differences between singlet maxima. The proton decoupling scheme presented has also been utilized in standard HSQC experiments, resulting in a fully-decoupled pure shift correlation map with significantly improved resolution.

1. Introduction

Residual dipolar couplings (RDCs) provide invaluable long-range constraints for structure determination of molecules, conveying information on the distances between dipolar-coupled nuclei and on the orientations of the corresponding internuclear bond vectors. In recent years residual dipolar couplings have therefore been widely utilized in structural studies of proteins, nucleic acids, carbohydrates, organic and organometallic compounds in the liquid state, and have been shown to improve considerably the precision of structures [1–9].

For weakly aligned samples, RDCs manifest themselves in NMR spectra as an increase or decrease in the splittings due to scalar (J) couplings between nuclei. Their magnitudes can therefore be extracted by measuring changes of splitting in isotropic compared to anisotropic sample conditions.

Here we propose a modification of F_2-coupled CLIP/CLAP-HSQC [10] experiments in which the unwanted additional splittings caused by co-evolution of proton–proton couplings are eliminated with the aid of an isotope-selective BIRD-based broadband proton decoupling scheme applied during signal evolution. Thus one-bond heteronuclear couplings can be determined from the resulting spectra simply by measuring the frequency differences between the peak maxima of singlets, instead of between the centers of complex multiplets.

We also demonstrate that the proposed broadband proton decoupling scheme, when built into the standard gradient enhanced HSQC experiment, leads to pure shift correlation spectra of enhanced resolution, offering significant advantages for automated spectral analysis such as automated peak-picking or automated intensity measurement in HSQC-based relaxation experiments.

2. Experimental

All experiments were performed on a Bruker Avance II 500 spectrometer (Bruker BioSpin GmbH, Rheinstetten, Germany) equipped with a TXI z-gradient probe. All spectra were processed with TopSpin 2.1, 2.5 or 3.0 (Bruker Biospin GmbH, Karlsruhe, Germany). For testing the experiments a sample of ^{13}C-labeled [C-1]-methyl-α,β-D-glucopyranoside (**1**) (30 mg) dissolved in 500 μl D_2O was used. The measurement of RDCs was demonstrated on a

☆ Submitted jointly with J. Magn. Reson. 239 (2014) 132–140. DOI: http://dx.doi.org/10.1016/j.jmr.2013.12.004

* Corresponding author.
E-mail address: kover@science.unideb.hu (K.E. Kövér).

1090-7807/$ - see front matter © 2013 Elsevier Inc. All rights reserved.
http://dx.doi.org/10.1016/j.jmr.2013.10.023

sample of tetra-sodium-(1-methyl-2,3,**4**-tri-*O*-sulfonato-6-deoxy-6-*C*-sulfonatomethyl-α-D-glucopyranoside) (**2**) (20 mg), dissolved in 500 µl D_2O for isotropic condition. The liquid crystalline phase was prepared as described by Rückert and Otting [11] from ether/alcohol (hexaethylene glycol monododecyl ether ($C_{12}E_6$)/n-hexanol, 5%, $r = 0.64$, $J_Q = 25$ Hz). The $C_{12}E_6$ and n-hexanol were purchased from Sigma–Aldrich and used without further purification. The variants of the HSQC sequence were tested on a sample of D-sucrose (**3**) (30 mg) dissolved in 500 µl D_2O. For all measurements the nominal temperature was set to 298 K unless indicated otherwise. All F_2-coupled CLIP/CLAP-HSQC spectra were acquired with a high spectral resolution of 0.3 Hz/point, for accurate measurement of small residual dipolar couplings. The ^{15}N–^{1}H pure shift HSQC spectrum was recorded for 1.6 mM [U–^{15}N]–*Penicillium* antifungal protein (PAF) (95%: 5% H_2O:D_2O), pH 5.0, at 300 K.

Spectra were recorded with a proton 90° pulse of 15 µs, a carbon 90° pulse of 15.7 µs for acquisition, a carbon 90° pulse of 80.0 µs for GARP decoupling, smoothed chirp pulses (Crp60,0.5,20.1) of 500 µs duration for broadband ^{13}C inversion and (Crp60comp.**4**) of 2 ms for broadband ^{13}C refocusing. ^{1}H–^{15}N HSQC spectra were collected with nitrogen 90° pulses of 29 µs for acquistion and 250 µs for WALTZ16 decoupling.

For processing the 3D raw data sets acquired with the pulse sequences presented, a Bruker AU program (available at http://nmr.chemistry.manchester.ac.uk) was used to reconstruct the 2D interferograms. Prior to 2D Fourier transformation, the data were apodized by multiplying with a 90° shifted sine-squared function and then zero-filled by a factor of two in both dimensions, to yield a spectral resolution of 0.3–0.5 Hz/point in the ^{1}H dimension.

3. Results and discussion

Due to the increasing interest in the use of RDCs in recent years, numerous methods based on measuring frequency differences between multiplet components have been developed for the measurement of one-bond heteronuclear coupling constants. The most widely used approach is based on the HSQC experiment, with heteronuclear couplings retained in the F_1 or F_2 dimension. To circumvent spectral crowding due to the increased number of cross-peaks in the coupled spectra, E-COSY [12], spin-state selective [13–15], IPAP [16] and TROSY [17–19] methods have been proposed. Unfortunately, all these methods suffer from additional splittings of cross-peaks due to the co-evolution during data acquisition of coupling interactions other than the desired heteronuclear one-bond coupling.

To eliminate line-splittings caused by multiple bond heteronuclear couplings in the F_1-coupled HSQC sequence, a gradient enhanced BIRD$^{(r)}$ module has been employed during the evolution period t_1, yielding simplified cross peaks with only splittings due to the desired one-bond couplings in the F_1 dimension [20,21]. However, heteronuclear correlation experiments coupled in the indirect F_1 dimension are limited by the necessity of acquiring large numbers of t_1 points to achieve sufficiently high digital resolution, therefore making the experiment rather time-consuming. For this reason, measurement of one-bond heteronuclear coupling constants from F_2 multiplets appears more favorable due to the high digital resolution affordable in the F_2 dimension. However, the complexity and asymmetry of multiplet structures due to proton–proton scalar/dipolar couplings may render the accurate definition of peak positions difficult or even impossible.

A breakthrough in the removal of unwanted line-splittings is offered by the use of broadband homonuclear decoupling methods that have been reported in the last few years [22–31]. Such experiments can be classified into two groups, depending on the decoupling approach employed. The first group [22,23,25,26,28,30] utilizes the Zangger–Sterk approach [22], which achieves broadband homonuclear decoupling by combining a hard 180° and a selective 180° proton pulse, the latter applied under the action of a weak gradient field pulse to give an effect that is both spatially- and frequency-selective. As a result, in a given slice of the sample the on-resonance magnetization experiences no net effect, whereas all other proton magnetizations are inverted, refocusing any homonuclear scalar couplings to the observed spin. The second group [24,27,29,31] of experiments performs broadband

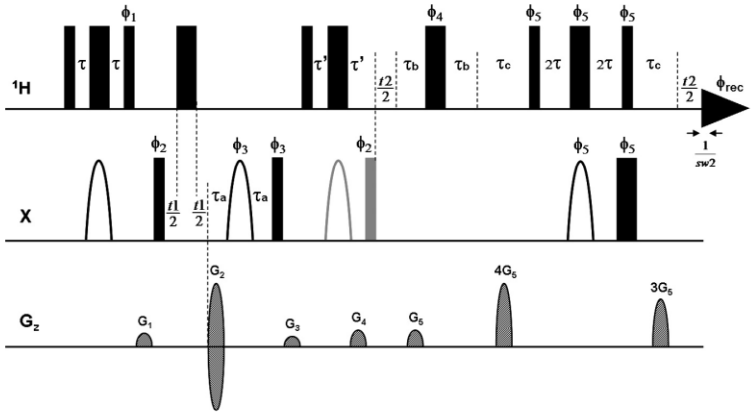

Fig. 1. Broadband proton-decoupled CLIP- and CLAP-HSQC experiments designed for the measurement of ($^{1}J_{CH} + {}^{1}D_{CH}$) couplings. Narrow and wide filled bars correspond to 90° and 180° pulses, respectively, with phase *x* unless indicated otherwise. Smoothed chirp inversion and refocusing X pulses are shown as half-ellipses. Phases are $\varphi_1 = y$; $\varphi_2 = x, -x$; $\varphi_3 = x,x,-x,-x$; $\varphi_4 = y,y,y,y,y,y,y,y,-x,-x,-x,-x,-x,-x,-x,-x$; $\varphi_5 = y,y,y,y,-x,-x,-x,-x$; and $\varphi_{rec} = x,-x,-x,x,-x,x,x,-x,x,-x,-x,x,-x,x,x,-x,x,-x,-x,x$. Delays are set as follows: $\tau = 1/(4 * {}^{1}J_{XH})$, $\tau_a = p16 + d16$, $\tau_b = 1/(4 * sw2)$, $\tau_c = p16 + d16 + 350$ µs, $\tau'_{(CLIP)} = \tau$; $\tau'_{(CLAP)} = p16 + d16$. Coherence order selection and echo–antiecho phase sensitive detection in the X-dimension are achieved with gradient pulses G_2 and G_4 in the ratio 80:20.1 for ^{13}C and 80:8.1 for ^{15}N, respectively. Purging gradient pulses G_1, G_3 are set to 15%, 11% of maximum gradient strength (50 G/cm), typically of 1 ms duration ($p16$) followed by a recovery delay $d16 = 50$ µs. Coherence selection gradient pulses used in the extra proton-decoupled dimension have $G_5 = 18\%$. In the CLIP-HSQC sequence an additional carbon 90° pulse (shown in gray) is employed to remove the undesired residual dispersive antiphase proton magnetization prior to detection, as proposed by Enthart et al. [10]. In contrast, in the CLAP-HSQC experiment the antiphase proton magnetization is retained and detected after X → ^{1}H back-transfer, so only a short spin-echo sequence ($2 * \tau'$) with a proton 180° pulse in the middle is used to accommodate the gradient pulse G_4. The purging carbon 90° pulse and a carbon 180° pulse (shown in gray) used in the CLIP-experiment are omitted in this case.

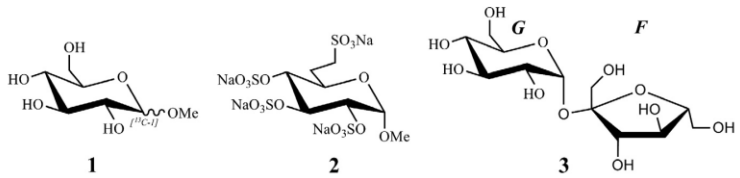

Scheme 1. Model compounds used for testing the experiments. ^{13}C-labeled [C-1]-methyl-α,β-D-glucopyranoside (**1**), tetra-sodium-(1-methyl-2,3,4-tri-*O*-sulfonato-6-deoxy-6-*C*-sulfonatomethyl-α-D-glucopyranoside) (**2**) and D-sucrose (**3**).

homonuclear decoupling with a bilinear rotation decoupling (BIRD) module [32], utilizing isotope selection instead of the slice/chemical shift filtering of the Zangger–Sterk approach. Depending on the phases of BIRD pulse elements, either the direct or the remote protons attached to ^{13}C/^{15}N isotopes can be independently and selectively inverted.

The BIRD approach is used in the variants of the gradient enhanced CLIP/CLAP-HSQC experiments presented here, and yields spectra with simple, pure absorptive in- or anti-phase F_2 doublets displaying only the desired $^1J_{XH}$ splitting in isotropic or ($^1J_{XH}$ + $^1D_{XH}$) splitting in anisotropic solution, respectively and allowing high spectral resolution along the F_2 dimension. The one exception is that because the BIRD module does not distinguish between methylene protons, geminal ^{1}H–^{1}H couplings are not suppressed.

3.1. Broadband proton-decoupled CLIP- and CLAP-HSQC experiments

In the modified CLIP/CLAP-HSQC experiments reported here, broadband proton decoupling in the ^{1}H dimension is achieved by replacing the conventional data acquisition of a free induction decay (FID) $s(t_2)$ at the end of the HSQC pulse sequence with a second evolution time, t_2, at the centre of which a hard 180° proton pulse and a BIRD pulse sequence element are applied in succession, followed by acquisition of a FID $s(t_3)$. The BIRD$^{(d)}$ pulse selectively inverts all proton magnetization directly attached to the X nuclei, but leaves the magnetizations of remotely bound protons and X nuclei unperturbed. In combination with the non-selective 180° proton pulse, therefore, the net effect is for the ^{1}H chemical shift and the heteronuclear one-bond coupling to continue to evolve throughout t_2. The measurement is repeated, acquiring FIDs $s(t_3)$ while incrementing t_2 in steps of 1/*sw2*, where the second indirect spectral width, *sw2*, is large compared to the widths of the proton multiplets. Once a full dataset $s(t_1, t_2, t_3)$ has been acquired, a pseudo-2D dataset is produced by stitching together chunks of $s(t_3)$ of duration 1/*sw2* for successive increments of t_2. The result is a pseudo-2D dataset $s(t_1, t_2')$ in which signal evolves as normal (δ_C only) as a function of t_1, and as a pure shift ^{1}H signal in t_2' (δ_H, $^2J_{HH}$ and $^1J_{CH}$ only). Typically *sw2* is 40–100 Hz, and 16–32 FIDs $s(t_3)$ are acquired, giving a maximum t_2' of 160–800 ms and yielding ample spectral resolution for coupling constant measurement. It is important to note that the best results require very careful timing of the BIRD$^{(d)}$ and ^{1}H 180° pulse decoupling elements. Therefore, the correct setting of the delays in the sequences of Fig. 1, as detailed in the figure legend, is critical.

As in the original CLIP-HSQC experiment [10], a carbon 90° pulse is employed to purge the undesired residual dispersive antiphase proton magnetization prior to detection. In the case of the CLAP-HSQC sequence, proton magnetization is detected in antiphase, so only a short spin-echo sequence to accommodate the coherence selection gradient pulse (G_4) follows, and the purging carbon pulse is omitted here.

The broadband proton-decoupled sequences of Fig. 1 have been tested on the small model compounds depicted in Scheme 1.

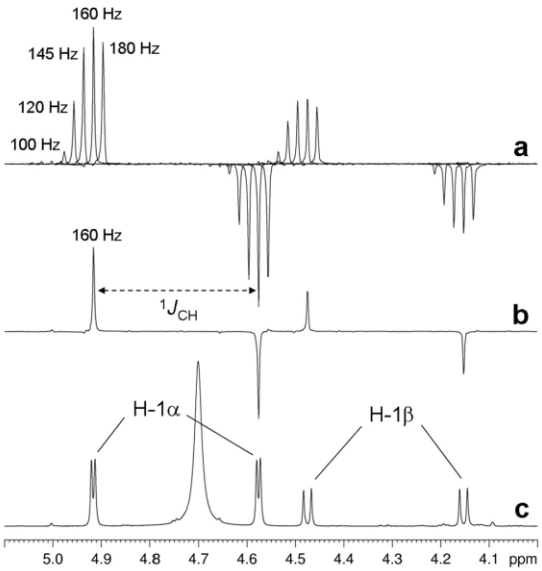

Fig. 2. Illustration of the robustness of the proposed CLAP-HSQC experiment with regard to mismatch between the INEPT and BIRD delays in the sequence and $^1J_{XH}$. Spectra of ^{13}C-labeled [C-1]-methyl-α,β-D-glucopyranoside (a,b) were recorded using the sequence of Fig. 1 with the incremented delay t_1 replaced by a constant delay of 3 μs, to give broadband proton-decoupled 1D spectra. These were recorded with different durations of INEPT and BIRD delays (corresponding to the values of $^1J_{XH}$ shown above the relevant spectra in (a,b)). Spectra in (a) were normalized to allow proper evaluation of the relative signal intensities and their dependence on the delays. Normal ^{1}H NMR spectrum of **1** is shown in (c). Spectra (a,b) were recorded with spectral widths in the ^{1}H dimension = 6.0371 ppm, relaxation delay = 1.7 s, number of scans = 4, number of t_2 increments (i.e. number of FID chunks) = 32, duration of FID chunk = 21.197 ms, number of data points of constructed FID in ^{1}H dimension = 4096 complex data points.

First, to investigate the robustness and tolerance of the experiments with regard to mismatch of the BIRD/INEPT delays in the sequence, a ^{13}C-labeled compound, [C-1]-methyl-α,β-D-glucopyranoside (**1**), was used. The results are shown in Fig. 2, which presents the C-1 doublets obtained with the broadband proton-decoupled CLAP-HSQC sequence using BIRD/INEPT delays adjusted to a range of nominal one-bond heteronuclear coupling constant spanning 100–180 Hz. It can clearly be seen that the intensities of the signals are, as expected, significantly degraded when the delays are mismatched to the coupling constant, but that the pure absorptive quality of the lineshapes remains basically unaffected, allowing accurate measurement of couplings even in anisotropic samples where net coupling constants vary widely. These results clearly demonstrate that the proposed sequences, used in combination with the pulsed field gradient coherence selection scheme illustrated in Fig. 1, efficiently remove the

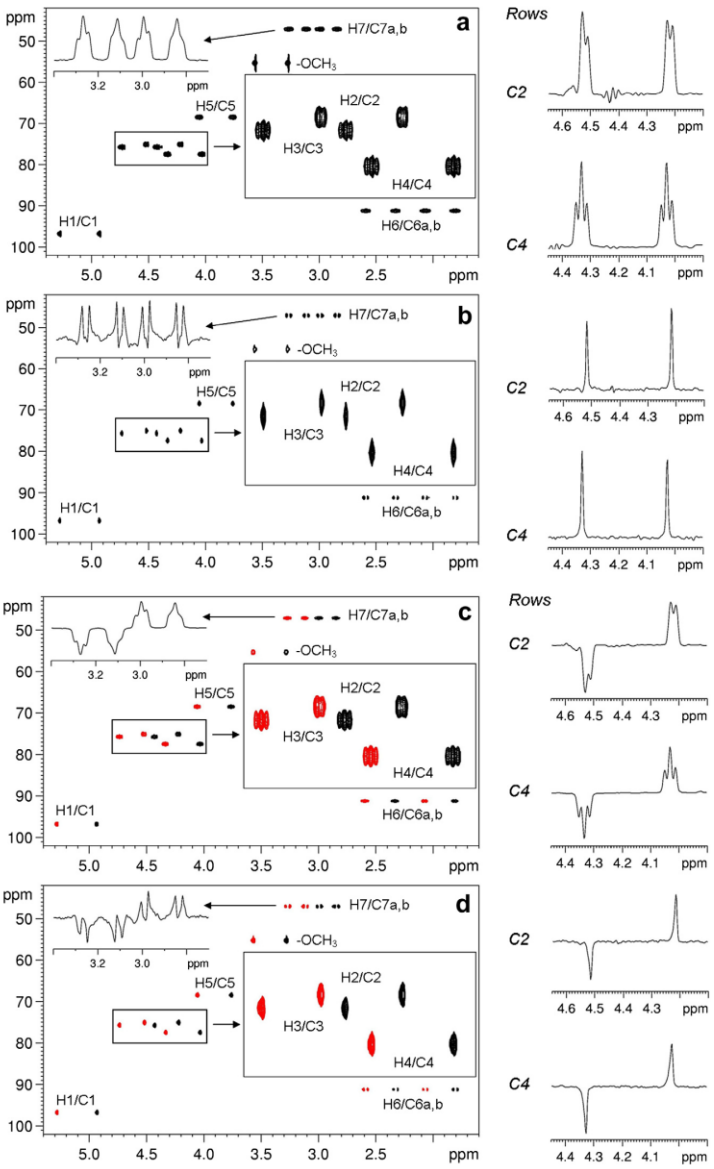

Fig. 3. Representative CLIP- and CLAP-HSQC spectra recorded with the conventional sequences [10] (a and c) and the new broadband proton-decoupled sequences of Fig. 1 (b and d) on an isotropic sample of compound **2** dissolved in D_2O. The carbon traces shown next to the corresponding spectra illustrate the characteristic differences in multiplet structure observed in the different experiments. Spectra were recorded at 300 K with spectral width in ^{13}C (^1H) dimension = 65.0 (4.9887) ppm, relaxation delay = 1.7 s, number of t_1 increments = 200, number of scans = 64 using the conventional CLIP/CLAP-HSQC sequences. The broadband decoupled spectra were collected with number of scans = 4, number of t_2 increments (i.e. number of FID chunks) = 16, duration of FID chunk = 20.842 ms, number of data points of constructed FID in ^1H dimension = 1664 complex data points.

undesired residual dispersive coherences arising from the mismatch between delays and $^1J_{CH}$.

Applications of the broadband proton-decoupled CLIP/CLAP-HSQC experiments of Fig. 1 under isotropic and partially orienting sample conditions are demonstrated using model compound **2** (Scheme 1). A comparison between CLIP- and CLAP-HSQC spectra acquired with the conventional sequence [10] and the broadband decoupled sequence of Fig. 1 is given in Fig. 3. The selected carbon traces presented at the right hand side of the corresponding spectra nicely demonstrate that the decoupled experiments result in collapsed proton multiplets for XH spin systems. The pure absorptive in- or antiphase doublets, with splittings due solely to the desired one-bond couplings, allow the direct and accurate determination of the scalar coupling constants.

To investigate their potential use for RDC measurement, we have also tested the performance of the new sequences on the same model compound (**2**) but this time dissolved in a weakly-orienting liquid crystalline phase of ether/alcohol mixture,

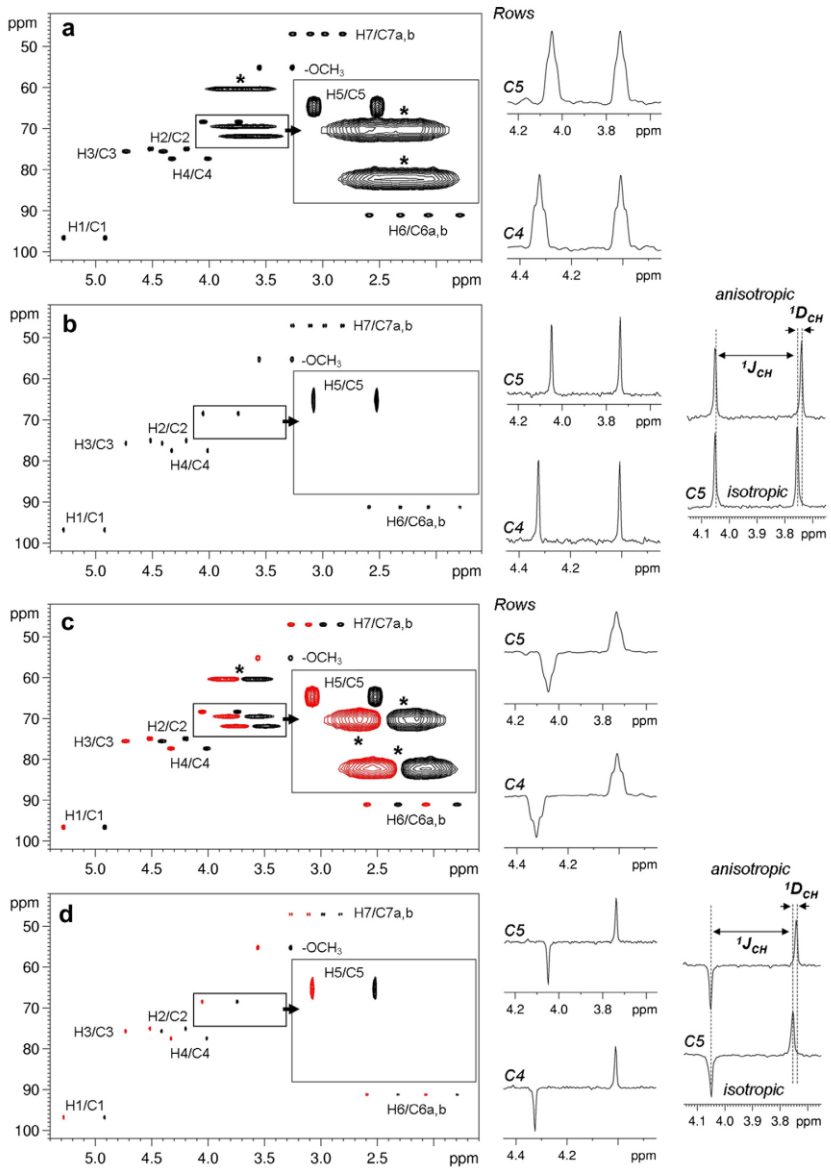

Fig. 4. Representative CLIP- and CLAP-HSQC spectra recorded with the conventional sequences [10] (a and c) and the broadband proton-decoupled sequences of Fig. 1 (b and d) on an anisotropic sample of compound **2** dissolved in the weakly-orienting phase Otting media [11]. The high quality of the spectra and of the carbon traces extracted confirm that the good performance of the experiments is maintained under anisotropic condition, ensuring the accuracy of dipolar contributions measured from the splittings, as shown for representative multiplets of C5. (*Note:* We use the convention of total coupling constant ($^1J_{XH} + {}^1D_{XH}$) throughout the text.) Spectra were recorded at 300 K with spectral widths in ^{13}C (^1H) dimension = 65.0 (6.0371) ppm, relaxation delay = 1.7 s, number of t_1 increments = 200, number of scans = 64 using the conventional CLIP/CLAP-HSQC sequences. The broadband decoupled spectra were collected with number of scans = 8, number of t_2 increments (i.e. number of FID chunks) = 16, duration of FID chunk = 21.197 ms, number of data points of constructed FID in ^1H dimension = 2048 complex data points.

as proposed by Rückert and Otting [11]. The high quality of the spectra and the selected carbon traces, with pure absorptive in- or antiphase doublets, shown in Fig. 4 demonstrates the good performance of these experiments, and promises the reliable measurement of RDCs, as exemplified for selected multiplets of C5.

It should be mentioned here that the undesired extra signals marked by asterisks (*) in Fig. 4, which arise from the weakly orienting phase in the anisotropic sample, show considerably reduced intensity in the broadband proton-decoupled spectra, but this is simply due to T_2 relaxation during the extended acquisition scheme of the decoupled sequences.

It is also important to note that following the IPAP-approach, as proposed earlier [16] (that is, adding and subtracting CLIP- and CLAP-HSQC spectra) allows quantitative extraction of one-bond coupling constants even in the case of complete overlap of α and β components of different doublets.

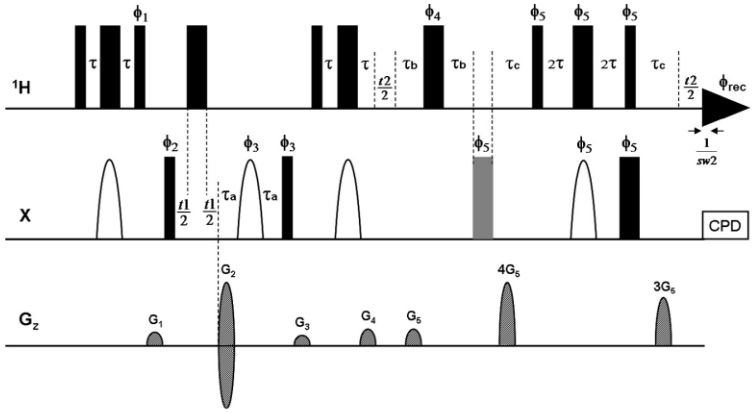

Fig. 5. Scheme of the broadband proton-decoupled (pure shift) HSQC (PS-HSQC) experiment. Narrow and wide filled bars correspond to 90° and 180° pulses, respectively, with phase *x* unless indicated otherwise. Smoothed chirp inversion and refocusing X pulses are shown as half-ellipses. Phases are $\varphi_1 = y$; $\varphi_2 = x, -x$; $\varphi_3 = x, x, -x, -x$; $\varphi_4 = y, y, y, y, y, y, -x, -x, -x, -x, -x, -x, -x, -x$; $\varphi_5 = y, y, y, y, -x, -x, -x, -x$; and $\varphi_{rec} = x, -x, -x, x, -x, x, x, -x, -x, x, x, -x, x, -x, -x, x$. Delays are set as follows: $\tau = 1/(4 * {}^1J_{XH})$, $\tau_a = p16 + d16$, $\tau_b = 1/(4 * sw2)$, $\tau_c = p16 + d16 + 350$ μs. Coherence order selection and echo–antiecho phase sensitive detection in the X-dimension are achieved with gradient pulses G_2 and G_4 in the ratio 80:20.1 for ^{13}C and 80:8.1 for ^{15}N, respectively. Purging gradient pulses G_1, G_3 are set to 15%, 11% of maximum gradient strength (50 G/cm), typically with 1 ms duration (*p16*) followed by a recovery delay *d16* = 50 μs. Coherence selection gradient pulses are used in the extra proton-decoupled dimension with G_5 = 18%. An additional carbon 180° pulse (shown in gray) is employed to refocus the evolution of one-bond heteronuclear coupling between FID chunks. CPD decoupling is turned on during detection.

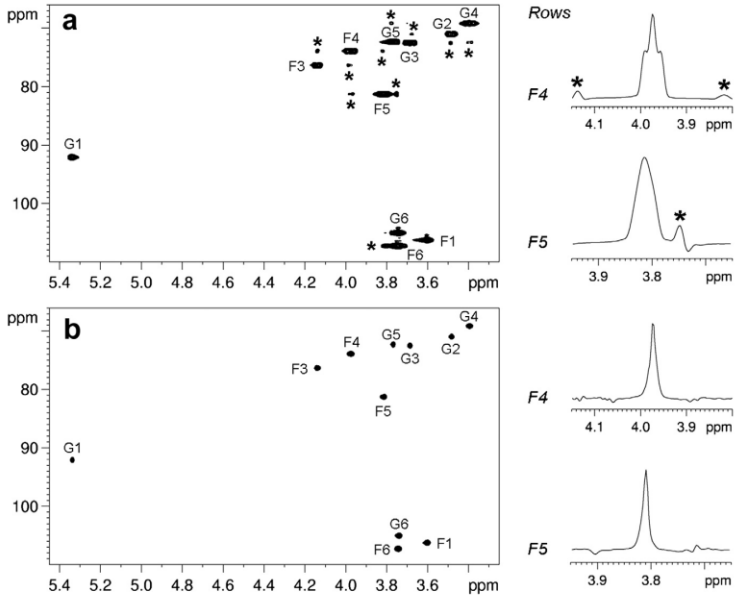

Fig. 6. Comparison of HSQC spectra recorded without (a) and with (b) broadband proton decoupling for D-sucrose dissolved in D_2O (30 mg/500 μl). Long-range correlation artifacts resulting from strong coupling effects observed in spectrum (a) acquired with the standard gradient enhanced HSQC sequence are labeled with asterisks (*) in both the correlation map and the selected carbon traces. In the broadband decoupled spectrum (b) these artifacts are almost entirely suppressed, resulting in a high quality pure shift correlation map with collapsed proton multiplet structure, suitable for automated spectral analysis. Spectra were recorded with spectral widths in ^{13}C (^1H) dimension = 45.0 (6.0371) ppm, relaxation delay = 1.7 s, number of t_1 increments = 180. Number of scans = 32 was used with the conventional HSQC sequence. The broadband decoupled spectrum was collected with number of scans = 2, number of t_2 increments (i.e. number of FID chunks) = 16, duration of FID chunk = 21.197 ms, number of data points of constructed FID in ^1H dimension = 2048 complex data points.

3.2. Broadband proton-decoupled, pure shift HSQC experiment

With a slight modification of the CLIP-HSQC sequence described above, a new method for generating broadband proton-decoupled (pure shift) HSQC (PS-HSQC) spectra is proposed. Such spectra have hitherto required a different experimental approach [24].

The PS-HSQC sequence depicted in Fig. 5 starts with the CLIP-HSQC block of the sequence in Fig. 1, but here the last purging carbon 90° pulse (which becomes superfluous when X-decoupling is used during detection) is omitted. In addition, the acquisition scheme detailed in the previous section is extended with two elements: (1) an appropriately-positioned carbon inversion 180°

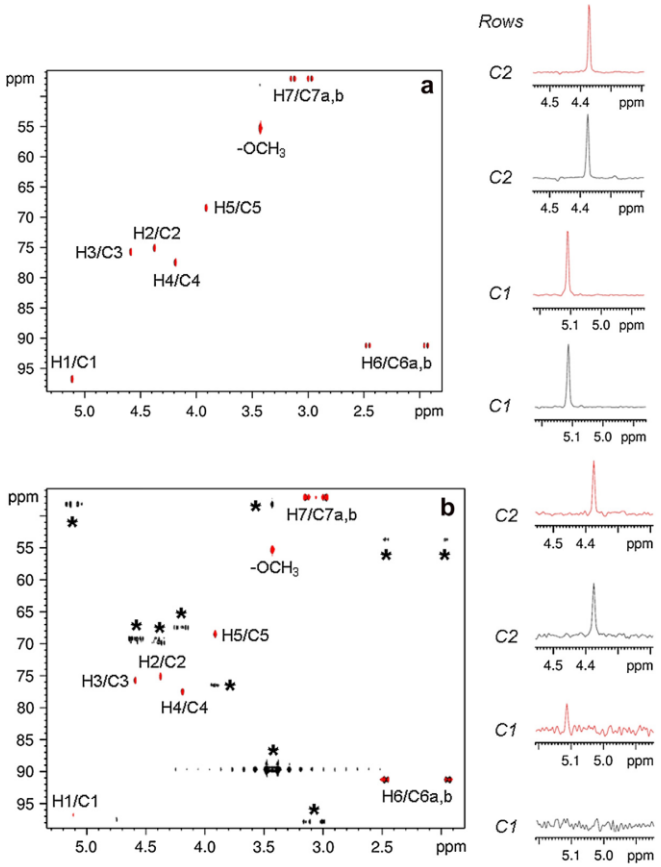

Fig. 7. Comparison of HSQC spectra recorded with the present (red lines) and earlier reported [24] (black lines) broadband proton-decoupled sequences for an isotropic sample of compound **2**. Experiments were performed with the same experimental parameters and data acquisition scheme, and the same data processing was used. To compare the sensitivity and robustness of sequences, spectra were collected with INEPT/BIRD delays adjusted to nominal $^1J_{XH}$ values of 145 Hz (a) and 100 Hz (b) (deliberately misset), respectively. The intensities of the signals in the spectra displayed are normalized, allowing proper comparison of sensitivity and of artifact (marked by ∗) amplitudes. Spectra were recorded with spectral widths in ^{13}C (^1H) dimension = 65.0 (4.9887) ppm, relaxation delay = 1.7 s, number of t_1 increments = 200, number of scans = 2, number of t_2 increments (i.e. number of FID chunks) = 16, duration of FID chunk = 20.842 ms, number of data points of constructed FID in ^1H dimension = 1664 complex data points. (For interpretation of the references to color in this figure legend, the reader is referred to the web version of this article.)

pulse (shown in gray) is needed to refocus the evolution of one-bond heteronuclear coupling between the detected FID chunks; and (2) composite pulse X-decoupling is turned on during FID acquisition $s(t_3)$ to remove the undesired heteronuclear coupling interactions and so to obtain a fully decoupled, pure shift (PS) X–^{1}H correlation spectrum.

The beneficial features of the PS-HSQC sequence presented are illustrated in Fig. 6, which compares the HSQC spectra of D-sucrose and representative F_2 traces recorded with the standard non-decoupled and decoupled experiments. It is evident from the spectra presented that the removal of proton–proton splittings from X–^{1}H correlation spectra yields a considerable resolution improvement, making unambiguous spectral assignments and automated analyses feasible even in crowded spectra. The reduction of signal width due to proton–proton broadband decoupling, together with the pseudo-3D acquisition scheme employed, is particularly interesting for the collection of high resolution data. Specifically, in the PS-HSQC experiment presented, the resolution attainable in the direct dimension is not limited by the sample heating of X-decoupling during detection, but simply by the number of t_2 increments. Thus spectra with large numbers of t_2 increments, offering high resolution in F_2, can be collected even under the action of broadband heteronuclear decoupling.

An additional advantageous side-product of the BIRD$^{(d)}$ filter employed in the acquisition scheme presented is the efficient suppression of undesired long-range cross peaks arising from strong coupling effects, as demonstrated in Fig. 6. The strong coupling artifacts, marked by asterisk (∗) in the standard HSQC spectrum (Fig. 6a) and the corresponding carbon traces at F4, F5, are almost entirely suppressed in the PS-HSQC spectrum (Fig. 6b), yielding a high quality pure shift correlation map for further spectral analysis. Note that this beneficial purging feature of the BIRD module has been utilized earlier in the standard HSQC experiment [33,34].

To compare the sensitivity and robustness of the present pure shift HSQC experiment and the earlier method of Sakhaii et al. [24], HSQC spectra were recorded using the two pulse sequences with identical experimental parameters, but employing the same data acquisition scheme and processing, to ensure comparability. The signal intensities measured in the correlation spectra of Fig. 7 and illustrated by representative carbon traces at the right

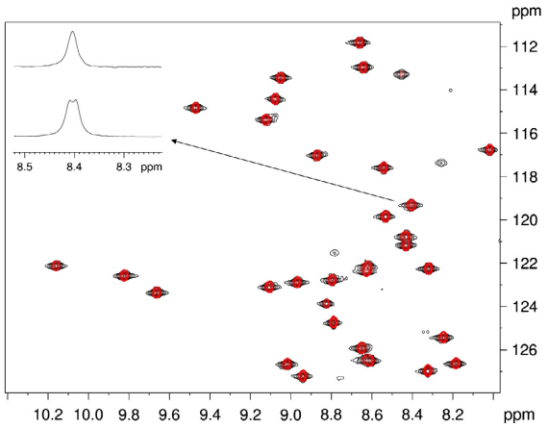

Fig. 8. Comparison of $^{1}H–^{15}N$ HSQC peak linewidths of PAF in spectra recorded without (black lines and lower trace at the left) and with (red lines and upper trace at the left) broadband proton decoupling. The advantage of the broadband decoupled sequence of Fig. 5 for macromolecules is demonstrated by the collapsed proton doublet structures, resulting in considerable reduction of the observed linewidth, and unequivocal peak definition for automated data analysis. Spectra were recorded with spectral widths in ^{15}N (^{1}H) dimension = 19.0 (4.9887) ppm, relaxation delay = 1.7 s, number of t_1 increments = 128. Number of scans = 64 was used with the conventional HSQC sequence. The broadband decoupled spectrum was collected with number of scans = 4, number of t_2 increments (i.e. number of FID chunks) = 16, duration of FID chunk = 21.245 ms, number of data points of constructed FID in ^{1}H dimension = 1696 complex data points. (For interpretation of the references to color in this figure legend, the reader is referred to the web version of this article.)

show that the sensitivity of the two experiments is comparable. Interestingly, the HSQC spectra recorded with intentionally mismatched INEPT/BIRD delays corresponding to $^{1}J_{XH}$ = 100 Hz show significant dissimilarity in the appearance of artifacts. The purging and coherence selection gradient scheme employed in the broadband proton-decoupled HSQC sequence of Fig. 5 seem to suppress the effects of the proportion of magnetization that does not experience perfect rotation by the BIRD$^{(d)}$ module with high efficiency, yielding clean and artifact-free spectra even for a wide range of BIRD delays and hence for a wide range of one-bond coupling constants.

As noted earlier, the basic BIRD approach to broadband homonuclear decoupling is not able to suppress the effects of geminal couplings. Thus in Figs. 3 and 4 the F_2 multiplets corresponding to CH_2 groups with non-equivalent (diastereotopic) geminal protons are doublets of doublets, with both $^{1}J_{CH}$ and $^{2}J_{HH}$ splittings. Example traces extracted at carbon C7 for compound **2** in Fig. 3 also illustrate this characteristic multiplet structure of CH_2 moieties. A method for the suppression of these undesired splittings will be the subject of a later publication.

In order to study the improvements in resolution that can be achieved for macromolecules, a $^{1}H–^{15}N$ HSQC experiment incorporating the proposed broadband proton decoupling scheme during acquisition was carried out on a ^{15}N-labeled, 55 amino acid residue, *Penicillium* antifungal protein (PAF) [35,36]. As expected, decoupling of proton–proton interactions yields a significant decrease in F_2 linewidths (illustrated in Fig. 8), allowing direct and accurate measurements of NH chemical shifts and of cross-peak intensities from the broadband decoupled singlets using automated peak picking.

4. Conclusions and future outlook

The broadband proton-decoupled CLIP/CLAP-HSQC experiments proposed here allow direct and accurate measurement of one-bond heteronuclear coupling constants and their dipolar contributions in XH moieties, and greatly simplified measurements in XH_2. The coupling constants can be determined directly, by measuring the splitting of pure absorptive in- or antiphase F_2 doublets, or by measuring the frequency difference between the relevant α and β multiplet components in the edited (added and subtracted) IPAP spectra. The latter approach allows the extraction of one-bond couplings even in the case of complete overlap of multiplet components. The robustness of the decoupled sequences presented with respect to variation in $^{1}J_{XH}$ ensures their applicability for RDC measurement, where wide distributions of ($^{1}J_{XH}$ + $^{1}D_{XH}$) are common.

We acknowledge work going in a similar direction by the group of Luy (T. Reinsperger, B. Luy, J. Magn. Reson. (submitted in parallel) [37]).

Modification of HSQC-based relaxation sequences, such as T_1, T_2, NOE, cross-correlated relaxation and relaxation dispersion experiments, to use the pure shift approach presented is in progress, with the promise of considerable benefits in the automated analysis of the resulting pure shift HSQC spectra.

Acknowledgments

The authors thank Sára Balla for her skilful technical assistance in preparation of anisotropic samples. Dr. Gyula Batta and Dr. Mihály Herczeg are acknowledged for their generous gifts of ^{15}N-labeled PAF and the monosaccharide sample, respectively. Financial support from TÁMOP-4.2.2/A-11/1/KONV-2012-0025 and OTKA K 105459 (to K.E.K), from Richter Gedeon Talentum Alapítvány (Ph.D. scholarship to I.T.), from ERC starting Grant No. 257041 (to C.M.T.), from the Merck Society for Arts and Science Foundation (Ph.D. scholarship to L.K.), and from the Engineering and Physical Sciences Research Council (Grant Numbers EP/I007989 and EP/H024336) is gratefully acknowledged. The research of István Timári was supported by the European Union and the State of Hungary, co-financed by the European Social Fund in the framework of TÁMOP 4.2.4. A/2-11-1-2012-0001 'National Excellence Program'.

References

[1] E. de Alba, N. Tjandra, NMR dipolar couplings for the structure determination of biopolymers in solution, Prog. Nucl. Magn. Reson. Spectrosc. 40 (2002) 175–197.
[2] A. Bax, Weak alignment offers new NMR opportunities to study protein structure and dynamics, Protein Sci. 12 (2003) 1–16.
[3] J.H. Prestegard, C.M. Bougault, A.I. Kishore, Residual dipolar couplings in structure determination of biomolecules, Chem. Rev. 104 (2004) 3519–3540.
[4] M. Blackledge, Recent progress in the study of biomolecular structure and dynamics in solution from residual dipolar couplings, Prog. Nucl. Magn. Reson. Spectrosc. 46 (2005) 23–61.
[5] J.R. Tolman, K. Ruan, NMR residual dipolar couplings as probes of biomolecular dynamics, Chem. Rev. 106 (2006) 1720–1736.
[6] C.M. Thiele, Residual dipolar couplings (RDCs) in organic structure determination, Eur. J. Org. Chem. 2008 (2008) 5673–5685.
[7] G. Kummerlöwe, B. Luy, Residual dipolar couplings for the configurational and conformational analysis of organic molecules, in: Annual Reports on NMR Spectroscopy, Academic Press, 2009, pp. 193–232 (Chapter 4).
[8] B. Böttcher, C.M. Thiele, Determining the Stereochemistry of Molecules from Residual Dipolar Couplings (RDCs), eMagRes. http://dx.doi.org/10.1002/9780470034590.emrstm1194.
[9] B. Böttcher, V. Schmidts, J.A. Raskatov, C.M. Thiele, Determination of the conformation of the key intermediate in an enantioselective palladium-catalyzed allylic substitution from residual dipolar couplings, Angew. Chem., Int. Ed. 49 (2010) 205–209.
[10] A. Enthart, J.C. Freudenberger, J. Furrer, H. Kessler, B. Luy, The CLIP/CLAP-HSQC: pure absorptive spectra for the measurement of one-bond couplings, J. Magn. Reson. 192 (2008) 314–322.
[11] M. Rückert, G. Otting, Alignment of biological macromolecules in novel nonionic liquid crystalline media for NMR experiments, J. Am. Chem. Soc. 122 (2000) 7793–7797.
[12] C. Griesinger, O.W. Sørensen, R.R. Ernst, Practical aspects of the E.COSY technique. Measurement of scalar spin–spin coupling constants in peptides, J. Magn. Reson. 75 (1987) 474–492.

[13] P. Andersson, A. Annila, G. Otting, An α/β-HSQC-α/β experiment for spin-state selective editing of IS cross peaks, J. Magn. Reson. 133 (1998) 364–367.
[14] P. Andersson, J. Weigelt, G. Otting, Spin-state selection filters for the measurement of heteronuclear one-bond coupling constants, J. Biomol. NMR 12 (1998) 435–441.
[15] F. Cordier, A.J. Dingley, S. Grzesiek, A doublet-separated sensitivity-enhanced HSQC for the determination of scalar and dipolar one-bond J-couplings, J. Biomol. NMR 13 (1999) 175–180.
[16] M. Ottiger, F. Delaglio, A. Bax, Measurement of *J* and dipolar couplings from simplified two-dimensional NMR spectra, J. Magn. Reson. 131 (1998) 373–378.
[17] K. Pervushin, R. Riek, G. Wider, K. Wüthrich, Attenuated T_2 relaxation by mutual cancellation of dipole–dipole coupling and chemical shift anisotropy indicates an avenue to NMR structures of very large biological macromolecules in solution, Proc. Natl. Acad. Sci. U. S. A. 94 (1997) 12366–12371.
[18] M. Czisch, R. Boelens, Sensitivity enhancement in the TROSY experiment, J. Magn. Reson. 134 (1998) 158–160.
[19] J. Weigelt, Single scan, sensitivity- and gradient-enhanced TROSY for multidimensional NMR experiments, J. Am. Chem. Soc. 120 (1998) 10778–10779.
[20] K. Fehér, S. Berger, K.E. Kövér, Accurate determination of small one-bond heteronuclear residual dipolar couplings by F1 coupled HSQC modified with a G-BIRD$^{(r)}$ module, J. Magn. Reson. 163 (2003) 340–346.
[21] C.M. Thiele, W. Bermel, Speeding up the measurement of one-bond scalar (^1J) and residual dipolar couplings (^1D) by using non-uniform sampling (NUS), J. Magn. Reson. 216 (2012) 134–143.
[22] K. Zangger, H. Sterk, Homonuclear broadband-decoupled NMR spectra, J. Magn. Reson. 124 (1997) 486–489.
[23] M. Nilsson, G.A. Morris, Pure shift proton DOSY: diffusion-ordered 1H spectra without multiplet structure, Chem. Commun. (2007) 933–935.
[24] P. Sakhaii, B. Haase, W. Bermel, Experimental access to HSQC spectra decoupled in all frequency dimensions, J. Magn. Reson. 199 (2009) 192–198.
[25] J.A. Aguilar, S. Faulkner, M. Nilsson, G.A. Morris, Pure shift 1H NMR: a resolution of the resolution problem?, Angew Chem., Int. Ed. 49 (2010) 3901–3903.
[26] G.A. Morris, J.A. Aguilar, R. Evans, S. Haiber, M. Nilsson, True chemical shift correlation maps: a TOCSY experiment with pure shifts in both dimensions, J. Am. Chem. Soc. 132 (2010) 12770–12772.
[27] J.A. Aguilar, M. Nilsson, G.A. Morris, Simple proton spectra from complex spin systems: pure shift NMR spectroscopy using BIRD, Angew. Chem., Int. Ed. 50 (2011) 9716–9717.
[28] J.A. Aguilar, A.A. Colbourne, J. Cassani, M. Nilsson, G.A. Morris, Decoupling two-dimensional NMR spectroscopy in both dimensions: pure shift NOESY and COSY, Angew. Chem., Int. Ed. 51 (2012) 6460–6463.
[29] A. Lupulescu, G.L. Olsen, L. Frydman, Toward single-shot pure-shift solution 1H NMR by trains of BIRD-based homonuclear decoupling, J. Magn. Reson. 218 (2012) 141–146.
[30] N.H. Meyer, K. Zangger, Simplifying proton NMR spectra by instant homonuclear broadband decoupling, Angew. Chem., Int. Ed. 52 (2013) 7143–7146.
[31] L. Paudel, R.W. Adams, P. Király, J.A. Aguilar, M. Foroozandeh, M.J. Cliff, M. Nilsson, P. Sándor, J.P. Waltho, G.A. Morris, Simultaneously enhancing spectral resolution and sensitivity in heteronuclear correlation NMR spectroscopy, Angew. Chem., Int. Ed. (2013), http://dx.doi.org/10.1002/anie.201305709.
[32] J.R. Garbow, D.P. Weitekamp, A. Pines, Bilinear rotation decoupling of homonuclear scalar interactions, Chem. Phys. Lett. 93 (1982) 504–509.
[33] V. Rutar, T.C. Wong, W. Guo, Manipulated heteronuclear two-dimensional NMR bilinear pulses in the presence of strong coupling, J. Magn. Reson. 64 (1985) 8–19.
[34] G.V.T. Swapna, R. Ramachandran, N. Reddy, A.C. Kunwar, Virtual coupling effects in heteronuclear chemical-shift correlation spectroscopy, J. Magn. Reson. 88 (1990) 135–140.
[35] G. Batta, T. Barna, Z. Gáspári, S. Sándor, K.E. Kövér, U. Binder, B. Sarg, L. Kaiserer, A.K. Chhillar, A. Eigentler, É. Leiter, N. Hegedüs, I. Pócsi, H. Lindner, F. Marx, Functional aspects of the solution structure and dynamics of PAF – a highly-stable antifungal protein from *Penicillium chrysogenum*, FEBS J. 276 (2009) 2875–2890.
[36] G. Váradi, G.K. Tóth, Z. Kele, L. Galgóczy, Á. Fizil, G. Batta, Synthesis of PAF, an antifungal protein from *P. chrysogenum*, by native chemical ligation: native disulfide pattern and fold obtained upon oxidative refolding, Chem. – Eur. J. 19 (2013) 12684–12692.
[37] T. Reinsperger, B. Luy, Homonuclear BIRD-decoupled spectra for measuring one-bond couplings with highest resolution: CLIP/CLAP-RESET and constant-time-CLIP/CLAP-RESET, J. Magn. Reson. (2013), this issue, http://dx.doi.org/10.1016/j.jmr.2013.11.015.

7.3. Development of CLIP- and CLAP-HSQC Experiments with perfectBIRD decoupling

The previous section illustrates the advantages of using F_2-BIRD decoupling in CLIP/CLAP-HSQC experiments for high accuracy measurements of one-bond RDCs: The lineshape of signals can be significantly simplified in the proton dimension facilitating the extraction of one-bond couplings, in particular for weakly aligned samples.

A major limitation of this experiment, which is common to experiments using BIRD for decoupling in proton-dimensions, is the fact that BIRD-decoupling is not able to introduce a decoupling of the geminal $^2J_{HH}$ coupling of diastereotopic methylene protons[251, 254, 267]. This would not be largely distracting in the context of RDC measurements, if the remaining homonuclear decoupling would lead to a pure-phase doublet of doublets appearance of the resulting spectra. However, as was illustrated in the previous section for the protons H7a+b of **3**, the remaining coupling leads to a quite unfavourable mixed-phase appearance for these signals, which also interferes with coupling constant extraction[343].

An alike problem was first considered a nuisance in applications of BIRD to F_1 broadband decoupling of HETCOR experiments[302], when BIRD was proposed as an alternative to constant time decoupling[36, 224]. While full homonuclear decoupling could be observed at tertiary carbon positions and for methyl groups, in these spectra a doublet appearance remained for methylene groups. Obviously, we were facing the exact same challenge in the F_2-BIRD CLIP/CLAP-HSQC experiments described in the previous section.

To solve this problem, it was proposed for HETCOR experiments to introduce BIRD-decoupling into experiments with constant time evolutions in the proton dimension[228, 229], a strategy later also adopted by REINSPERGER and LUY in their constant-time CLIP/CLAP-RESET experiment[342]. Such experiments are able to provide full homonuclear decoupling in the proton dimension, yet suffer from the problems inherent in constant time experiments: The limited resolution accessible, the strong signal attenuation through relaxation over the constant time period and the possible modulation of the signal intensities by the geminal couplings, if the constant time period cannot be matched to all $^2T_{HH}$ coupling constants simultaneously. Both the compromise between relaxation losses and accessible resolution and the requirement for matching the constant time delay to all $^2T_{HH}$ are circumvented in the technique that is described in the following. In particular in the context of RDC-extraction this is favourable, as transverse relaxation is faster than in isotropic solution and because $^2T_{HH}$ coupling constants may often vary strongly.

It was at a very early stage of the investigations described in the previous section, that I came up with a practical solution to the problem of remaining geminal coupling evolution in methylene groups, which does not use the constant-time strategy. The perfectBIRD homonuclear decoupling technique[213] I developed enables full homonuclear decoupling of methylene groups, while also retaining decoupling of all vicinal or longer-range homonuclear couplings. Thereby it does not require a tuning of the experiment settings to $^2T_{HH}$ couplings and in addition is less affected by relaxation, than the constant-time approach, which makes it well suitable for RDC measurements.

In the following, the working principle of the technique is described (section 7.3.1). Subsequently it is demonstrated, that F_2-perfectBIRD decoupled CLIP/CLAP-HSQCs enable highly precise and accurate one-bond RDC measurements for small molecule studies (section 7.3.2). In addition, in Project C (chapter 8) the use of this technique in applications where signal dispersion normally is insufficient is demonstrated.

7.3.1. Working principle of perfectBIRD homonuclear decoupling

It is described, that BIRD decoupling[251] is able to introduce virtual decoupling of protons ($^1H^d$; d is for "direct") that are directly attached to a heteronucleus (typically ^{13}C or ^{15}N) from protons that are not ($^1H^r$; r is for "remote") by inversion of only one of the groups of protons half-way through a delay. For

detection, couplings between the two groups of protons are masked by refocusing of the coupling evolution at the end of the delay. The two groups of spins, $^1H^d$ and $^1H^r$, are thereby discriminated from each other by their respective heteronuclear coupling, which is much larger for all $^1H^d$, than it is for all $^1H^r$. For organic molecules containing ^{13}C as the heteronucleus we typically find $^1J_{CH} > 110$ Hz, but $|^{n\geq2}J_{CH}| < 15$ Hz with one notable exception being terminal alkynes.
If we would like to fully decouple the protons observed in ^1H-^{13}C-HSQC experiments, which is the group of $^1H^d$, this can clearly only be achieved with the BIRD technique, if no couplings are observed between protons belonging to that group. In substances with natural-abundance ^{13}C content, this situation is frequently achieved if the ^{13}C-atoms only carry a single proton, because the likelihood of finding two ^{13}C atoms in close proximity is negligibly small. If, however two protons are directly bound to the same ^{13}C, the BIRD element will affect both protons in the same way, and in consequence geminal couplings continue to evolve undisturbed. Two exemplary isotopomers of (+)-isopinocampheol illustrating the situation are shown in Figure 7.3.

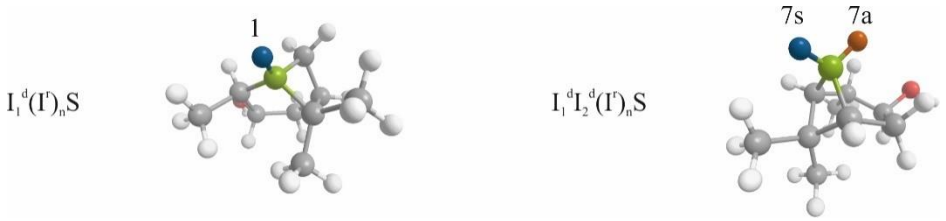

Figure 7.3: Two exemplary isotopomers of (+)-isopinocampheol carrying a single ^{13}C (marked in green) at different positions. ^{12}C positions are shown in dark grey. On the left, the ^{13}C is at a tertiary position (position 1), carrying a single $^1H^d$, marked in blue, surrounded by remotely attached protons (marked in light gray). On the right, the ^{13}C is at a secondary position (position 7), carrying two $^1H^d$ (marked in blue and orange). The case shown in the left represents an $I^d_1(I^r)_nS$ spin system, while the case represents an $I^d_1I^d_2(I^r)_nS$ spin system.

The solution strategy I proposed to refocus geminal couplings in methylene groups was inspired by previous investigations of the so-called “perfect echo” sequence[195-200]. This pulse sequence block was initially presented as a method to refocus both chemical shift evolution and weak coupling evolution simultaneously for a homonuclear two spin system[195]. The basic technique consists of two Hahn-echoes with a single 90°-flip pulse inserted in the middle (see Figure 7.4).

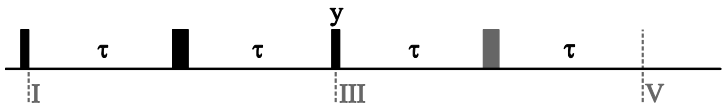

Figure 7.4: Simple perfect echo sequence. Narrow pulses are 90° pulses; wide pulses are 180° pulses. If not explicitly stated, pulses are applied with phase x. Labels for different timepoints (I, III and V) are introduced for convenience. N.b.: In the initial report[195] by TAKEGOSHI *et al.* a more general phase cycling scheme is presented and the sequence element between time points I and V is executed in looped fashion.

In contrast to the Hahn-echo which does refocus chemical shift evolution, but leads to an accumulation of coupling evolution throughout the echo, the perfect echo block is able to refocus both chemical shift evolution and weak coupling evolution at the end of the echo (V). I want to illustrate the effect in a simple product operator analysis[186]:
The analysis shall be carried out for a weakly coupled two-spin-1/2 system. The two spins I_1 and I_2 shall have Larmor frequencies which shall have an offset from the frequency of the rotating frame of Ω_1 and Ω_2, respectively and shall be weakly coupled by J_{12}. For interested readers, the product operator analysis was also carried out for larger weakly coupled spin systems by van Zijl *et al.*[196]. Further, Mulkern *et al.*

presented the analysis of the perfect echo element for a strongly coupled two-spin system[197], and its application to citrate imaging with PRESS-experiments.
We start analysis from a situation, where different initial z-magnetizations M_1 and M_2 may be present. Initial excitation generates coherence

$$M_1 I_{1,z} + M_2 I_{2,z} \xrightarrow{90°_x} -M_1 I_{1,y} - M_2 I_{2,y}, \tag{7.1}$$

which evolves throughout the first Hahn-echo period. To simplify the analysis, we take advantage of the knowledge, that Hahn-echoes introduce no net chemical shift evolution, but unperturbed J-coupling evolution. We therefore condense the propagator for the Hahn echo

$$\xrightarrow{\pi J_{12}\tau}\xrightarrow{\Omega_1\tau}\xrightarrow{\Omega_2\tau}\xrightarrow{180°_x}\xrightarrow{\Omega_2\tau}\xrightarrow{\Omega_1\tau}\xrightarrow{\pi J_{12}\tau} \tag{7.2}$$

to

$$\xrightarrow{\pi J_{12}2\tau}\xrightarrow{180°_x}, \tag{7.3}$$

the validity of which is well documented in literature[17] We propagate the previous result accordingly, to arrive at

$$\begin{aligned} &-M_1 I_{1,y} - M_2 I_{2,y} \xrightarrow{\pi J_{12}2\tau}\xrightarrow{180°_x} \\ &M_1\left[+\cos(\pi J_{12}2\tau)\, I_{1,y} - \sin(\pi J_{12}2\tau)\, 2I_{1,x}I_{2,z}\right] + M_2\left[+\cos(\pi J_{12}2\tau)\, I_{2,y} - \sin(\pi J_{12}2\tau)\, 2I_{2,x}I_{1,z}\right]. \end{aligned} \tag{7.4}$$

Subsequent rotation by the 90°$_y$-pulse at time point III introduces a mixing, as well as a sign change for the anti-phase coherences.

$$\begin{aligned} &\xrightarrow{90°_y} \\ &M_1\left[+\cos(\pi J_{12}2\tau)\, I_{1,y} + \sin(\pi J_{12}2\tau)\, 2I_{1,z}I_{2,x}\right] + M_2\left[+\cos(\pi J_{12}2\tau)\, I_{2,y} + \sin(\pi J_{12}2\tau)\, 2I_{2,z}I_{1,x}\right] \end{aligned} \tag{7.5}$$

Again, the result is subject to a Hahn-echo element, which leads to

$$\begin{aligned} &\xrightarrow{\pi J_{12}2\tau}\xrightarrow{180°_x} \\ &M_1\left[-\cos(\pi J_{12}2\tau)\cos(\pi J_{12}2\tau)\, I_{1,y} + \cos(\pi J_{12}2\tau)\sin(\pi J_{12}2\tau)\, 2I_{1,x}I_{2,z}\right. \\ &\qquad\left. - \sin(\pi J_{12}2\tau)\cos(\pi J_{12}2\tau)\, 2I_{1,z}I_{2,x} - \sin(\pi J_{12}2\tau)\sin(\pi J_{12}2\tau)\, I_{2,y}\right] \\ &+M_2\left[-\cos(\pi J_{12}2\tau)\cos(\pi J_{12}2\tau)\, I_{2,y} + \cos(\pi J_{12}2\tau)\sin(\pi J_{12}2\tau)\, 2I_{2,x}I_{1,z}\right. \\ &\qquad\left. - \sin(\pi J_{12}2\tau)\cos(\pi J_{12}2\tau)\, 2I_{2,z}I_{1,x} - \sin(\pi J_{12}2\tau)\sin(\pi J_{12}2\tau)\, I_{1,y}\right] \end{aligned} \tag{7.6}$$

$$\begin{aligned} &= \\ &-I_{1,y}\frac{1}{2}(M_1[1+\cos(\pi J_{12}4\tau)] + M_2[1-\cos(\pi J_{12}4\tau)]) \\ &-I_{2,y}\frac{1}{2}(M_1[1-\cos(\pi J_{12}4\tau)] + M_2[1+\cos(\pi J_{12}4\tau)]) \\ &+2I_{1,x}I_{2,z}\frac{1}{2}(M_1\sin(\pi J_{12}4\tau) - M_2\sin(\pi J_{12}4\tau)) \\ &+2I_{1,z}I_{2,x}\frac{1}{2}(-M_1\sin(\pi J_{12}4\tau) + M_2\sin(\pi J_{12}4\tau)). \end{aligned} \tag{7.7}$$

For rearrangement, I used the identities

$$\cos(x)\cos(y) = \frac{1}{2}[\cos(x-y) + \cos(x+y)] \tag{7.8}$$

$$\sin(x)\sin(y) = \frac{1}{2}[\cos(x-y) - \cos(x+y)] \tag{7.9}$$

$$\sin(x)\cos(y) = \frac{1}{2}[\sin(x-y) + \sin(x+y)] \tag{7.10}$$

In equation (7.7), the two inphase terms $I_{1,y}$ and $I_{2,y}$ have exchanged magnetization throughout the perfect echo element, with the amount of magnetization that is transferred oscillating with the frequency $\pi J_{12} 4\tau$. The exchange of magnetization between these two in-phase terms with differing initial magnetizations M_1 and M_2 that is introduced by the perfect echo will be exploited in Project D to generate COSY-like spectra with full in-phase character (chapter 9). The two initial magnetizations M_1 and M_2 will be modulated by a different chemical shift evolution period t_1, that will precede the perfect echo element. In contrast, the perfectBIRD decoupling scheme described in this chapter is restricted to cases in which the two initial magnetizations are approximately equal, even after t_1 labelling of the magnetization.

From (7.7) we see, that for the case $M_1 = M_2 = M$, the initial state $-M\,(I_{1,y} + I_{2,y})$ present before the echo (at time point I in Figure 7.4) is restored. Even though magnetization transfer has taken place, for this idealized analysis, the final coherence observed at instant 4τ is indistinguishable from the initial state with no net chemical shift or coupling evolution observable. To now introduce a net chemical shift evolution, without reintroducing the coupling evolution between the two spins, the simple modification that we have to do to the pulse sequence shown in Figure 7.4 is to omit the second 180° pulse (shown in grey). When using the result shown in equation (7.5) and carrying out the analysis for a free evolution period of 2τ, J-coupling evolution first restores equation (7.7) (with changes of sign introduced by the lack of the 180°-pulse)

$$
\begin{aligned}
(7.5) \xrightarrow{\pi J_{12} 2\tau} \\
& I_{1,y} \frac{1}{2}(M_1[1 + \cos(\pi J_{12} 4\tau)] + M_2[1 - \cos(\pi J_{12} 4\tau)]) \\
& + I_{2,y} \frac{1}{2}(M_1[1 - \cos(\pi J_{12} 4\tau)] + M_2[1 + \cos(\pi J_{12} 4\tau)]) \\
& - 2I_{1,x} I_{2,z} \frac{1}{2}(M_1 \sin(\pi J_{12} 4\tau) - M_2 \sin(\pi J_{12} 4\tau)) \\
& - 2I_{1,z} I_{2,x} \frac{1}{2}(-M_1 \sin(\pi J_{12} 4\tau) + M_2 \sin(\pi J_{12} 4\tau)),
\end{aligned}
\qquad (7.11)
$$

but in addition, introduce a chemical shift labelling during the second half of the modified perfect echo.

$$
\begin{aligned}
(7.11) \xrightarrow{\Omega_1 2\tau} \xrightarrow{\Omega_2 2\tau} \\
& \big(\cos(\Omega_1 2\tau)\, I_{1,y} - \sin(\Omega_1 2\tau)\, I_{1,x}\big) \frac{1}{2}(M_1[1 + \cos(\pi J_{12} 4\tau)] + M_2[1 - \cos(\pi J_{12} 4\tau)]) \\
& + \big(\cos(\Omega_2 2\tau)\, I_{2,y} - \sin(\Omega_2 2\tau)\, I_{2,x}\big) \frac{1}{2}(M_1[1 - \cos(\pi J_{12} 4\tau)] + M_2[1 + \cos(\pi J_{12} 4\tau)]) \\
& - \big(\cos(\Omega_1 2\tau)\, 2I_{1,x} I_{2,z} + \sin(\Omega_1 2\tau)\, 2I_{1,y} I_{2,z}\big) \frac{1}{2}(M_1 \sin(\pi J_{12} 4\tau) - M_2 \sin(\pi J_{12} 4\tau)) \\
& - \big(\cos(\Omega_2 2\tau)\, 2I_{1,z} I_{2,x} \cos(\Omega_2 2\tau)\, 2I_{1,z} I_{2,y}\big) \frac{1}{2}(-M_1 \sin(\pi J_{12} 4\tau) + M_2 \sin(\pi J_{12} 4\tau))
\end{aligned}
\qquad (7.12)
$$

In the ideal case of $M_1 = M_2 = M$ this simplifies to

$$
\big(\cos(\Omega_1 2\tau)\, I_{1,y} - \sin(\Omega_1 2\tau)\, I_{1,x}\big) M + \big(\cos(\Omega_2 2\tau)\, I_{2,y} - \sin(\Omega_2 2\tau)\, I_{2,x}\big) M. \qquad (7.13)
$$

By this simple modification to the perfect echo experiment, it is therefore possible to create a pulse sequence element that fully refocuses coupling evolution, but that introduces chemical shift labelling. With this at hand, this simple sequence should be able to provide homonuclear decoupling of the two spins. The analysis of spin systems with more than one coupling partners that VAN ZIJL *et al.* provided clearly shows that this effect breaks down for more than two homonuclear coupling partners, due to the presence of coherences such as $4I_{1,y}I_{2,z}I_{3,z}$ during the application of the central mixing pulse, which are not refocused after 4τ.

The demonstration, that indeed pure shift spectra with high sensitivity can be acquired with this strategy for homonuclear two spin systems is given in Figure 7.5. This is something that, to my best knowledge has not been presented at the time of the investigation. For 2,3-Dibromothiophene **5**, pure shift proton spectra could be collected with this technique.

The technique offers very high sensitivity, however the restriction to only two spin systems is such a severe one, that in practice very few applications may be conceivable. As soon as three or more spins are coupling, the homonuclear decoupling method fails (even if coupling partners are magnetically equivalent). It should further be noted, that, as chemical shift evolution is only accumulated during the second half of the echo, contributions of transverse relaxation to the linewidths observed are doubled. For partial homonuclear decoupling in low-resolution indirect dimensions however, an analogue homonuclear decoupling scheme recently has been presented by BAISHYA and VERMA[350].

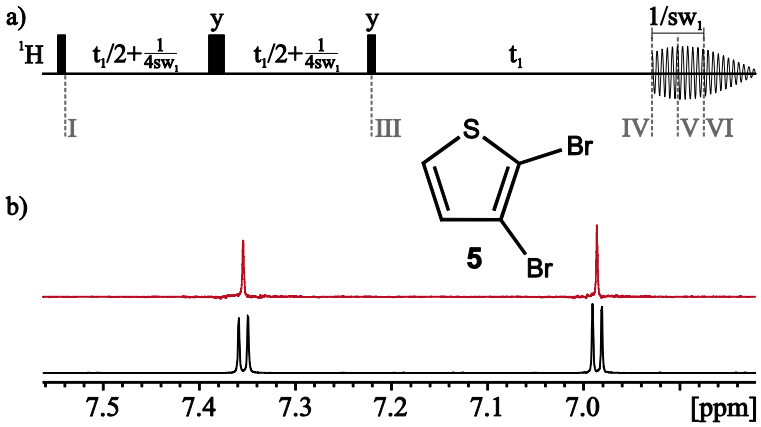

Figure 7.5: Experimental demonstration of the perfect echo based homonuclear decoupling for a two spin system. a) Interferogram-based perfect echo homonuclear decoupling experiment with timing adjusted to refocus homonuclear decoupling in the middle of the data chunk used for processing (from IV to VI). The length of the data chunk used amounts to the increment of t_1, $1/sw_1$. b) ^1H spectra of 2,3-Dibromothiophene (**5**) in CD_2Cl_2. Top: Pure shift ^1H Spectrum acquired with the pulse sequence shown in a) using an interferogram-based approach. Bottom: Conventional single-scan ^1H spectrum. Full experimental details are given in the appendices (14.1.2).

Homonuclear decoupling sequences that are only applicable to de-facto two-spin-1/2 systems, such as the methylene groups in citrate[197] or those of benzyl-groups, obviously may only be of interest in very specialized applications.

When working on the F_2-BIRD CLIP/CLAP-HSQCs described in section 7.2, I realized, that a combination of BIRD decoupling and the perfect echo approach would be highly interesting, because the two homonuclear decoupling techniques are somewhat complementary to each other: For organic molecules in isotropic solution, the BIRD-method is able to refocus all homonuclear couplings but the $^2J_{HH}$-couplings in diastereotopic methylene groups. Thus BIRD decoupling can modify the coupling evolution of even complex spin systems to mimic that of systems with maximum two coupling spins. Coupling evolution between two coupling partners however can be reversed by the modified perfect echo scheme of Figure 7.5 a), as shown above, without introducing additional signal loss (if relaxation is neglected). Thus inserting BIRD elements halfway through the t_1-evolution periods of the perfect echo homonuclear decoupling scheme shown was conceived as a practical solution for full F_2-homonuclear decoupling using the resulting "perfectBIRD" decoupling scheme.

Two conceptual pulse sequences for acquiring ^1H-spectra with perfectBIRD decoupling (which in practice would require additional $^1H^r$-suppression) are shown in Figure 7.6. Please note that these experiments have never been implemented and just serve the purpose of illustrating the basic concepts used later.

Figure 7.6 a) shows the direct analogue of Figure 7.5 a), where the 180°-pulse in the first half of the perfect echo was replaced by a BIRD^d pulse cascade[304]. As the BIRD^d element inverts $^1H^d$, but leaves $^1H^r$ and ^{13}C net unaffected in the ideal case, it acts on $^1H^d$ just like the 180°-pulse previously at that position,

but leads to a refocusing of weak homonuclear couplings to $^{1}H^{r}$ and to a refocusing of heteronuclear couplings between $^{1}H^{d}$ and ^{13}C. Due to the effect of this first BIRD element, even for a ^{13}C-centered methylene group in an extended (weakly coupled) spin network (such as that exemplified in the right of Figure 7.3), equation (7.4) describes the product operators present at time point III (if we set $\tau = t_1/2+1/(4sw_1)$). The simplification of the spin system evolution by refocusing long range homonuclear couplings ($^{n\geq3}J_{HH}$-couplings) introduced at time point III is of central importance for the experiment to work. Halfway through the second t_1-evolution period, a $BIRD^{r,X}$ element is inserted, which inverts $^{1}H^{r}$ and ^{13}C, but in effect does not invert the $^{1}H^{d}$ we aim to observe. At time point IV, therefore couplings to $^{1}H^{r}$ and ^{13}C are refocused again for $^{1}H^{d}$. Broadband decoupling during acquisition suppresses heteronuclear one-bond couplings during acquisition, which evolve much faster than ^{1}H-^{1}H-couplings.
One problem that arises is that with the timing used in Figure 7.6 a), $^{2}J_{HH}$-couplings are refocused at instant V, while all other homonuclear couplings are refocused at IV. Already for our work on F_2-BIRD CLIP/CLAP-HSQC spectra, we therefore used an implementation with an additional ^{1}H-180° pulse, which enables refocusing of $^{n\geq3}J_{HH}$-couplings at V, in the middle of the acquired data chunk. Refocusing of couplings in the middle of the acquired data chunk, as first used in DOSY experiments[253], enables the length of the data chunk sampled to be doubled at comparable artefact amplitude. For this reason, throughout most of this work, a modified timing, shown in Figure 7.6 b) and with $\Delta = 1/(4sw_1)$, was used. In the final implementations, additional delays were introduced surrounding both BIRD-elements (called τ_e in ref. [213]) to compensate for gradient pulses used and for switching from pulsing to acquisition.
For Project C (chapter 8), we also used a timing of the experiment introduced by WOLFGANG BERMEL, who suggested also an implementation with $\Delta = 0$ to be used, depending on the application. Setting $\Delta = 0$ refocuses homonuclear couplings at the beginning of the acquired data chunk, reducing the number of points per scan that can effectively be used for processing, but shortens the homonuclear decoupling element by 1.5 times the chunk length, which can be beneficial in terms of sensitivity. In addition, setting $\Delta = 0$ enables very short increments to be used for t_1, a choice that can be beneficial when applying the RESET processing strategy[254], he developed.
To achieve the proper timing required for homonuclear decoupling with these pulse sequences, a number of conditions have to be fulfilled, that will be explained in the following. Setting up the timing based on these simplifying phenomenological rules is a handy alternative to full product operator analysis of these rather lengthy homonuclear decoupling elements. The following conditions were used to create implementations that can be used for homonuclear decoupling:

1. No net $^{1}H^{d}$ chemical shift evolution is tolerated by the perfect echo at time point III. This is achieved in Figure 7.6 a) by using a $BIRD^{d}$ element. In all implementations used throughout, all delays between I and III will feature 180°-^{1}H pulses to make sure this condition is fulfilled, even in BIRD rotation is incomplete.
2. The net $^{1}H^{d}$ chemical shift evolution between III and IV has to sum up to t_1.
3. $^{2}J_{HH}$ coupling evolution needs to be refocused in the time frame of acquisition. For implementations, which refocus coupling evolution in the middle of the data chunk this means that the overall length of the pulse sequence between I and III has to equal that between III and V (note that this requires $\Delta = 1/(4*sw_1)$). For implementations which refocus coupling evolution at IV, equal lengths for the periods I to III and III to IV are required which can be obtained by using $\Delta = 0$.
4. $^{n\geq3}J_{HH}$ couplings evolution needs to be refocused both at III and at V (or at IV, for coupling refocusing at the beginning of the acquired data chunk). This is achieved by placing the appropriate BIRD rotations half-way between I and III, as well as between III and V (or IV, respectively).
5. $^{1}J_{CH}$ evolution needs tight control at III and at IV. Between time points I and III this is achieved by the $BIRD^{d}$ element in the conceptual pulse sequences shown in Figure 7.6, or by the 180°-^{1}H-

pulses used to also refocus $^1H^d$ chemical shift evolution throughout this period. To set up the proper timing between III and IV we have to decide between two cases: The case of experiments where clear-phase heteronuclear one-bond-splittings ($^1J_{CH}$ or $^1T_{CH}$) shall be obtained and the case where heteronuclear decoupling shall be achieved.

a. If heteronuclear decoupling shall be achieved, it is required to fully refocus $^1J_{CH}$ evolution at IV. This can be achieved, as shown in Figure 7.6 b) by using a BIRD^d element and simultaneously placing a 180°-^{13}C-pulse in-between Δ and τ_e. Further possibilities to achieve $^1J_{CH}$-refocusing at IV are discussed in chapter 8.2 (project C).
b. If pure-phase heteronuclear doublet should be obtained, net $^1J_{CH}$ (or $^1T_{CH}$) evolution needs to accumulate for t_1. In addition, broadband heteronuclear decoupling needs to be omitted during acquisition. A strategy for achieving this is illustrated in Figure 7.7 a).

This set of conditions tightly defines the timing in all the pulse sequences shown in the following. For given settings of the chunk length and the BIRD/INEPT delay used, the only variable that can be adjusted freely is τ_e, which was chosen to be as short as possible with the restriction that it needs to accommodate a final gradient. All other delays (τ_a, τ_b, τ_c, τ_d) are fixed according to these conditions.

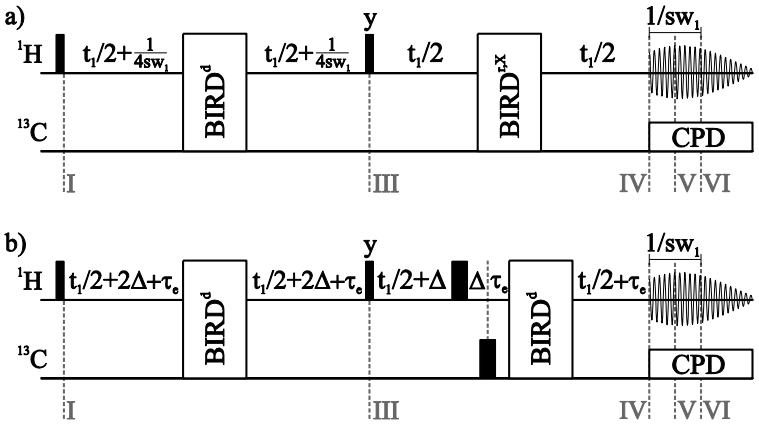

Figure 7.6: Conceptual pulse sequence schemes for the acquisition of ^{1}H spectra with perfectBIRD homonuclear decoupling. BIRD-pulse cascades inserted are symbolized by open rectangles. The superscripts in their labels indicate, which spin groups are inverted under ideal performance of the BIRD element. BIRD^d inverts $^1H^d$, but leaves $^1H^r$ and ^{13}C net unaffected. BIRD^{r,X} inverts $^1H^r$ and ^{13}C, but leaves $^1H^d$ net unaffected. Heteronuclear broadband decoupling during acquisition is indicated by the box labelled "CPD". The delay Δ takes either $\Delta = 0$ or $\Delta = 1/(4sw_1)$ to achieve full refocusing of homonuclear couplings at time points IV or V, respectively. For simplicity, aspects of filtration of signals from $^1H^r$ are not included (phase cycling or gradient filtration would be required in addition). Further explanations are given in the text.

Rather than applying the perfectBIRD decoupling scheme for the acquisition of broadband-decoupled ^{1}H spectra, so far, we solely used it for decoupling in the proton dimension of ^{1}H-^{13}C-HSQC spectra. The combination of this homonuclear decoupling approach with HSQC spectra with gradient-based signal filtration[351] is particularly interesting because of the very clean suppression of the signals from all $^1H^r$. Furthermore, in HSQC experiments, signal observation already is restricted to $^1H^d$, so for this experiment the homonuclear decoupling approach does not introduce severe additional sensitivity losses.

It should be of particular note for HSQC experiments, that the condition of equal initial magnetization imposed by the perfect echo ($M_1 \approx M_2$), which is required for homonuclear decoupling (see equation (7.13)), will hold true to a good approximation in most cases considered, even though a t_1-mixing period precedes F_2-perfectBIRD decoupling. The protons in ^{13}C-centred diastereotopic groups, which are the only groups that need to be considered here, very often have similar relaxation rates, so effects of relaxation will only introduce minor differences. In addition, the results presented later in this chapter seem to indicate, that differences of INEPT transfer efficiency, induced by different one-bond couplings, do not interfere severely with the homonuclear decoupling, even for weakly aligned samples. Finally, frequency labelling in t_1 is the same for the magnetization of both protons of the methylene group, and

in turn also does not lead to differences between M_1 and M_2. When implementing perfectBIRD decoupling the F_2-dimension of two-dimensional experiments, the fate of source magnetization throughout the experiment clearly has to be considered, while restrictions in possible applications to F_1-decoupling may be less stringent.
During my work, I designed different HSQC experiments based on the perfectBIRD homonuclear decoupling principle. In the following section, experiments with full homonuclear decoupling and simultaneous pure in-phase appearance of the heteronuclear coupling in the homodecoupled F_2-dimension are described. Experiments with full homo- and heteronuclear decoupling are described in Project C (see chapter 8).

7.3.2. Accurate and precise one-bond RDCs measurement in F_2-perfectBIRD CLIP/CLAP HSQCs

The potential interest in measuring one bond RDCs from the direct dimension of HSQC experiments with simultaneous suppression of all homonuclear couplings along this dimension has been described in chapter 7.2. The results shown therein illustrate that pronounced signal narrowing can be achieved for signals in isotropic solution and even more pronounced in the case of weakly aligned samples, in the direct dimension of HSQC experiments, if BIRD decoupling is applied[342, 343]. The problem of $^2J_{HH}$-coupling evolution however remained.
I used the approach outlined in Figure 7.6 to provide a first implementation of CLIP/CLAP-HSQC experiments with F_2-perfectBIRD homonuclear decoupling. To introduce a clean phase appearance of the heteronuclear one-bond coupling, the scheme was slightly altered, as is shown in Figure 7.7 a): The heteronuclear decoupling was omitted and the second BIRD element, which previously was BIRD^{r,X}, was replaced by a BIRD^{d} cluster to introduce seemingly unperturbed evolution of the heteronuclear coupling. Note that net $^1T_{CH}$-evolution is zero at $t_2 = 0$ and $t_3 = 0$ in this implementation, which ensures clean-phase heteronuclear doublets to be observed. Furthermore a BIRD^{d,X} cluster sandwiched between two proton inversion pulses was used in the first half of the double echo to ensure full chemical shift refocusing for $^1H^d$ at time point III, even in the case of incomplete BIRD inversion. For the implementation in F_2-perfectBRID CLIP/CLAP-HSQC experiments, the second INEPT (or alternatively the gradient decoding in CLAP experiments) is included into the homonuclear decoupling element to avoid homonuclear coupling evolution otherwise present in these elements and to shorten the experiment.
With this implementation, I was able to first prove that indeed fully homodecoupled high quality HSQC spectra could be collected (see Figure 7.8). It is apparent from the figure, that even for the diastereotopic protons, good suppression of all homonuclear couplings is achieved. In addition, the signals feature the clean in-phase heteronuclear doublets, we hoped to find for $^1J_{CH}$ extraction. The general scheme shown in Figure 7.7 a) thus seems to work properly and is able to provide full homonuclear decoupling, if applied in HSQC experiments.

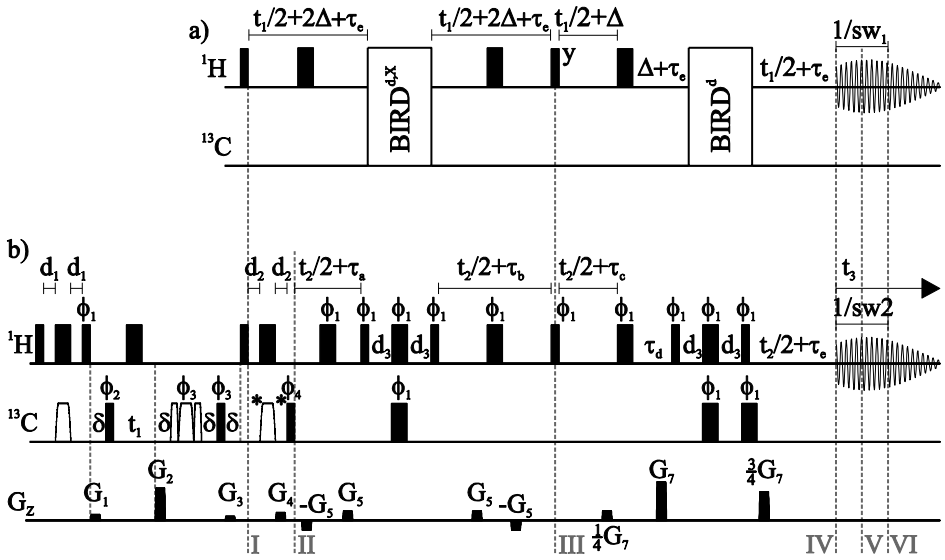

Figure 7.7: a) Conceptual scheme for a perfectBIRD decoupling element with clean phase appearance of $^1J_{CH}$. b) Pulse sequence scheme for F_2-perfectBIRD CLIP/CLAP HSQC experiments, in the initial implementation using phase encoding in F_1 based on the States-Ruben-Haberkorn-method[92] (ϕ_2 was incremented for phase encoding). Filled symbols are for hard pulses, open symbols are for adiabatic inversion/refousing pulses. δ equals the length of a gradient pulse (1 ms) plus a recovery delay (200 µs). $d_1 = 0.5*d_3 \approx (^1J_{CH})$, $\tau_c = \Delta$, $\tau_d = \tau_e + \Delta$, $\tau_b = \tau_e + 2\Delta$, , $\tau_a = \tau_e + 2\Delta$ – *length of INEPT*. For CLIP experiments $d_2 = d_1$, for CLAP experiments the pulses marked with an asterisk are omitted and $d_2 = \delta$. The phase cycling used was: ϕ_1 = y, ϕ_2 = x, -x incremented by $\pi/2$ for each t_1-increment, ϕ_3 = x, x, -x, -x, ϕ_4 = x, -x, and the receiver phase used is ϕ_{rec} = -x, x, x, -x.

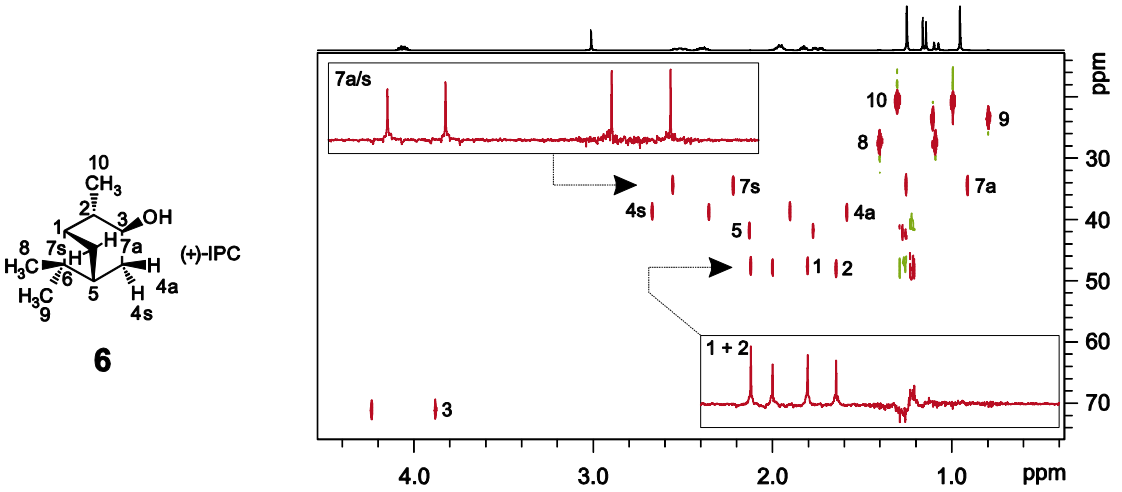

Figure 7.8: F_2-perfectBIRD CLIP-HSQC of (+)-IPC in CD_2Cl_2, acquired in 55 min using the pulse sequence shown in Figure 7.7 b). Full experimental parameters are given in 14.1.3.

Something that is quite unusual for modern HSQC experiments, is to use the States-Ruben-Haberkorn-method[92] for F_1-frequency encoding, as I did for the experiment shown in Figure 7.7 b). This choice leads to the signals apparent around the ^{13}C-transmitter frequency (45 ppm) in Figure 7.8, which are most intense at the proton chemical shifts around 1.2 ppm. (Shifting these signals to the edges of the spectrum by the TPPI-approach would have clearly been possible.) Usually the so-called Echo-Antiecho-TPPI-method[219] would be used for HSQC experiments, due to the better spectral quality that can be achieved. However, when initially implementing the experiment in the Echo-Antiecho-TPPI-method, the spectrum appeared mirrored around the ^{13}C-transmitter frequency, a problem that I was only able to resolve by changing the F_1-frequency encoding method. It was KATALIN KÖVÉR, who realized that for using Echo-Antiecho-TPPI-encoding in F_1, a two-step phase cycle (y, x) of the 90° proton pulse at time point III was necessary to avoid F_1-mirror images to appear. Thus apparently this pulses causes a mixing of p- and n-

type coherence pathways (even if the decoding gradient G_4 is moved directly prior to acquisition; data not shown). As a single-scan alternative to the phase-cycling proposed, I enforced proper coherence filtration with gradients across this pulse which also enables Echo-Antiecho-TPPI-encoding in F_1. With further introduction of adiabatic inversion pulses, rearrangements in the phase-cycling and the additional option to not increase t_2 in the first half of the perfect echo (leading to an in-phase doublet appearance of geminal splittings, instead of their collapse), the pulse sequence scheme shown in Figure 1 of the publication included was obtained.

Together with ANDREAS KOLMER, I could show that the pulse sequence scheme not only is able to produce high quality spectra for samples with low-viscosity isotropic samples, but that in addition, the technique is well suitable for studies of weakly aligned solutes. The potential benefit of also extracting high precision one-bond RDCs from singlet signals is evident. We conducted a series of measurements on a sample containing (+)-isopinocampheol **6** (structure shown in Figure 7.8) aligned in a lyotropic liquid crystal composed of poly-γ-benzyl-D-glutamate dissolved in CD_2Cl_2 and showed that quite considerable reductions in linewidths in the proton dimension can be observed (see Figure 3 of the manuscript, as well as Figures S2, S5, S6, S8 and S13 of the Electronic Supplementary Information). It should be of particular note that signals free of homonuclear coupling structure could even be obtained for the protons H7a and H7s, which share a geminal coupling of roughly -38.4 Hz. While initially signals at these positions appeared strongly distorted, clean signals could be recovered by reducing the lengths of the data chunks used for FID-concatenation. The inverse of the chunk-length can be regarded in these experiments as a measure for the bandwidth of the homonuclear decoupling scheme. The shorter the data chunks, the larger homonuclear couplings (in size) can be suppressed. While long data chunks enable sampling of the FID in fewer scans, all J_{HH} have to be much smaller than the inverse chunk length used. With short data chunk lengths, it was therefore possible to collect spectra with signals free from homonuclear coupling patterns, even for an anisotropic sample.

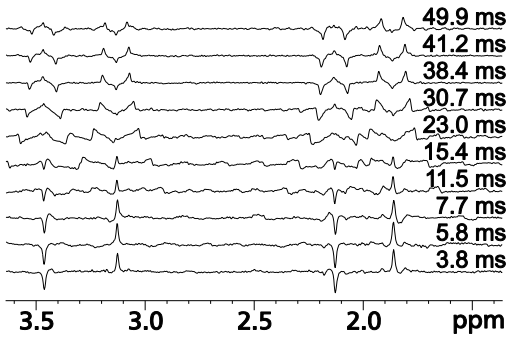

Figure 7.9: F_2-traces extracted at the C7 chemical shift from F_2-perfectBIRD CLAP-HSQC spectra, acquired with different chunk lengths. Please note, that the data shown in this Figure was collected with the (outdated) implementation shown in Figure 7.7 b). All experimental details are given in 14.1.4.

Having shown, that F_2-perfectBRID CLIP/CLAP-HSQC experiments can produce high quality spectra even for weakly aligned samples, together with ANDREAS KOLMER, VOLKER SCHMIDTS and CHRISTINA THELE, I carried out a systematic study to establish if one-bond couplings could reliably be measured from these spectra. We wanted to investigate, if the one-bond couplings apparent in the spectra would accurately reflect the true coupling constants to exclude bias from possible systematic errors introduced by the technique. In addition, we wanted to evaluate the precision with which these coupling constants could be extracted from the spectra and we intended to provide a comparison of the F_2-perfectBIRD CLIP/CLAP-HSQC technique to the F_2-BIRD CLIP/CLAP-HSQC technique described in section 7.2 and to the CLIP/CLAP-HSQC technique without homonuclear decoupling. Parts of this study initially were performed for publication in the article printed in section 7.2[343], but later were moved to the publication contained in this section to provide a complete discussion of all three techniques.

For benchmarking the accuracy of the coupling constant measurement, we chose a very simple test system for which a good reference value for the true $^1J_{CH}$ coupling constant could be measured. For $CHCl_3$, a high accuracy reference value for $^1J_{CH}$ was measured from a number of proton spectra. F_2-perfectBIRD CLIP-HSQC experiments were then used to measure the same coupling constant to evaluate the absolute accuracy of the method under optimal measurement conditions and the robustness of this accuracy towards experimental parameters, such as transmitter offset. It was shown that the experiment only introduces very small systematic deviations of the apparent splitting from the true coupling constant and that a lower-bound confidence interval as small as ± 0.05 Hz would be sufficient to take into account experiment bias on the apparent coupling constants. (For RDC-applications, we later conclude to use ± 0.1 Hz as the very conservative estimate desired in these applications. In addition, error estimates describing the uncertainty of coupling constant extraction should also be considered, e.g. using the method described in ref. [352]). For comparison, also F_2-BIRD CLIP-HSQCs, F_1-BIRD-scaled coupled HSQCs and gated-decoupled ^{13}C-spectra were used to measure the reference $^1J_{CH}$. Benchmarking experiments with chloroform were conducted together with CHRISTINA THIELE.

To provide evidence, that homonuclear decoupling indeed increases the precision of the coupling constant measurement, coupling constants were extracted from the same datasets, by three different individuals (ANDREAS KOLMER, VOLKER SCHMIDTS and myself). It could be observed, that indeed the homonuclear decoupling increases the precision of the data extraction. Interestingly, the highest precision was obtained when using F_2-BIRD decoupled spectra. In isotropic solution, the gain in precision obtained by using the pure shift methods is only small: The maximum deviations observed for the coupling constants extracted are 0.18 Hz (for H7s) for the CLAP-HSQC without homonuclear decoupling, 0.08 Hz (for H7a) for F_2-BIRD CLAP HSQC and 0.14 Hz (for H5) for F_2-perfectBIRD CLAP-HSQC (standard deviations are listed in the Electronic Supplementary Information). In contrast, the increase in precision is very pronounced for measurements in anisotropic solution: Maximum deviations observed here were 1.59 Hz (for H1) for the CLAP-HSQC without homonuclear decoupling, 0.29 Hz (for H4s) for F_2-BIRD CLAP-HSQC and 0.57 Hz (for H5) for F_2-perfectBIRD CLAP-HSQC. It should be of particular note that in the experiment without homonuclear decoupling, deviations above 1 Hz were also observed for H2 (1.14 Hz) and for H7s (1.22 Hz), where in both cases deviations in the homodecoupled spectra were < 0.2 Hz. This nicely illustrates that for RDC-extraction, where coupling constant extraction precision often is a major source of experimental errors, the pure shift approaches presented provide significant improvements.

The extraction of RDCs from the full set of measurements (CLIP/CLAP-HSQC without decoupling, F_2-BIRD CLIP/CLAP-HSQC and F_2-perfectBIRD CLIP/CLAP HSQC) was performed by ANDREAS KOLMER[353]. To also contrast the accuracy and precision of the different approaches by an alternate mean than comparing coupling constants extracted from different methods, he tested the RDCs obtained for agreement with a structural model for the compound. He used a the DFT-derived rigid structural model (B3LYP; 6-311+G(d) basis set; reported in ref. [140]) already used previously to test for agreement with the data. A slight improvement of the RMSD measured could be noted for CLIP data (0.159 Hz for CLIP-HSQC without homonuclear decoupling, 0.155 Hz for F_2-BIRD CLIP-HSQC and 0.139 Hz for F_2-perfectBIRD CLIP-HSQC) though it could clearly be debated, that such small deviations actually are significant. For CLAP experiments however the difference is much more pronounced. The RMSD between measured and back-calculated RDCs reduced from 0.322 Hz for the CLAP-HSQC without homonuclear decoupling to 0.142 Hz for F_2-BIRD CLAP-HSQC and to 0.139 Hz for F_2-perfectBRID CLAP-HSQC.

The deviation seen between CLIP and CLAP data acquired without homonuclear decoupling can to a large extent be attributed to partial signal overlap with $^2J_{CH}$ cross peaks in the CLAP-HSQC without decoupling (the $^2J_{C1H2}$ peak overlaps with the low-field component of the $^1J_{C1H1}$ multiplet). Long-range peaks are not observed in the CLIP-HSQC without homonuclear decoupling due to the CLIP-pulse used. If the IPAP-principle is used to extract the $^1D_{C1H1}$ coupling from experiments without homonuclear

decoupling, the results are biased towards the value extracted from CLAP-HSQC alone (CLIP-HSQC: $^1D_{C1H1} = 10.05 \pm 3.43$ Hz, CLAP: $^1D_{C1H1} = 11.06 \pm 1.72$ Hz, IPAP (homocoupled spectra): $^1D_{C1H1} = 10.78 \pm 1.9$ Hz, error-weighted average of all back-calculated values: $^1D_{C1H1} = 9.95$ Hz).
In homodecoupled spectra long-range correlations are not observed due to their anti-phase character and thus are not interfering with coupling constant extraction. Well separated signals are observed in this case (see Figure 7.10). This illustrates, that even comparably mild signal overlap can have strong impacts on the quality factors typically used to draw structural conclusions (note that also the error-weighted Q, as defined in ref. [119] more than doubles).

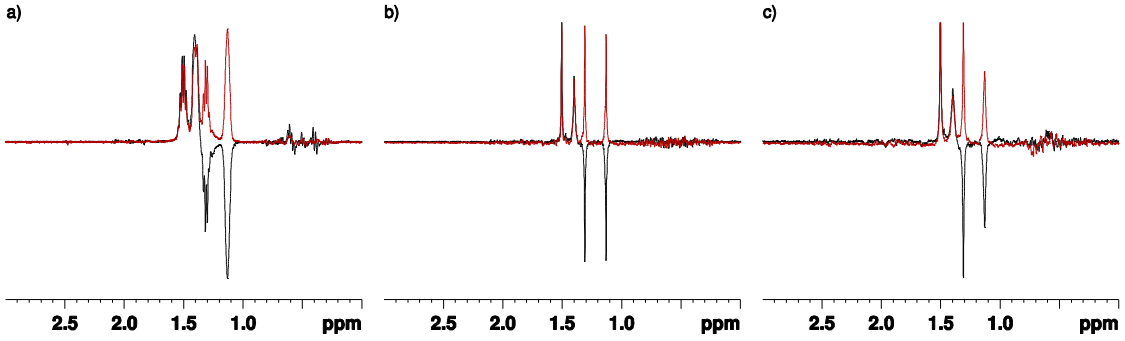

Figure 7.10: F_2-traces extracted at the F_1-frequency of C1, which at the F_1-resolution used is not separated from C2. Traces are extracted from the spectra shown in Figure 3 and S2 of the manuscript attached. a) CLIP-HSQC (red) and CLAP-HSQC without homonuclear decoupling, b) F_2-BIRD CLIP/CLAP-HSQC and c) F_2-perfectBIRD CLIP/CLAP-HSQC.

Having shown, that both F_2-BIRD CLIP/CLAP-HSQC and F_2-perfectBIRD CLIP/CLAP-HSQC enable very accurate one-bond coupling measurements (well covered if a lower-bound ± 0.1 Hz error range is used), that these experiments increase the precision of RDC extraction (user bias for $^1T_{CH}$-extraction is below 0.6 Hz for all cases studied, for F_2-BIRD decoupling even below 0.3 Hz) and that the agreement with the structural model is at least slightly improved, we concluded, that the pure shift techniques developed are indeed most suitable for one-bond RDC measurements in small molecule applications. We therefore did not only develop new homonuclear decoupling techniques which provide high quality pure shift HSQC spectra even for weakly aligned samples, but in addition showed, that these techniques enable one-bond RDCs to be measured with very high accuracy and precision.

L. Kaltschnee, A. Kolmer, I. Timári, V. Schmidts, R. W. Adams, M. Nilsson,K. E. Kövér, G. A. Morris, C. M. Thiele, ""Perfecting" pure shift HSQC: full homodecoupling for accurate and precise determination of heteronuclear couplings", *Chem. Commun.* **2014**, *50*, 15702 – 15705,
DOI: 10.1039/C4CC04217D.

ChemComm

COMMUNICATION

View Article Online
View Journal | View Issue

Cite this: *Chem. Commun.*, 2014, 50, 15702

Received 2nd June 2014,
Accepted 16th October 2014

DOI: 10.1039/c4cc04217d

www.rsc.org/chemcomm

"Perfecting" pure shift HSQC: full homodecoupling for accurate and precise determination of heteronuclear couplings†

L. Kaltschnee,[a] A. Kolmer,[a] I. Timári,[b] V. Schmidts,[a] R. W. Adams,[c] M. Nilsson,[cd] K. E. Kövér,[b] G. A. Morris[c] and C. M. Thiele*[a]

Fully homodecoupled HSQC spectra can be obtained through the use of a new pulse sequence element, "perfectBIRD". By way of illustration, we show that perfectBIRD decoupling allows one-bond residual dipolar couplings (RDCs), which provide important NMR restraints for structure elucidation, to be measured with outstanding precision, even in methylene groups.

The ever-growing drive in modern chemistry to create increasingly complex systems creates a need for improved analytical tools for their study. While it is usually considered desirable to *increase* the amount of information provided by a given analytical technique, there are times when information overload means that it is far more useful instead to *decrease* it. High-resolution solution state NMR spectroscopy, in which narrow chemical shift ranges conspire with extensive scalar coupling to give highly overlapped spectra, is a case in point. Here "pure shift" techniques can be used to suppress the effects of homonuclear couplings,[1] collapsing multiplets to singlets, simplifying spectra and facilitating the extraction of information previously obscured.

Among the different approaches used to achieve broadband homonuclear decoupling of NMR spectra in the real-time direct dimension,[1c,d,2] in indirect dimensions,[3] or in a pseudo-direct, interferogram, dimension,[4] the bilinear rotation decoupling (BIRD) scheme[3b] is particularly suitable for many heteronuclear correlation experiments involving dilute heteronuclei (*e.g.* natural abundance ^{13}C). In such cases isotope filtration incurs no extra sensitivity penalty; indeed the signal-to-noise ratio increases in some applications when multiplet structures collapse.[1b,d,5]

The BIRD element allows control over the effects of vicinal and long-range homonuclear couplings and both one-bond and long-range heteronuclear couplings. However it relies on the one-bond coupling to a dilute heteronucleus to distinguish between homonuclear coupling partners, and hence cannot be used to decouple geminal interactions. The latter not only cause remaining signal multiplicity due to homonuclear interactions to be present, but can also lead to significant spectral distortion. This makes BIRD pure shift methods less attractive for the study of systems containing diastereotopic methylene protons, frequently encountered in organic compounds.

To circumvent this limitation, we have incorporated BIRD decoupling into a modified perfect echo pulse sequence,[6] to form what we refer to as a "perfectBIRD" pulse sequence element. This new sequence element provides full homonuclear broadband decoupling even in the case of diastereotopic methylene protons, at the expense of a doubling of the natural (but not instrumental) linewidth.

Here we illustrate the use of perfectBIRD decoupling in experiments to determine one-bond RDCs. RDCs have proven to be very useful for the structure determination of organic and organometallic compounds.[7] However, RDC analysis in organic compounds is usually prone to be underdetermined, due to the small number of couplings observable. Thus it is of prime importance to obtain all possible information, including the two one-bond RDCs for diastereotopic methylene protons.

For simple AX spin systems the (original) perfect echo pulse sequence (Fig. 1a) refocuses fully both chemical shift and coupling evolution, at time 4τ, for all τ.[6,8] Dropping the last pulse of the perfect echo (shown in grey) yields a sequence element which refocuses homonuclear coupling evolution in AX systems at time 4τ, while introducing a net chemical shift evolution over a period 2τ. Differential chemical shift evolution however prohibits the repetitive application of perfect echoes with small τ, recently used in other

[a] *Clemens-Schöpf-Institut für Organische Chemie und Biochemie, Technische Universität Darmstadt, Alarich-Weiss-Straße 16, D-64287 Darmstadt, Germany. E-mail: cthiele@thielelab.de; Tel: +49 (0)6151 165112*
[b] *Department of Inorganic and Analytical Chemistry, University of Debrecen, Egyetem tér 1, H-4032 Debrecen, Hungary*
[c] *School of Chemistry, University of Manchester, Oxford Road, Manchester M13 9PL, UK*
[d] *Department of Food Science, University of Copenhagen, Rolighedsvej 30, DK-1958 Fredriksberg C, Denmark*

† Electronic supplementary information (ESI) available: Experimental details of the spectra shown, spectra with absorptive doublet features for geminal protons, experimental analysis of $^1J_{CH}$ accuracy and precision, figures with characteristic spectral features for strongly coupled systems, further spectra used for RDC extraction, pulse programs, structural models for IPC and RDC analysis results. See DOI: 10.1039/c4cc04217d

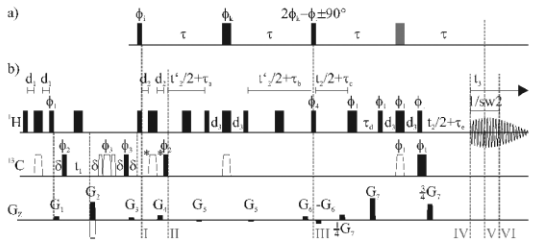

Fig. 1 (a) Perfect echo pulse sequence as proposed by Takegoshi, Ogura and Hikichi.[6] The pulse shown in grey can be dropped to introduce a net chemical shift evolution during 2τ. (b) A generalized pulse sequence for perfectBIRD homodecoupled HSQC experiments. Hard 90°-pulses are shown as narrow filled bars and 180°-pulses as wide filled bars, broadband inversion and refocusing pulses used on ^{13}C are shown as open symbols. All experiments shown in the main text use $t'_2 = t_2$ to achieve decoupling for diastereotopic protons. In contrast, setting $t'_2 = 0$ for all t_2 allows the acquisition of clean absorptive doublets even for protons with non-negligible geminal coupling during d_2 (see the ESI†). The delays d_1 and d_3 are adjusted to match $(4\ ^1J_{CH})^{-1}$ and $(2\ ^1J_{CH})^{-1}$, respectively. In CLIP (CLean In-Phase) experiments $d_2 = d_1$ and the pulses marked with an asterisk are used, while in CLAP (CLean Anti-Phase) experiments these pulses are omitted and $d_2 = \delta$.[10] δ equals the length of the gradients plus a recovery delay, $\tau_a = (4\ sw2)^{-1} + \tau_c + \tau_e + p_1 - 2\ d_2 - p_3 - p_{14}$, $\tau_b = (4\ sw2)^{-1} + \tau_c + \tau_e + p_1$, $\tau_c = (4\ sw2)^{-1}$, $\tau_d = \tau_c + \tau_e$, $\tau_e = \delta + 350$ μs, where p_1 and p_3 are the lengths of the hard 90° pulse on proton and carbon respectively and p_{14} is the length of the broadband inversion pulse on ^{13}C. G_2 and G_4 are set according to the ratio of gyromagnetic ratios and G_2 is inverted in alternating experiments to achieve the frequency sign encoding along t_1 according to the echo/antiecho procedure. The pulse phases used are: $\Phi_1 = 1$, $\Phi_2 = 0\ 2$, $\Phi_3 = 0\ 0\ 0\ 0\ 2\ 2\ 2\ 2$, $\Phi_4 = 1\ 1\ 3\ 3$, $\Phi_{rec} = 0\ 2\ 0\ 2\ 2\ 0\ 2\ 0$.

methods,[9] to achieve decoupling even in complex spin systems. As BIRD pulse elements are able to refocus the effects of weak coupling between protons that are bound to a ^{13}C nucleus directly through one bond ($^1H^d$) and those that are remotely attached ($^1H^r$),[3b,5b] replacement of the first 180° pulse in the original perfect echo sequence by a BIRD^{d,X} element (inversion for $^1H^d$ and ^{13}C) leaves only geminal couplings and strong coupling contributions not refocused at the central 90° pulse in the perfect echo, enabling its use to refocus weak couplings for two geminal coupling partners $^1H^d$ even if embedded in a complex spin system. To make sure that both $^1J_{CH}$ evolution and chemical shift evolution of $^1H^d$ are refocused at time (III), proton inversion pulses are used at the midpoints of periods $t'_2/2 + \tau_a$ and $t'_2/2 + \tau_b$. A combination of a broadband proton inversion and a BIRD^d element (inversion for $^1H^d$ only) is then used to replace the second 180° pulse of the perfect echo, preserving chemical shift evolution and heteronuclear couplings for $^1H^d$ while refocusing couplings between the prefocused diastereotopic protons, $^1H^d$ and $^1H^r$, as well as heteronuclear long-range couplings, at the end of the pulse sequence element.

A generalized pulse scheme for CLean In-/Anti-Phase[10] (CLIP/CLAP) HSQC experiments, widely employed in the measurement of one-bond scalar and total couplings, that uses the perfectBIRD homonuclear decoupling element is given in Fig. 1b. The perfect echo period spans times (I) to (V), with its central mixing pulse positioned at (III). In contrast to the CLIP/CLAP HSQC experiments without homodecoupling, the direct acquisition period normally found after (II) is replaced by the perfectBIRD element described above.

Construction of a free induction decay with negligible homonuclear coupling modulation is achieved using the interferogram-based approach, recently employed in F_2-heterocoupled CLIP/CLAP HSQC spectra with BIRD decoupling in the proton dimension.[5g,h] Data are collected between times (IV) and (VI), for time 1/sw2 equal to the time increment in t_2 and centred on the point of full coupling refocusing. Keeping $1/sw2 \ll 1/(2\ J_{HH})$, where J_{HH} is of the order of typical proton–proton couplings, restricts data collection to times over which proton–proton coupling evolution can be neglected. A full 3D time domain signal $s(t_1, t_2, t_3)$ is collected, from which a 2D signal $s(t_1, t_2^*)$ is constructed such that $t_2^* = t_2 + t_3$. This leads to a signal sampled uniformly in t_2^* for the total time $(1/sw2)\ TD_{F_2}$, where TD_{F_2} is the number of points sampled in t_2. This data treatment requires 1/sw2 to be an integer multiple of the dwell time used for F_3. Construction of the 2D time signal from the 3D dataset is performed conveniently using a Bruker AU program available at http://nmr.chemistry.manchester.ac.uk/. Afterwards $s(t_1, t_2^*)$ can be subjected to double Fourier transformation as usual.

To illustrate the potential of perfectBIRD decoupled HSQC experiments, we determined one-bond ^1H–^{13}C-RDCs for (+)-isopinocampheol (IPC, structure shown in Fig. 2) along the pure shift dimension (F_2^*) of the experiments. This compound is frequently used for method

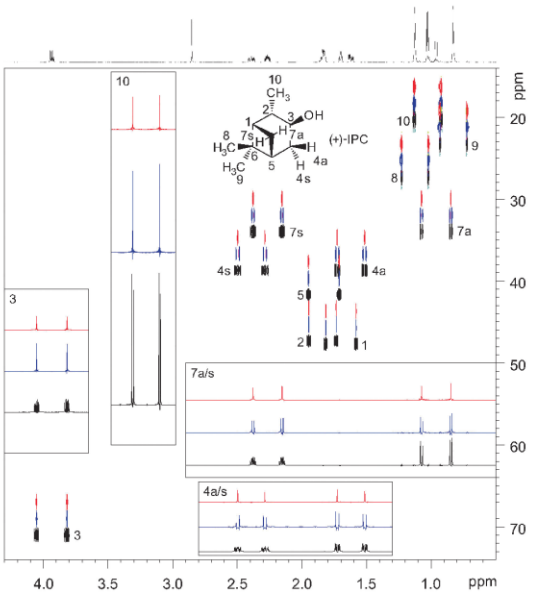

Fig. 2 F_2-heterocoupled CLIP HSQC spectra without homonuclear decoupling (black), and with BIRD (blue) and with perfectBIRD (red) homonuclear decoupling during acquisition, collected for (+)-IPC in isotropic CD_2Cl_2 solution at 600 MHz proton frequency. Experiment durations were 10.5 min, 7.1 h and 9.4 h, respectively. The structure of the analyte is shown in the figure, with the numbering used. The corresponding proton spectrum is displayed at the top. For selected protons, traces along the proton dimension are shown. The decoupled spectra are shifted in the carbon dimension for easier comparison.

development in RDC analysis due to its rigidity, the chemically differing entities present in the molecule and its good signal dispersion.

For the measurement of scalar one-bond heteronuclear coupling constants ($^1J_{CH}$), we collected ^{13}C–^1H F_2-heterocoupled CLIP/CLAP HSQC spectra without ^1H–^1H homodecoupling,[10] and with BIRD[5h] and perfectBIRD decoupling in the proton dimension, for a sample containing (+)-IPC in isotropic solution. As shown in Fig. 2, good homonuclear decoupling is achieved for protons that are bound to primary and tertiary carbons with both BIRD and perfectBIRD decoupling. In contrast, geminal couplings in methylene groups, and signal distortions stemming from geminal coupling evolution during the pulse sequences, are only suppressed when the perfectBIRD decoupling element is used. A very clean baseline is obtained in homodecoupled CLAP spectra, as cross-peaks arising from long-range ^1H–^{13}C-couplings are also suppressed by the decoupling scheme applied (see Fig. S1, ESI†). For many applications, these very favourable spectral properties more than compensate for the additional experiment time needed to collect the pure shift NMR spectra. It should be noted that there is also a modest (at least for small, rapidly-tumbling molecules) reduction in the signal intensity, and additional line broadening, due to transverse relaxation during the decoupling element. In our current implementation we chose to include the gradient pulses labelled 6 in Fig. 1, sacrificing a further factor of two in signal, in order to minimise spectral artefacts.

While one-bond coupling constant extraction is usually a minor problem in isotropic solution, the larger proton–proton couplings, resulting in increased line widths, and the wider range of one-bond coupling constants frequently complicate coupling constant extraction for weakly aligned samples. As shown in Fig. 3, homonuclear decoupling can lead to significant simplification of the spectra observed for weakly aligned samples, facilitating spectral interpretation and coupling constant extraction. The example shown demonstrates clearly the advantage of introducing the additional decoupling of diastereotopic methylene protons, although the reduction in signal intensity between BIRD and perfectBIRD decoupled experiments is more pronounced here, as transverse relaxation is faster in the aligned sample.

A particular challenge in this system is the decoupling of protons 7a and 7s: at roughly −38.4 Hz, the geminal total coupling between these two protons is much larger than couplings typically observed in isotropic solution – a problem frequently encountered in RDC measurements. The solution is to increase the decoupling range by shortening the data chunk duration 1/sw2, once again allowing clean singlets to be obtained, but at a reduced signal to noise ratio.

During this study an alternative approach to suppress geminal couplings, using a constant-time variant of the BIRD decoupled experiment, was proposed.[5g] The constant-time approach necessarily limits the range of couplings accessible, while the perfectBIRD method can accommodate a wide range of $^2T_{HH}$, making perfectBIRD particularly attractive for measurements on aligned samples.

Fig. 3 also illustrates a limitation of the perfectBIRD decoupling element when applied to anisotropic samples: decoupling only works properly for groups with a maximum of two geminal coupling partners. This is a direct consequence of the fact that the perfect echo only leads to full refocusing of coupling evolution for a single

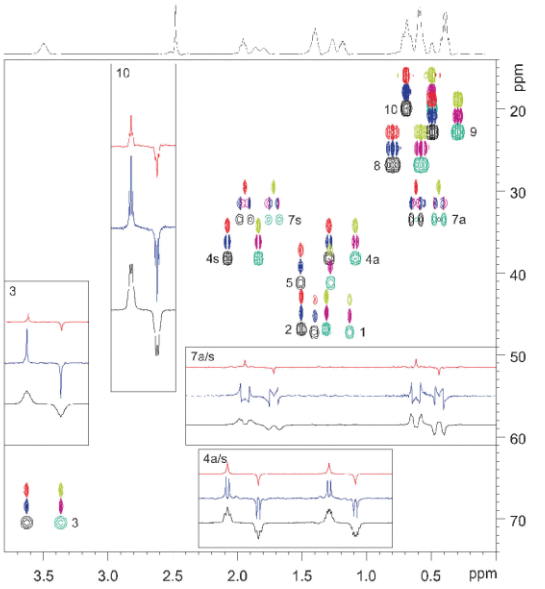

Fig. 3 F_2-heterocoupled CLAP HSQC spectra of (+)-IPC in the PBDG/CD_2Cl_2 lyotropic liquid crystalline phase ($\Delta\nu_Q$ = 107.6 Hz), collected without homonuclear decoupling (pos. black, neg. cyan), and with BIRD (pos. blue, neg. magenta) and with perfectBIRD (pos. red, neg. green) decoupling in the proton dimension at 600 MHz proton frequency. Experiment durations were 10.5 min, 2.8 h and 3.2 h, respectively. Traces taken along the proton dimension are shown in the insets. In the proton dimension, no chemical shift referencing has been applied.

coupling, or if τ is short compared to all $1/T_{HH}$. As both conditions are violated for methyl groups in anisotropic samples, the triplets observed using BIRD decoupling are only partially collapsed using perfectBIRD decoupling (see inset **10**). In isotropic solution this problem does not arise.

In small organic molecules, strong coupling effects are quite common, though not present in the case studied. Neither the perfect echo nor the BIRD element will fully refocus the effects of strong coupling,[3b,11] and complete decoupling of strongly coupled protons remains an unsolved challenge in pure shift NMR (as in many other methods). The precise measurement of RDCs from strongly coupled spins is an issue best addressed using specialized approaches;[12] as illustrated in the ESI†, strong coupling can be identified in homodecoupled spectra through characteristic changes in signal shapes.

The spectra shown for (+)-IPC, and additional experiments on chloroform, representing a simple AX test system, were used to test the influence of perfectBIRD homonuclear decoupling on the accuracy and precision of coupling constant measurements (see ESI†). Considering accuracy first, under the experimental conditions used, systematic errors in homodecoupled measurements of coupling constants were less than 0.05 Hz, greater than those for measurements by some conventional methods but negligible in the context of RDC measurements that typically have uncertainties of several tenths of a Hz. In contrast, the precision of $^1T_{CH}$ measurements was significantly improved by homodecoupling in

Table 1 Scalar couplings extracted from the CLIP HSQC spectra of (+)-IPC in isotropic CD_2Cl_2 solution shown in Fig. 2

	No decoupling	BIRD decoupling	PerfectBIRD decoupling
	$^1J_{CH}$ / Hz	$^1J_{CH}$ / Hz	$^1J_{CH}$ / Hz
FID-res:	0.76 Hz	1.02 Hz	1.02 Hz
1	140.57 ± 0.32	140.56 ± 0.11	140.59 ± 0.11
2	126.67 ± 0.17	126.65 ± 0.11	126.59 ± 0.12
3	141.67 ± 0.11	141.69 ± 0.11	141.71 ± 0.12
4s	126.35 ± 0.18	126.35 ± 0.24	126.34 ± 0.13
4a	127.04 ± 0.12	127.02 ± 0.19	127.07 ± 0.13
5	140.79 ± 0.32	140.72 ± 0.14	140.64 ± 0.23
7s	134.87 ± 0.35	134.81 ± 0.13	134.79 ± 0.17
7a	136.98 ± 0.15	136.94 ± 0.20	136.94 ± 0.12
8	124.56 ± 0.16	124.51 ± 0.12	124.51 ± 0.12
9	123.61 ± 0.11	123.66 ± 0.11	123.70 ± 0.12
10	124.75 ± 0.13	124.69 ± 0.11	124.64 ± 0.15

Table 2 Total couplings extracted from the CLIP HSQC spectra of (+)-IPC in anisotropic CD_2Cl_2/PBDG solution ($\Delta\nu_Q$ = 107.6 Hz) shown in Fig. S2 (ESI)

	No decoupling	BIRD decoupling	PerfectBIRD decoupling
	$^1T_{CH}$ / Hz	$^1T_{CH}$ / Hz	$^1T_{CH}$ / Hz
FID-res:	0.76 Hz	3.05 Hz	3.05 Hz
1	160.67 ± 3.42	160.92 ± 0.84	160.19 ± 0.54
2	117.27 ± 1.60	117.00 ± 0.19	116.53 ± 0.47
3	158.31 ± 0.51	158.38 ± 0.33	158.51 ± 0.44
4s	144.03 ± 0.12	143.85 ± 0.37	143.83 ± 0.19
4a	122.54 ± 0.16	122.59 ± 0.44	122.56 ± 0.12
5	138.10 ± 0.97	137.40 ± 0.82	137.12 ± 1.00
7s	133.78 ± 1.77	134.03 ± 2.86	133.79 ± 0.32
7a	106.89 ± 1.04	106.98 ± 0.86	106.81 ± 0.77
8	131.70 ± 0.48	131.82 ± 0.59	131.66 ± 0.29
9	118.57 ± 0.19	118.71 ± 0.56	118.96 ± 0.47
10	121.28 ± 0.21	121.09 ± 0.60	120.87 ± 0.77

the practical example of (+)-IPC, because of the simplification of line shapes and the avoidance of signal overlap caused by homonuclear couplings.

The confidence intervals shown in Tables 1 and 2 have two contributions: a very conservative estimate of the possible effects of the systematic errors noted (±0.1 Hz, double the observed uncertainty range) and the results of confidence interval estimation performed according to the procedure of Kummerlöwe *et al.*[13] In many cases these confidence intervals show a significant improvement with BIRD and perfectBIRD, particularly for methylene signals in the latter case. Couplings extracted from the CLAP HSQC spectra are given in Table S5 (ESI†). From the values obtained we conclude that homonuclear decoupling can indeed improve the precision of coupling constant measurements in the high-resolution proton dimension, which is particularly beneficial for RDC-based structure analysis in the case of diastereotopic methylene protons.

In this communication, we have introduced a homonuclear decoupling element, based on the BIRD and perfect echo techniques, which is able to collapse splittings due to geminal couplings between diastereotopic methylene protons. Pure shift F_2-heteronuclear coupled HSQC spectra of exceptional quality can be obtained, allowing highly precise measurements of one-bond couplings in the high-resolution proton dimension, even in weakly aligned media. We expect that the extended measurement times needed for these experiments will prove to be well justified, by the higher precision of the coupling constants extracted and the improved ease of analysis, when complex structures are to be solved. Modifications of the technique that also achieve heteronuclear decoupling in the high-resolution dimension are under development, and could be used to collect HSQC spectra with full homo- and heteronuclear decouplings in both dimensions as well as very high resolution in the proton dimension.

Financial support of this work by the Merck Society for Arts and Science Foundation, the ERC (grant no. 257041), the Engineering and Physical Sciences Research Council (grant nos. EP/I007989/1 and EP/L018500/1) and by TÁMOP-4.2.2/A-11/1/KONV-2012-0025, OTKA K 105459, TÁMOP-4.2.4.A/2-11-1-2012-0001, Richter Gedeon Talentum Alapítvány is gratefully acknowledged.

Notes and references

1 (*a*) M. Nilsson and G. A. Morris, *Chem. Commun.*, 2007, 933–935; (*b*) P. Sakhaii, B. Haase and W. Bermel, *J. Magn. Reson.*, 2009, **199**, 192–198; (*c*) N. H. Meyer and K. Zangger, *Angew. Chem., Int. Ed.*, 2013, **52**, 7143–7146; (*d*) L. Paudel, R. W. Adams, P. Király, J. A. Aguilar, M. Foroozandeh, M. J. Cliff, M. Nilsson, P. Sándor, J. P. Waltho and G. A. Morris, *Angew. Chem., Int. Ed.*, 2013, **52**, 11616–11619.
2 A. Lupulescu, G. L. Olsen and L. Frydman, *J. Magn. Reson.*, 2012, **218**, 141–146.
3 (*a*) A. Bax, A. F. Mehlkopf and J. Smidt, *J. Magn. Reson.*, 1979, **35**, 167–169; (*b*) J. R. Garbow, D. P. Weitekamp and A. Pines, *Chem. Phys. Lett.*, 1982, **93**, 504–509.
4 (*a*) K. Zangger and H. Sterk, *J. Magn. Reson.*, 1997, **124**, 486–489; (*b*) A. J. Pell, R. A. E. Edden and J. Keeler, *Magn. Reson. Chem.*, 2007, **45**, 296–316.
5 (*a*) A. Bax, *J. Magn. Reson.*, 1983, **53**, 517–520; (*b*) D. Uhrín, T. Liptaj and K. E. Kövér, *J. Magn. Reson., Ser. A*, 1993, **101**, 41–46; (*c*) T. N. Pham, T. Liptaj, K. Bromek and D. Uhrín, *J. Magn. Reson.*, 2002, **157**, 200–209; (*d*) K. Fehér, S. Berger and K. E. Kövér, *J. Magn. Reson.*, 2003, **163**, 340–346; (*e*) K. E. Kövér and G. Batta, *J. Magn. Reson.*, 2004, **170**, 184–190; (*f*) C. M. Thiele and W. Bermel, *J. Magn. Reson.*, 2012, **216**, 134–143; (*g*) T. Reinsperger and B. Luy, *J. Magn. Reson.*, 2014, **239**, 110–120; (*h*) I. Timári, L. Kaltschnee, A. Kolmer, R. W. Adams, M. Nilsson, C. M. Thiele, G. A. Morris and K. E. Kövér, *J. Magn. Reson.*, 2014, **239**, 130–138.
6 K. Takegoshi, K. Ogura and K. Hikichi, *J. Magn. Reson.*, 1989, **84**, 611–615.
7 (*a*) C. M. Thiele, *Concepts Magn. Reson., Part A*, 2007, **30A**, 65–80; (*b*) C. M. Thiele, *Eur. J. Org. Chem.*, 2008, 5673–5685; (*c*) G. Kummerlöwe and B. Luy, *TrAC, Trends Anal. Chem.*, 2009, **28**, 483–493; (*d*) R. R. Gil, *Angew. Chem., Int. Ed.*, 2011, **50**, 7222–7224; (*e*) B. Böttcher and C. M. Thiele, *eMagRes*, John Wiley & Sons, Ltd, 2012, vol. 1, pp. 169–180.
8 P. C. M. van Zijl, C. T. W. Moonen and M. von Kienlin, *J. Magn. Reson.*, 1990, **89**, 28–40.
9 (*a*) J. A. Aguilar, M. Nilsson, G. Bodenhausen and G. A. Morris, *Chem. Commun.*, 2012, **48**, 811–813; (*b*) R. W. Adams, C. M. Holroyd, J. A. Aguilar, M. Nilsson and G. A. Morris, *Chem. Commun.*, 2013, **49**, 358–360; (*c*) B. Baishya, C. L. Khetrapal and K. K. Dey, *J. Magn. Reson.*, 2013, **234**, 67–74; (*d*) T. F. Segawa and G. Bodenhausen, *J. Magn. Reson.*, 2013, **237**, 139–146; (*e*) J. A. Aguilar, R. W. Adams, M. Nilsson and G. A. Morris, *J. Magn. Reson.*, 2014, **238**, 16–19.
10 A. Enthart, J. C. Freudenberger, J. Furrer, H. Kessler and B. Luy, *J. Magn. Reson.*, 2008, **192**, 314–322.
11 R. V. Mulkern, J. L. Bowers, S. Peled, R. A. Kraft and D. S. Williamson, *Magn. Reson. Med.*, 1996, **36**, 775–780.
12 (*a*) B. Yu, H. van Ingen, S. Vivekanandan, C. Rademacher, S. E. Norris and D. I. Freedberg, *J. Magn. Reson.*, 2012, **215**, 10–22; (*b*) B. Yu, H. van Ingen and D. I. Freedberg, *J. Magn. Reson.*, 2013, **228**, 159–165.
13 G. Kummerlöwe, S. Schmitt and B. Luy, *Open Spectrosc. J.*, 2010, **4**, 16–27.

7.3.3. Comparison of the perfectBIRD and the constant-time BIRD techniques

As opposed to techniques, which introduce BIRD decoupling into constant-time evolution periods[228, 229, 342], BIRD decoupling was herein introduced into the perfect echo homonuclear decoupling element shown in Figure 7.5. The strategy in both cases is to use BIRD decoupling to refocus all long-range homonuclear couplings and to use a complementary homonuclear decoupling technique to suppress the remaining geminal couplings. The two strategies have notably different characteristics, caused complementary homonuclear decoupling strategies used: Constant time BIRD (CT-BIRD) can be used with a single BIRD refocusing element in the middle of the constant time period, while perfectBIRD requires full refocusing of all $^{n\geq3}J_{HH}$ at time point III and thus requires two BIRD decoupling elements over the full evolution period. It may therefore be anticipated, that CT- BIRD provides a higher robustness towards misset of the BIRD delays. The perfectBIRD experiment also requires chemical shift evolution to be refocused at time point III. This leads to an effective doubling of contributions from transverse relaxation, but not from field inhomogeneity, to the linewidth observed. This situation is less drastic in the CT-BIRD approach, as larger fractions of the constant time evolution period can be used for net chemical shift evolution (Reinsperger and Luy used 93%[342]). The most critical disadvantage of CT-BIRD however is the constant length of the homonuclear decoupling element. In such experiments, transverse relaxation leads to signal intensity losses which increase drastically for longer time delays, rendering studies with high resolution in the pure shift dimension, as has been presented for $^{1}J_{CH}$ measurements using F_2-perfectBIRD CLIP/CLAP-HSQCs (time domain signals were sampled for 1 s in the pure shift dimension[213]), practically impossible. While the perfectBIRD strategy also introduces dead times of 30 to 60 ms (depending on the experimental settings) during which transverse relaxation is effective before sampling of the first data point, this normally is considerably less than in the CT-BIRD approach. An advantage of the perfectBIRD approach, that is particularly interesting for RDC measurement applications is, that no tuning of the experiment according to the apparent geminal coupling constants is required. In the CT-BIRD approach, considerable signal losses are apparent, if the total constant time delay is not matched to the geminal couplings. However, in aligned samples $^{2}T_{HH}$ values may vary significantly and their absolute values typically are not well known beforehand. This may lead to severe signal losses for weakly aligned samples. In the perfectBIRD approach, this is not an issue, as long as the data chunks acquired are sufficiently short for suppression of these couplings. In the context of RDC extraction, it should be further noted, that the CT-BIRD approach in principle would also enable full suppression of $^{2}T_{HH}$ in methyl groups – something that cannot be achieved with the perfectBIRD approach. Note however, that to date, no example for one-bond RDC extraction using the CT-BIRD approach has been provided.

7.4. CLIP- and CLAP-HSQC Experiments with real-time BIRD decoupling

The narrowing of signals by pure shift acquisition in F_2-BIRD and F_2-perfectBIRD homodecoupled CLIP-HSQC experiments discussed in the previous sections can enable measurements of RDCs at higher precision than that in the CLIP-HSQC experiment, albeit requiring longer experiment durations. The evident alteration of the experiment avoiding this drawback in F_2-BIRD homodecoupled experiments is the use of real-time BIRD decoupling[256, 273, 305, 307, 309, 354], which emerged during the course of our studies. The real-time (also termed “instant”) decoupling approach[256, 257, 355] enables the full FID in the homodecoupled dimension of the experiment to be measured in a single scan, as opposed to methods constructing the FID from an interferogram. This can reduce the time demand of pure shift experiments to be collected in virtually the same time as experiments without homonuclear decoupling. In addition, for real-time BIRD HSQCs with broadband heteronuclear decoupling it could be shown that the pure shift approach can increase the experiment sensitivity, in addition to the improvement in signal

dispersion obtained[305, 354]. We therefore started developing alternations of the existing real-time BIRD decoupling technique, which would allow extraction of heteronuclear one-bond coupling constants in the pure shift dimension. The aim was to design real-time BIRD-homodecoupled CLIP-CLAP-HSQC experiments which would enable precise one-bond coupling constant extraction from the pure shift dimension and which could be recorded in the same experimental time as its counterpart without homonuclear decoupling[166].

The original implementation again was provided by KATALIN KÖVÉR, who used BIRD^{d}-elements[304] with two successive inversions on the heteronucleus in each homonuclear decoupling element. With this strategy, she achieved continued coupling evolution from data chunk to data chunk with no net one-bond coupling evolution during the homonuclear decoupling elements, a prerequisite for seamlessly undisturbed evolution of these couplings in the resulting FID.

The spectral quality obtained looked quite promising from the beginning. However, at an early stage of testing the experiment, it was observed by FELIX ROTH during an internship I supervised, that some of the the signal separations from which one-bond couplings should be extracted differed conceivably from the ones apparent in F_2-BIRD decoupled CLIP-HSQCs the interferogram-based approach. The deviations noted were prohibitively large for the experiment to be used for RDC-measurements, where the accuracies required for one-bond coupling measurements normally need to be better than 1 Hz.

The cause of the signal separations observed in spectra to differ from the heteronuclear coupling constants associated can be found in the real-time homonuclear decoupling approach we used: Real-time homonuclear decoupling uses the repeated application of a homonuclear decoupling block, interleafed with periods of acquisition, to sample the full FID in a single scan (for comparison, see Figure 4.15). None of the homonuclear decoupling blocks available is able to produce the inversion of all passive spins without introducing small perturbations to the magnetization of the active spins – in short, no homonuclear decoupling element available is entirely perfect. As opposed to interferogram-based experiments where no repetition of the homonuclear decoupling block is used, in real-time decoupling techniques even small imperfections, such as relaxation during the decoupling elements, incomplete signal inversion or phase errors can accumulate during the course of the acquisition.

The usual way to filter-out signals that are undesired from an FID, such as decoupling sidebands, is the use of phase cycling and gradient filtration methods. However, in addition to applying a phase cycling from one scan to the other, we figured that real-time pure shift techniques may particularly benefit from a phase-cycling during acquisition, applied from one homonuclear decoupling element to the next ("chunk-to-chunk phase cycling"), in a similar way as phase-cycling is commonly applied in heteronuclear decoupling methods[233-236, 356].

An extensive search for a good combination of phase cycling schemes was performed which would be able to reduce systematic errors of the coupling constants measured. ISTVÁN TIMÁRI and MÁRIA RAICS made big efforts to test different phase cycling schemes empirically. RALPH ADAMS provided complementary information from spin system simulations with the aim to rationally choose good phase cycling combinations. DUSAN UHRÍN, in addition, studied if using BIRD modules with matched frequency-swept pulses for approximate *J*-compensation would provide conceivable improvements.

By measuring the apparent methyl-$^{1}J_{CH}$ splitting in methyl-α-D-mannopyranoside under different experimental conditions (transmitter offsets, BIRD/INEPT delays, pulse miscalibration) and comparing these to a reference value, ISTVÁN TIMÁRI and MÁRIA RAICS were able to identify a pulse sequence scheme which strongly reduces systematic deviations of the coupling constants measured. In the best-performing phase cycling scheme (see figure legend of Figure 1 in the submitted manuscript) all six pulses of the homonuclear decoupling element are subject to phase cycling both from one decoupling element to the next and from scan to scan.

It is shown that the phase cycling scheme is able to limit experimental inaccuracies over the tested range of experimental parameters (^{1}H-transmitter offsets of up to 1980 Hz, BIRD/INEPT-mismatch of up to

30 Hz from the $^1J_{CH}$-value of the test substance, pulse miscalibration by up to 5 %) to fall within a 1 Hz error range, while in extreme cases deviations of up to 1.4 Hz were measured.

The range of experimental parameters the real-time BIRD CLIP/CLAP-HSQC described is able to cover is ideally suitable for amide one-bond RDC ($^1D_{NH}$) measurements in weakly aligned small proteins, as ISTVÁN TIMÁRI and MÁRIA RAICS were able to demonstrate: For the uniformally ^{15}N 55-residue penicillium anti-fungal protein (PAF), the $^1J_{NH}$ values measured with real-time BIRD decoupling are in very good agreement (maximum deviation of 0.46 Hz; only 4 residues with deviations bigger than 0.35 Hz) with results of the high-accuracy interferogram-based F_2-BIRD CLIP/CLAP-HSQC described in section 7.2. With a weakly aligned sample of the protein (Otting-phase[138], 5 % C_8E_5 and n-octanol in 95% H_2O/5 %D_2O), they further were able to extract 49 backbone amine RDCs (out of the 54 maximum possible).

The considerably different challenges inherent in studies of proteins and those of small molecules, such as the considerably larger variety of the homonuclear coupling networks that can be present in small molecules as compared to protein backbones, allow only limited generalization of the conclusions obtained to studies of other substance classes. That is why in parallel to the investigations of ISTVÁN TIMÁRI and MÁRIA RAICS, I further evaluated if the real-time BIRD CLIP/CLAP-HSQC experiment would also be suitable for small molecule studies.

To this end, I performed an evaluation of the performance of the real-time BIRD CLIP/CLAP-HSQC technique described using the small molecule test analyte (+)-isopinocampheol also used in the investigations described in section 7.3 for direct comparison with the other CLIP/CLAP-HSQC variants[166, 213, 342, 343] studied throughout.

For scalar coupling constant measurements ($^1J_{CH}$), I found that a reduction in coupling constant measurement accuracy results from the homonuclear decoupling approach, at least for well separated signals, even if the full phase cycling scheme is applied. Deviations from the results obtained with the F_2-perfectBIRD CLIP-HSQC amount up to 0.91 Hz for real-time experiments with long acquisition periods (20.48 ms in this case), a setting I showed can be recommended. Deviations from the results obtained with the F_2-perfectBIRD CLIP-HSQC are much smaller for the fully homocoupled CLIP/CLAP-HSQCs (maximum deviation of 0.20 Hz) as well as for other experiments using interferogram-based homonuclear decoupling (maximum deviation of 0.08 Hz). This illustrates, that use of the real-time BIRD CLIP/CLAP-HSQC technique (at least in its current implementation) can only be recommended for $^1J_{CH}$ measurements in small molecules, if the homonuclear decoupling is able to significantly increase the precision of the coupling constant extraction, e.g. by separating peaks that previously were overlapping. The situation notably changes for the sample in which the test molecule is weakly aligned (using a high molecular weight poly-γ-benzyl-D-glutamate/dichloromethane-d_2 liquid crystalline medium[131, 140]). For the case studied, the line-narrowing introduced by the pure shift approach was found to be sufficiently beneficial that even for well separated signals the real-time BIRD CLIP/CLAP-HSQC provides one-bond RDCs with alike quality as can be achieved with the CLIP/CLAP-HSQC without homonuclear decoupling. Again using the F_2-perfectBIRD CLIP-HSQC as a reference, maximum deviations of the RDCs measured are in the range of 1.52 to 1.96 Hz for real-time BIRD CLIP/CLAP-HSQCs with 20.48 ms chunk-duration, while for CLIP/CLAP-HSQCs without homonuclear decoupling, maximum deviations of 1.01 to 3.40 Hz were observed. In addition to comparing the RDCs measured to a reference dataset, also the agreement with an existing structural model[140] was used for testing the experimental performance. While the RDCs from interferogram-based pure shift experiments showed the best agreement with the structural model, RDCs obtained with real-time BIRD CLIP/CLAP-HSQC were able to describe the structural model just as well as RDCs extracted from CLIP/CLAP-HSQCs without homonuclear decoupling. It was therefore concluded, that with the phase-cycling we introduced, real-time BIRD CLIP/CLAP-HSQCs can also be used in studies of small molecules.

While these results show high promise for the application of the technique described, limitations of the method for small molecule applications could also be identified:
As is common to all experiments with BIRD decoupling on protons[251, 254, 267, 305], the real-time BIRD CLIP-HSQC is not able to suppress $^{2}J_{HH}$ couplings frequently occurring in organic small molecules. Direct comparison with the interferogram-based F_2-BIRD CLIP-HSQC spectra measured on the same samples[213] illustrates that signal distortions are more pronounced in the real-time decoupled spectra. In the present case, this practically prevented the extraction of $^{1}T_{CH}$-values for protons H7a and H7s (n.b.: $^{2}T_{H7a,H7s} \approx$ -38.4 Hz), while comparably precise coupling constant extraction still was possible in the interferogram-based experiment.
One aspect that should additionally be noted as far as small molecule studies are concerned is, that in both applications we presented signals were dispersed only over a limited spectral width. Also the tests towards transmitter offset robustness initially performed on methyl-α-D-mannopyranoside only covered offset ranges of ± 2kHz. In small molecule applications, this offset range may not cover the entire spectrum. In particular the robustness towards transmitter offsets would provide room for improvement for interesting future developments.

I. Timári, L. Kaltschnee, M. Raics, F. Roth, N. G. A. Bell, R. W. Adams, M. Nilsson, D. Uhrín, G. A. Morris, C. M. Thiele and K. E. Kövér, "Real-time broadband proton-homodecoupled CLIP/CLAP-HSQC for automated measurement of heteronuclear one-bond coupling constants", *submitted the 2nd of June 2016*.
Manuscript and pages S17-S20 of the Supporting Information, the full SI is provided as electronic material

Journal Name

ARTICLE

Real-time broadband proton-homodecoupled CLIP/CLAP-HSQC for automated measurement of heteronuclear one-bond coupling constants

Received 00th January 20xx,
Accepted 00th January 20xx

DOI: 10.1039/x0xx00000x

www.rsc.org/

István Timári,[a] Lukas Kaltschnee,[b] Mária H. Raics,[a] Felix Roth,[b] Nicholle G. A. Bell,[c] Ralph W. Adams,[d] Mathias Nilsson,[d] Dušan Uhrín,[c] Gareth A. Morris,[d] Christina M. Thiele[b] and Katalin E. Kövér[a,*]

A new method is proposed that allows broadband homonuclear decoupled CLIP/CLAP-HSQC NMR spectra to be acquired at virtually no extra cost in measurement time. The real-time (windowed) acquisition protocol applied follows a scheme recently devised for recording pure shift (broadband homonuclear decoupled) heteronuclear single quantum correlation (HSQC) spectra. To minimize systematic errors in the apparent coupling constants obtained using real-time homonuclear decoupling, we extended the acquisition scheme to include cycling of radiofrequency phases both from chunk to chunk during windowed acquisition, and from scan to scan during time averaging, allowing robust coupling constant measurement. The new real-time pure shift CLIP/CLAP-HSQC experiments are designed to speed up coupling constant determination, to increase the sensitivity of measurement in favorable cases, and to simplify the extraction of accurate one-bond heteronuclear couplings from pure in- or anti-phase doublets using automatic peak picking. The scope and limitations of the method are discussed, and a variety of experimental tests are reported.

Introduction

CLIP/CLAP-HSQC (*CLean In-Phase/CLean Anti-Phase HSQC*) experiments[1] and their variants[2] are some of the most widely used NMR methods for measuring heteronuclear couplings ($^1J_{XH}$) between directly-bonded X–^{1}H spin pairs. In conventional CLIP/CLAP-HSQC spectra,[1] however, the X-coupled F_2 doublets retain the complex multiplet structures caused by proton-proton couplings, reducing the spectral resolution and, along with that, the precision of coupling constant measurement.

To circumvent this limitation of conventional experiments, recently-proposed pure shift (PS) CLIP/CLAP-HSQC methods[3-5] provide a practical remedy, giving resolution improvements of close to an order of magnitude. These pure shift methods use interferogram-based acquisition,[6, 7] enabling the acquisition of spectra of high spectral quality but requiring significantly longer experiments than the corresponding conventional techniques without homodecoupling.

To reduce the duration of pure shift HSQC experiments, it has recently been shown[8, 9] that it is possible to acquire decoupled signals using real-time acquisition, in a single free-induction decay during which homonuclear proton-proton coupling evolution is periodically refocused by applying a BIRD (*BIlinear Rotation Decoupling*) pulse sequence element[10] in combination with a non-selective 180° proton pulse. The Zangger-Sterk[11] and HOBS (*HOmonuclear Band-Selective*)/BASH (*Band-Selective Homonuclear*)[12-14] pulse sequence elements for homonuclear decoupling have also been combined with this real-time, or "instant"[15] acquisition strategy. The great advantage of real-time pure shift methods is that, in contrast to interferogram-based pure shift acquisition, they incur no extra experiment time penalty.[16-18] Indeed, in favorable circumstances real time pure shift methods can, by virtue of collapsing complex multiplets into strong single signals, show better sensitivity than their conventional analogs.[9]

While real-time BASH decoupling does not cause sensitivity loss, it is not broadband, only providing homonuclear decoupling for a defined spectral region that does not contain mutually *J*-coupled protons (such as the amide region in protein spectra).[12-14] In heteronuclear one-bond correlation experiments, the BIRD method is broadband and also retains full sensitivity: since in HSQC experiments only those protons directly coupled to X (e.g. ^{13}C, ^{15}N) are being detected, there is no extra signal loss when BIRD sequence elements are used.[9] We have recently compared in detail the performance of BIRD and BASH-decoupled ^{1}H-^{15}N HSQC methods, including the effectiveness of water signal suppression, in protein studies.[19] Here we demonstrate that it is possible to implement a real-

[a] Department of Inorganic and Analytical Chemistry, University of Debrecen, Egyetem tér 1, H-4032 Debrecen, Hungary. E-mail: kover@science.unideb.hu
[b] Clemens-Schöpf-Institut für Organische Chemie und Biochemie, Technische Universität Darmstadt, Alarich-Weiss-Straße 4, D-64287 Darmstadt, Germany
[c] EastCHEM School of Chemistry, University of Edinburgh, David Brewster Road, Edinburgh, EH9 3FJ, United Kingdom
[d] School of Chemistry, University of Manchester, Oxford Road, Manchester, M13 9PL, United Kingdom
Electronic Supplementary Information (ESI) available: details of experimental parameters, phase programs tested, tables of one-bond heteronuclear coupling constants measured, Bruker pulse sequence codes. See DOI: 10.1039/x0xx00000x

time pure shift acquisition scheme devised for variants of HSQC[9, 19, 20] in CLIP/CLAP-HSQC pulse sequences with preservation of the one-bond heteronuclear coupling. The use of real-time decoupling with simultaneous one-bond coupling measurement in the direct dimension is significantly less straightforward than it might at first sight seem, because of the potential for small systematic errors in successive *J*-refocusing pulse sequence elements to accumulate during acquisition, leading to slightly distorted spectra and to small but unwelcome errors in the one-bond coupling constants measured. It will be shown that such errors can be kept within acceptable limits by careful sequence design, with the choice of successive pulse phases during acquisition being particularly important.

Results and discussion

As in the real-time pure shift HSQC experiment,[9] trains of isotope-selective BIRD modules combined with non-selective ^{1}H 180° pulses are used here to refocus $^nJ_{HH}$ modulation midway through each of the acquired data chunks (n ≥ 3, here). The combined effect of the BIRD element and the hard 180° proton pulse is to leave protons directly coupled to X (e.g. ^{13}C, ^{15}N), whose signals are detected, unaffected, but to invert protons not directly coupled to X. Because CLIP/CLAP-HSQC experiments do not use broadband X decoupling during acquisition, in order to retain the one-bond couplings $^1J_{XH}$ it is necessary here to use the BIRD$^{(d)}$ module,[21] which differs from the parent BIRD$^{(d,X)}$ module in having an extra 180° X pulse added so that the X spin is not left inverted. In the real-time BIRD$^{(d)}$ CLIP-HSQC sequence of Figure 1 – as in most other HSQC experiments – a refocusing spin-echo element using a simultaneous ^{1}H/X 180° pulse pair at its midpoint is included before acquisition. Here, to generate pure in-phase magnetization for coupling constant measurement, an extra 90° X purging pulse is applied prior to the start of real-time PS acquisition.[1] In contrast, in the pure shift CLAP-HSQC experiment the greyed 180° and 90° X pulses in Figure 1 are discarded to retain anti-phase magnetization – generated by the X → ^{1}H coherence transfer step – for real-time acquisition of the X-coupled but proton-homodecoupled signal. The resultant PS CLIP/CLAP-HSQC spectra provide broadband proton-homodecoupled pure in- or anti-phase X-coupled doublets with significantly enhanced resolution, allowing direct and highly precise measurement of heteronuclear one-bond couplings.

One challenge that such real-time homodecoupling techniques present is that they require careful design if clean results are to be obtained. The central problem, spectral perturbations caused by the cumulative effect of successive imperfect pulse sequence elements, is one that is common to all experiments in which windowed acquisition, alternating spin manipulations and chunks of data acquisition, is used. In high resolution this includes real-time heteronuclear *J*-scaling[22] (for which a detailed analysis of the effects of pulse imperfections has been presented),[23] real-time pure shift NMR,[8, 9, 12, 14, 15, 19, 24] and *J*-up- and down-scaling.[25-27] With one honorable exception,[14] such problems have largely been ignored in the literature.

To take a simple example, consider a real-time experiment in which an imperfect pulse sequence element is applied at intervals τ during data acquisition. Possible (and indeed unavoidable) sources of imperfection include B_1 inhomogeneity, resonance offset, and (in BIRD-based experiments) *J* mismatch. Suppose that the imperfect element is equivalent to the ideal spin manipulation required plus a small extra flip angle α radians. The spins will see the average Hamiltonian sought, plus a periodic series of unwanted pulses that correspond in the frequency domain to a comb of very weak irradiations of amplitudes α/τ rad s^{-1} at the transmitter offset plus and minus integer multiples of $1/\tau$ Hz.[28] If, as will often be the case, these sidebands do not fall close to any resonance, they will be too weak to have any significant effect on the spectrum. If, however, one of the sidebands is close to or coincident with a spectral line, that line will be perturbed, for example by being split and/or slightly displaced. In many experiments, for example pure shift NMR, such effects can safely be neglected, but where, as here, accurate coupling constant measurements are required, precautions must be taken to minimize the impact of periodic errors on real-time measurements.

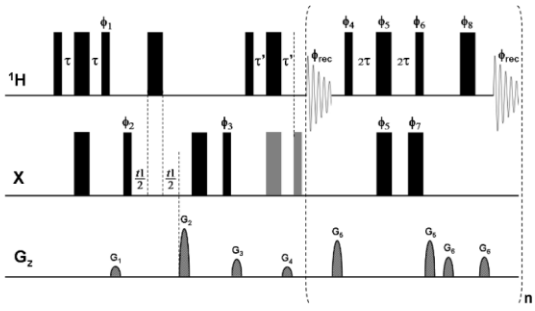

Figure 1 Pulse sequence scheme for real-time broadband proton-homodecoupled CLIP/CLAP-HSQC experiments. Narrow and wide filled bars correspond to 90° and 180° pulses, respectively, with phase x unless indicated otherwise. In the CLIP-HSQC sequence additional carbon 180° and 90° pulses (shown in gray) are employed to refocus antiphase proton magnetization and to remove undesired residual dispersive components respectively prior to detection. These pulses are omitted in the CLAP-HSQC experiment, where the antiphase proton magnetization is retained and detected. Delays are set as follows: $\tau = 1/(4*{}^1J_{XH})$, $\tau' = 1/(4*{}^1J_{XH})$ for NH/CH or $1/(8*{}^1J_{XH})$ as a compromise for all multiplicities. Coherence order selection and echo–antiecho phase sensitive detection in the X-dimension are achieved with gradient pulses G_2 and G_4 in the ratio of 80:20.1 for ^{13}C and 80:8.1 for ^{15}N, respectively. Purging gradient pulses G_1 and G_3 are used with typically of 1 ms duration (p16) followed by a recovery delay (d16) of 100 μs. Each *J*-refocusing block applied during acquisition consists of a BIRD$^{(d)}$ element, a hard 180° proton pulse, and a data acquisition window. The first and last chunks are half the duration (AQ/2n) of the remaining chunks (AQ/n). CTP selection gradient pulses G_5 and G_6 are used around the BIRD$^{(d)}$ block and the hard 180° proton pulse between data chunks, with 0.5 ms duration and 100 μs recovery delay. Phases are $\phi_1 = y$; $\phi_2 = (x)_4, (-x)_4$; $\phi_3 = (x)_8, (-x)_8$; $\phi_4 = x$; $\phi_5 = y, -y$; $\phi_6 = -x$; $\phi_7 = x, -x$; $\phi_8 = x, -x$; and $\phi_{rec} = (x)_4, (-x)_8, (x)_4$. Phase sequencing of *J*-refocusing elements: $\phi_{chunk\text{-}to\text{-}chunk}(n) = \{(x)_4, (-x)_6, (x)_4, (-x)_2\}_{runs\ over\ n}$; $\phi_4 = x + \phi_{chunk\text{-}to\text{-}chunk}(n)$; $\phi_5 = y, -y + \phi_{chunk\text{-}to\text{-}chunk}(n)$; $\phi_6 = -x + \phi_{chunk\text{-}to\text{-}chunk}(n)$; $\phi_7 = x, -x + \phi_{chunk\text{-}to\text{-}chunk}(n)$; $\phi_8 = x, -x + \phi_{chunk\text{-}to\text{-}chunk}(n)$. For the explicit phase sequences and cycles see Table S2.

Two obvious strategies for reducing the impact of pulse imperfections in real-time windowed acquisition are to minimize the cumulative effects of imperfect pulses by manipulating the phases of successive pulse sequence elements during acquisition of a single transient;[14] and to average out the perturbations that remain by manipulating those phases from transient to transient during time averaging. We refer here to the former as a phase sequence (within a single transient) and to the latter, as is customary, as a phase cycle (from transient to transient).

To assess the utility of the proposed real-time BIRD$^{(d)}$ CLIP/CLAP-HSQC sequences, tests of robustness with respect to proton resonance offset, J mismatch (BIRD/INEPT delay settings) and pulse (mis)calibration were made using a model sample of 0.345 M methyl α-D-mannopyranoside in D_2O. The one-bond ^{1}H-^{13}C coupling constant of the CH_3-group measured directly from the ^{13}C-satellites in the proton spectrum ($^1J_{CH}$ = 144.06 ± 0.02 Hz) was used as a reference for testing the accuracy of the experiments proposed. The phase sequencing of J-refocusing elements (BIRD$^{(d)}$ and 180° proton pulse) applied during acquisition and the scan to scan phase cycle were optimized empirically by testing various phase combinations (see details in Table S1 of the Supporting Information). The sequence and cycle which gave the best accuracy and the least sensitivity to variation of the proton resonance offset and duration of the BIRD/INEPT delay (2τ, τ) are given in the legends of Figure 1 and in Table S2.

To test the robustness of the phase program optimized sequences of Figure 1 with respect to proton resonance offset, the spectrometer operating (carrier) frequency was varied in two frequency ranges: from 700 Hz up to 780 Hz off-resonance from the CH_3-signal, and from 1900 Hz up to 1980 Hz off-resonance, both in steps of 2 Hz, to give 40 experiments in each case. The latter offset corresponds to half of an average protein NH-frequency window at 800 MHz. The 40 spectra recorded with the optimized phase program yielded an average value of $^1J_{CH}$ = 143.96 Hz with a maximum deviation of 0.42 Hz and a standard deviation (σ_J) of 0.17 Hz in the 700 – 780 Hz offset range, and $^1J_{CH}$ = 144.04 Hz with a maximum deviation of 1.05 Hz and σ_J of 0.40 Hz in the 1900 – 1980 Hz range (see Figures S1A and S1B for corresponding plots of apparent J vs. offset). As expected, the uncertainty in $^1J_{CH}$ increases with offset, so it can be helpful to make measurements with different carrier frequencies for best results. Figure S2 shows overlays of the 40 antiphase CH_3-doublets measured using the CLAP variant of the sequence of Figure 1 for the two offset ranges.

The impact of the duration of the BIRD/INEPT delays (2τ, τ) was also tested, with τ set for the range of $^1J_{CH}$ from 125 Hz to 175 Hz, corresponding to a typical spread of coupling constants in samples dissolved in weakly orienting media for RDC (*Residual Dipolar Coupling*) measurement. Using τ values set for a range of 15 Hz either side of the actual $^1J_{CH}$ value of 144 Hz gave a maximum deviation of 0.6 Hz, with τ values at the edges of the range tending to overestimate $^1J_{CH}$. As τ was moved further from the optimum value the latter tendency increased, with errors reaching 1.4 Hz at +/– 30 Hz (see experimental data in Table S3 of the Supporting Information). The proposed experiment is thus reasonably tolerant of variation in coupling constant, but if RDCs larger than +/- 30 Hz are anticipated and/or more accurate J/D values are required, then multiple experiments with different settings of the BIRD/INEPT delays should be performed.

Finally, the impact of miscalibration of ^{1}H and ^{13}C pulses on the accuracy of the measured J values was studied by setting the corresponding pulses longer of ca. 5 % in separate experiments, varying the ^{1}H offset in 40 steps over an 80 Hz range. It was found that at 5 % misset, the value of $^1J_{CH}$ remained basically unaffected, yielding J_{av} = 144.01 Hz with maximum deviation of 0.90 Hz and standard deviation σ_J = 0.37 Hz for a 5% error in ^{1}H pulse width, and J_{av} = 143.96 Hz with maximum deviation of 1.15 Hz and standard deviation σ_J = 0.57 Hz for a similar error in ^{13}C pulse width.

Full details of the phase cycling and sequencing combinations tested, together with the averages and standard deviations of $^1J_{CH}$ values and chemical shifts (δ) obtained for the CH_3-group of methyl α-D-mannopyranoside in the proton offset-dependence measurements, are given in Table S1 of the Supporting Information.

Having established the robustness of the new experiments, as a real case study the performance and reproducibility of the optimized real-time BIRD$^{(d)}$ CLIP/CLAP-HSQC sequences of Figure 1 were investigated on a 55-residue ^{15}N-labeled protein (PAF)[29, 30] sample in H_2O by running multiple measurements. Experiments for all three ^{1}H-^{15}N CLIP/CLAP-HSQC variants, conventional proton-coupled, BIRD$^{(d)}$ interferogram-based, and real-time homonuclear decoupled CLIP/CLAP-HSQCs, were performed for comparison. In general, triplicate measurements were carried out to estimate the uncertainties of the $^1J_{NH}$ values

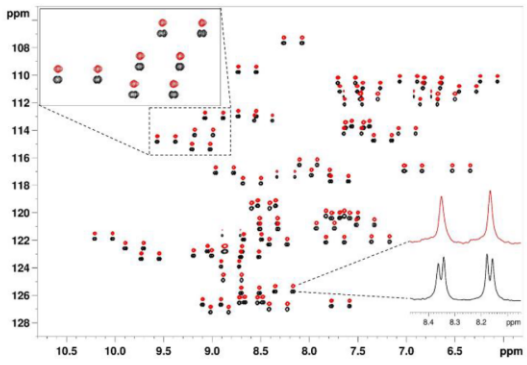

Figure 2 Overlay of ^{1}H-^{15}N CLIP-HSQC spectra of ^{15}N-labeled Penicillium antifungal protein (PAF, 1.7 mM in 95% H_2O / 5 % D_2O using 20 mM Na_3PO_4 pH 6.0 buffer, 40 mM NaCl, 0.04 % NaN_3, as 275 µl of solution in Shigemi NMR tube), acquired by the conventional proton-coupled (black, lower) and real-time broadband proton-homodecoupled (red, upper) pulse sequence. The decoupled spectrum is shifted in the nitrogen dimension for better visualization. An expansion and representative doublets are shown to demonstrate the simplification of peak patterns achieved by broadband proton homodecoupling using the pulse sequence of Figure 1. The following parameters were used in these experiments: spectral width in ^{1}H (^{15}N) dimension = 4.7880 (21.0) ppm, number of complex data points in ^{1}H dimension = 2048, number of t_1 increments = 256, number of scans = 8, relaxation delay = 1.7 s. Data acquisition in the pure shift experiment was divided into 16 chunks and the duration of each chunk was 26.7 ms.

obtained. $^1J_{NH}$ values determined from a BIRD$^{(d)}$ CLIP-HSQC spectrum recorded with interferogram-based acquisition, where cumulative errors are not a problem, were used as reference values. It has been recently shown[3] that the latter experiment provides reliable and precise $^1J_{XH}$ values by direct measurement of the separations of peak maxima in the X-coupled doublets. In the present study, for fast and automated evaluation of coupling constants the peak positions were simply determined using automatic peak picking in all spectra. In the case of the conventional, proton-coupled experiment, spectra were processed with sufficient line broadening in F_2 to ensure that proton-proton couplings were not resolved.

To demonstrate the spectral simplification and resolution enhancement achieved by the proposed method, an overlay of the proton-coupled (black) and real-time broadband proton-homodecoupled (red) ^{1}H-^{15}N CLIP-HSQC spectra of ^{15}N-labeled PAF, together with selected expansions and doublets, is shown in Figure 2. For detailed comparison of the three CLIP/CLAP-HSQC variants, representative CLIP doublets are also shown in Figure 3.

The almost perfect match between pure shift doublets measured in real-time (green) and in interferogram (black) experiments is remarkable. In contrast, the proton-coupled doublets (blue in Figure 3) show doublet fine structure due to proton-proton coupling that is slightly asymmetric, possibly as a result of relaxation effects or of homonuclear J modulation during the INEPT sequence elements. When severe weighting is used (red) to broaden out the homonuclear coupling structure to allow automated peak-picking, a systematic underestimation of $^1J_{CH}$ is evident. Consequently, the coupling constants extracted from the regular, proton-coupled CLIP/CLAP-HSQC spectra with automated peak analysis are biased (specifically, slightly underestimated), as demonstrated in Figure 4, where the $^1J_{NH}$ values of the well resolved resonances of PAF

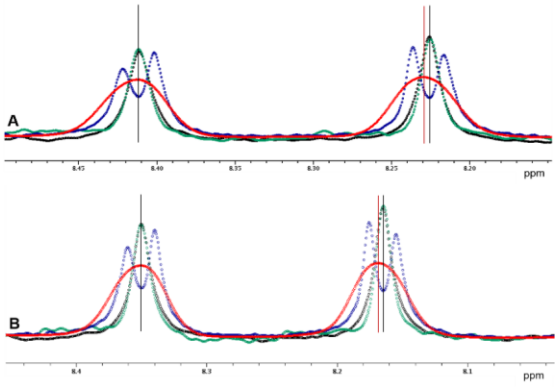

Figure 3 Representative doublets of Phe-25 (**A**) and Val-52 (**B**) in PAF extracted from the conventional proton-coupled (blue and red), interferogram-based decoupled (black) and real-time decoupled (green) ^{1}H-^{15}N CLIP-HSQC spectra of ^{15}N-labeled protein. Relevant experimental parameters are the same as given for Figure 2. In the interferogram-based experiment 4 scans and 16 chunks were used for construction of the FIDs. In the case of the proton-coupled variant, a strong Gaussian apodization function was applied during processing (red) to obscure splitting due to proton-proton coupling to aid automated spectral analysis.

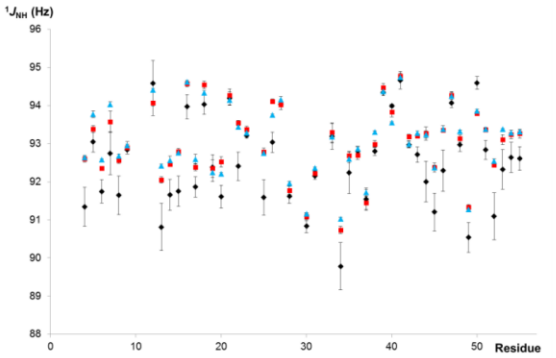

Figure 4 Comparison of $^1J_{NH}$ values measured using the three types of ^{1}H-^{15}N CLIP/CLAP-HSQC spectra of ^{15}N-labeled PAF (1.7 mM in 95% H_2O / 5% D_2O) as a function of residue number. Mean values of 6 experiments in the case of coupled (black diamonds) and real-time decoupled (red squares), and mean values of 3 experiments in the case of interferogram-based decoupled (blue triangles) method are plotted. Standard deviations based on multiple measurements are depicted as error bars. Peak positions were determined using automated peak-picking in each case, and a script (named RDC-calculator) implemented in CCPNMR was used for the calculation of coupling constants. $^1J_{NH}$ values are not shown in some cases due to low intensity signals/line broadening (Lys-2, Ser-10, Lys-11, Asp-32) or signal overlap (Tyr-3, Thr-24).

determined by automated analysis of the three CLIP/CLAP-HSQC variants are shown as a function of residue number. Note that almost all the $^1J_{NH}$ values determined from the proton-coupled spectra (labeled with black diamonds in Figure 4) are slightly smaller – with a maximum deviation of 1.6 Hz, and deviations > 1 Hz for 13 residues out of 47 – than the $^1J_{NH}$ values measured from the decoupled spectra. Noticeably smaller deviations, with a maximum of 0.46 Hz and only 4 residues > 0.35 Hz, were found between corresponding $^1J_{NH}$ values extracted from the real-time and the interferogram proton-homodecoupled spectra. The average standard deviation for the proton-homodecoupled experiments, based on six measurements (three real-time BIRD$^{(d)}$ CLIP-HSQCs and three real-time BIRD$^{(d)}$ CLAP-HSQC), was about half of that for the proton-coupled experiments. All the relevant data are summarized for comparison in Table S4 of the Supporting Information.

To mimic the variation in coupling constant typically expected in proteins under anisotropic conditions, multiple experiments were performed with different BIRD/INEPT delays, corresponding to the range of couplings from 66 Hz to 116 Hz in steps of 5 Hz. The $^1J_{NH}$ values measured for BIRD/INEPT delays set for 86 - 111 Hz for residues of PAF are plotted in Figure 5; the maximum average absolute deviation from the mean of $^1J_{NH}$ is only 0.33 Hz over this range. Importantly, even over the 50 Hz range of 66 - 116 Hz the maximum deviation increases only slightly, up to 1.05 Hz. All the data are summarized in Table S5 of the Supporting Information. These data, with only modest errors in $^1J_{NH}$ values, thus provide good evidence for the applicability of the proposed real-time experiments to N-H RDC measurements in proteins.

As a proof of principle, real-time BIRD$^{(d)}$ CLIP/CLAP-HSQC experiments were performed with the pulse sequence of Figure 1 on a ^{15}N-PAF sample prepared in the weakly orienting

Figure 5 Comparison of $^1J_{NH}$ values measured for well-resolved resonances of ^{15}N-labeled PAF (1.7 mM in 95% H_2O / 5% D_2O) using the real-time broadband proton-homodecoupled CLIP- and CLAP-HSQC sequences of Figure 1 with different settings of the INEPT/BIRD delays. The delays (τ, τ', 2τ in Figure 1) were varied to correspond to couplings from 86 to 111 Hz in steps of 5 Hz. $^1J_{NH}$ values are not shown in some cases due to low intensity signals/line broadening (Lys-2, Ser-10, Lys-11, Asp-32) or signal overlap (Tyr-3, Thr-24).

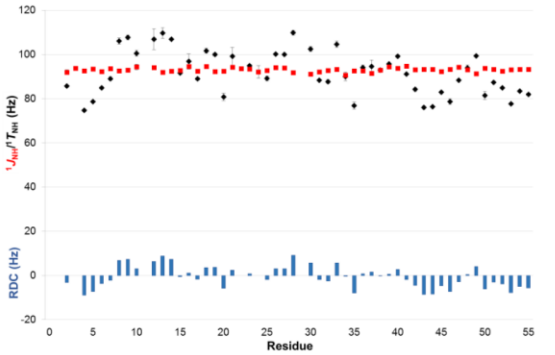

Figure 7 Comparison of $^1J_{NH}$ (red squares) and $^1T_{NH}$ = ($^1J_{NH}$ + 2 * $^1D_{NH}$) values (black diamonds) measured with the real-time broadband proton-homodecoupled CLIP- and CLAP-HSQC sequences proposed in ^{15}N-labeled PAF under isotropic (95 % H_2O / 5 % D_2O) and anisotropic conditions (5% C_8E_5, octanol),[31] respectively. Error bars shown are estimated from data scattering in multiple measurements. RDCs (blue columns), representing the value of $^1D_{NH}$, are also shown as a function of residue number.

medium[31] containing 5% C_8E_5 and octanol in H_2O. Representative excerpts from the ^{15}N-CLIP-HSQC spectra – proton-coupled in black and real-time BIRD$^{(d)}$ homodecoupled in red – together with selected doublets are shown in Figure 6. The sequence variation of $^1T_{NH}$ and $^1J_{NH}$, and their differences $^1D_{NH}$ as a measure of the RDCs, are plotted in Figure 7 for those residues that are not broadened and/or overlapping. As expected the average standard deviation of $^1T_{NH}$-values obtained in the anisotropic medium was somewhat larger (1.00 Hz) than that obtained under isotropic condition (0.17 Hz). All relevant data, including standard deviations (RMSD) assessed from multiple experiments, are supplied in Table S6 of the

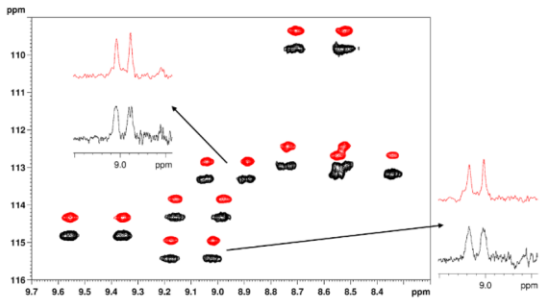

Figure 6 Overlay of parts of the ^{1}H-^{15}N CLIP-HSQC spectra of ^{15}N-labeled PAF protein (3.2 mg) dissolved in weakly orienting medium 5% C_8E_5 and octanol[31] in H_2O/D_2O (total 500 µl, pH = 6, phosphate buffer), acquired using the conventional proton-coupled (black, lower) and real-time broadband proton-homodecoupled (red, upper) sequence. The decoupled spectrum is shifted in the nitrogen dimension for better visualization. Representative doublets are shown to demonstrate the simplification of peak patterns achieved by broadband proton homodecoupling using the pulse sequence of Figure 1. The following parameters were used in these experiments: spectral width in ^{1}H (^{15}N) dimension = 4.7880 (21.0) ppm, number of complex data points in ^{1}H dimension = 1024 (2048 for coupled), number of t_1 increments = 256, number of scans = 32, relaxation delay = 1.7 s. Data acquisition in the pure shift experiment was divided into 8 chunks and the duration of each chunk was 26.7 ms. Traces are extracted at δ_{15N} = 113.3 ppm (top) and 115.4 ppm (right), respectively.

Supporting Information, and provide further evidence that the proposed real-time BIRD$^{(d)}$ CLIP/CLAP-HSQC experiments are suitable for reliable automated one-bond ^{1}H-^{15}N RDC measurements in proteins.

Having established that real-time BIRD$^{(d)}$ CLIP/CLAP-HSQC experiments are useful for $^1J_{NH}$ and $^1D_{NH}$ extraction for weakly aligned proteins, we now turn to the case of $^1J_{CH}$ and $^1D_{CH}$ measurements in a small organic molecule without isotopic enrichment. The challenges associated with one-bond coupling measurement in small organic molecules are different from those arising for backbone amides in proteins, as greater robustness of the experiment with respect to differences in coupling network and one-bond coupling is required in this case. On the other hand, the effects of transverse relaxation are much less pronounced in small molecules, increasing the benefits of homodecoupling.

To evaluate the techniques described, we measured real-time BIRD$^{(d)}$ CLIP/CLAP-HSQC spectra for the same samples used in a previous study,[5] containing (+)-isopinocampheol dissolved in dichloromethane-d_2 for measurements in isotropic phase, and in a high molecular weight poly-γ-benzyl-D-glutamate/dichloromethane-d_2 liquid crystalline medium[32, 33] for measurement under weak alignment. Initial concerns about sample stability arose when a slightly different deuterium quadrupolar splitting $\Delta\nu_Q$ = 110.5 Hz, instead of $\Delta\nu_Q$ = 107.6 Hz, was observed compared to the previous measurement 20 months earlier. The difference seen can probably be explained by a slight change (~ 0.5 K) that was found in the temperature calibration of the setup used, although ageing of the sample cannot be excluded even though the sample was thoroughly degassed and sealed. For comparison purposes, the total and dipolar couplings reproduced from the previous study have therefore been scaled here by the ratio of the quadrupolar splittings observed, to take into account the slight increase in order parameter.

For the isotropic sample, a reduction of the spectral quality obtained in the real-time BIRD$^{(d)}$ decoupled experiments is seen

compared to the experiments with interferogram-based BIRD$^{(d)}$ decoupling. Representative traces for direct comparison are given in Figure S3. The $^1J_{CH}$ coupling constants which are extracted from real-time BIRD$^{(d)}$ CLIP/CLAP-HSQCs reflect this, showing marked deviations from the values obtained from the spectra with interferogram-based homodecoupling, which in turn agree much better with the experiments without homodecoupling (real-time BIRD$^{(d)}$ CLIP/CLAP-HSQC: maximum deviations of 0.9 Hz and standard deviations σ_J of 0.4 Hz; CLIP/CLAP-HSQC without homodecoupling: maximum deviations of 0.2 Hz and standard deviations σ_J: of 0.1 Hz; see columns 1, 4 and 5 of Table S7). Thus for small organic molecules, the compromise between experiment duration and experimental accuracy required when moving from interferogram to real-time BIRD$^{(d)}$ decoupling is much less favorable than it is for proteins.

In addition to comparing different experiment types, Table S7 offers two further comparisons. First, it shows that for real-time decoupling, longer data chunks provide more accurate coupling constant measurement, since, as noted above, extending the period of the decoupling cycle reduces the amplitudes of the unwanted extra irradiation frequencies. The upper limit on chunk duration is determined by the acceptable level of the chunking sidebands that are caused by coupling evolution during data chunks. As a consequence, reducing the acquisition chunk duration from 20.48 ms to 15.36 ms and further to 10.24 ms leads to a progressive reduction in coupling constant measurement accuracy (compare columns 5 - 7 of Table S7). Second, it can be seen that using an 8 step phase cycle in place of the 16 step cycling used in the rest of this study leads to virtually identical results (compare columns 5 and 8 of Table S7).

In the case of the weakly aligned sample it is reassuring to see that the real-time BIRD$^{(d)}$ approach provides a significant linewidth reduction as compared to the experiment without homodecoupling, without any requirement to increase the experiment duration through the introduction of an additional homodecoupling time dimension (as in interferogram experiments). Figure 8 illustrates that for weakly aligned samples, just as for the PAF protein, marked reductions in signal widths are possible with real-time BIRD$^{(d)}$ decoupling. Decoupling sidebands are mostly below 5% of the main signal intensity, and therefore are likely to be masked by spectral noise for low concentration samples.

As in our previous study,[5] in anisotropic solution, the most challenging protons for homodecoupling techniques are protons H7a and H7s (for numbering, see Figure 8), which show a geminal splitting of $^2T_{CH}$ ≈ -38.4 Hz under the current alignment conditions. The poor lineshape observed, which is illustrated as an insert in Figure 8, prompted us to estimate very conservative experimental errors for the one-bond couplings extracted for these protons (5 to 7 Hz for the data sets acquired with 20.48 ms chunk length), while the error estimates are much smaller for other signals. In general, the BIRD homodecoupling is not able to suppress geminal couplings. From signals such as H4a/s and H8, it can be seen however, that

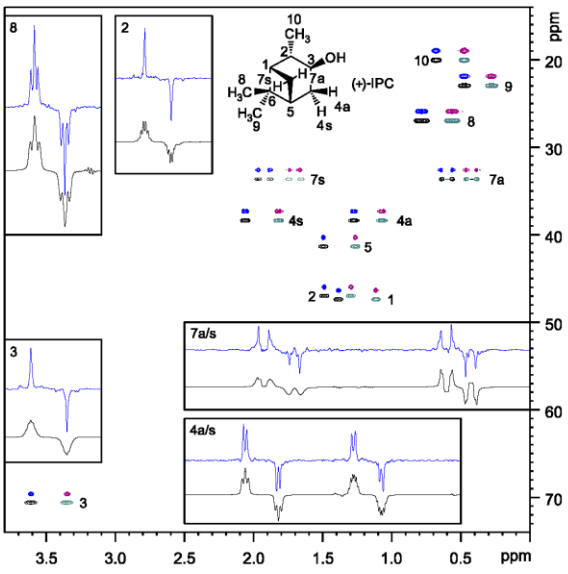

Figure 8 CLAP-HSQC spectra with real-time BIRD decoupling (pos. blue, neg. magenta; 20.48 ms chunk duration) and without homodecoupling (pos. black, neg. cyan) in the proton dimension. The spectra were acquired for a sample containing (+)-isopinocampheol dissolved in a PBLG/CD_2Cl_2 lyotropic liquid crystalline medium (9.05%-wt, $\Delta\nu_Q$ = 110.5 Hz). The selected F_2 traces shown are plotted at the same absolute intensity scale. In the proton numbering given, the descriptors "s" and "a" refer to *syn* or *anti* with respect to the dimethylmethylene bridge.

for smaller geminal couplings the residual homonuclear splittings do not prevent $^1T_{CH}$ extraction.

While for $^1J_{CH}$ couplings it was found that the measurement accuracy was reduced compared to the experiment without homodecoupling, this was not the case for the $^1T_{CH}$ couplings listed in Table S8. Restricting the discussion to the results obtained with a chunk length of 20.48 ms, data collected with real-time BIRD$^{(d)}$ decoupling and data collected with no homodecoupling agree equally well with the data from the perfectBIRD CLIP-HSQC experiment chosen as reference (real-time BIRD$^{(d)}$ CLIP/CLAP-HSQC: maximum deviations of 1.5 to 2.0 Hz and standard deviations σ_J of 0.7 to 0.9 Hz; CLIP/CLAP-HSQC without homodecoupling: maximum deviations of 1.0 to 3.4 Hz and standard deviations σ_J of 0.5 to 1.5 Hz; see columns 1, 4, 5 and 8 of Table S8). Taking the same experiment time, for small molecules the real-time decoupled experiment thus seems to perform as well as the experiment without decoupling, even in the absence of signal overlap.

The RDCs listed in Table S9 finally show that the real-time BIRD$^{(d)}$ decoupled experiment with a chunk length of 20.48 ms provides one-bond RDCs which agree sufficiently well with the reference data (maximum deviations of 1.1 to 1.2 Hz and standard deviations σ_J of 0.5 to 0.6 Hz; see columns 5 and 8 of Table S9) thus the use of this experiment in structural studies of small molecules is practical. Based on these data we suggest using a minimum confidence interval of ±1 Hz for RDCs measured in small molecules using real-time BIRD$^{(d)}$ homodecoupling. Compared to the results obtained for backbone N-H RDC measurement in the test protein system this

is a slight reduction in accuracy, which can be attributed to the differences in complexity of spin system between these two test samples. As in the case of the protein study, if larger variations in resonance offset or in one-bond coupling than used in this study occur, we recommend that either an independent evaluation of the experiment accuracy be performed, or that several experiments with different experimental parameters be used (the maximum offsets used here were 1540 Hz for ^{1}H and 4000 Hz for ^{13}C, and one-bond total couplings varied between 106 and 161 Hz).

In addition to comparing the one-bond couplings measured with those from a high accuracy reference dataset, we chose to evaluate the one-bond RDC measurement accuracy by testing the consistency of the different datasets against a structural model already used in previous studies.[5, 32-34] The agreement of the experimentally determined $^{1}D_{CH}$ values with the structural model, as expressed by the RMSD between the experimental and the back-calculated RDCs, confirms that the data measured using real-time BIRD$^{(d)}$ decoupled CLIP-HSQCs agree with the structure as well as the data obtained from CLIP-HSQCs without homodecoupling. The RMSD ranges from 0.15 Hz to 0.28 Hz for real-time BIRD CLIP/CLAP-HSQC experiments with 20.48 ms chunk length, and from 0.16 Hz to 0.26 Hz for CLIP/CLAP-HSQC experiments without homodecoupling (see columns 1, 7 – 10, 13 and 14 of Table S10).

This sample study of (+)-isopinocampheol illustrates that real-time BIRD$^{(d)}$ CLIP/CLAP-HSQC experiments can provide one-bond RDCs with sufficient accuracy for small molecule structural studies. While RDC measurement accuracies are higher in experiments using interferogram-based homodecoupling, the accuracy in the real-time BIRD$^{(d)}$-decoupled experiment can be comparable to that obtained in experiments without homodecoupling. The technique presented thus paves the way for rapid and pure shift RDC measurements in small molecules.

Conclusions

We have described experimental methods for obtaining pure shift CLIP/CLAP-HSQC spectra utilizing isotope-selective BIRD$^{(d)}$-based *J*-refocusing elements for real-time broadband proton-proton decoupling, leading to significant resolution enhancement in the directly detected (^{1}H) dimension at no extra cost in measurement time. The resultant real-time BIRD$^{(d)}$ CLIP/CLAP-HSQC spectra provide broadband proton-homodecoupled pure in- or anti-phase doublets with improved resolution, allowing direct and relatively precise measurement of one-bond heteronuclear couplings using quick automatic peak picking algorithms during spectral analysis of protein N-H regions.

The utility of the real-time pure shift sequences presented here has been demonstrated for coupling constant measurements under both isotropic and anisotropic conditions, on a protein sample and on a small test molecule. The numerous tests and comparisons with reference data demonstrate that the proposed real-time BIRD$^{(d)}$ CLIP/CLAP-HSQC experiments show good precision, reproducibility and robustness for the measurement of coupling constants. Applicable to samples in both isotropic and anisotropic media, they provide reliable and precise data for probing the structures and dynamics of molecules via RDC analysis.

Acknowledgements

This research was supported by the National Research, Development and Innovation Office of Hungary (grant numbers NKFI/OTKA NN 109671 and K 105459 to K. E. K.), by the Richter Gedeon Talentum Alapítvány (Ph.D. scholarship to I.T. and M.H.R.), by the Engineering and Physical Sciences Research Council (grant numbers EP/I007989/1 and EP/L018500/1), by the ERC (grant number 257041 to C.M.T.), and by the Merck Foundation for Arts and Science (Ph.D. scholarship to L.K.).
The authors thank Dr. Florentine Marx for providing the ^{15}N-labeled PAF protein sample.

Notes and references

1 A. Enthart, J. C. Freudenberger, J. Furrer, H. Kessler and B. Luy, *J. Magn. Reson.*, 2008, **192**, 314-322.
2 L. Castañar and T. Parella, in *Annual Reports on NMR Spectroscopy*, ed. A. W. Graham, Academic Press, 2015, vol. 84, pp. 163-232.
3 I. Timári, L. Kaltschnee, A. Kolmer, R. W. Adams, M. Nilsson, C. M. Thiele, G. A. Morris and K. E. Kövér, *J. Magn. Reson.*, 2014, **239**, 130-138.
4 T. Reinsperger and B. Luy, *J. Magn. Reson.*, 2014, **239**, 110-120.
5 L. Kaltschnee, A. Kolmer, I. Timári, V. Schmidts, R. W. Adams, M. Nilsson, K. E. Köver, G. A. Morris and C. M. Thiele, *Chem. Commun.*, 2014, **50**, 15702-15705.
6 M. Nilsson and G. A. Morris, *Chem. Commun.*, 2007, 933-935.
7 J. A. Aguilar, S. Faulkner, M. Nilsson and G. A. Morris, *Angew. Chem. Int. Ed.*, 2010, **49**, 3901-3903.
8 A. Lupulescu, G. L. Olsen and L. Frydman, *J. Magn. Reson.*, 2012, **218**, 141-146.
9 L. Paudel, R. W. Adams, P. Király, J. A. Aguilar, M. Foroozandeh, M. J. Cliff, M. Nilsson, P. Sándor, J. P. Waltho and G. A. Morris, *Angew. Chem. Int. Ed.*, 2013, **52**, 11616-11619.
10 J. R. Garbow, D. P. Weitekamp and A. Pines, *Chem. Phys. Lett.*, 1982, **93**, 504-509.
11 K. Zangger and H. Sterk, *J. Magn. Reson.*, 1997, **124**, 486-489.
12 L. Castañar, P. Nolis, A. Virgili and T. Parella, *Chem. Eur. J.*, 2013, **19**, 17283-17286.
13 R. W. Adams, L. Byrne, P. Király, M. Foroozandeh, L. Paudel, M. Nilsson, J. Clayden and G. A. Morris, *Chem. Commun.*, 2014, **50**, 2512-2514.
14 J. Ying, J. Roche and A. Bax, *J. Magn. Reson.*, 2014, **241**, 97-102.
15 N. H. Meyer and K. Zangger, *Angew. Chem. Int. Ed.*, 2013, **52**, 7143-7146.
16 R. W. Adams, in *eMagRes*, John Wiley & Sons, Ltd, 2014, vol. 3, pp. 295-310.
17 L. Castañar and T. Parella, *Magn. Reson. Chem.*, 2015, **53**, 399-426.
18 K. Zangger, *Prog. Nucl. Magn. Reson. Spectrosc.*, 2015, **86–87**, 1-20.
19 P. Kiraly, R. W. Adams, L. Paudel, M. Foroozandeh, J. A. Aguilar, I. Timári, M. J. Cliff, M. Nilsson, P. Sándor, G. Batta, J. P. Waltho, K. E. Kövér and G. A. Morris, *J. Biomol. NMR*, 2015, **62**, 43-52.

20 M. Perez-Trujillo, L. Castanar, E. Monteagudo, L. T. Kuhn, P. Nolis, A. Virgili, R. T. Williamson and T. Parella, *Chem. Commun.*, 2014, **50**, 10214-10217.
21 D. Uhrin, T. Liptaj and K. E. Kover, *J. Magn. Reson., Ser A*, 1993, **101**, 41-46.
22 G. A. Morris, G. L. Nayler, A. J. Shaka, J. Keeler and R. Freeman, *J. Magn. Reson.*, 1984, **58**, 155-160.
23 A. J. Shaka, J. Keeler, R. Freeman, G. A. Morris and G. L. Nayler, *J. Magn. Reson.*, 1984, **58**, 161-166.
24 V. M. Kakita and J. Bharatam, *Magn. Reson. Chem.*, 2014, **52**, 389-394.
25 S. Glanzer and K. Zangger, *J. Am. Chem. Soc.*, 2015, **137**, 5163-5169.
26 S. Glanzer and K. Zangger, *ChemPhysChem*, 2015, **16**, 3313-3317.
27 S. Glanzer, O. Kunert and K. Zangger, *J. Magn. Reson.*, 2016, **268**, 88-94.
28 G. A. Morris and R. Freeman, *J. Magn. Reson.*, 1978, **29**, 433-462.
29 G. Batta, T. Barna, Z. Gáspári, S. Sándor, K. E. Kövér, U. Binder, B. Sarg, L. Kaiserer, A. K. Chhillar, A. Eigentler, É. Leiter, N. Hegedüs, I. Pócsi, H. Lindner and F. Marx, *FEBS Journal*, 2009, **276**, 2875-2890.
30 G. Váradi, G. K. Tóth, Z. Kele, L. Galgóczy, Á. Fizil and G. Batta, *Chem. Eur. J.*, 2013, **19**, 12684-12692.
31 M. Rückert and G. Otting, *J. Am. Chem. Soc.*, 2000, **122**, 7793-7797.
32 A. Marx, V. Schmidts and C. M. Thiele, *Magn. Reson. Chem.*, 2009, **47**, 734-740.
33 A. Marx and C. Thiele, *Chem. Eur. J.*, 2009, **15**, 254-260.
34 N. C. Meyer, A. Krupp, V. Schmidts, C. M. Thiele and M. Reggelin, *Angew. Chem. Int. Ed.*, 2012, **51**, 8334-8338.

Table S7. Scalar one-bond couplings ($^1J_{CH}$) measured for (+)-isopinocampheol in CD_2Cl_2. For comparison, the values reported previously are reproduced here. Standard deviations (σ_i) and maximum deviations (Δ_{max}) reported are calculated with respect to the interferogram perfectBIRD decoupled CLIP-HSQC experiment.

		Values reproduced from ref.[1], ‡			Values for this work (same sample, measurement 20 months later)				
		CLIP	BIRD CLIP	perfectBIRD CLIP	CLIP	rt-BIRD CLIP	rt-BIRD CLIP	rt-BIRD CLIP	rt-BIRD CLIP
NS		2	2	2	16	16	16	16	8
FID-res		0.76 Hz	1.02 Hz	1.02 Hz	1.53 Hz	0.76 Hz	1.53 Hz	1.53 Hz	0.76 Hz
chunk duration		-	15.36 ms	15.36 ms	-	20.48 ms	15.36 ms	10.24 ms	20.48 ms
exp. time		10.5min	7h 8min	9h 26min	3h 20min	3h 20min	3h 20min	3h 20min	1h 40min
C	H		$^1J_{CH}$ / Hz				$^1J_{CH}$ / Hz		
1	1	140.57 ± 0.32	140.56 ± 0.11	140.59 ± 0.11	140.63 ± 0.25	140.47 ± 1.00	141.59 ± 1.50	141.44 ± 0.20	140.38 ± 1.50
2	2	126.67 ± 0.17	126.65 ± 0.11	126.59 ± 0.12	126.72 ± 0.20	126.86 ± 0.30	126.72 ± 0.10	126.13 ± 0.60	126.88 ± 0.40
3	3	141.67 ± 0.11	141.69 ± 0.11	141.71 ± 0.12	141.66 ± 0.10	141.73 ± 0.50	141.87 ± 0.80	142.32 ± 0.80	141.75 ± 1.00
4	4s	126.35 ± 0.18	126.35 ± 0.24	126.34 ± 0.13	126.44 ± 0.25	127.25 ± 0.80	126.72 ± 1.00	127.92 ± 2.00	127.16 ± 0.90
4	4a	127.04 ± 0.12	127.02 ± 0.19	127.07 ± 0.13	126.98 ± 0.20	127.60 ± 0.90	127.11 ± 0.90	128.06 ± 1.40	127.68 ± 0.60
5	5	140.79 ± 0.32	140.72 ± 0.14	140.64 ± 0.23	140.78 ± 0.50	140.11 ± 1.00	139.94 ± 1.60	139.98 ± 3.00	140.05 ± 1.00
7	7s	134.87 ± 0.35	134.81 ± 0.13	134.79 ± 0.17	134.96 ± 0.40	134.79 ± 1.30	135.12 ± 1.00	135.69 ± 0.60	134.79 ± 1.00
7	7a	136.98 ± 0.15	136.94 ± 0.20	136.94 ± 0.12	137.02 ± 0.20	136.43 ± 1.60	136.46 ± 1.40	136.62 ± 0.70	136.51 ± 0.80
8	8	124.56 ± 0.16	124.51 ± 0.12	124.51 ± 0.12	124.56 ± 0.15	124.49 ± 0.30	124.69 ± 0.20	125.03 ± 0.90	124.54 ± 0.20
9	9	123.61 ± 0.11	123.66 ± 0.11	123.70 ± 0.12	123.60 ± 0.10	123.60 ± 0.60	123.80 ± 0.80	123.23 ± 0.50	123.52 ± 0.40
10	10	124.75 ± 0.13	124.69 ± 0.11	124.64 ± 0.15	124.71 ± 0.15	124.58 ± 0.60	125.26 ± 0.50	124.36 ± 0.30	124.53 ± 0.30
δ; Δ_{max} / Hz		0.08; 0.15	0.05; 0.08	reference	0.11; 0.17	0.40; 0.91	0.48; 1.00	0.79; 1.58	0.40; 0.82
		CLAP	BIRD CLAP	perfectBIRD CLAP	CLAP	rt-BIRD CLAP	rt-BIRD CLAP	rt-BIRD CLAP	rt-BIRD CLAP
NS		2	2	2	16	16	16	16	8
FID-res		0.76 Hz	1.02 Hz	1.02 Hz	1.53 Hz	0.76 Hz	1.53 Hz	1.53 Hz	0.76 Hz
chunk duration		-	15.36 ms	15.36 ms	-	20.48 ms	15.36 ms	10.24 ms	20.48 ms
exp. time		10.5min	7h 8min	9h 26min	3h 20min	3h 20min	3h 20min	3h 20min	1h 40min
C	H		$^1J_{CH}$ / Hz				$^1J_{CH}$ / Hz		
1	1	140.54 ± 0.26	140.58 ± 0.15	140.56 ± 0.11	140.49 ± 0.20	140.63 ± 0.70		141.34 ± 0.20	
2	2	126.71 ± 0.16	126.63 ± 0.12	126.56 ± 0.14	126.79 ± 0.20	126.94 ± 0.25		126.03 ± 0.60	
3	3	141.67 ± 0.12	141.71 ± 0.12	141.75 ± 0.13	141.63 ± 0.15	142.11 ± 0.70		141.78 ± 0.70	
4	4s	126.37 ± 0.15	126.32 ± 0.22	126.31 ± 0.18	126.39 ± 0.30	127.19 ± 0.60		127.71 ± 2.00	
4	4a	127.06 ± 0.12	127.06 ± 0.19	127.08 ± 0.16	126.95 ± 0.25	127.58 ± 0.80		128.14 ± 1.20	
5	5	140.73 ± 0.29	140.71 ± 0.24	140.60 ± 0.20	140.81 ± 0.40	140.15 ± 1.00		139.19 ± 2.00	
7	7s	134.85 ± 0.31	134.84 ± 0.11	134.78 ± 0.13	134.91 ± 0.50	134.80 ± 0.80		135.63 ± 0.70	
7	7a	136.99 ± 0.12	137.01 ± 0.22	136.93 ± 0.12	136.99 ± 0.15	136.46 ± 0.70		136.46 ± 0.80	
8	8	124.60 ± 0.14	124.48 ± 0.12	124.47 ± 0.11	124.56 ± 0.10	124.58 ± 0.20		124.64 ± 0.60	
9	9	123.63 ± 0.10	123.69 ± 0.11	123.69 ± 0.11	123.60 ± 0.10	123.61 ± 0.30		123.32 ± 0.40	
10	10	124.74 ± 0.13	124.67 ± 0.11	124.59 ± 0.15	124.75 ± 0.10	124.78 ± 0.40		124.13 ± 0.50	
δ; Δ_{max} / Hz		0.08; 0.12	0.04; 0.07	0.04; 0.05	0.12; 0.20	0.41; 0.85		0.82; 1.45	

Table S8. One-bond couplings ($^1T_{CH}$) measured for (+)-isopinocampheol weakly aligned in CD_2Cl_2/PBDG (9.05%-wt, $\Delta\nu_Q$ = 110.5 Hz). Values previously reported are scaled by the ratio of the quadrupolar splittings ($T_{i,scaled} = J_i + (T_{i,original} - J_i)*(\Delta\nu_{Q,\,scaled}/\Delta\nu_{Q,\,original})$). Standard deviations ($\sigma_J$) and maximum deviations (Δ_{max}) reported are calculated with respect to the interferogram perfectBIRD decoupled CLIP-HSQC experiment.

		Values reproduced from ref.[1] (scaled for comparison), ‡			Values for this work (same sample, measurement 20 months later)				
		CLIP	BIRD CLIP	perfectBIRD CLIP	CLIP	rt-BIRD CLIP	rt-BIRD CLIP	rt-BIRD CLIP	rt-BIRD CLIP
NS		2	2	2	16	16	16	16	8
FID-res		0.76 Hz	3.05 Hz	3.05 Hz	1.53 Hz	1.53 Hz	1.53 Hz	1.53 Hz	0.76 Hz
chunk duration		-	10.24 ms	10.24 ms	-	20.48 ms	15.36 ms	10.24 ms	20.48 ms
exp. time		10.5min	2h 49min	3h 13min	3h 20min	3h 20min	3h 20min	3h 20min	1h 40min
C	H		$^1T_{CH}$ / Hz				$^1T_{CH}$ / Hz		
1	1	161.21 ± 3.51	161.47 ± 0.87	160.72 ± 0.56	162.36 ± 2.80	161.57 ± 0.90	161.85 ± 3.00	162.59 ± 1.20	161.46 ± 0.90
2	2	117.02 ± 1.65	116.74 ± 0.19	116.26 ± 0.48	116.40 ± 1.40	116.37 ± 1.40	116.24 ± 1.50	116.53 ± 2.00	116.33 ± 1.30
3	3	158.76 ± 0.53	158.83 ± 0.35	158.96 ± 0.45	157.83 ± 0.60	157.68 ± 0.80	156.43 ± 0.80	158.07 ± 0.90	157.70 ± 0.80
4	4s	144.51 ± 0.12	144.32 ± 0.39	144.30 ± 0.20	144.65 ± 0.40	144.26 ± 0.80	145.46 ± 2.50	146.03 ± 3.00	144.10 ± 0.80
4	4a	122.42 ± 0.17	122.47 ± 0.46	122.44 ± 0.12	121.70 ± 0.60	121.91 ± 1.00	122.13 ± 2.60	121.61 ± 2.30	122.15 ± 1.00
5	5	138.03 ± 1.00	137.31 ± 0.85	137.03 ± 1.03	139.03 ± 1.40	138.59 ± 0.30	138.94 ± 0.60	138.83 ± 1.20	138.54 ± 0.40
7	7s	133.75 ± 1.82	134.01 ± 2.94	133.76 ± 0.33	133.06 ± 1.90	*133.46 ± 6.00*	*134.04 ± 15.00*	*132.21 ± 7.00*	*133.19 ± 7.00*
7	7a	106.08 ± 1.07	106.17 ± 0.89	106.00 ± 0.80	106.06 ± 0.50	*105.15 ± 5.00*	*104.27 ± 15.00*	*106.31 ± 14.00*	*105.32 ± 5.00*
8	8	131.89 ± 0.49	132.02 ± 0.61	131.85 ± 0.30	132.00 ± 0.80	132.12 ± 1.40	131.50 ± 1.20	132.88 ± 2.80	132.40 ± 1.20
9	9	118.43 ± 0.19	118.58 ± 0.58	118.83 ± 0.48	118.76 ± 0.40	118.89 ± 1.50	118.88 ± 1.80	118.58 ± 0.90	118.88 ± 1.00
10	10	121.19 ± 0.21	120.99 ± 0.62	120.77 ± 0.80	121.16 ± 0.30	120.85 ± 0.80	121.18 ± 1.40	121.08 ± 1.80	120.90 ± 1.00
δ; Δ_{max} / Hz		0.46; 1.01	0.32;0.76	reference	0.93; 2.01	0.74; 1.57	1.22; 2.54	1.17; 1.88	0.72; 1.52
		CLAP	BIRD CLAP	perfectBIRD CLAP	CLAP	rt-BIRD CLAP	rt-BIRD CLAP	rt-BIRD CLAP	rt-BIRD CLAP
NS		2	2	2	16	16	16	16	8
FID-res		0.76 Hz	3.05 Hz	3.05 Hz	1.53 Hz	1.53 Hz	1.53 Hz	1.53 Hz	1.53 Hz
chunk duration		-	10.24 ms	10.24 ms	-	20.48 ms	15.36 ms	10.24 ms	20.48 ms
exp. time		10.5min	2h 49min	3h 13min	3h 20min	3h 20min	3h 20min	3h 20min	1h 40min
C	H		$^1T_{CH}$ / Hz				$^1T_{CH}$ / Hz		
1	1	163.26 ± 1.75	161.21 ± 1.26	161.01 ± 0.46	164.11 ± 2.60	161.06 ± 1.20		162.56 ± 1.00	
2	2	117.00 ± 2.02	116.66 ± 0.24	116.44 ± 0.45	116.41 ± 2.00	116.36 ± 1.20		116.31 ± 1.70	
3	3	158.75 ± 1.12	158.85 ± 0.60	159.01 ± 0.47	155.97 ± 1.20	157.01 ± 1.00		157.39 ± 1.40	
4	4s	144.53 ± 0.13	144.35 ± 0.54	144.34 ± 0.16	144.64 ± 0.50	144.39 ± 0.60		145.64 ± 1.20	
4	4a	122.36 ± 0.41	122.48 ± 0.43	122.48 ± 0.18	121.67 ± 0.50	121.88 ± 0.80		121.32 ± 2.20	
5	5	138.29 ± 1.22	137.35 ± 0.59	137.06 ± 0.67	139.01 ± 1.20	138.60 ± 0.30		138.86 ± 1.10	
7	7s	134.33 ± 3.75	133.97 ± 3.17	133.77 ± 0.26	133.49 ± 2.40	*134.55 ± 7.00*		*132.41 ± 8.00*	
7	7a	106.15 ± 0.31	106.13 ± 2.93	105.97 ± 0.23	106.29 ± 0.40	*106.23 ± 7.00*		*113.94 ± 11.00*	
8	8	132.19 ± 0.38	132.10 ± 0.60	131.95 ± 0.17	131.91 ± 0.90	132.00 ± 1.00		132.55 ± 1.90	
9	9	118.24 ± 0.25	118.66 ± 0.35	118.82 ± 0.34	118.89 ± 0.20	119.28 ± 1.40		117.94 ± 0.80	
10	10	121.25 ± 0.32	121.00 ± 0.14	120.70 ± 0.34	121.36 ± 0.40	121.68 ± 1.00		120.11 ± 2.00	
δ; Δ_{max} / Hz		0.94; 2.54	0.26; 0.50	0.12; 0.29	1.53; 3.40	0.88; 1.96		2.68; 7.95	

‡: *Chem.Commun.*, 2014, **50**, 15702 – Published by The Royal Society of Chemistry

Table S9. One-bond RDCs ($^1D_{CH}$) measured for (+)-isopinocampheol weakly aligned in CD_2Cl_2/PBDG (9.05%-wt, $\Delta\nu_Q$ = 110.5 Hz). Values previously reported are scaled by the ratio of the quadrupolar splittings ($D_{i,scaled} = D_{i,original}*(\Delta\nu_{Q,\ scaled}/\ \Delta\nu_{Q,\ original})$. Standard deviations ($\sigma_i$) and maximum deviations (Δ_{max}) reported are calculated with respect to the interferogram perfectBIRD decoupled CLIP-HSQC experiment.

		Values reproduced from ref.[1] (scaled for comparison), ‡			Values reported in this work (same sample, measurement 20 months later)				
		CLIP	BIRD CLIP	perfectBIRD CLIP	CLIP	rt-BIRD CLIP	rt-BIRD CLIP	rt-BIRD CLIP	rt-BIRD CLIP
NS		2	2	2	16	16	16	16	8
chunk duration		-	differs for $^1J_{CH}$ and $^1T_{CH}$ measurement		-	20.48 ms	15.36 ms	10.24 ms	20.48 ms
C	H		$^1D_{CH}$ / Hz				$^1D_{CH}$ / Hz		
1	1	10.32 ± 3.52	10.45 ± 0.87	10.06 ± 0.56	10.87 ± 2.80	10.55 ± 1.00	10.13 ± 3.00	10.58 ± 1.20	10.54 ± 1.50
2	2	-4.83 ± 1.65	-4.96 ± 0.22	-5.17 ± 0.49	-5.16 ± 1.40	-5.25 ± 1.40	-5.24 ± 1.50	-4.80 ± 2.00	-5.28 ± 1.30
3	3	8.54 ± 0.53	8.57 ± 0.36	8.63 ± 0.46	8.09 ± 0.60	7.98 ± 0.80	7.28 ± 0.80	7.88 ± 0.90	7.97 ± 1.00
4	4s	9.08 ± 0.22	8.99 ± 0.45	8.98 ± 0.24	9.11 ± 0.40	8.51 ± 0.80	9.37 ± 2.50	9.06 ± 3.00	8.47 ± 0.90
4	4a	-2.31 ± 0.21	-2.27 ± 0.49	-2.32 ± 0.17	-2.64 ± 0.60	-2.85 ± 1.00	-2.49 ± 2.60	-3.23 ± 2.30	-2.77 ± 1.00
5	5	-1.38 ± 1.05	-1.70 ± 0.85	-1.81 ± 1.05	-0.88 ± 1.40	-0.76 ± 1.00	-0.50 ± 1.60	-0.57 ± 3.00	-0.76 ± 1.00
7	7s	-0.56 ± 1.85	-0.40 ± 2.94	-0.51 ± 0.37	-0.95 ± 1.90	*-0.66 ± 6.00*	*-0.54 ± 15.00*	*-1.74 ± 7.00*	*-0.80 ± 7.00*
7	7a	-15.45 ± 1.08	-15.38 ± 0.90	-15.47 ± 0.80	-15.48 ± 0.50	*-15.64 ± 5.00*	*-16.10 ± 15.00*	*-15.16 ± 14.00*	*-15.60 ± 5.00*
8	8	3.67 ± 0.51	3.75 ± 0.62	3.67 ± 0.32	3.72 ± 0.80	3.82 ± 1.40	3.41 ± 1.20	3.93 ± 2.80	3.93 ± 1.20
9	9	-2.59 ± 0.22	-2.54 ± 0.59	-2.43 ± 0.49	-2.42 ± 0.40	-2.36 ± 1.50	-2.46 ± 1.80	-2.33 ± 0.90	-2.32 ± 1.00
10	10	-1.78 ± 0.25	-1.85 ± 0.63	-1.94 ± 0.81	-1.78 ± 0.30	-1.87 ± 0.80	-2.04 ± 1.40	-1.64 ± 1.80	-1.82 ± 1.00
δ; Δ_{max} / Hz		0.20; 0.43	0.16; 0.40	reference	0.45; 0.94	0.47; 1.05	0.62; 1.35	0.68; 1.24	0.47; 1.06
		CLAP	BIRD CLAP	perfectBIRD CLAP	CLAP	rt-BIRD CLAP	rt-BIRD CLAP	rt-BIRD CLAP	rt-BIRD CLAP
NS		2	2	2	16	16	16	16	8
chunk duration		-	differs for $^1J_{CH}$ and $^1T_{CH}$ measurement		-	20.48 ms	15.36 ms	10.24 ms	20.48 ms
C	H		$^1D_{CH}$ / Hz				$^1D_{CH}$ / Hz		
1	1	11.36 ± 1.77	10.32 ± 1.26	10.22 ± 0.47	11.81 ± 2.60	10.22 ± 1.20		10.61 ± 1.00	
2	2	-4.86 ± 2.02	-4.99 ± 0.27	-5.06 ± 0.46	-5.19 ± 2.00	-5.29 ± 1.20		-4.86 ± 1.70	
3	3	8.54 ± 1.12	8.57 ± 0.61	8.63 ± 0.48	7.17 ± 1.20	7.45 ± 1.00		7.80 ± 1.40	
4	4s	9.08 ± 0.20	9.02 ± 0.58	9.02 ± 0.24	9.12 ± 0.50	8.60 ± 0.60		8.97 ± 2.00	
4	4a	-2.35 ± 0.42	-2.29 ± 0.46	-2.30 ± 0.24	-2.64 ± 0.50	-2.85 ± 0.80		-3.41 ± 2.20	
5	5	-1.22 ± 1.25	-1.68 ± 0.64	-1.77 ± 0.70	-0.90 ± 1.20	-0.78 ± 1.00		-0.16 ± 2.00	
7	7s	-0.26 ± 3.76	-0.44 ± 3.16	-0.50 ± 0.29	-0.71 ± 2.40	*-0.13 ± 7.00*		*-1.61 ± 8.00*	
7	7a	-15.42 ± 0.33	-15.44 ± 2.94	-15.48 ± 0.26	-15.35 ± 0.40	*-15.12 ± 7.00*		*-11.26 ± 11.00*	
8	8	3.79 ± 0.40	3.81 ± 0.61	3.74 ± 0.20	3.68 ± 0.90	3.71 ± 1.00		3.96 ± 1.90	
9	9	-2.70 ± 0.27	-2.52 ± 0.36	-2.43 ± 0.35	-2.36 ± 0.20	-2.17 ± 1.40		-2.69 ± 0.80	
10	10	-1.75 ± 0.34	-1.83 ± 0.17	-1.95 ± 0.37	-1.70 ± 0.40	-1.55 ± 1.00		-2.01 ± 2.00	
δ; Δ_{max} / Hz		0.46; 1.30	0.13; 0.26	0.07; 0.16	0.76; 1.75	0.56; 1.18		1.48; 4.22	

Table S10. Quality factors obtained from an error-weighted fitting of the RDCs reported in Table S9 (including values reported in brackets) to the DFT-derived structural model previously used.[1, 3-5]

	Values reproduced from ref.[1], ‡						Values for this work (same sample, measurement 20 months later)							
	CLIP	CLAP	BIRD CLIP	BIRD CLAP	perfectBIRD CLIP	perfectBIRD CLAP	CLIP	CLAP	rt-BIRD CLIP	rt-BIRD CLAP	rt-BIRD CLIP	rt-BIRD CLIP	rt-BIRD CLAP	rt-BIRD CLIP
NS	2		2		2		16		16		16	16		8
chunk duration	-		differs for $^1J_{CH}$ and $^1T'_{CH}$ measurement				-		20.48 ms		15.36 ms	10.24 ms		20.48 ms
RMSD [Hz]	0.159	0.322‡	0.155	0.142	0.139	0.139	0.230	0.258	0.258	0.150	0.414	0.324	1.307	0.275
Q[a]	0.028	0.030	0.040	0.044	0.026	0.021	0.013	0.010	0.035	0.016	0.017	0.027	0.046	0.038

[a]: The error weighted quality factor Q was used as defined in ref.[6] ‡: this value is biased towards higher discrepancies by partial signal overlap occurring due to low F_1-resolution, as has been described previously.[1]

7.5. Conclusion on Project B

In this chapter a whole class of novel pure shift NMR experiments is described, which were tailored to improve the precision of one-bond RDC measurement for solution state structure elucidation. The class of methods described enables extraction of scalar ($^1J_{CH}$) and total ($^1T_{CH}$) one-bond coupling constants from the high-resolution proton dimension of modified CLIP/CLAP-HSQC[166] experiments, which feature proton-proton broadband homonuclear decoupling in the dimension of coupling constant extraction. Their ability to collapse even very broad and featureless signals, often observed for weakly aligned samples, into comparably narrow and well-defined peaks clearly makes these techniques highly interesting for application in future RDC-based studies.

Two basic interferogram-based pure shift extensions of the CLIP/CLAP HSQC experiment are presented in sections 7.2 and 7.3, which feature excellent quality of the resulting spectra and high accuracy and precision for coupling constant measurements. At least for small molecule studies these techniques outperform most of the existing techniques in terms of RDC extraction precision. In RDC-based solution structure studies, compound isolation or synthesis, sample preparation and the data analysis following the measurement of RDCs are often quite time consuming and laborious. Therefore, obtaining the maximum amount of structural information at the highest possible accuracy and precision often is of prime importance. Possible gains in RDC data quality may thus be well worth the increased demand in experiment time of these techniques. Additionally, the common benefit of pure shift techniques to reduce the likelihood of signal overlap by reduced signal widths may strongly reduce systematic errors introduced by partial signal overlap. If signal overlap completely prohibits RDC-extraction in experiments without suppression of long-range couplings, pure shift experiments may even reveal key information previously inaccessible, in particular if only a small number of RDCs is available at all.

For applications, where RDCs need to be measured rapidly or where experimental sensitivity is of prime importance, furthermore a F_2-real-time BIRD CLIP/CLAP-HSQC experiment is presented. This experiment was equipped with a complex phase cycling, which reduced systematic errors to the apparent coupling constants measured by phase cycling both from scan to scan and from one homonuclear decoupling element to the next. The accumulation of systematic errors through the homonuclear decoupling technique thereby is actively counteracted, making the experiment sufficiently robust for use in RDC-measurements, if large parameter offsets are avoided. The experiment proofed particularly well suitable for $^1D_{NH}$ measurement in the amide region of the 55-residue penicillium antifungal protein used for testing. For (+)-isopinocampheol, a purely aliphatic small organic test substance, it could be shown, that the RDC data that can be obtained is of comparable quality than the data obtained from experiments without homonuclear decoupling in this case, while the experiment narrows down the signal widths observed significantly, virtually without introducing extra costs in experiment durations. While the quality of the RDC data that can be obtained clearly lacks behind the performance of interferogram-based experiments, the F_2-real-time BIRD CLIP/CLAP-HSQC experiment offers a good alternative, wherever the extra cost in experiment duration inherent in interferogram-based experiments should be avoided.

Having the full set of F_2-homodecoupled CLIP/CLAP-HSQC experiments at hand clearly offers the user additional valuable choices for experimental methods for RDC measurement. For challenging questions of solution structure investigation the experimental challenges inherent in RDC-measurement are very manifold. As a consequence, a single experimental technique will not be able to replace the rich information content that can be obtained by combining different experimental techniques. Whenever several different techniques are combined, however, the question of differences in experimental accuracies and precisions has to be carefully addressed to avoid improper weighting of the results obtained with different methods. With the very careful investigation of experimental (in-)accuracies and precisions in these projects we provide a solid base for realistic error estimation, which is of key importance for RDC solution structure investigations.

The new experimental methods presented also contain significant methodological advances in terms of experiment development. With these investigations, one-bond coupling constant extraction has moved to the high resolution broadband proton-proton decoupled proton dimension of F_2-coupled experiments. This previously could not be achieved.

Of particular note should be the development of a new homonuclear decoupling approach. The introduction of BIRD decoupling into a modified perfect echo element, offers a very versatile alternative to constant-time BIRD decoupling[228, 229, 342] if full broadband proton-proton decoupling is required in proton dimensions of HSQC spectra. PerfectBIRD decoupling is particularly interesting because of its ability to even decouple diastereotopic methylene protons in a broadband experiment, without the need for a constant time delay, which always requires a compromise between experimental sensitivity and achievable resolution to be made. This is particularly critical for pure shift experiments, in which the homonuclear decoupling achieved can only be exploited, if high resolution is achieved in the homodecoupled dimension. The utilization of the perfectBIRD homonuclear decoupling in other experiments can be perceived.
For methods development of real-time pure shift techniques, the benefit of phase-cycling during acquisition clearly is demonstrated. It can be expected, that the real-time decoupling technique used here is not the only technique that suffers from small but notable systematic changes of apparent signal positions or coupling constants. Despite the close analogy of the problem arising to the well-known problem of Bolch-Siegert-shifts[258] in double-resonance experiments[258, 357] and in band-selective homonuclear decoupling during acquisition[248, 249], explicit note of these aspects has only been given by a few authors[298, 307]. It would be highly desirable, if it became common-place to use phase cycling strategies, as the one outlined, to reduce such systematic errors in future investigations.
The results of this chapter clearly illustrate the great potential of pure shift techniques with respect to precise measurements of coupling constants and thus of the structural information contained therein. It is shown, that in particular interferogram-based experiments are able to provide high quality experimental RDCs as valuable parameters for solution-based structure elucidation. While in Project A it was concluded that the extraction of NOE-based structural information from pure shift spectra requires a compromise in precision of the relative integral measurement to accepted, it is shown here, that pure shift approaches can increase the precision with which frequency differences can be measured, and in turn also increase the precision with which one-bond coupling constants can be determined. Pure shift experiments thus are not exclusively of value in the case of severe signal overlap, but can also facilitate and improve the extraction of information in solution-state NMR experiments.

8. Project C: Fully homodecoupled high resolution HSQC experiments

8.1. Motivation

In Chapter 7.3, a homonuclear decoupling approach was developed, which enabled full homonuclear decoupling of HSQC experiments in the proton dimension (as far as measurements in isotropic solution are concerned)[213]. HSQC experiment derived therein were tailored for heteronuclear one-bond coupling constant measurements along the pure shift dimension, an approach which largely benefits from the reduced line widths in the proton dimension. Narrower lines improved the precision of the coupling constant extraction and further reduced the likelihood for signal overlap to occur.
Better signal separation clearly also is beneficial for signal assignment purposes, and has been one of the major driving forces for increasing instrument B_0-field strengths over the past decades. In addition to increases in field strength, multidimensional methods [20, 34, 97] have been very successful in reducing signal overlap and enabling even highly sophisticated signal assignments.
When it comes to samples without isotope labelling, the very high resolution that can readily be achieved in ^{1}H-^{13}C-HSQC experiments typically is the best that is available in terms of signal dispersion, and for most cases studied clearly is sufficient. However, cases exist, in which also these methods come to their limits. This is most often the case, if chemical shift differences become small due to the chemical nature of the sample studied, e.g. if multiple signal sets exist for slowly interconverting conformers[358].
A variety of pure shift spectra has already been proposed for improving signal separation in HSQC experiments with heteronuclear decoupling[254, 305-307, 310, 312, 342, 343]. These techniques can reduce linewidths in the proton dimension of the experiment and thus complement methods which aim to improve the resolution in the carbon dimension per unit time, such as spectral aliasing[359], non-uniform data sampling[360, 361] and ASAP-techniques[362, 363]. In particular BIRD-based pure shift experiments have been introduced into HSQC experiments[254, 305, 307, 342, 343], because of their ability to produce broadband decoupled HSQC experiments, without introducing strong additional signal losses - in favourable cases, BIRD decoupling can even increase signal intensity in these experiments[305, 307].
With BIRD-based decoupling, however full broadband decoupling cannot be achieved in the case of diastereotopic methylene groups, as was extensively discussed in project B, unless constant-time approaches are used[229, 231, 342]. Furthermore, band-selective techniques are often limited in this case, by the small chemical shift difference between the two corresponding signals.
When presenting the perfectBIRD decoupling approach in section 7.3.1, a strategy was presented in Figure 7.6 b) that could possibly enable full homonuclear decoupling even of methylene groups in a BIRD-based approach, without resorting to the constant-time modification discussed. The potential use of fully homo- and heteronuclear broadband decoupled HSQC experiments in studies of extreme signal overlap led us to explore the extension of heteronuclear decoupled HSQC experiment with the F_2-perfectBIRD homonuclear decoupling technique.
The first section describes how a pulse sequence scheme was designed, which shows high robustness towards ^{13}C-transmitter offset and the second section is devoted to the case study of a peptidomimetic with only very poor signal resolution, which is a direct consequence of its constitution.

8.2. Implementation of F_2-perfectBIRD decoupling in heteronuclear decoupled HSQC experiments

As compared to the implementation of F_2-perfectBIRD decoupling in CLIP/CLAP-HSQC experiments (without homonuclear decoupling), as shown in Figure 1 b) of ref. [213], there are only very minor modifications required, to implement F_2-perfectBIRD decoupling into HSQC-experiments, according to

the homonuclear decoupling scheme in Figure 7.6 b). The first implementation that resulted is shown in Figure 8.1 a). The implementation between time points III and VI (excluding G_6) was adapted from the F_2-BIRD HSQC with heteronuclear decoupling[343] which had been implemented by KATALIN KÖVÉR. As compared to the experiment without heteronuclear decoupling, a single 180°-^{13}C-pulse (first blue ^{13}C-pulse in Figure 8.1 a)) was added to the delay that previously was τ_d (and now is $\tau_c + \tau_e$) and further heteronuclear decoupling is enabled during acquisition (labelled "CPD"). The timing is adjusted, such that for all t_2 heteronuclear one-bond couplings are refocused at time-point IV and that weak homonuclear couplings are refocused at time point V. In addition, chemical shift evolution is refocused at time point IV for $t_2 = 0$.

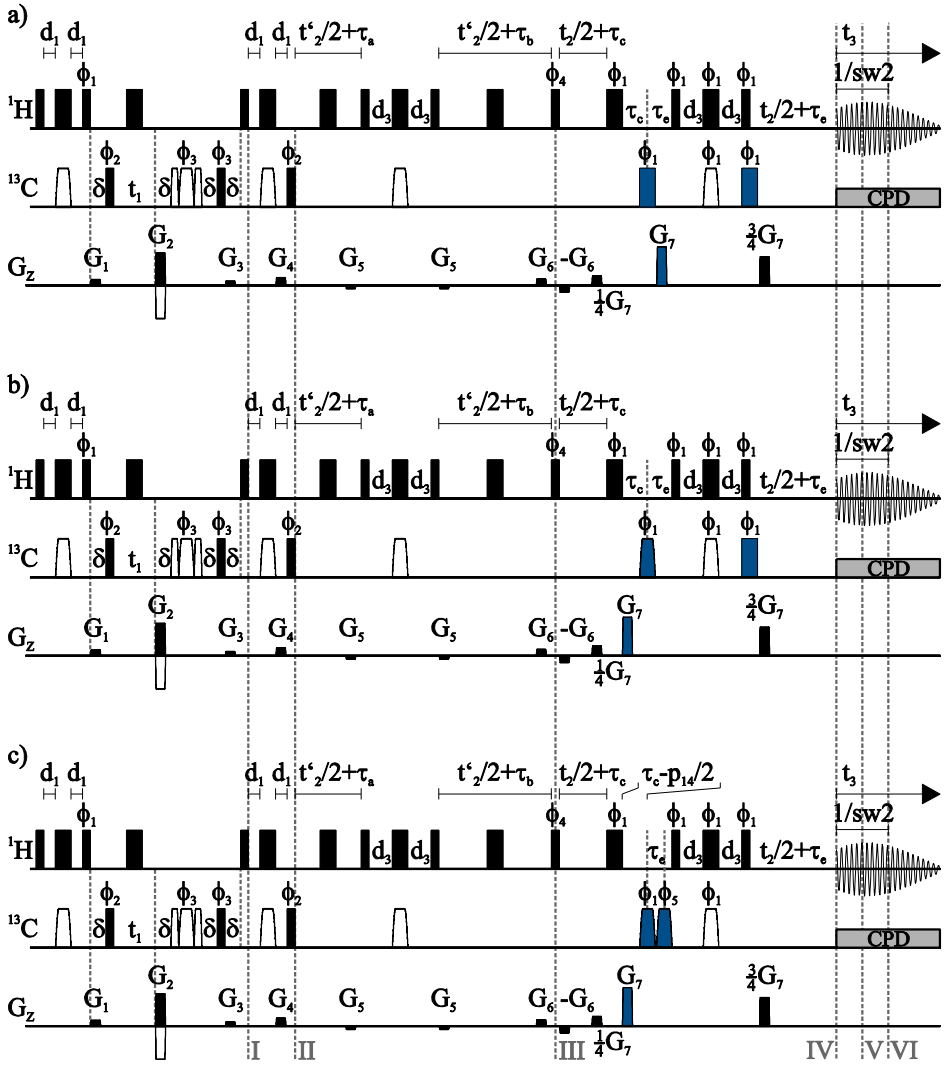

Figure 8.1: Different versions of the heteronuclear decoupled F_2-perfectBIRD HSQC. a) Hard-pulse implementation with timing according to Figure 7.6 (pulse program hsqcCLIP_EA_pBIRD_CPD.r1.4.lk; direct adaption of the timing in Fig. 5 of ref. [343]). b) Timing with replacement of one hard ^{13}C-pulse by a broadband adiabatic pulse (pulse program hsqcCLIP_EA_pBIRD_CPD.r2.1.lk). c) Pulse program using only broadband adiabatic pulses for inversion and refocusing on ^{13}C (pulse program hsqcCLIP_EA_pBIRD_CPD.r2.2.lk; the pulse programs reset_hsqcetgpsp_pe.t10.be for $\Delta = 1/(4*sw_1)$ and reset_hsqcetgpsp_pe.t11.be for $\Delta = 0$ use the same general scheme). All pulse sequences use Echo-Antiecho phase encoding in F_1, with inversion of G_2 every alternate scan. Rectangular symbols are for hard pulses, shaped symbols are for adiabatic inversion/refousing pulses if on the ^{13}C channel or for shaped gradients. δ equals the length of a gradient pulse plus a recovery delay. $d_1 = 0.5*d_3 \approx (^1J_{CH})$, $\tau_e = \delta$, $\tau_c = \Delta$, $\tau_b = \tau_e + 2\Delta$, , $\tau_a = \tau_e + 2\Delta$ – *length of INEPT*. p14 is the length of an adiabatic pulse used for inversion. The phase cycling used was: ϕ_1 = y, ϕ_2 = x, -x, ϕ_3 = x, x, x, x, -x, -x, -x, -x, ϕ_4 = y, y, -y, -y, ϕ_5 = -y, and the receiver phase used is ϕ_{rec} = x, -x, x, -x, -x, x, -x, x.

Initial tests on Cyclosporine A (**7**, structure shown in Figure 8.2), which were performed at a 9.4 T system (400 MHz ^{1}H frequency) provided clean spectra with full homonuclear- and heteronuclear decoupling along both dimensions (see Figure 8.3). Notable resolution improvements were achieved, albeit at comparably low signal-to-noise and with increased demands in experiment duration, which have two-fold origin: The homonuclear decoupling reduces linewidths and thus narrows signals broadened by signal multiplicity. Furthermore, the pseudo-3D acquisition scheme used loosens restrictions in F_2-resolution, normally inherent in HSQC experiments with heteronuclear decoupling. Normally in such experiments, the duration during which heteronuclear decoupling can be switched on is limited to roughly 100 to 150 ms by sample and instrument heating during decoupling[236]. While for small molecules, proton signals normally are detectable for roughly 1 s, the limited time that the heteronuclear decoupling can be used strongly limits the resolution usually available in HSQC experiments. However, the pseudo-3D acquisition method used here for generating pure shift data only samples small pieces of FID (typically 5 to 30 ms) in separate scans, avoiding long uninterrupted periods of acquisition with heteronuclear decoupling, and thus enables sampling of the F_2-time-domain signal for a time period that can be adjusted according to the experiment duration available. In the case shown here, the time-domain signal was acquired for 409.6 ms, which in itself results in a notable resolution enhancement for HSQC experiments.

To illustrate that both the increase in F_2-acquisition duration and the homonuclear decoupling bring significant improvements to the signal separation, we also applied the trick of sampling long FIDs in pseudo-3D acquisition mode to an HSQC experiment without homonuclear decoupling (the pulse sequence of which is shown in Figure 8.4). While there is a marked increase in resolution available with this experiment (see purple traces in Figure 8.3), for many signals the overall signal width is very similar to that obtained in the HSQC with only 102.4 ms of acquisition, due to the presence of signal multiplet structure. The homonuclear decoupling therefore is essential to make full use of the increased resolution of the experiment.

In cases where resolution shall be improved, but where signal multiplicity is not distracting, the pseudo-3D experiment has clear advantages, as the data chunks acquired can be acquired for the full length of broadband homonuclear decoupling possible (100 to 150 ms, as stated above), so a smaller number of repetitions is required to sample long FIDs. Please also note the pronounced loss in signal-to-noise ratio, that results from the less crude apodization used for this experiment. Further note, that on some experimental setups (e.g. probes with liquid-nitrogen-cooled coils), the limit on maximum acquisition durations with heteronuclear decoupling is less stringent than on the setups that were available here, if sample heating can be tolerated.

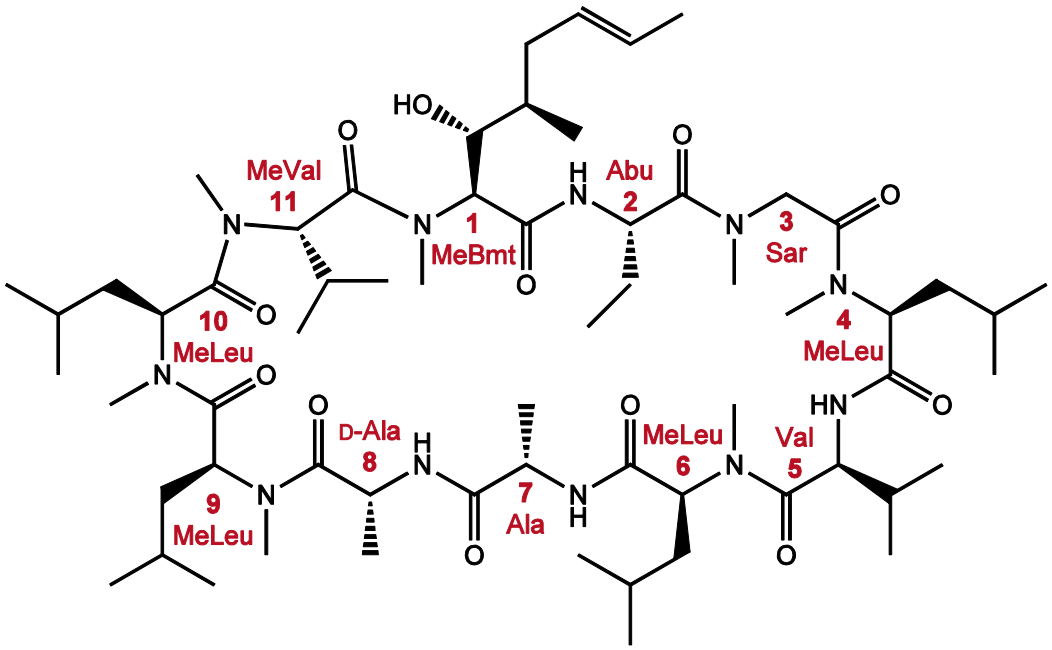

7

Figure 8.2: Cyclosporine A (**7**) structure with numbering of the amino acids. The numbering and the signal assignment used below was adapted from ref. [364].

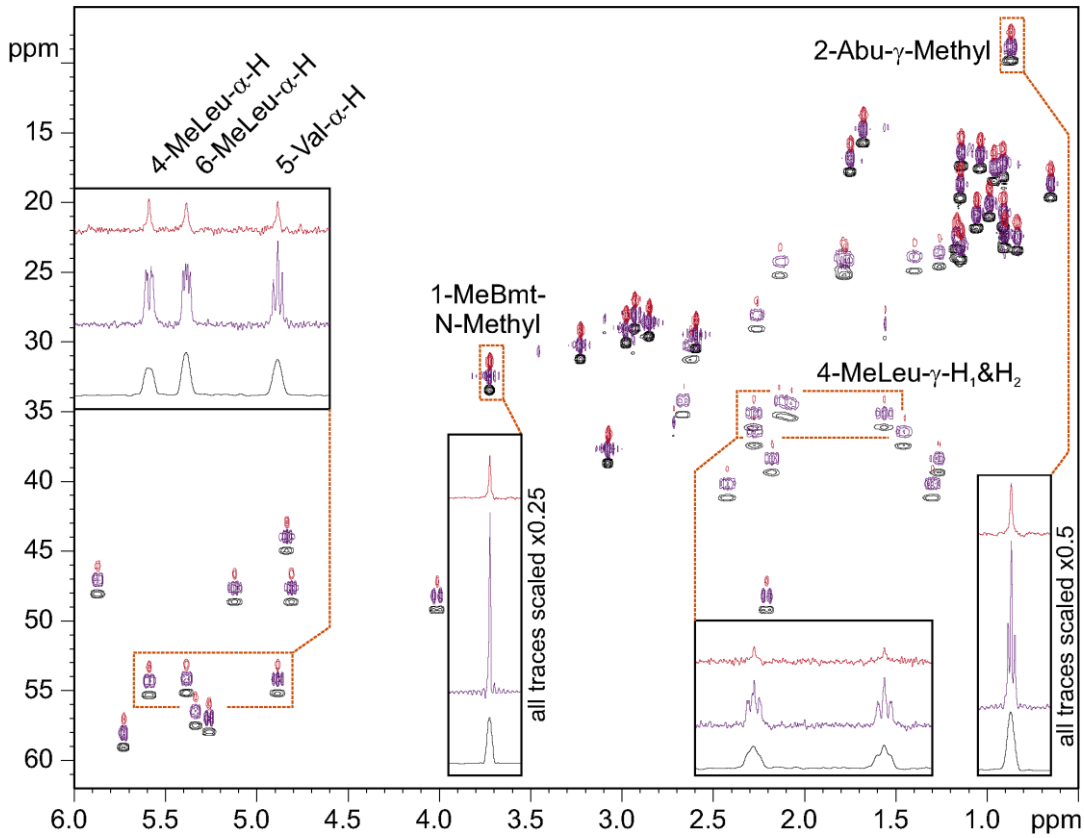

Figure 8.3: Cyclosporine A spectra acquired at 400 MHz ^{1}H frequency, with different HSQC variants. Black: gradient-selected ^{1}H-^{13}C-HSQC without homonuclear decoupling with 102.4 ms acquisition (56 min experiment duration). Purple: gradient-selected ^{1}H-^{13}C-HSQC without homonuclear decoupling with 409.6 ms acquisition (4 h 6 min experiment duration), enhanced by the pseudo-3D acquisition scheme illustrated in Figure 8.4. Red: F_2-perfectBIRD-HSQC with heteronuclear decoupling with 409.6 ms acquisition (18 h 21 min experiment duration), acquired with the pulse sequence scheme shown in Figure 8.1 a). Experimental parameters are provided in paragraph 14.1.5.

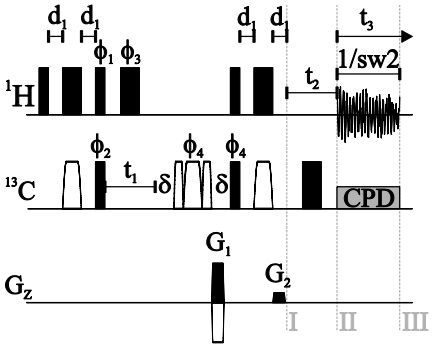

Figure 8.4: gradient-selected HSQC with pseudo-3D acquisition scheme for sampling in the proton dimension for durations that exceed the maximum duration tolerated with broadband heteronuclear decoupling (pulse sequence scheme: hsqcetgpsp.2_3D_r1.4.lk). A 2D dataset can be constructed from the pseudo-3D dataset obtained with the pshift-AU also used to rearrange interferogram-based pure shift data.

Limitations of the pulse sequence scheme shown in Figure 8.1 a) got apparent, when performing experiments at a 11.4 T system (600 MHz ^{1}H frequency), instead of at the 9.4 T system (400 MHz ^{1}H frequency). For all signals observed in the F_2-perfectBIRD HSQC with heteronuclear decoupling signal multiplicity was collapsed by the homonuclear decoupling, however unwelcome sidebands got apparent at the base of the very intense methyl signals in spectra of Cyclosporine A (**7**) (see traces shown in red in Figure 8.5). These sidebands clearly could not be caused by residual homonuclear couplings, as they even appeared for signals, such as the N-bound methyl groups, that appear as singlets in spectra without homonuclear decoupling. Furthermore, a pronounced reduction of signal intensity could be observed at large ^{13}C-transmitter offsets (the ^{13}C-transmitter was placed at 75 ppm for the spectra shown in Figure 8.5, resulting in a ^{13}C offset of 9.8 kHz for the γ-methyl-carbon of residue 2 – (2-aminobutyric acid)). These observations clearly pointed at an insufficient ^{13}C-offset robustness of the implementation shown in Figure 8.1 a). Increases in the GARP decoupling level lead to virtually identical results (data not shown), so a first guess was, that the two hard ^{13}C inversion pulses were likely to be the limiting factor in this case. Unfortunately, dropping these two pulses introduces a net $^{1}J_{CH}$-evolution during $2\tau_e$, which may lead to strong signal losses for unfortunate choices of τ_e.

Subsequent replacement of the hard ^{13}C-inversion pulses by adiabatic inversion pulses indeed solved the problem, but required a rearrangement of the pulse sequence timing between time points III and IV. First, I did not alter the hard ^{13}C-pulse being part of the BIRD^{d} element, but only replaced the first hard 180°-inversion pulse by an adiabatic broadband inversion (Figure 8.1 b)), because no timing using adiabatic inversion pulses was found that would fully refocus $^{1}J_{CH}$-evolution at time point IV. The pulse sequence in Figure 8.1 b) also only approximately achieves this. To keep τ_e short, the gradient marked in blue was moved in front of the adiabatic pulse. At a later stage, it was found that by moving both pulses in front to the BIRD element provides a pulse sequence where both ^{13}C-pulses shown in blue can be replaced by adiabatic broadband inversion pulses. Fully consistent timing is achieved, if both inversion pulses are spaced by τ_e, measured from the middle of each pulse, and if the direction of the frequency sweep is the same for both pulses. A similar sweep-direction and speed is critical here, to avoid ^{13}C-offset dependencies in the timing. The corresponding pulse sequence is shown in Figure 8.1 c). The effect the sequential replacement of hard pulses by adiabatic pulses has on the line shape observed is illustrated in Figure 8.6 for two representative methyl signals. With the pulse sequence shown in Figure 8.1 c) the peaks shown have the desired shape, while sidebands and a broadening at the base is observed with the previous versions of the pulse program.

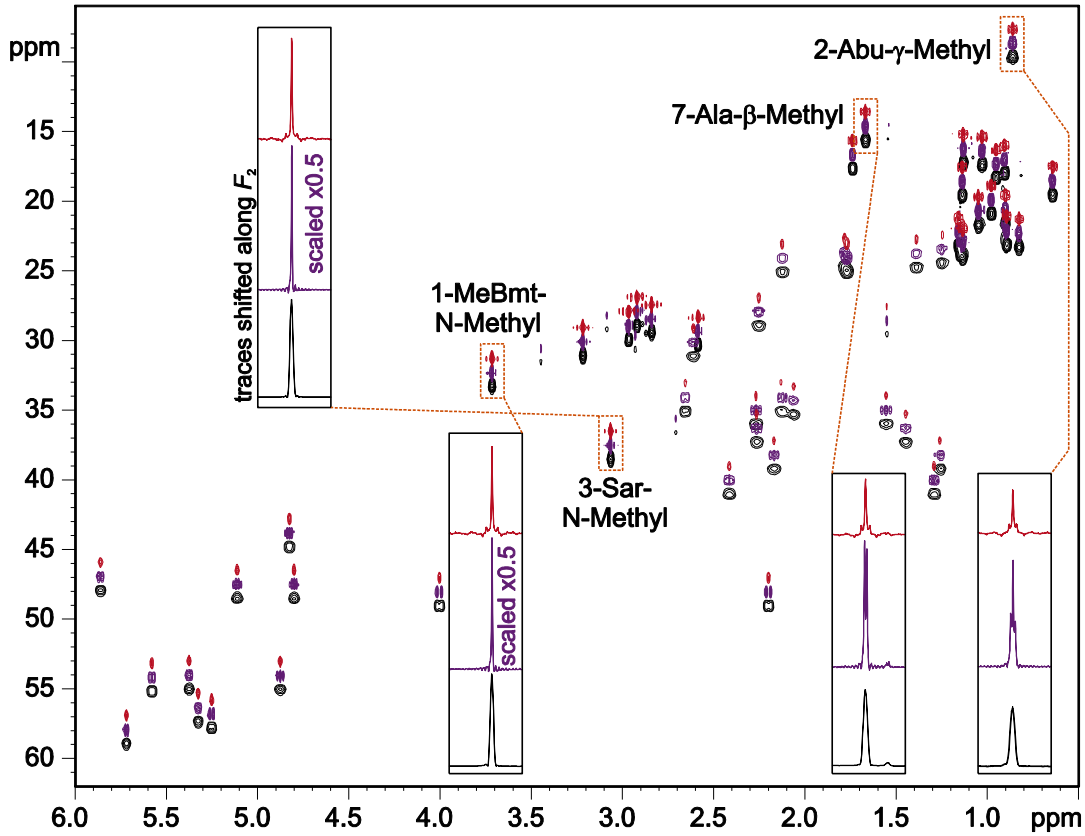

Figure 8.5: Cyclosporine A spectra acquired at 600 MHz ^{1}H frequency, with different HSQC variants. Black: gradient-selected ^{1}H-^{13}C-HSQC without homonuclear decoupling with 100 ms acquisition (30 min experiment duration). Purple: gradient-selected ^{1}H-^{13}C-HSQC without homonuclear decoupling with 352 ms acquisition (2 h 9 min experiment duration), enhanced by the pseudo-3D acquisition scheme illustrated in Figure 8.4. Red: F_2-perfectBIRD-HSQC with heteronuclear decoupling with 400 ms acquisition (13 h 14 min experiment duration, only the first 352 ms of t_2-data used for processing), acquired with the pulse sequence scheme shown in Figure 8.1 a). Experimental parameters are provided in paragraph 14.1.6.

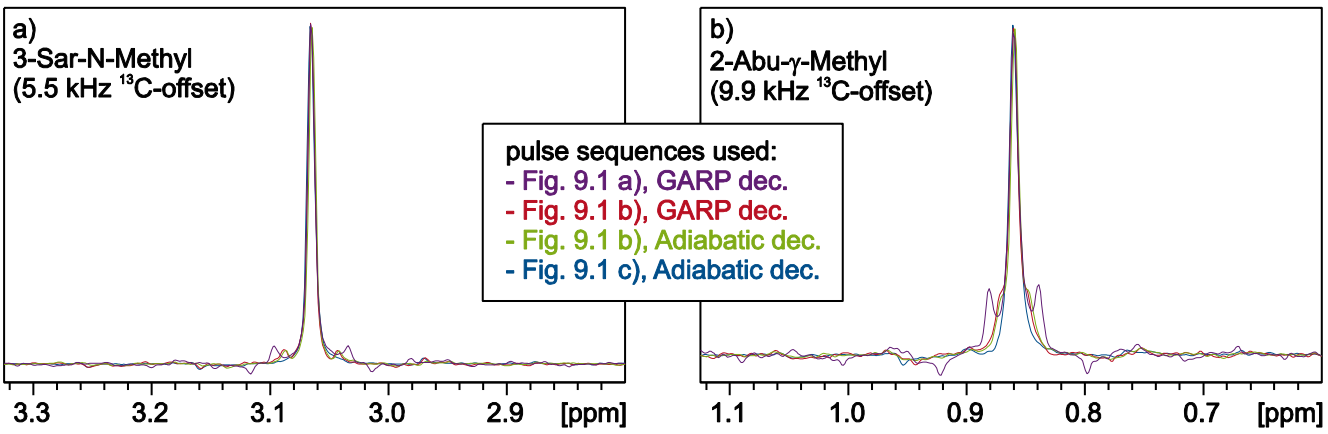

Figure 8.6: Comparison of the signal shape of two representative methyl groups, obtained with the different implementations of the F_2-perfectBIRD HSQC. Traces shown in purple are extracted from the homonuclear decoupled spectrum shown in Figure 8.5, acquired with the pulse sequence shown in Figure 8.1 a). Traces shown in blue are extracted from the homonuclear decoupled spectrum shown in Figure 8.9, acquired with the pulse sequence shown in Figure 8.1 c). Traces shown in red and in green are extracted from experiments with the pulse sequence shown in Figure 8.1 b). For these traces, experimental parameters are given in section 14.1.7. As indicated in the figure legend, different settings were used for heteronuclear broadband decoupling for the traces shown (GARP decoupling or adiabatic bi-level decoupling; for details see 14.1.6 and 14.1.7). Note that all traces have been scaled to the same height for easier comparison.

Throughout the development of these alternations to the pulse sequences, a series of measurements was performed on a chloroform sample, we chose for testing the experiment performance for a well isolated ^{1}H-^{13}C pair. The results are shown here, as they give interesting insights into the limiting factors for broadband applications of this experiment.

First, tolerance of the experiment towards misset of the BIRD/INEPT delays was tested for the pulse sequence shown in Figure 8.1 b). When offsetting this delay from its optimal value (for the sample used, $^{1}J_{CH}$ = 209.1 Hz), only a reduction in signal intensity was observed, yet no distortion of the signal shape and no appearance of artefacts was noted (see plots on the right of Figure 8.7). This illustrates that the experiment is reasonable tolerant towards BIRD/INEPT misset for most applications. In the implementation used, the signal intensity is decreased to roughly 60%, for a mismatch of - 50 Hz. If the avoidance of signal loss over a large range of coupling constants is critical, alternations using approximate compensations for these effects[365-369] might be introduced into the experiment.

In addition to the effect of *J*-mismatch, the effect of ^{13}C-offset was tested on this system. At increasing offsets up to 10 kHz, a broadening of the signal at the base which evolves to sidebands becomes apparent, as previously observed for Cyclosporine A. Above 10 kHz a sudden collapse of the signal is observed together with intense sidebands that are appearing. This behaviour is expected, as the GARP decoupling scheme used here is tightly matched to the typical spectral window on ^{13}C on this instrument to minimize sample and instrument heating (10 kHz correspond to 66 ppm on ^{13}C at 11.4 T).

The 10 kHz bandwidth clearly is too little for high field applications of the experiment, which in-fact is the most interesting scenario of application. Thus, further tests were performed to improve experimental robustness towards ^{13}C-transmitter offset. For the implementation shown in Figure 8.1 c) it could be shown, that the ^{13}C-offset tolerance can be largely increased (to above 22 kHz), if a broadband adiabatic decoupling scheme is used, instead of composite pulse decoupling (see left part of Figure 8.8). With alike high robustness towards ^{13}C-transmitter offset, the experiment is well-suitable even for applications at the highest fields, now available (e.g.: 22 kHz correspond to a 88 ppm spectral width on ^{13}C at 23.5 T (1 GHz ^{1}H resonance frequency)). I did not evaluate, if adiabatic sweeps over larger frequency ranges would increase ^{13}C-transmitter offset tolerance even further, even though for the homonuclear decoupled experiment, an increase in decoupling power mostly is not an issue, because only relatively short periods (< 30 ms) of heteronuclear decoupling are used.

A subtle difference, that may be noted for the F_2-perfectBIRD HSQC is, that in the tolerated ^{13}C-offset range, the decoupling sidebands, that are inherent to the heteronuclear decoupling scheme used do not appear at the positions they normally do (centred around the signal at entire multiples of the inverse pulse length used for heteronuclear decoupling; in this case $(1.5\ \text{ms})^{-1}$ = 333 Hz), but at positions close to the original sideband position, which are separated from the central signal by entire multiples of the chunk length used (see right part of Figure 8.8).

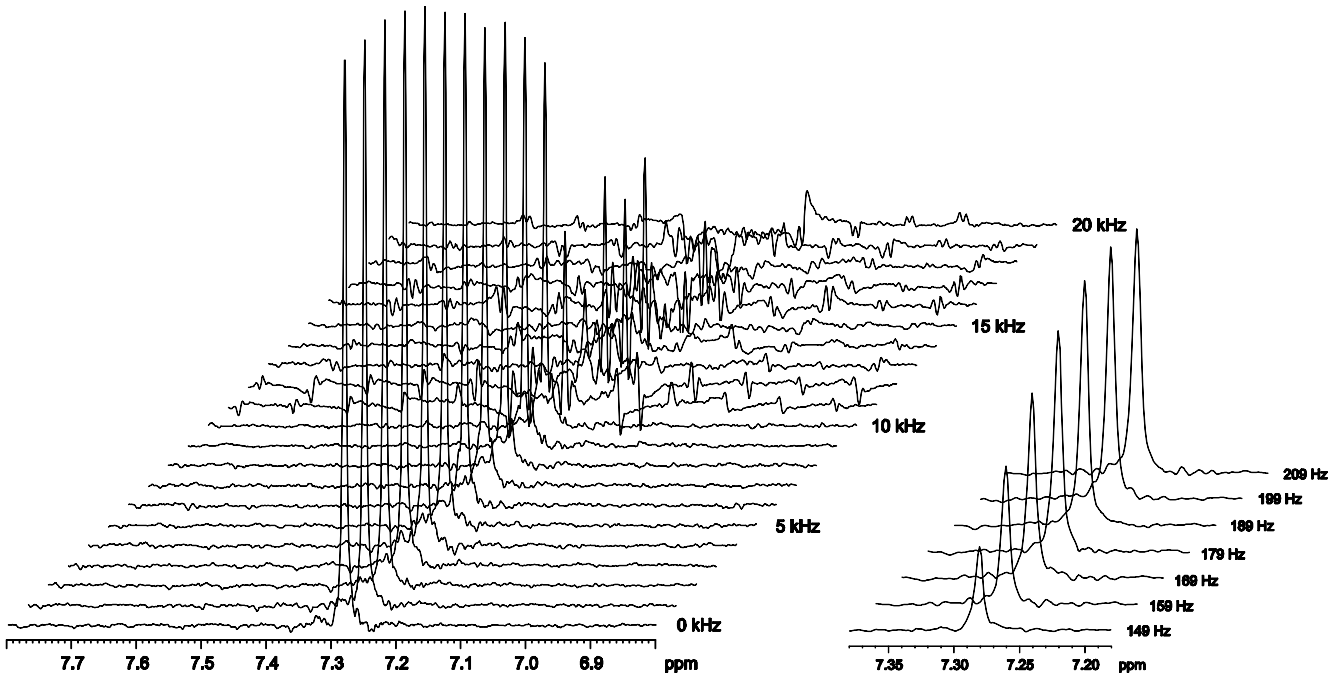

Figure 8.7: Tests of the pulse sequence shown in Figure 8.1 b) with a $CHCl_3$-sample at a 11.4 T instrument (600 MHz on protons). GARP-decoupling with the power level adjusted for a 60 µs 90°-^{13}C-pulse was used. Left: Dependence of the signal appearance on the ^{13}C-transmitter offset. The offset frequency was incremented in steps of 1 kHz, as indicated at the edges of the spectra. Right: Signal behaviour upon change of the BIRD/INEPT delays. Settings for CNST2 which is used to define the INEPT delays (d_1 = 1/(4*CNST2)) and BIRD delays (d_1 = 1/(2*CNST2)) are indicated with the spectra. Experimental setting are provided in section 14.1.8.

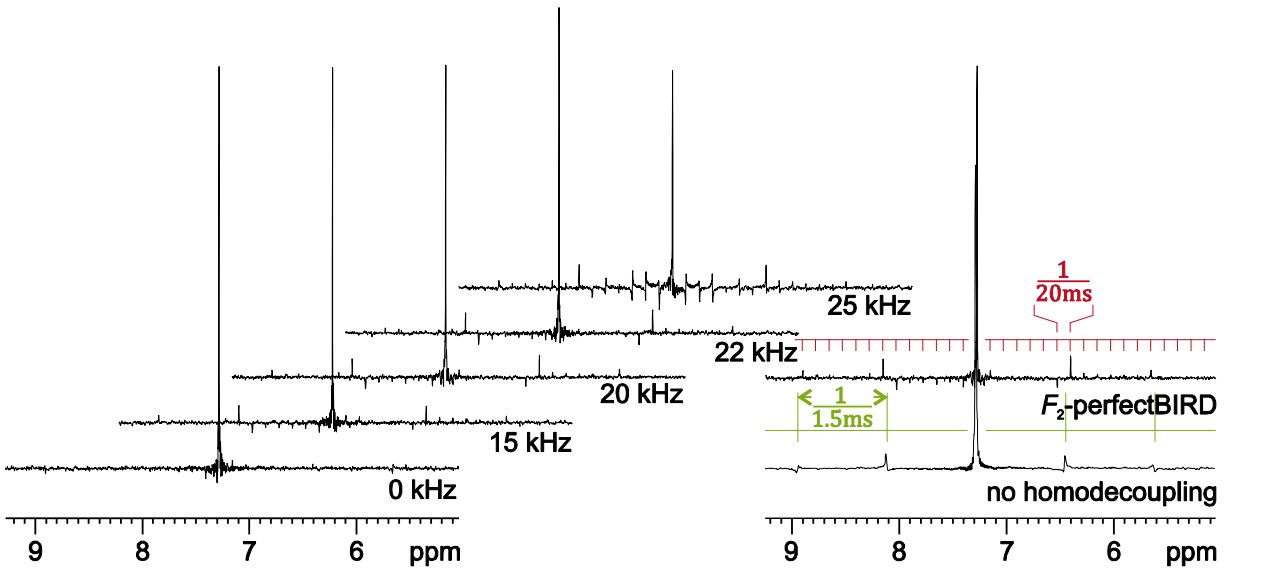

Figure 8.8: Test of ^{13}C offset tolerance of the experiment shown in Figure 8.1 c) with a $CHCl_3$-sample at a 9.4 T instrument (400 MHz on protons). Adiabatic decoupling using sweeps over 60 kHz and a 1.5 ms repetition rate was used. Left: variation of the ^{13}C-transmitter frequency. Offsets from the on-resonance condition are given with the traces. Right: comparison between a F_2-perfectBIRD HSQC and an HSQC without homonuclear decoupling, both acquired with a ^{13}C-transmitter offset of +20 kHz. The red scale indicates positions separated by entire multiples of 50 Hz (= 1/(20 ms) = 1/(sw_2)) from the signal centre and the green scale indicates positions separated by entire multiples of 333.33 Hz (= 1/(1.5 ms)) from the signal centre. Full experimental parameters are given in paragraph 14.1.9.

With the optimization of the pulse sequence timing and the adjustment of the experimental settings, in particular of the heteronuclear decoupling method, it is now possible to record fully homo- and heteronuclear decoupled F_2-perfectBIRD HSQC spectra with high quality, as exemplified in Figure 8.9. A clean singlet appearance is observed for all signals of cyclosporine A. In combination with the increased resolution that can be achieved with the chunked data acquisition scheme used, this leads to notable reductions to the signal widths over the entire chemical shift range. As opposed to pure shift HSQC experiments with BIRD-based homonuclear decoupling[254, 305, 307, 342, 343], the technique also yields clean in-phase and fully decoupled signals for methylene positions, which might be particularly interesting when studying small molecule solutes. We therefore wanted to demonstrate the potential use of the technique developed, as described in the following paragraph.

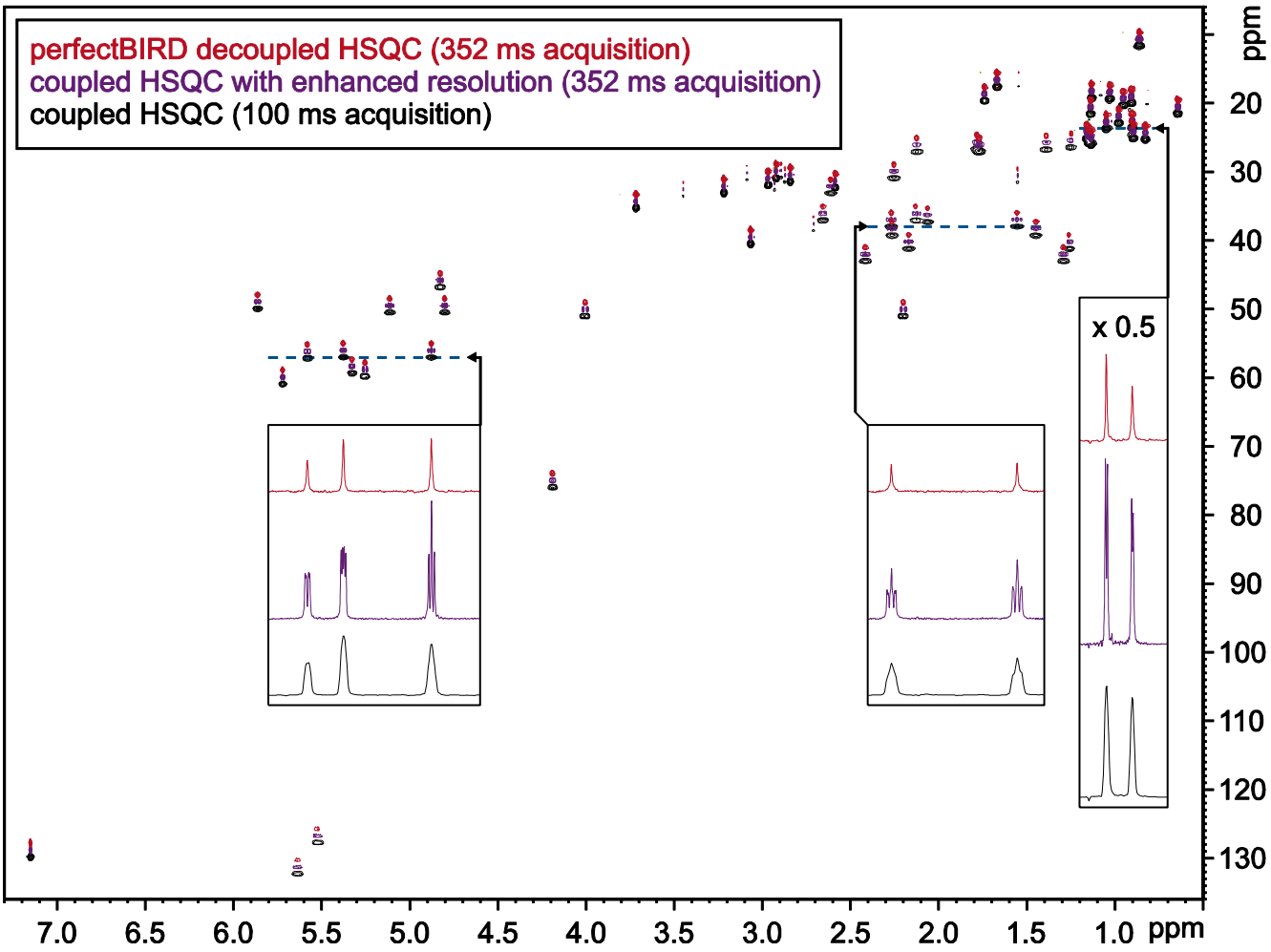

Figure 8.9: Cyclosporine A spectra acquired at 600 MHz ^{1}H frequency, with different HSQC variants. Black: gradient-selected ^{1}H-^{13}C-HSQC without homonuclear decoupling with 100 ms acquisition (30 min experiment duration). Purple: gradient-selected ^{1}H-^{13}C-HSQC without homonuclear decoupling with 352 ms acquisition (2 h 9 min experiment duration), enhanced by the pseudo-3D acquisition scheme illustrated in Figure 8.4. Red: F_2-perfectBIRD-HSQC with heteronuclear decoupling with 352 ms acquisition (13 h 14 min experiment duration), acquired with the pulse sequence scheme shown in Figure 8.1 a). Experimental parameters are provided in paragraph 14.1.10.

8.3. Resolving small chemical shift differences with F_2-perfectBIRD HSQC experiments – The case study of an oligourea with repeating building blocks

As demonstrated for cyclosporine A, F_2-perfectBIRD HSQC experiments can provide a notable narrowing of F_2-signal widths, as compared HSQC experiments without homonuclear decoupling. The high resolving power of 2D ^{1}H-^{13}C-correlations, such as HSQC experiments, is mainly caused by the fact, that peaks have to have similar chemical shifts in both spectral dimensions to actually overlap. As the ^{13}C-dimension features a large chemical shift dispersion, in most cases this is unlikely. The likelihood that chemical shifts are similar in both spectral dimensions however significantly increases, if systems are studied that feature different molecules or molecular subunits with very alike chemical structure. The case of slow conformational interconversion was already mentioned as an example[358]. Other scenarios where chemical shifts are likely to be very similar are studies of mixtures of configurational isomers[370-372] or studies of oligomers with identical building units[293, 373].

YULIA MOSKALENKO found herself facing such a challenge when studying the self-aggregating properties of different oligourea, that had been synthesized by KAROLINA PULKA-ZIACH[374]. For N,N'-linked oligourea with linkage at the β-position it had been shown previously that very stable secondary helical structures are formed in solution[375, 376]. For L-amino acid derived oligomers of this class, intramolecular hydrogen bonding stabilizes (*P*)2.5 helices in different organic media that structurally resembles the (*P*)2.6$_{14}$-helix formed by γ-peptides, even for short oligomers (e.g. heptamers).

Amongst the substances studied was the N-capped hexameric structure **8** shown in Figure 8.10, which features strong clustering of NMR signals in combination with comparably broad and featureless signals in the back-bone region. The proton spectrum shown provides a rough overview of the proton spectrum. The large chemical shift difference observed between the pro-(R) and the pro-(S) protons at the α-positions (> 1 ppm) is considered as evidence for the existence of the helical structure motive[377]. In particular, in the region containing the pro-(R)-α-protons and the γ-protons, severe signal overlap is present, that persists even in HSQC experiments.

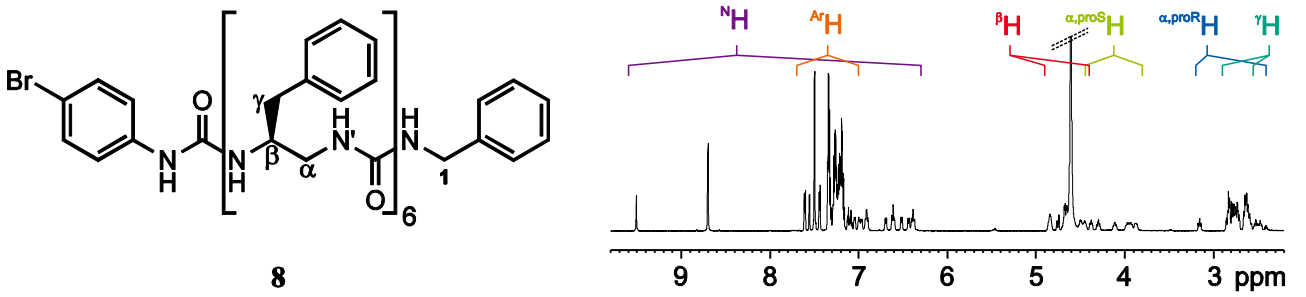

Figure 8.10: Left: Structure of the oligourea **8** studied. Repeated residues are numbered starting with the residue attached to the benzyl-cap. Right: ^{1}H-spectrum of oligourea **8** (1.9 mM) in pyridine-d_5, acquired at 320 K. Chemical shift regions are indicated for the different sites in the repetitive building blocks.

It was the task of TIMO IMHOF in his Bachelor thesis[378] under my supervision to test, if the F_2-perfectBIRD HSQC experiment developed simplifies the site-specific signal assignment for this challenging case and to identify possible benefits of the decoupling.

The HSQC of oligourea **8** is largely empty, apart from three regions within which signals cluster together (see Figure 8.11). As in the case of cyclosporine A, the F_2-perfectBIRD HSQC is able to provide significant signal narrowing in the proton dimension as compared to an HSQC without homonuclear decoupling. The backbone signals highlighted in Figure 8.11 appear mostly separated, facilitating spectral analysis.

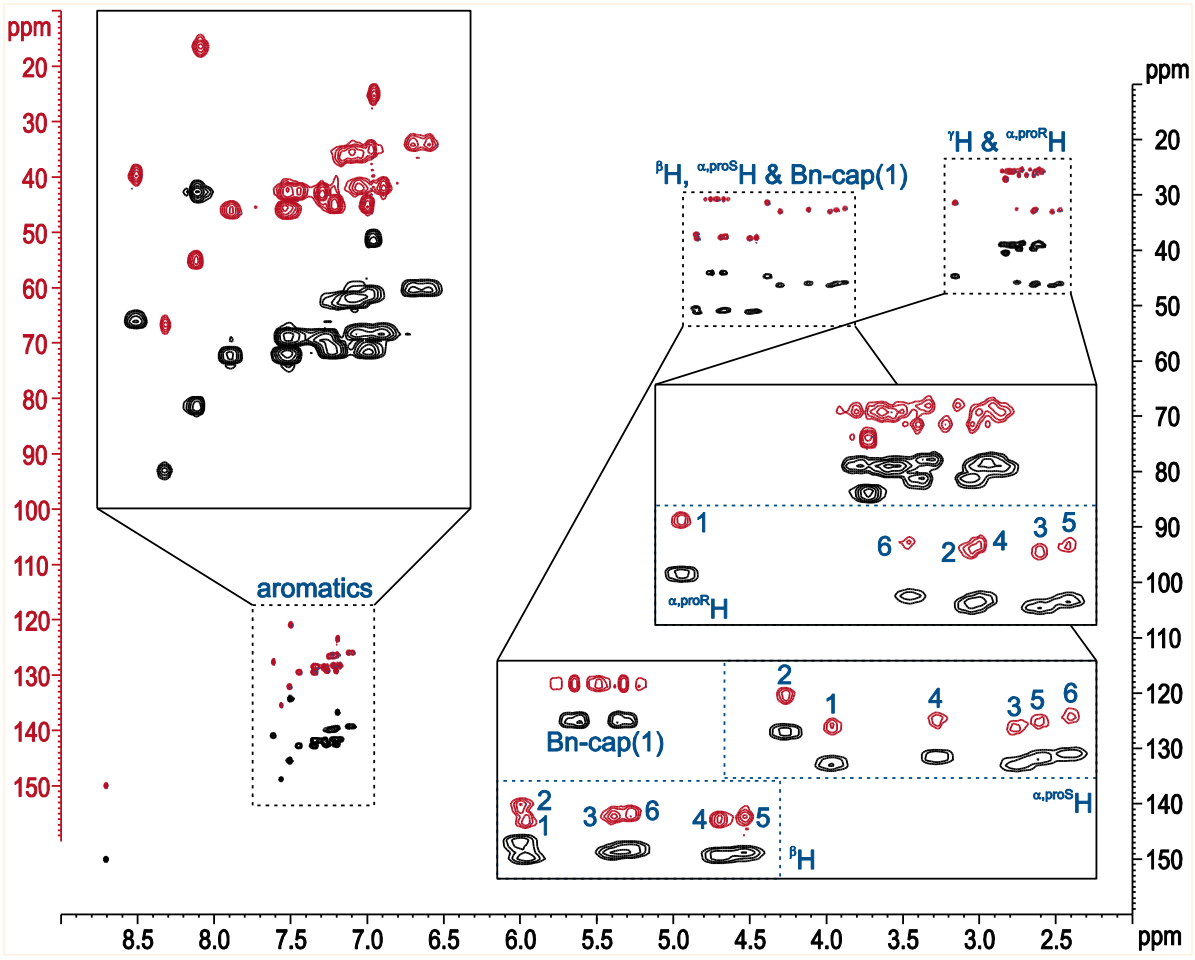

Figure 8.11: Comparison of ^{1}H-^{13}C-HSQC spectra collected for oligourea **8** (1.9 mM) in pyridine-d_5, acquired at 320 K. Data without homonuclear decoupling is shown in black (28 min), data with F_2-perfectBIRD homonuclear decoupling is shown in red (17 h 8 min). Signal assignments provided for the backbone region are adopted from the Bachelor thesis of TIMO IMHOF[378]. Experimental parameters are given in section 14.1.11. No FID-averaging was used.

As for this substance proton signal assignment along the backbone can conveniently be performed with a combination of ROESY, TOCSY and DQF-COSY experiments, the HSQC experiments mainly were used to derive ^{13}C-assignments from the proton assignment. All backbone and γ-positions were assigned by TIMO IMHOF.

The assignment of the γ-proton pairs was pivotal for assigning ortho and meta positions of the aromatic sidechains, which I was able to add later (see signal assignment in section Table 14.1). Assignment of the aromatic signals was performed with an additional HMBC experiment that was recorded after termination of the Bachelor thesis (experimental parameters in section 14.1.12) and the combination of HSQCs with high resolution in different dimensions. An HSQC with a large number of t_1-increments provided high resolution in F_1 and the F_2-perfectBIRD HSQC was used for correlating peaks in the proton dimension. As an alternative, the ability of spectral folding to achieve a combined high resolution in both dimensions was investigated for the F_2-perfectBIRD HSQC.

Signal assignment of most aromatic signals could be achieved with this approach, with the single exception being signals for residue 5 and 6, for which two sets of signals could be identified, but correlation to the backbone was not achieved due to the very small chemical shift difference (< 6Hz) of both ortho (ε) and meta (ζ) protons. In such cases, combinations of the F_2-perfectBIRD HSQC with high proton-resolution HMBC[207] or HSQMBC[287, 310, 311] techniques may be required to take full advantage of

the homonuclear decoupled technique presented here. If the sample concentration is sufficient, INADEQUATE techniques[44] could be considered as an alternative.

One particular advantage we hoped to achieve, when using the F_2-perfectBIRD HSQC experiment for studies of oligourea **8** is full decoupling of all methylene protons contained. However, in Figure 8.11 it can clearly be seen, that clean decoupling is not achieved for the signals of the strongly coupled pair of protons 1 of the benzyl cap (contained in the insert showing the $^{\beta}$H and $^{\alpha,proS}$H backbone signals; $\Delta\nu = 59$ Hz, $^2J_{HH} = 15.4$ Hz). Very intense homonuclear decoupling artefacts are observed at positions that are empty in the experiment without homonuclear decoupling. Upon inspection of the γ-H region it was found, that at least for two of the γ-H-pairs intense artefacts are observed in the middle of the coupling signal pairs, just as it is the case of protons 1 of the benzyl cap. Apparently the perfectBIRD decoupling is producing artefacts for strongly coupled methylene proton pairs.
While we did not manage to reduce the artefact intensity by changes of the experiment settings, it turned out, that different settings for data processing can be used to reduce the relative artefact intensity of the very intense central artefact. As illustrated in Figure 4.16, for data rearrangement there are two general methods described that can be used: Either data is sampled with the maximum possible increment (typically Δ_{max}=25 ms; see Figure 4.16 left) in the homonuclear decoupling dimension that still enables suppression of homonuclear couplings, to achieve sampling of a long time domain signal in as little experiment time as possible. Alternatively, data can be sampled with smaller increments in the homonuclear decoupling dimension than the usable data acquisition duration. Still using the full allowable data acquisition period for processing in this case leads to an "overlap" of different acquisition time points of several scans in the constructed time domain signal, enabling an averaging of the time domain signal of different scans (see Figure 4.16 right). This so-called RESET-processing approach was initially designed to increase the signal-to-noise ratio in pure shift data of mass-limited samples[254].
As illustrated in Figure 8.12 for protons 1 of the benzyl-cap and in Figure 8.13 for the $^{\gamma}$H region, in particular for the central artefact, a decreased intensity relative to the sharp peaks near the actual chemical shifts of the signals is observed, when using different settings for FID averaging. The signal assignment for the $^{\gamma}$H region can be found in Figure 8.14, in which spectra are shown with increased F_1-resolution using by spectral folding.
As can be seen, the suppression of the artefact peaks is not perfect, but clearly improves the situation. Processing of the same data with different settings for signal averaging can be used to identify the most intense artefacts arising from strong coupling, because their relative intensity significantly decreases when the signal averaging procedure is used. This behaviour was observed both for position 1 of the benzyl cap, as well as for the γ-positions. To conclude if this behaviour is general for the experiment used, a study of a broader range of test substances or alternatively a closed description of the mode of action of the averaging procedure on the artefacts observed may be required. While clearly the experimental method used here is limited in the case of strong coupling, we have found a method to at least reduce strong coupling artefacts arising in homonuclear decoupled HSQC experiments. It should be noted at this point, that for none of the pure shift HSQC methods described[213, 254, 305-307, 310, 312, 342, 343, 379], a complete robustness towards strong coupling, in particular in the case of strong coupling between diastereotopic methylene protons, has been described to date.
A question we could only touch on for the single case of the position 1 in the benzyl-cap is, if the apparent ^{1}H-chemical shift that can be read from the F_2-perfectBIRD HSQC still reflects the actual chemical shift, even in the case of strongly coupled signals. For strongly coupled signals, the chemical shift cannot be directly read from the signal centres any more, and knowledge of the homonuclear coupling constants is required to extract unbiased chemical shifts. The analysis of signal multiplet structure in the case of well-resolved signals can actually provide unbiased chemical shifts either through closed analytical formula, or by spin-system simulations[90]. These approaches however rely on the resolution of

homonuclear signal multiplicities, which in most cases is not achieved in HSQC experiments. It would therefore be very interesting to have a pure shift HSQC experiment, in which chemical shifts can directly be extracted from the apparent signal positions, even for strongly coupled systems

The only position in oligourea **8**, where signal resolution in the ^{1}H-spectrum is sufficient to extract unbiased chemical shifts for strongly coupled methylene protons are protons 1 from the benzyl cap. For these signals, we performed a numerical simulation to extract unbiased chemical shifts (see Figure 8.12 c) and section 14.1.13 for simulation details). For this system, it was observed that the chemical shifts determined by simulation are well represented by the two sharp peaks in the F_2-perfectBIRD HSQC and that the agreement of the signal positions with the reference values is best for the choice of FID-averaging producing minimal artefacts. Also for this aspect, a more detailed study is required to evaluate, if this is a general feature of the combination of experiment and processing chosen. For future work we plan to answer questions concerning the behaviour of the experiment for the case of strong coupling by spin-system simulations.

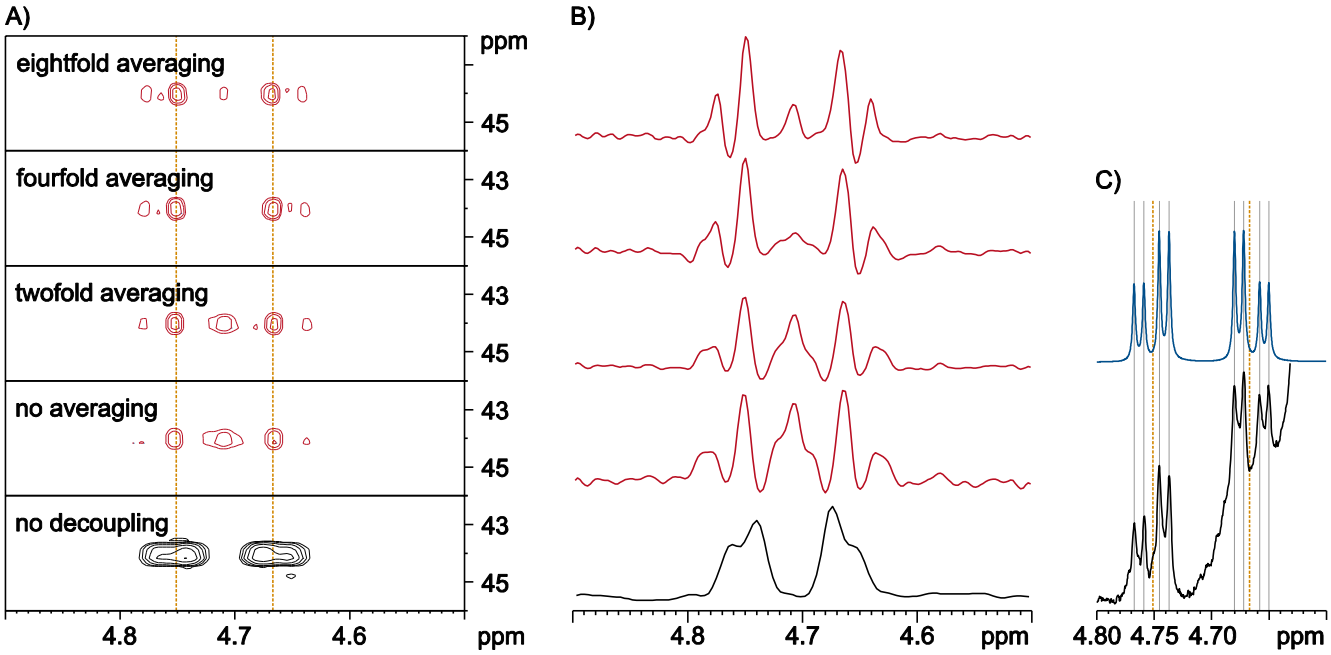

Figure 8.12: Effect of FID-averaging during data rearrangement on the signal appearance for the methylene protons 1 of the benzyl cap. A) Spectra obtained from the same raw data as used in Figure 8.11 with different settings for averaging during FID concatenation. B) F_2-traces extracted from the spectra shown in A). C) Extraction of chemical shifts for the two signals. In black a single-scan proton spectrum is shown. The apparent baseline bent is caused by onset of the residual water signal found at 4.606 ppm. A simulated ^{1}H spectrum for an isolated three-proton system is shown in blue. The input parameters for the simulation were adjusted to minimize deviations between the signal positions as indicated by grey guidelines. The chemical shifts used as input parameters are shown as orange dashed lines in A) and in C). Experimental details of the chemical shift extraction procedure are given in section 14.1.13.

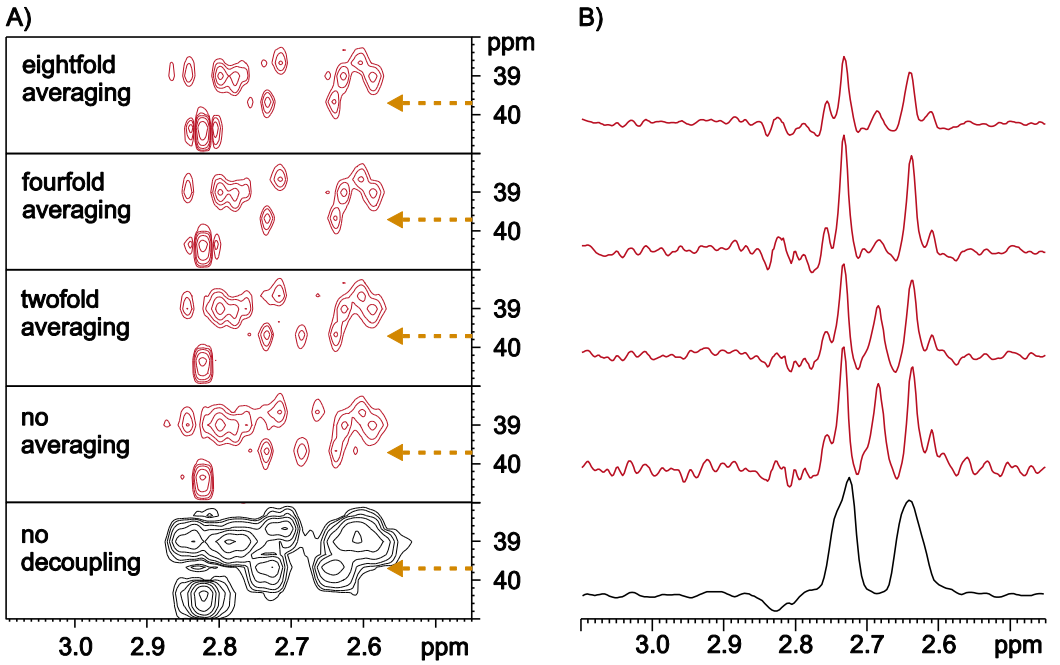

Figure 8.13: Effect of FID-averaging during data rearrangement on the signal appearance in the $^{\gamma}$H region. A) The same spectra are shown as in Figure 8.12 for a different spectral region. B) F_2-traces extracted at the ^{13}C chemical shifts of the γ-position in residue 2. The position of the traces is indicated in A) by arrows.

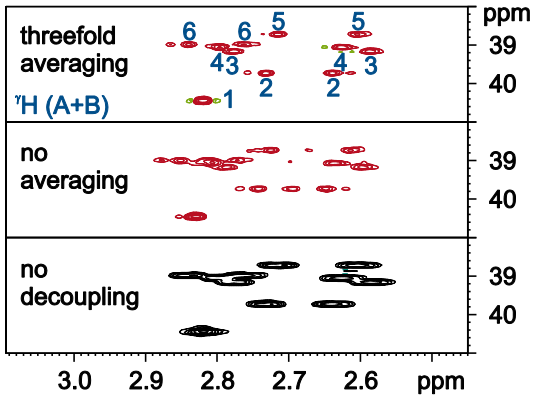

Figure 8.14: The section containing the γ-signals from spectra acquired with spectral folding. Experimental settings equal those of data shown in Figure 8.11 (details given in section 14.1.11), with the only exception being that the spectral width in the ^{13}C-dimension was reduced to 40 ppm.

8.4. Discussion and Conclusion on Project C

In this chapter it could be demonstrated, that the perfectBIRD homonuclear decoupling technique which was derived in chapter 7.3 for homonuclear decoupling of F_2-heterocoupled HSQC spectra in the proton dimension can be adapted for the acquisition of fully broadband homo- and heteronuclear decoupled HSQC experiments. In comparison with other pure shift HSQC methods, the experiments derived may be particularly useful because they enable full decoupling even for diastereotopic methylene protons, without the requirement to resort to constant time acquisition schemes.
It was possible to derive a pulse sequence scheme, which is readily applicable to broadband applications even at highest fields available to date. The very robust nature of the experiment enables its application even in very challenging cases such as the exemplary study of oligourea **8**. The value of the experiment to studies of very challenging solutes is nicely represented by the fact that the experiment was included

into the TopSpin™ standard pulse sequence library with the release of version 3.5 (pulse sequence *reset_hsqcetgppesp*), with the implementation shown in Figure 8.1 c).
The interferogram-based approach of the experiment enables spectra with very clean broadband homonuclear decoupling to be acquired, albeit at the cost of an increased experiment duration. A nice feature of the experiment is, that the resolution in the experiment can be freely scaled in the pure shift proton dimension, enabling the acquisition of HSQC experiments with two fully broadband decoupled high resolution dimensions, if required. In the course of this project, the possibilities of recording these spectra in the most time-efficient manner, in particular in combination with NUS approaches, could not fully be explored. This field may be interesting in future investigations.
The study of oligourea **8** illustrates, that even cases with very high chemical shift degeneracy can be studied with the method presented. Pronounced signal narrowing in the proton dimension can be observed in all parts of the spectrum shown in Figure 8.11, which clearly facilitates signal assignments. What got apparent throughout the study, however is, that for making full use of the higher F_2-resolution offered by F_2-perfectBIRD HSQC experiments, a combination with heteronuclear long-range correlation experiments with homonuclear decoupling in the proton dimension (HMBC[207] or HSQMBC[287, 310, 311]) is required. It remains to be evaluated which long-range correlation experiment is most suitable to be combined with the F_2-perfectBIRD HSQC for a signal assignment strategy with high resolution pure shift acquisition in the proton dimension.
A very unique feature of the experiment may be its ability to achieve (partial) decoupling even for diastereotopic methylene protons in the strong coupling regime. For diastereotopic methylene protons it is quite common that chemical shift differences in the proton dimension are small, while in the ^{13}C-dimension the chemical shift is always identical. If it was possible to find a fortunate combination of experimental settings and spectral processing that would reliably enable the direct extraction of chemical shifts without the requirement for signal fitting this may prove useful for many signal assignment purposes. Further efforts, however, are necessary to test if this goal could realistically be achieved: It needs to be established if the processing approach used really is applicable to a broad range of situations and if the apparent chemical shifts are a good representation of the unperturbed chemical shifts (within a minimum applicable error range). These aspects remain to be further investigated, together with the question, if alternations to the pulse sequence or to the processing approach could be used to further suppress artefacts from strong coupling.

The results outlined clearly illustrate, that pure shift techniques can offer useful strategies if complex chemical structures are studied. The discussions in this chapter were centred around applications at high-field instruments. Applications, however, can not only be perceived in high field studies.
In many laboratories instruments with very high static fields are not available for two reasons: First, because of the high acquisition and maintenance costs of high field instruments, but also because most tasks can as well be solved using experiments with lower static field and high field instruments are simply not required for every-day work.
It may be interesting in such cases to have a suite of pure shift experiments at hand that, for challenging cases, improve signal resolution if required without the need for higher field instruments. Increased demands in experiment duration may be less critical, if these cases only appear from time to time, while a good robustness of the pure shift approach certainly is critical if challenging signal assignments are to be tackled. The F_2-perfectBIRD HSQC discussed in this chapter, therefore is also potentially useful for intermediate-field applications.
As has been discussed however, such applications would require that a full suite of these pure shift experiments is available. If only some of the experiments routinely used for signal assignment are available as pure shift experiments, while others cannot be recorded as homodecoupled counterparts, it is possible that the full potential of homonuclear decoupling cannot be exploited. In the next chapter,

the development of a new experimental technique is described, which has the potential to close one of the gaps currently existing.

9. Project D: A Rapid Experimental Approach to Full In-Phase COSY-like Spectra

The contents of this chapter have been published in
M. R. M. Koos, G. Kummerlöwe, L. Kaltschnee, C. M. Thiele, B. Luy,
Angew. Chem. **2016**, *128*, 7785-7789, DOI: 10.1002/ange.201510938;
Angew. Chem. Int. Ed. **2016**, *55*, 7655-7659, DOI: 10.1002/anie.201510938;

The previous chapter was devoted to the development of pure shift techniques, which can be used to improve signal separation in HSQC spectra, thus enabling a facilitated assignment of signals which normally are overlapping. The facilitated signal assignment that pure shift techniques can offer has evoked a large interest for the development of techniques facilitating signal assignment even in cases of drastic signal overlap. In many multidimensional experiments designed for signal assignment, such as TOCSY[266, 294], NOESY[297, 298], HSQC[254, 305], HMBC[207] and *J*-resolved experiments[276, 380], pure shift techniques have therefore been implemented to decouple the high resolution direct dimension.
Despite their wide use for signal assignment, for COSY techniques, the constant-time approach applied along the low-resolution indirect dimension, has long been the only practical route to experimentally introduce pure shift dimensions, though[36, 297]. Note that there is one single very recent exception to this which uses the high sensitivity band-selective pure shift approach[372]. As a homonuclear correlation spectrum just like ^{1}H-^{1}H-TOCSY and ^{1}H-^{1}H-NOESY, however ^{1}H-^{1}H-COSY would largely benefit from pure shift approaches, because both spectral dimensions feature signal overlap at the same positions. Obviously there must be a fundamental problem opposing straightforward application of pure shift techniques, such as Zangger-Sterk decoupling[252, 257], in the direct dimension of the commonplace COSY experiments, such as DQF-COSY[381].
The reason, why broadband homonuclear decoupling techniques have not been used in the direct dimension of COSY experiments can be attributed to the fact that typically so-called anti-phase signals are observed. Most COSY techniques require homonuclear couplings to evolve during acquisition for signals to be observable. In these experiments anti-phase FIDs start off at zero intensity and grow to observable signal through the action of homonuclear couplings. Obviously, homonuclear decoupling would prevent signals to become observable at all.
In NOESY experiments we used this feature of pure shift techniques to suppress COSY-type cross-peaks, called zero quantum artefacts in that context. In the context of NOESY-type applications, this filtration between homonuclear in- and anti-phase signals can thus be quite useful, however it forces us to look for COSY-like techniques, which produce in-phase signals.
Studies of the perfect echo element, discussed in chapter 7.3 quite naturally lead to a COSY-like technique which, just like NOESY and TOCSY, produce in-phase signals, a goal long sought. The CLIP-COSY technique derived in this chapter not only is amenable to homonuclear decoupling in the direct dimension, it further features many other advantages:
It allows rapid and robust, single-scan acquisition of COSY-like spectra. In contrast to the techniques normally used for rapid acquisition of COSY spectra, however, it is able to produce absorptive in-phase signals, and thus offers a resolution advantage over techniques normally used in routine analytics. It therefore has the potential to replace the techniques used nowadays for routine analytics and further is highly interesting for metabolomics[8] applications.
Before discussing the features of this technique, a very simplistic analysis of the underlying pulse sequence is presented, to illustrate the working principle of the experiment.

9.1. Working principle of the CLIP-COSY

The ability of the perfect echo[195] to introduce a mixing of coherences of two spins was already mentioned in section 7.3.1 (equations (7.1) to (7.7)). By the action of the pulse sequence of Figure 9.1 a) (with $\phi_i = \phi_k = 0$), the initial state

$$M_1 I_{1,z} + M_2 I_{2,z} \xrightarrow{90°_x} -M_1 I_{1,y} - M_2 I_{2,y} \tag{7.1}$$

of the weakly coupled homonuclear two spin system studied transformed to

(7.1) $\xrightarrow{\text{I through V}}$

$$\begin{aligned} &-I_{1,y}\frac{1}{2}(M_1[1+\cos(\pi J_{12}4\tau)] + M_2[1-\cos(\pi J_{12}4\tau)]) \\ &-I_{2,y}\frac{1}{2}(M_1[1-\cos(\pi J_{12}4\tau)] + M_2[1+\cos(\pi J_{12}4\tau)]) \\ &+2I_{1,x}I_{2,z}\frac{1}{2}(M_1\sin(\pi J_{12}4\tau) - M_2\sin(\pi J_{12}4\tau)) \\ &+2I_{1,z}I_{2,x}\frac{1}{2}(-M_1\sin(\pi J_{12}4\tau) + M_2\sin(\pi J_{12}4\tau)). \end{aligned} \tag{7.7}$$

under the action of the pulse element enclosed between time points I and V.

When using the perfect echo for homonuclear decoupling in HSQC experiments, it actually is not apparent from the spectra that magnetization was exchanged between pairs of protons by the perfect echo element. This is because, the application is limited to diastereotopic methylene protons, where the initial magnetizations M_1 and M_2 on the two coupling partners I_1 and I_2 are approximately equal and where t_1-frequency labelling affects M_1 and M_2 equally ($M_1 \approx M_2$).

Herein, in contrast, we use the perfect echo to transfer magnetization between the two in-phase coherence terms $I_{1,y}$ and $I_{2,y}$ after different frequency labelling of M_1 and M_2.

A simple t_1-labelling element, which is able to create the initial state required ($M_1 \neq M_2$), is shown in Figure 9.1 b) prior to time point I.

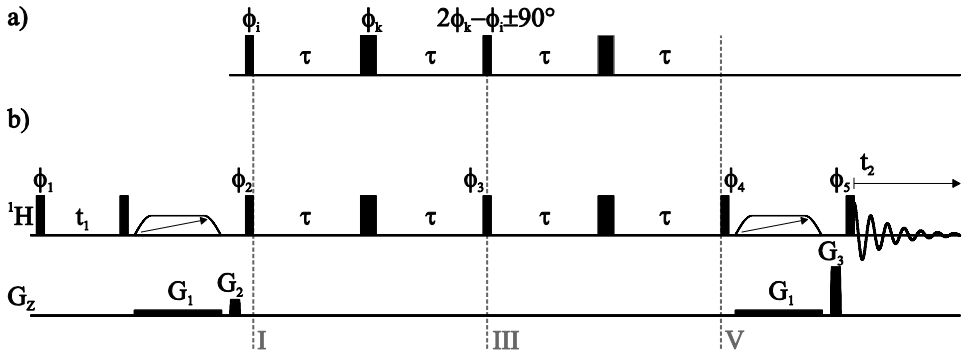

Figure 9.1: a) Pulse sequence of a single perfect echo element as presented by Takegoshi et al.[195]. b) Initial implementation of the CLIP-COSY experiment, used to generate the results shown in Figure 9.2. Narrow and wide filled bars are 90°- and 180°-pulses applied along x, unless otherwise stated. Open shapes with arrows indicate frequency swept adiabatic pulses. Pulse phases are ϕ_1 = x, -x incremented by $\pi/2$ for each t_1-increment, ϕ_2 = -x, ϕ_3 = y, y, -y, -y, ϕ_4 = (x)$_4$, (-x)$_4$, ϕ_5 = (-x)$_4$, (x)$_4$ and the receiver phase used is ϕ_{rec} = x, -x.

Suppose that for the weakly coupled homonuclear two spin system that is considered here for simplicity, the initial longitudinal magnetization for both nuclear sites is equal to M_0. In this case, excitation and t_1-evolution lead to

$$M_0 I_{1,z} + M_0 I_{2,z} \xrightarrow{90°_x} -M_0 I_{1,y} - M_0 I_{2,y} \tag{9.1}$$

$$\xrightarrow{\Omega_1 t_1}\xrightarrow{\Omega_2 t_1}\xrightarrow{\pi J_{12} t_1}$$

$$\begin{aligned} &-M_0 I_{1,y}\cos(\Omega_1 t_1)\cos(\pi J_{12} t_1) + M_0 I_{1,x}\sin(\Omega_1 t_1)\cos(\pi J_{12} t_1) \\ &+M_0 2I_{1,x}I_{2,z}\cos(\Omega_1 t_1)\sin(\pi J_{12} t_1) + M_0 2I_{1,y}I_{2,z}\sin(\Omega_1 t_1)\sin(\pi J_{12} t_1) \\ &-M_0 I_{2,y}\cos(\Omega_2 t_1)\cos(\pi J_{12} t_1) + M_0 I_{2,x}\sin(\Omega_2 t_1)\cos(\pi J_{12} t_1) \\ &+M_0 2I_{2,x}I_{1,z}\cos(\Omega_2 t_1)\sin(\pi J_{12} t_1) + M_0 2I_{2,y}I_{1,z}\sin(\Omega_2 t_1)\sin(\pi J_{12} t_1). \end{aligned} \tag{9.2}$$

These coherences are subsequently filtered by a $90°_x$ – z-filter – $90°_{-x}$ block, to only retain the $I_{i,y}$ coherences.

(9.2) $\xrightarrow{90°_x}$

$$\begin{aligned} &-M_0 I_{1,z}\cos(\Omega_1 t_1)\cos(\pi J_{12} t_1) + M_0 I_{1,x}\sin(\Omega_1 t_1)\cos(\pi J_{12} t_1) \\ &-M_0 2I_{1,x}I_{2,y}\cos(\Omega_1 t_1)\sin(\pi J_{12} t_1) - M_0 2I_{1,z}I_{2,y}\sin(\Omega_1 t_1)\sin(\pi J_{12} t_1) \\ &-M_0 I_{2,z}\cos(\Omega_2 t_1)\cos(\pi J_{12} t_1) + M_0 I_{2,x}\sin(\Omega_2 t_1)\cos(\pi J_{12} t_1) \\ &-M_0 2I_{2,x}I_{1,y}\cos(\Omega_2 t_1)\sin(\pi J_{12} t_1) - M_0 2I_{2,z}I_{1,y}\sin(\Omega_2 t_1)\sin(\pi J_{12} t_1) \end{aligned} \tag{9.3}$$

First $I_{i,y}$-terms are flipped onto the z-axis through the $90°_x$ pulse and then z-filtration is applied. Let us suppose, that the z-filter is able to filter out all coherences, leaving only z-magnetization terms.

$$(9.3) \xrightarrow{\text{z-Filter}} -M_0 I_{1,z}\cos(\Omega_2 t_1)\cos(\pi J_{12} t_1) - M_0 I_{2,z}\cos(\Omega_2 t_1)\cos(\pi J_{12} t_1) \tag{9.4}$$

z-Magnetization is converted back to observable coherences after filtration by the $90°_{-x}$ pulse. In the case of optimal z-filtration, we are able to generate the initial state of equation (7.1), where M_1 and M_2 have been modulated by the chemical shift of the respective spins.

$$(9.4) \xrightarrow{90°_{-x}} -M_0 I_{1,y}\cos(\Omega_1 t_1)\cos(\pi J_{12} t_1) - M_0 I_{2,y}\cos(\Omega_2 t_1)\cos(\pi J_{12} t_1) \tag{9.5}$$

We thus obtain

$$M_{1\ or\ 2} = M_0\cos(\Omega_{1\ or\ 2} t_1)\cos(\pi J_{12} t_1). \tag{9.6}$$

As we can see, the coherences entering the mixing period at time point I are modulated by the respective chemical shifts and in addition feature cosine modulation with respect to the active coupling between the spins. For an ideal filtration by the z-filter, these features are also obtained for larger spin-systems enabling a pure in-phase modulation of the signals in F_1. Generation of chemical shift sine modulation can be achieved, by shifting ϕ_1 by 90°.

For z-filtration, I used the combination of a Thrippleton-Keeler filter[95] and a strong field gradient. The Thrippleton-Keeler filter can be regarded as the state-of-the-art for suppressing zero-quantum coherences contained e.g. in the term $2I_{1,x}I_{2,y}$. For this method it is known, that the suppression efficiency breaks down, if two spins are separated by a frequency smaller or comparable to the inverse length of the filter[96]. Thus, the assumption of an ideal z-filter may therefore not always be valid.

From the coherences we obtain at time point V after mixing by the perfect echo element, again we filter out all but the I_y components using another $90°_x$ – z-Filter – $90°_{-x}$ block.

At V:

$$
\begin{aligned}
&-I_{1,y}\frac{1}{2}M_0\cos(\pi J_{12}t_1)\left(\cos(\Omega_1 t_1)\left[1+\cos(\pi J_{12}4\tau)\right]+\cos(\Omega_2 t_1)\left[1-\cos(\pi J_{12}4\tau)\right]\right)\\
&-I_{2,y}\frac{1}{2}M_0\cos(\pi J_{12}t_1)\left(\cos(\Omega_1 t_1)\left[1-\cos(\pi J_{12}4\tau)\right]+\cos(\Omega_2 t_1)\left[1+\cos(\pi J_{12}4\tau)\right]\right)\\
&+2I_{1,x}I_{2,z}\frac{1}{2}M_0\cos(\pi J_{12}t_1)\left(\cos(\Omega_1 t_1)\sin(\pi J_{12}4\tau)-\cos(\Omega_2 t_1)\sin(\pi J_{12}4\tau)\right)\\
&+2I_{1,z}I_{2,x}\frac{1}{2}M_0\cos(\pi J_{12}t_1)\left(-\cos(\Omega_1 t_1)\sin(\pi J_{12}4\tau)+\cos(\Omega_2 t_1)\sin(\pi J_{12}4\tau)\right)
\end{aligned}
\tag{7.7}
$$

$$
\xrightarrow{90^\circ_x}\xrightarrow{\text{z-Filter}}\xrightarrow{90^\circ_{-x}}
$$

$$
\begin{aligned}
&-I_{1,y}\frac{1}{2}M_0\cos(\pi J_{12}t_1)\left(\cos(\Omega_1 t_1)\left[1+\cos(\pi J_{12}4\tau)\right]+\cos(\Omega_2 t_1)\left[1-\cos(\pi J_{12}4\tau)\right]\right)\\
&-I_{2,y}\frac{1}{2}M_0\cos(\pi J_{12}t_1)\left(\cos(\Omega_1 t_1)\left[1-\cos(\pi J_{12}4\tau)\right]+\cos(\Omega_2 t_1)\left[1+\cos(\pi J_{12}4\tau)\right]\right)
\end{aligned}
\tag{9.7}
$$

Also at the start of the acquisition period, only pure in-phase magnetization should be observed at this stage. The experiment therefore provides pure in-phase character of all signals in both dimensions, in contrast to all COSY methods that are routinely used nowadays. It should be noted at this stage, that this was achieved analysing only the first phase cycling step, indicating that a single phase cycling step may be sufficient to achieve these desirable properties.

Both in-phase coherences are amplitude modulated by two components: One that is frequency modulated by Ω_1 during t_1 and one that is modulated by Ω_2 during t_1, creating diagonal and cross-peaks. For the two-spin-system studied here, the relative amplitude of the two peaks varies with $\pi J_{12}4\tau$, and thus the optimal choice for τ depends on the spin system studied.

9.2. Pulse sequence testing on strychnine

With the pulse sequence shown in Figure 9.1 b), I performed initial tests on strychnine which proved that indeed COSY-type spectra with in-phase character could be obtained. As shown in Figure 9.2, the correlation information obtained for the test substance is basically identical to the information that is obtained, when using a gradient selected magnitude processed COSY[211, 382], as would be used for most routine applications. Both spectra are measured with a single scan per t_1-increment and with a short relaxation delay (0.66 s of acquisition + 1 s delay).

When setting up the experiment, a choice is required concerning the setting of the delay τ, which determines the coherence transfer efficiency of the experiment. In the previous section, a product operator analysis is shown for an isolated two-spin system not undergoing relaxation, to illustrate the mode of action of the experiment. It was seen, that when setting $\tau = 1/(4^*|J_{HH}|)$, cross peaks are maximized which is desirable (for further discussions, I use J_{HH} as a typical ^{1}H-^{1}H coupling constant).

For more complex spin systems than the one used for illustration, however, the transfer efficiency of the perfect echo block as a mixing element is modulated by the other spins present and further relaxation reduces the signal intensity observed with increasing length of the mixing element. For finding a good choice for τ, a series of experiments were performed with different settings for τ. Figure 9.3 illustrates, how cross-peak intensity starts growing from zero for a $1/(4\tau)$ that is larger than typical proton-proton couplings, up to the point where $1/(4\tau) \approx 20$ Hz. A further decrease in $1/(4\tau)$ (an increase in length of the mixing element) can introduce severe signal loss, full signal disappearance or even signal sign inversion.

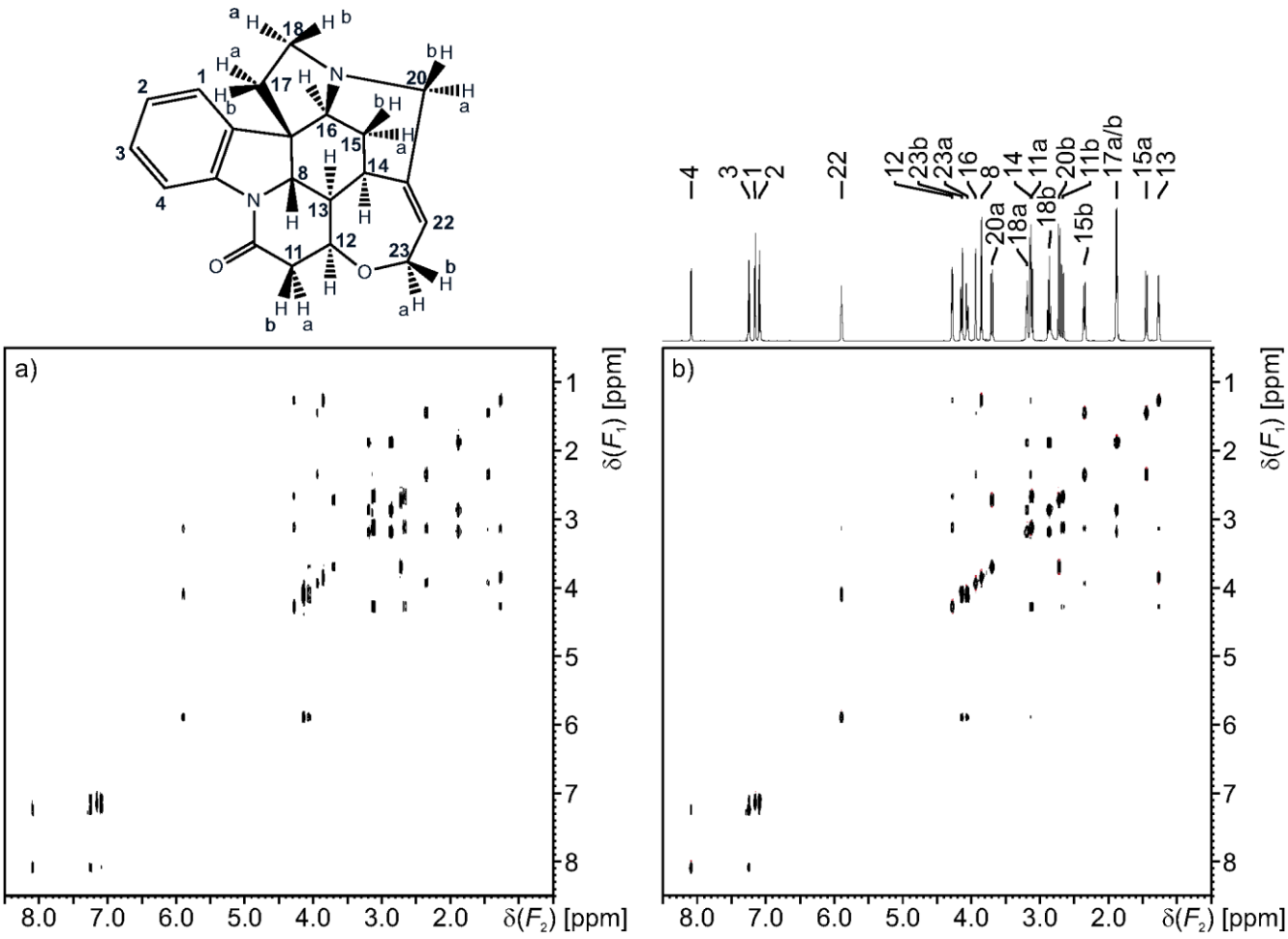

Figure 9.2: a) gradient selected magnitude processed COSY and b) CLIP-COSY, measured for a strychnine (267 mM) in $CDCl_3$. Spectra were acquired with identical resolution in both dimensions in 4 min 2 s and in 4 min 12 s respectively. The CLIP-COSY used the pulse sequence provided in Figure 9.1 b), with τ = 1/(4*30 Hz) = 8.33 ms. Full experimental details are given in section 14.1.14.

This can be readily understood, when performing the product operator analysis of the action of the mixing element used for an arbitrarily large weakly coupled spin system (see section 14.3). In large spin systems, the cross-peak amplitude $A_{1,2}$ of a cross-peak between two coupling spins is proportional to

$$A_{1,2} \propto \sin^2(\pi J_{1,2} 2\tau) \prod_{n \neq 1,2} \cos(\pi J_{1,n} 2\tau) \prod_{p \neq 1,2} \cos(\pi J_{2,p} 2\tau) \qquad (9.8)$$

(compare to equation (14.9) in the appendices; equivalent to equation (1) of the publication printed below). In the proportionality factor, the initial magnetization before mixing as well as factors describing relaxation during mixing are contained.

If we are restricting the discussion to values of τ smaller than all realistic values for $1/(4^*|J_{HH}|)$ (e.g.: if we set $\tau = 1/(4^*30\,\text{Hz})$), all cosine terms will be positive (because $-\pi/2 < \pi J 2\tau < \pi/2$). The amplitude of all cross peaks appearing will thus be positive (It will appear with the same sign as the diagonal).

For values of τ comparable to or larger than typical $1/(4^*|J_{HH}|)$ however, signal amplitudes can easily zero, if for one of the coupling constants $J_{a,b}$ present $\tau \approx 1/(4^*|J_{a,b}|)$. Also sign inversions can occur for larger τ. It can be expected at this point, that intensity based measurements of coupling constants, could be performed, paralleling methods using CT-COSY experiments[180, 383].

For measurement of COSY-type correlation maps such cross-peak nulling is very unfavourable, as important correlations may be missing. It is therefore recommended to set $1/(4\tau)$ to values larger than

typical coupling constants. For typical proton-proton coupling networks, good choices are 20 Hz to 40 Hz, with a bias to higher values for systems with faster transverse relaxation.
As could be illustrated using the strychnine test sample, the experiment proposed in Figure 9.1 b) is able to generate high quality COSY-type spectra within short experiment time. The experiment I proposed is able to generate absorptive in-phase cross and diagonal peaks without the need for phase-cycling, and therefore is a potential basis for pure-shift COSY-type spectra that can be recorded with homonuclear decoupling in either dimension.

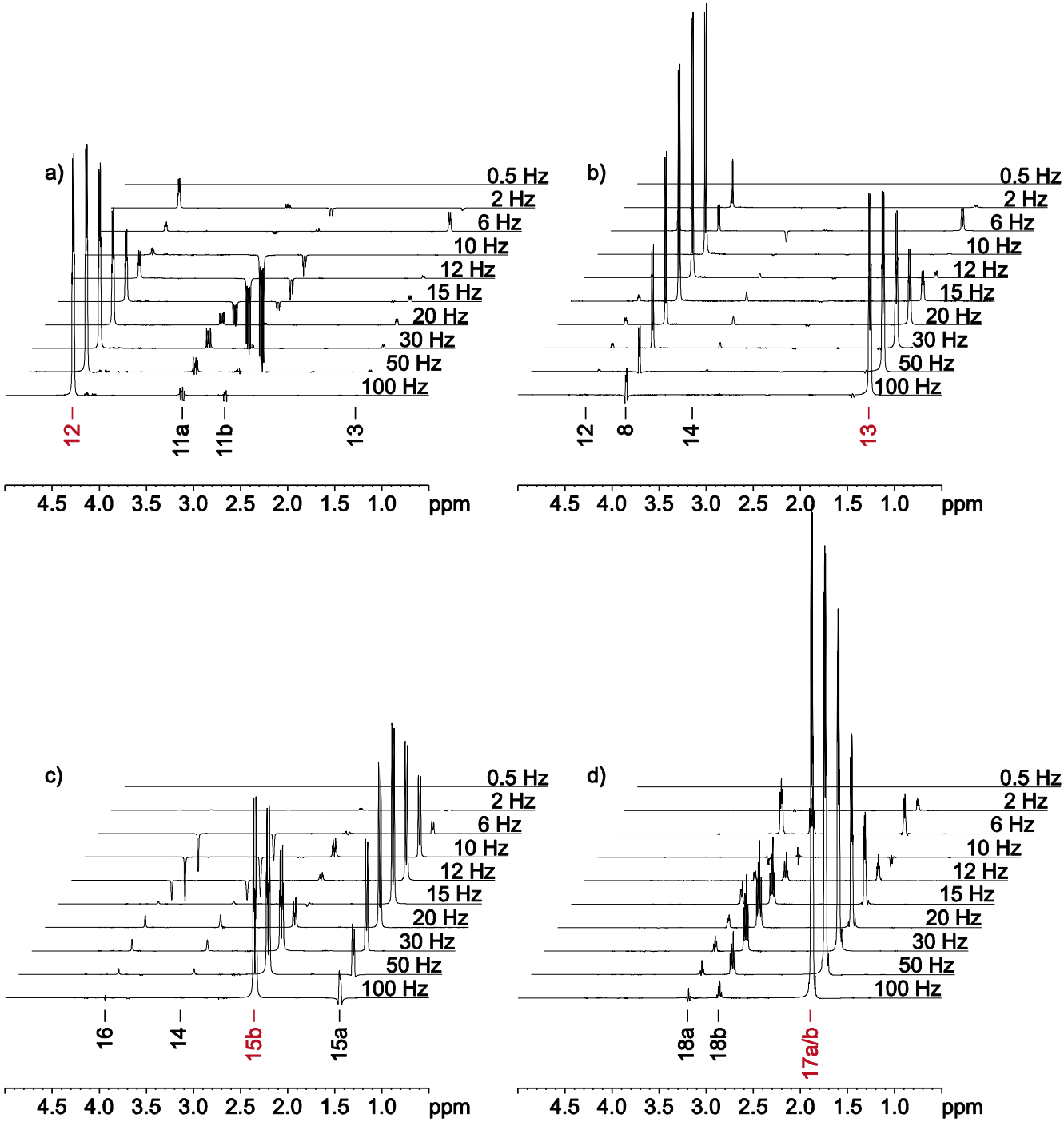

Figure 9.3: Variation of the delay τ in CLIP-COSY experiments. At the side of the traces the value 1/(4*τ), the optimization value for the perfect echo mixing period, is reported. All other experimental settings are equal to those for the CLIP-COSY from Figure 9.2 b). F_2-traces are shown at different F_1-frequencies, and the diagonal peak positions chosen are highlighted in red (H12 for a), H13 for b), H15b for c) and H17a/b for d)). All traces are plotted at the same absolute intensity scale.

9.3. Performance of CLIP-COSY experiments in the presence of line-broadening by conformational and chemical exchange

The potential use of in-phase COSY techniques for generation of pure shift COSY-derivatives has stimulated a reinvestigation of in-phase COSY techniques not only in our group. At the EUROMAR 2015 conference (05. – 10.07.2015, Prague, Czech Republic, http://www.euromar2015.org/) MARTIN KOOS and BURKHARD LUY presented COSY-type spectra obtained with a very similar pulse sequence to the one shown in Figure 9.1 b)[384] (differences existed only in the absence of G_2, in a different phase cycling for more than one scan and in the choice of different pulses for z-filtration). Realizing, that very similar investigations were carried out in both groups, they agreed to continue the work on the CLIP-COSY experiment in collaboration with us.

For the CLIP-COSY implementation reported in the paper printed below, MARTIN KOOS had already provided a comparison of the experiment properties to the DQF-COSY technique[381], as one of the most frequently used COSY techniques. He later complemented the discussion with comparisons to the IP-COSY technique[385], a COSY version with constant time t_1-evolution also able to generate in-phase absorptive signals in both dimensions, and to a TOCSY experiment[42]. He was able to show, that CLIP-COSY technique is a very versatile method to collect COSY-type spectra with absorptive, phase sensitive line shape.

As compared to a gradient-filtered DQF-COSY experiment[382, 386], CLIP-COSY provides higher signal intensity for the test sample containing hydroquinidine in $CDCl_3$ and furthermore it is not bound to a minimum number of t_1-increments that needs to be sampled to avoid significant signal loss.

The closely related pulse sequences of the IP-COSY and the CLIP-COSY experiment result in very similar characteristics for both experiments. The limitation of IP-COSY to only moderate F_1-resolutions due to the constant time evolution used, however, is sidestepped in the CLIP-COSY, making it particularly suitable for high-resolution work. For samples with fast transverse relaxation, the IP-COSY may be more suitable, because of the shorter pulse-sequence.

In addition, MARTIN KOOS discussed extensions of the CLIP-COSY approach: He implemented a version of the experiment that is optimized for large molecule work and contains a solvent suppression scheme before acquisition, which he tested on an aqueous sample containing the 14 kDa protein lysozyme (hen egg). Further, he provided a proof-of-principle, that F_2-homodecoupled COSY-type pure shift spectra can be obtained, with the CLIP-COSY approach.

To the paper, I added a discussion of the effect of line-broadening by exchange phenomena on the spectra. Two different exchange phenomena were studied, namely the broadening of lines due to the fast interconversion of the solute between different conformations and the effect that chemical exchange of OH-protons with water can have on the spectra.

I showed that a major advantage of the CLIP-COSY approach becomes apparent when studying broadened signals, which is directly related to the fact that in-phase signals are observed:

When measuring COSY experiments with anti-phase signal multiplets, positive and negative signal components literally start cancelling, if they overlap. Pictorially, this is described in Figure 1 of the manuscript. This problem can already arise for signals with narrow lines, however it becomes most pronounced, if signals are severely broadened, e.g. by exchange phenomena. In contrast, when collecting in-phase signals, all signal components have the same phase and therefore add up, independent of the linewidth. It can therefore be expected, that in-phase COSY variants show comparably high robustness towards the effects of line-broadening, while in COSY experiments that detect anti-phase signals, signals effectively cancel out if pronounced line-broadening is present.

I was able to illustrate the superior performance of in-phase over anti-phase COSY-type experiments for a system that shows line broadening due to conformational exchange. For N-methyl-4-piperidinol I

showed that the ring-inversion occurring in this molecule[387, 388] largely attenuates signals when using the DQF-COSY experiment. In contrast, when using in-phase COSY variants such as IP- or CLIP-COSY, the signal loss is much less severe, and spectra can still be used for signal assignment. The same effect can be expected if other sources of line broadening, such as fast transverse relaxation, are present.
When studying systems undergoing chemical exchange (as opposed to the conformational exchange just discussed), the user should however also be aware of a potential limit of the method: The z-filters used in the CLIP-COSY experiment introduce delays during which chemical exchange can take place, leading to cross-peaks caused by chemical exchange. I illustrated this effect, using the natural sweetener rebaudioside A as a test substance. These peaks feature the same absorptive in-phase signal shape as cross-peaks caused by *J*-couplings and thus the problem of distinction between the two potential sources for cross-peaks may arise. When analysing sites that can undergo chemical exchange, the user therefore should proceed with caution.
I also used the spectra of rebaudioside A (for signal assignment see section 14.4 of the appendices) to illustrate that the CLIP-COSY experiment is robust towards a truncation of the relaxation delay, as was previously observed when using strychnine as test molecule (described in section 9.2). In contrast to this, DQF-COSY can produce false peaks for experiment repetition rates faster than relaxation, as can be observed in Figure S10 B in the Supporting Information of the manuscript. The ability to collect CLIP-COSY data with very short relaxation delays without introducing notable artefacts is very favourable in terms of using this experiment for signal assignment purposes.

In conclusion, the CLIP-COSY experiment offers a versatile experimental access to COSY-type spectra with the particular advantage of offering a favourable absorption-mode in-phase line shape in both spectral dimensions. It could be shown that high quality spectra that can be measured rapidly, with the favourable features of in-phase signals, such as a high signal intensity even at low resolution and only comparably mild signal loss in the case of broadened lines. We were therefore able to present a rapid COSY-type experiment with high resolution and sensitivity, fulfilling all requirements for the application in many fields of solution-state analytics.

The contents of this chapter have been published in
M. R. M. Koos, G. Kummerlöwe, L. Kaltschnee, C. M. Thiele, B. Luy,
Angew. Chem. **2016**, *128*, 7785-7789, DOI: 10.1002/ange.201510938;
Angew. Chem. Int. Ed. **2016**, *55*, 7655-7659, DOI: 10.1002/anie.201510938;

NMR Spectroscopy

International Edition: DOI: 10.1002/anie.201510938
German Edition: DOI: 10.1002/ange.201510938

CLIP-COSY: A Clean In-Phase Experiment for the Rapid Acquisition of COSY-type Correlations

*Martin R. M. Koos, Grit Kummerlöwe, Lukas Kaltschnee, Christina M. Thiele, and Burkhard Luy**

Abstract: *The COSY experiment is an essential homonuclear 2D NMR experiment for the assignment of resonances. Its multiplet line shape, however, is often overly complicated, potentially leads to signal intensity losses, and is responsible for long minimum overall acquisition times. Herein, we present CLIP-COSY, a COSY-type experiment yielding clean in-phase peaks. It can be recorded within a few minutes and benefits from enhanced signal intensities for most cross-peaks. In combination with non-uniform sampling, the experiment times can be further reduced, and the in-phase multiplets enable the application of modern homonuclear decoupling techniques in both dimensions. As antiphase cancelations are avoided, CLIP-COSY can also be applied to macromolecules and other samples with broadened lines.*

The COSY experiment was the first 2D NMR experiment reported;[1] however, it is still invaluable for the structure elucidation of small molecules as it enables the assignment of resonances of adjacent protons in a covalently bonded network. The COSY experiment can be recorded either in a phase-insensitive or a phase-sensitive way, the latter offering higher resolution. To date, many routine applications use phase-insensitive COSY experiments to reduce the experiment duration. Because of the enhanced resolution of pure phase spectra, it would be highly desirable to be able to acquire phase-sensitive COSY spectra within a few minutes for routine NMR spectroscopy of small molecules and metabolomics-type applications. Herein, we introduce the CLIP-COSY experiment, which provides COSY data in short acquisition times without introducing unfavorable dispersion-mode signals and is compatible with homonuclear decoupling during acquisition, which can simplify the spectra.

Variants of COSY with improved phase behavior,[2] suitable signal shape for coupling measurements,[3] constant-time acquisition,[4] and relayed transfer steps have already been reported.[5] All of these experiments, including the widely used double quantum filtered COSY (DQF-COSY),[2a] acquire so-called antiphase multiplets with severe disadvantages as will be discussed in the following.

A sine-modulated antiphase FID starts at zero intensity and therefore requires a minimum acquisition of data points to avoid a severe reduction in signal intensity (Figure 1 A). Thus the digital resolution must be high enough to resolve the active coupling to avoid cancelation of the positive and negative multiplet components (Figure 1 B). Assuming typical ^{1}H–^{1}H coupling constants of $J = 4$–10 Hz, a minimum of 1024 real points typically have to be acquired for t_1 on a 600 MHz spectrometer, leading to acquisition times of at least 30 minutes per sample, independent of the signal intensity.

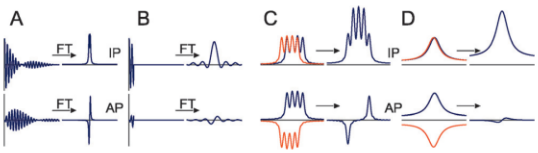

Figure 1. Comparison of in-phase (IP) and antiphase (AP) multiplet patterns. A) Cosine- and sine-modulated FIDs lead to in-phase and antiphase multiplet patterns, respectively. B) Truncated FIDs limit the signal intensities in the antiphase case. C) Overlapping multiplet components originating from passive couplings (here: doublet of doublets) partially cancel antiphase signals. D) Linewidths that are broader than the underlying coupling attenuate antiphase signals.

A second drawback emerges in the case of unresolved multiplet components: Passive couplings lead to the partial cancelation of positive and negative multiplet components, reducing the sensitivity (Figure 1 C). Similarly, broad lines originating from field inhomogeneities, exchange broadening, or fast transverse relaxation lead to cancelation of antiphase signals (Figure 1 D). Therefore, for fast acquisition of spectra and to avoid cancelation artefacts, a COSY-type pulse sequence with in-phase multiplets is required.

Several in-phase variants of COSY have already been reported: SUPER-COSY[6] provides absorptive in-phase cross-peaks but leads to undesired dispersive antiphase

[*] M. R. M. Koos, Prof. Dr. B. Luy
Institut für Organische Chemie and Institut für Biologische Grenzflächen 4—Magnetische Resonanz
Karlsruher Institut für Technologie (KIT)
Fritz-Haber-Weg 6, 76131 Karlsruhe (Germany)
E-mail: Burkhard.Luy@kit.edu
Homepage: http://ioc.kit.edu/luy
Dr. G. Kummerlöwe
Institut für Organische Chemie
Technische Universität München
Lichtenbergstrasse 4, 85747 Garching (Germany)
L. Kaltschnee, Prof. Dr. C. M. Thiele
Clemens-Schöpf-Institut für Organische Chemie und Biochemie
Technische Universität Darmstadt
Alarich-Weiss-Strasse 16, 64287 Darmstadt (Germany)

Supporting information (sample composition, experiment parameters, and pulse program source code) and the ORCID identification numbers for the authors of this article can be found under http://dx.doi.org/10.1002/anie.201510938.

diagonal peaks. ISECR-COSY[7] results in a similar behavior in the directly detected dimension. DQF-ISECR-COSY[7] finally provides the desired absorptive cross- and diagonal peaks, but requires a large number of scans per increment to be acquired. IP-COSY[8] also leads to the desired signal shapes, but the constant-time approach in the indirect dimension limits the accessible resolution and potentially distorts the peak intensities.

As none of the published in-phase experiments enables the rapid acquisition of COSY-type correlations, we designed a pulse sequence based on the general scheme introduced by Thrippleton and Keeler.[9,12] In the presented clean in-phase COSY (CLIP-COSY) experiment (Figure 2 A), in-phase to in-phase coherence transfer between directly coupled spins is ensured using a perfect echo sequence[13] as the mixing element. Antiphase and zero quantum contributions are removed by two single-scan z-filter elements flanking this mixing period.

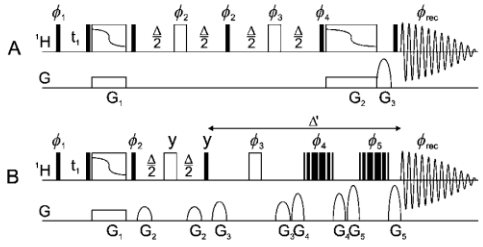

Figure 2. A) CLIP-COSY pulse sequence. The experiment can be acquired with a single scan per F_1 point; for additional scans, the pulse phases were $\phi_1=(x)_4(-x)_4$; $\phi_2=y, -y, -y, y$; $\phi_3=-y, -x, -y, -x$; $\phi_4=x, x, -x, -x$; $\phi_{rec}=x, -x, -x, x, -x, x, x, -x$. The States-TPPI progression was performed on ϕ_1. Pulse phases are x unless denoted otherwise. Filled rectangles represent 90° pulses, and open rectangles represent 180° pulses; open rectangles with frequency sweep and simultaneous application of gradients indicate z-filters.[9] The version with shaped pulses can be found in the Supporting Information. B) CLIP-COSY pulse sequence modified for solvent suppression and optimized for large molecules, such as proteins in H_2O. The second z-filter element has been replaced by excitation sculpting[10] using a binomial 3-9-19 sequence;[11] pulse phases have been adapted to avoid $-z$ magnetization; $\phi_1=x$; $\phi_2=x, -x$; $\phi_3=y, -y$; $\phi_4=(x)_4(y)_4(-x)_4(-y)_4$; $\phi_5=(x)_2(y)_2(-x)_2(-y)_2$; $\phi_{rec}=x, -x$ with States-TPPI progression of ϕ_1.

The previously published IP-COSY[8] method can be seen as a nested constant-time variant of CLIP-COSY, optimized for systems where resolution is limited by the inherent linewidth. The CLIP-COSY pulse sequence can be applied using a single scan per increment and has full flexibility concerning the acquisition parameters in both dimensions. Water suppression may be applied either by presaturation during the recovery delay or by the addition of WATERGATE,[11,14] excitation sculpting,[10] or PE WATERGATE[15] before acquisition.

The performance of the Thrippleton–Keeler z-filters increases with their duration, but polarization transfer by nuclear Overhauser enhancement (NOE), chemical exchange, or conformational interconversion and TOCSY-type transfer between strongly coupled spins may occur during this period, leading to artifacts (see the Supporting Information). Therefore, a compromise between short duration and good performance has to be found. The desired adiabatically swept inversion can be achieved by CHIRP[16] or BIP/BIBOP-type pulses[17] or by specific, optimal control (OC) derived pulses. Simulations have shown that quasi-adiabatic pulses are highly efficient down to a length of about 5 ms. For shorter pulses, OC pulses have slightly better artifact suppression efficiencies (unpublished results). In our experience, the best results for CLIP-COSY are obtained with z-filters of 0.25–0.5 ms for large molecules such as proteins and with filters of 10–20 ms for small molecules with slow NOE build-up.

In Figure 3, a conventional DQF-COSY, a variant of the IP-COSY with the Thrippleton–Keeler z-filter, and a TOCSY experiment with a short mixing time are compared with CLIP-COSY (see also the Supporting Information, Figures S4–S9).

The DQF-COSY spectrum, although recorded with high resolution in the indirect dimension, has the lowest intensity. The spectrum had to be scaled by a factor of four to show the main cross-peaks, and some of the cross-peaks are still missing compared to the in-phase spectra. The IP-COSY, acquired with an overall mixing period of $2(T_c+T_m)=52$ ms as a good compromise between efficient coherence transfer and constant-time resolution, achieves significantly better cross-peak intensities. The CLIP-COSY spectra are of even higher intensity owing to the independently adjustable mixing period. Finally, the DIPSI-2 TOCSY experiment enables the acquisition of intense spectra with a short mixing time of 35 ms, but a number of cross-peaks from relayed correlations are visible, which are undesired in COSY-type applications.

The comparison also shows the dramatic reduction of the overall experiment time that can be achieved without a significant compromise in F_1 resolution. CLIP-COSY can be easily combined with non-uniform sampling (NUS) methods,[18] such as compressed sensing. In this case, it is sufficient to acquire 76 data points for t_1, corresponding to 256 real data points with a NUS density of 30 %, further extended to 512 points by linear prediction, for collecting a highly resolved and well-interpretable CLIP-COSY spectrum in three minutes (Figure 3 D). It should further be noted that the CLIP-COSY experiment enables a drastic reduction of the recovery delay (see, e.g., the spectrum of rebaudiosoide A in Figure S10 A). To facilitate the comparison of signal intensities, this was avoided in Figure 3.

As CLIP-COSY spectra feature full in-phase multiplets, homonuclear decoupling methods for pure shift spectra[19] can directly be applied in both dimensions. As a proof of principle, we recorded a CLIP-COSY spectrum with F_2-PSYCHE decoupling[19b] for menthol (Figure S12).

The CLIP-COSY method can be conveniently applied to molecules dissolved in water using the mentioned water suppression schemes. For protein samples, the second z-filter can be replaced by an excitation sculpting element as for large molecules, zero quantum artifacts are less of an issue (Figure 2 B). In Figure 4, the fingerprint region of hen egg-white

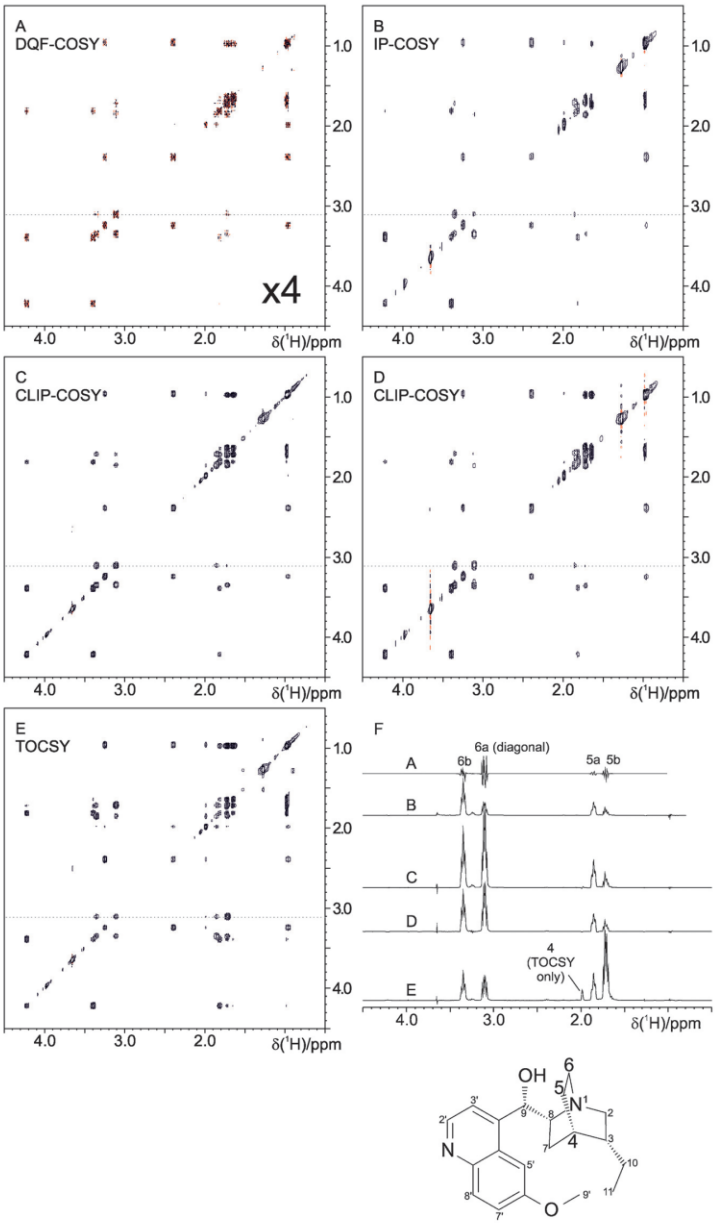

Figure 3. Aliphatic regions of example spectra acquired for 13.7 mM hydroquinidine in $CDCl_3$. A) Conventional DQF-COSY, 4096×1024 points recorded in 32 min 46 s. The peak intensities were multiplied by a factor of four to show the main cross-peaks. B) IP-COSY with the *z*-filter, 4096×384 points recorded in 13 min 3 s. The F_1 resolution is limited by the IP-COSY's constant time/overall mixing period of 52 ms. C) CLIP-COSY, 4096×1024 points recorded in 34 min 18 s using an overall mixing period of $2\Delta = 33.33$ ms. D) CLIP-COSY, 4096×76 non-uniformly sampled points (30% NUS), recorded in 2 min 59 s, reconstructed to 4096×512 points using compressed sensing and linear prediction; $2\Delta = 33.33$ ms. E) TOCSY with the *z*-filter, 4096×1024 points recorded in 34 min 24 s using DIPSI-2 with a mixing time of 34.5 ms. F) F_2 traces extracted from spectra (A)–(E) at 3.11 ppm as indicated by the dashed gray line. Spectra A, C, and E were acquired at the same resolution. For the signal assignment, see the Supporting Information.

lysozyme, which consists of 129 amino acids, is shown as an example.

The in-phase COSY variants show their full strength when lines are broadened by exchange or fast transverse relaxation. In such cases, DQF-COSY experiments suffer from prohibitive signal intensity losses. As demonstrated for *N*-methyl-4-piperidinol, which shows broadened lines owing to ring inversion,[20] the sensitivity advantage obtained with the in-phase COSY techniques can be quite drastic (see Figure 5; for the full spectra, see Figure S11).

For a critical evaluation of the CLIP-COSY method, the two potential drawbacks also have to be discussed in detail: Because of the central in-phase to in-phase coherence transfer step, in contrast to conventional COSY experiments, it is necessary to specify a mixing period of a certain duration. This implies that the coherence transfer will vary between different mixing delays Δ and will depend on the actual spin system. In the weak-coupling limit and neglecting relaxation, integrated cross-peak intensities in the CLIP-COSY are described by Eq. (1), with the active coupling J_{12} and

$$I_{12} = \sin^2\pi J_{12}\Delta \prod_{i\neq 1,2}^{n} \cos\pi J_{1i}\Delta \prod_{j\neq 1,2}^{m} \cos\pi J_{2j}\Delta \qquad (1)$$

the passive couplings J_{1i} and J_{2j} to the $(n-2)$ and $(m-2)$ neighboring spins of corresponding spin systems.

In theory, for a two-spin system, mixing times with Δ up to 50 ms should be practical. However, in our studies, we found that delays of $\Delta = 15$–25 ms are a better compromise for more complex coupling networks. In most applications with active coupling constants of $J > 3$ Hz, mixing times of around $\Delta = 15$ ms are advantageous whereas the detection of weaker couplings might require longer mixing times. In contrast to CT experiments such as IP-COSY, such short mixing periods do not limit F_1 resolution.

Aside from variations in the signal intensities, the specified mixing period also potentially leads to relayed cross-peaks if at least two spins of the spin system are strongly coupled. This effect has been discussed previously and is common to all in-phase COSY approaches (see Ref. [8] and the Supporting Information). Finally, it should

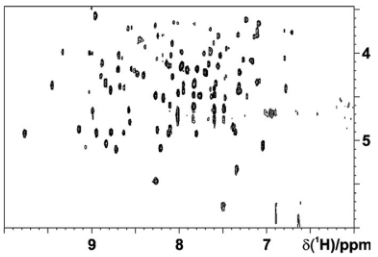

Figure 4. H^N–H^α fingerprint region of a CLIP-COSY spectrum of 1 mM lysozyme in 90% H_2O/10% D_2O using the pulse sequence shown in Figure 2B. The transfer delays were set to $\Delta = 16.7$ ms and $\Delta' = 25$ ms; 4096×512 points were recorded in 1 h 27 min, with four transients per F_1 point.

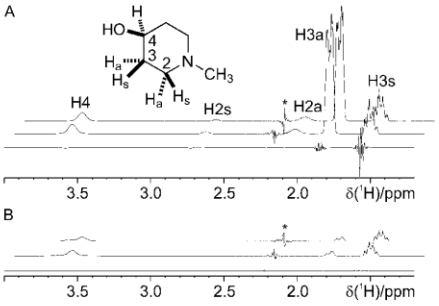

Figure 5. F_2 traces extracted from CLIP-COSY (upper traces), IP-COSY (middle traces), and DQF-COSY (lower traces) spectra, collected for *N*-methyl-4-piperidinol at 283 K. The traces were extracted at F_1 frequencies of A) H^3s and B) H^4. All traces were plotted at the same noise level. For the CLIP- and IP-COSY spectra, 64 F_1 points were collected, and the same effective mixing time was used, $2\Delta = 2(T_c + T_m) = 52$ ms. The DQF-COSY spectrum was collected with 512 F_1 points to avoid truncation (8-fold experiment duration). Signals marked with asterisks are caused by t_1 noise at the N–CH_3 frequency.

be mentioned that the performance of the *z*-filter inherently must break down close to the diagonal,[9] and corresponding multiplets might get distorted. Such distortions, however, are inherent to all COSY-type experiments for strongly coupled spins.

In summary, the CLIP-COSY method has been introduced as an easy-to-handle COSY experiment that provides high quality in-phase multiplet patterns. The main advantage of the CLIP-COSY experiment is the possibility to rapidly acquire spectra with full absorptive line shapes in a few minutes, especially when combined with non-uniform sampling methods. For signals with line broadening due to exchange, large improvements in sensitivity can be achieved compared to DQF-COSY experiments. The sequence does not limit the F_1 resolution and enables the combination of COSY with modern homodecoupled acquisition methods as for TOCSY/NOESY experiments.[19a,21] Owing to the strongly reduced experiment time, the acquisition of absorptive COSY-type correlation spectra will be amenable as a routine NMR method and might also find applications in metabolomics studies and quality control as a sensitive high-resolution 2D experiment.

Acknowledgements

B.L. and M.R.M.K. thank the Deutsche Forschungsgemeinschaft (LU 835/6-2, LU 835/13-1, instrumentation facility Pro²NMR), the HGF program BIFTM and the Fonds der Chemischen Industrie for financial support. Funding by the ERC (257041) and by the Merck Foundation for Arts and Science is acknowledged by C.M.T. and L.K.

Keywords: analytical methods · COSY · NMR spectroscopy · perfect echo · rapid acquisition

How to cite: *Angew. Chem. Int. Ed.* **2016**, *55*, 7655–7659
Angew. Chem. **2016**, *128*, 7785–7789

[1] W. P. Aue, E. Bartholdi, R. R. Ernst, *J. Chem. Phys.* **1976**, *64*, 2229–2246.
[2] a) U. Piantini, O. W. Sørensen, R. R. Ernst, *J. Am. Chem. Soc.* **1982**, *104*, 6800–6801; b) D. Marion, A. Bax, *J. Magn. Reson.* **1988**, *80*, 528–533; c) M. Rance, O. W. Sørensen, G. Bodenhausen, G. Wagner, R. R. Ernst, K. Wüthrich, *Biochem. Biophys. Res. Commun.* **1983**, *117*, 479–485; d) H. Oschkinat, A. Pastore, P. Pfändler, G. Bodenhausen, *J. Magn. Reson.* **1986**, *69*, 559–566; e) A. J. Pell, R. A. E. Edden, J. Keeler, *Magn. Reson. Chem.* **2007**, *45*, 296–316.
[3] a) C. Griesinger, O. W. Sørensen, R. R. Ernst, *J. Magn. Reson.* **1987**, *75*, 474–492; b) C. Griesinger, O. W. Sørensen, R. R. Ernst, *J. Chem. Phys.* **1986**, *85*, 6837–6852; c) C. Griesinger, O. W. Sørensen, R. R. Ernst, *J. Am. Chem. Soc.* **1985**, *107*, 6394–6396; d) L. Mueller, *J. Magn. Reson.* **1987**, *72*, 191–196; e) A. Bax, R. Freeman, *J. Magn. Reson.* **1981**, *44*, 542–561.
[4] a) S. Berger, *Spectrosc. Lett.* **2000**, *33*, 1–8; b) M. E. Girvin, *J. Magn. Reson. Ser. A* **1994**, *108*, 99–102; c) M. Rance, G. Wagner, O. W. Sørensen, K. Wüthrich, R. R. Ernst, *J. Magn. Reson.* **1984**, *59*, 250–261; d) J. A. Aguilar, A. A. Colbourne, J. Cassani, M. Nilsson, G. A. Morris, *Angew. Chem. Int. Ed.* **2012**, *51*, 6460–6463; *Angew. Chem.* **2012**, *124*, 6566–6569.
[5] G. Eich, G. Bodenhausen, R. R. Ernst, *J. Am. Chem. Soc.* **1982**, *104*, 3731–3732.
[6] A. Kumar, R. V. Hosur, K. Chandrasekhar, *J. Magn. Reson.* **1984**, *60*, 143–148.
[7] S. Talluri, H. A. Scheraga, *J. Magn. Reson.* **1990**, *86*, 1–10.
[8] Y. Xia, G. Legge, K.-Y. Jun, Y. Qi, H. Lee, X. Gao, *Magn. Reson. Chem.* **2005**, *43*, 372–379.
[9] M. J. Thrippleton, J. Keeler, *Angew. Chem. Int. Ed.* **2003**, *42*, 3938–3941; *Angew. Chem.* **2003**, *115*, 4068–4071.
[10] T.-L. Hwang, A. J. Shaka, *J. Magn. Reson. Ser. A* **1995**, *112*, 275–279.
[11] M. Liu, X. Mao, C. Ye, H. Huang, J. K. Nicholson, J. C. Lindon, *J. Magn. Reson.* **1998**, *132*, 125–129.
[12] K. E. Cano, M. J. Thrippleton, J. Keeler, A. J. Shaka, *J. Magn. Reson.* **2004**, *167*, 291–297.
[13] a) L. Kaltschnee, A. Kolmer, I. Timári, V. Schmidts, R. W. Adams, M. Nilsson, K. E. Kövér, G. A. Morris, C. M. Thiele, *Chem. Commun.* **2014**, *50*, 15702–15705; b) A. M. Torres, G. Zheng, W. S. Price, *Magn. Reson. Chem.* **2010**, *48*, 129–133; c) P. C. M. van Zijl, C. T. W. Moonen, M. von Kienlin, *J. Magn. Reson.* **1990**, *89*, 28–40; d) K. Takegoshi, K. Ogura, K. Hikichi, *J. Magn. Reson.* **1989**, *84*, 611–615.
[14] M. Piotto, V. Saudek, V. Sklenář, *J. Biomol. NMR* **1992**, *2*, 661–665.

[15] R. W. Adams, C. M. Holroyd, J. A. Aguilar, M. Nilsson, G. A. Morris, *Chem. Commun.* **2013**, *49*, 358–360.
[16] a) J.-M. Böhlen, I. Burghardt, M. Rey, G. Bodenhausen, *J. Magn. Reson.* **1990**, *90*, 183–191; b) J.-M. Böhlen, M. Rey, G. Bodenhausen, *J. Magn. Reson.* **1989**, *84*, 191–197.
[17] a) K. Kobzar, T. E. Skinner, N. Khaneja, S. J. Glaser, B. Luy, *J. Magn. Reson.* **2008**, *194*, 58–66; b) K. Kobzar, T. E. Skinner, N. Khaneja, S. Glaser, B. Luy, *J. Magn. Reson.* **2004**, *170*, 236–243; c) M. A. Smith, H. Hu, A. J. Shaka, *J. Magn. Reson.* **2001**, *151*, 269–283.
[18] M. Mobli, J. C. Hoch, *Prog. Nucl. Magn. Reson. Spectrosc.* **2014**, *83*, 21–41.
[19] a) N. H. Meyer, K. Zangger, *Angew. Chem. Int. Ed.* **2013**, *52*, 7143–7146; *Angew. Chem.* **2013**, *125*, 7283–7286; b) M. Foroozandeh, R. W. Adams, N. J. Meharry, D. Jeannerat, M. Nilsson, G. A. Morris, *Angew. Chem. Int. Ed.* **2014**, *53*, 6990–6992; *Angew. Chem.* **2014**, *126*, 7110–7112; c) K. Zangger, H. Sterk, *J. Magn. Reson.* **1997**, *124*, 486–489; d) J. R. Garbow, D. P. Weitekamp, A. Pines, *Chem. Phys. Lett.* **1982**, *93*, 504–509; e) T. Reinsperger, B. Luy, *J. Magn. Reson.* **2014**, *239*, 110–120; f) I. Timári, L. Kaltschnee, A. Kolmer, R. W. Adams, M. Nilsson, C. M. Thiele, G. A. Morris, K. E. Kövér, *J. Magn. Reson.* **2014**, *239*, 130–138.
[20] a) C.-Y. Chen, R. J. W. Le Fèvre, *Tetrahedron Lett.* **1965**, *6*, 4057–4063; b) T. A. Crabb, A. R. Katrizky, *Adv. Heterocycl. Chem.* **1984**, *36*, 1–173.
[21] a) G. A. Morris, J. A. Aguilar, R. Evans, S. Haiber, M. Nilsson, *J. Am. Chem. Soc.* **2010**, *132*, 12770–12772; b) J. J. Koivisto, *Chem. Commun.* **2013**, *49*, 96–98; c) M. Foroozandeh, R. W. Adams, M. Nilsson, G. A. Morris, *J. Am. Chem. Soc.* **2014**, *136*, 11867–11869; d) L. Castañar, P. Nolis, A. Virgili, T. Parella, *Chem. Eur. J.* **2013**, *19*, 17283–17286.

Received: November 25, 2015
Revised: February 5, 2016
Published online: May 19, 2016

9.4. Discussion and Conclusion on Project D

The desire to collect COSY-type experiments with pure shift acquisition in the direct acquisition dimension has stimulated the reinvestigation of the longstanding problem of producing COSY-type experiments with absorptive in-phase multiplicity. More than just providing an experiment that now enables straightforward combination with pure shift acquisition techniques in both spectral dimensions, this has led to the development of a very promising experimental technique for the rapid acquisition of COSY-type spectra.
Whereas other examples of pure shift NMR have mostly used existing core experiments and have replaced normal-mode acquisition by a pure shift technique, in this case, the alternation of the core experiment itself is the most important novelty. It remains to be seen, if it is actually the CLIP-COSY experiment that will find broad application, yet it is likely, that in addition to the anti- and mixed- phase COSY variants currently in use, in-phase COSY variants will be added to the standard toolbox of NMR spectroscopy because of the favourable features of this signal shape.
Pure shift techniques have been the stimulus for current research interest to develop in-phase COSY-type experiments, however the improvement of the signal shape in COSY spectra has already stimulated numerous investigations[34, 225, 263, 381, 385, 389-392] and it is quite notable, that the problem of finding a practical solution to this goal has remained. It may likely be attributed to the development of efficient single-scan zero-quantum filtration[95] by MICHAEL THRIPPLETON and JAMES KEELER, that a technique could be developed that provides more convenient access to in-phase COSY-type spectra than methods previously reported[385, 391].
Despite being of central importance to the experiment, these pulse sequence elements also are the major cause for possible limitations for the experiment presented: The quality of filtration increases with the duration of these filters, so in practice filters have an inherent minimum length, which is dictated by the system studied and the requirements on spectral quality. The most evident problem related to this is the relaxation loss to the signal that is unavoidable in this period. If filters are shortened, substantial anti-phase contributions to the signals may become apparent. In addition to signal loss, NOE and chemical exchange processes can occur during the period of z-filtration, which lead to signals, that are *a priori* indistinguishable from the COSY-type cross peaks that are desired.
To minimize interference from such sources, it would be desirable in future investigations to design filter elements, which are shorter in length and where the filtration efficiency scales more favourably with the signal frequency difference. It would be interesting in this respect, to explore combinations of the Thrippleton-Keeler filter with trim-pulses lead to significant improvements, or if the z-filtration can be replaced by transverse filtration elements. As in principle pure shift methods should lead to a significant attenuation of anti-phase signal contributions in either spectral dimension, the obvious extension with existing pure shift techniques could also be of interest also from the perspective of reducing demands on the z-filters.

In the work presented, properties of the basic CLIP-COSY experiment have been discussed. It is shown how the CLIP-COSY experiment inherits many of its favourable properties from the in-phase character of the signals. The signal shape reduces signal losses, if spectra with reduced resolution in the indirect dimension are collected and facilitates combination with methods for processing non-uniformly sampled data (NUS), such as compressed sensing (CS)[393, 394] or multi-dimensional decomposition[360, 395] (MDD). The in-phase signal shape possibly also makes it interesting to use covariance calculation methods[396, 397] for processing of CLIP-COSY data. Furthermore, the in-phase signal character leads to a good robustness of the experiment towards signal loss when lines are broadened e.g. due to conformational exchange. The applicability of the experiment is shown for a wide range of substrate.

Aspects of J_{HH} coupling constant measurements based on this basic experiment or on its modifications were not covered in the work presented and will require deeper investigation. The experiment potentially is interesting for J_{HH} measurements from the apparent in-phase multiplet shape as well as from intensity modulations for varying transfer delays and therefore could be useful in the context of coupling constant measurement under various situations. It may also be interesting to investigate, if reductions of the signal multiplicity similar to that in β-COSY[34, 36] or E.COSY[389, 390] techniques can be achieved.

The versatility of the perfect echo in-phase to in-phase mixing block further opens up many different possibilities for modifications of the experiment. Combinations of various homonuclear decoupling techniques (e.g. band-selective decoupling[242, 249, 271], Zangger-Sterk decoupling[252, 257] or PSYCHE decoupling[264]) should be possible in both spectral dimensons, to build various homodecoupled COSY-type experiments for high-resolution signal assignment purposes. The manuscript shows F_2-PSYCHE decoupling for CLIP-COSY as one possibility and other techniques currently are under investigation. It remains to be evaluated for what sort of applications good combinations can be found.

In addition to providing a basic experiment for different pure shift variants, the perfect echo mixing element can potentially also be used as TOCSY-like planar mixing element that introduces mixing only between direct coupling partners, but which does not introduce mixing involving multiple magnetization transfer steps (if strong coupling is absent). The difference to TOCSY-like mixing is two-fold in these applications: The information concerning the spin-system topology is different, as only signals from direct coupling partners are observed and the sensitivity of the transferred cross-peak may be significantly higher, as the magnetization is distributed over a smaller number of resonances with the additional possibility for tuning the mixing element for specific coupling constants.

This opens a large variety of different experiments that become possible, predominantly in the field of hybrid experiments: The in-phase character of the resulting signals could be favourable for many homonuclear hybrid experiments like COSY-COSY[97, 259, 398], NOESY-COSY[97, 259, 398], DOSY-COSY[399] as well as in heteronuclear correlations such as HMQC-COSY[98] and selHSQMBC-COSY[184, 185] and variants of HETLOC[182] and HECADE[183] experiments.

It can easily be seen, that a big variety of future investigations could build on the basic CLIP-COSY mixing element we introduced in this work. We expect, that this basic building block therefore will find widespread application and possibly also modification. It remains a future challenge, to discriminate which of these and other possible extensions actually yield advantages over existing experimental techniques.

10. Summary (English)

The dissertation “Development and Evaluation of Experiments for Pure Shift Solution-State Magnetic Resonance Spectroscopy” (Lukas Kaltschnee, Technical University of Darmstadt) reports methodological developments in the field of high resolution solution state magnetic resonance spectroscopy. The work adds to the field of homonuclear broadband decoupling, which recently attracted renewed attention as the field of “pure shift NMR”. The work is separated in four distinct projects.

In **Project A,** it is investigated, if the addition of the homonuclear decoupling scheme originally proposed by ZANGGER and STERK disrupts signal integrals measured in ^{1}H, 2D NOESY, and pulse-field gradient selected NOE spectra. From investigations of the homonuclear decoupled ^{1}H experiment it is concluded that indeed the pure shift acquisition method can lead to distortions of relative signal integrals and that for the test system of strychnine dissolved in $CDCl_3$, these amount up to 25%.
It is shown, that despite such deviations, the homonuclear decoupling technique does not hamper NOE-based distance determination for high signal-to-noise data significantly. For low signal-to-noise data obtained with homonuclear broadband decoupling it is concluded, that the homonuclear decoupling approach reduces the upper limit distances, that can be determined. For distances shorter than this the inherent limit imposed by sensitivity, the homonuclear decoupled techniques provide accurate NOE-derived distances from pure shift spectra. **(accepted manuscript published by the Journal of Magnetic Resonance; DOI:** 10.1016/j.jmr.2016.08.007**)**

Project B describes the development and testing of homodecoupled HSQC experiments, based on the CLIP-/CLAP-HSQC experiments, designed for accurate measurement of one-bond residual dipolar couplings (RDCs). All experiments described in this chapter enable extraction of the heteronuclear coupling constants in the high-resolution proton dimension, which features partial or full suppression of homonuclear coupling pattern. It is shown in the successive works that homonuclear decoupling along the spectral dimension of coupling constant extraction can improve the accuracy of experimental RDC determination.
In the first section of the project the implementation and characterization of the F_2-BIRD CLIP-/CLAP-HSQC experiments is described **(published in ref. [343])**. It is shown that the experimental technique provides high quality spectra with significantly reduced signal widths both for measurements in isotropic solution and with weakly aligned samples. The capability of an F_2-BIRD HSQC with full heteronuclear decoupling to provide high quality heteronuclear correlation spectra for small molecule test substances and a small protein (55 amino acid residues, *Penicillium* antifungal protein) are demonstrated.
Subsequently, a homonuclear decoupling approach is presented, which sidesteps a major drawback of the BIRD decoupling scheme used in the first section – namely, that diastereotopic methylene protons cannot be decoupled, but lead to phase distorted signals. The perfectBIRD decoupling scheme avoids this problem, leading to fully homodecoupled spectra. An F_2-perfectBIRD CLIP-/CLAP-HSQC experiments is presented **(published in ref. [213])**, again with the emphasis of heteronuclear one-bond coupling constant measurements in the context of RDC extraction. For evaluating the experimental performance, both the accuracy and the precision of the coupling constant extraction procedure are tested. It is shown that in particular for the diastereotopic methylene protons, for which full homonuclear decoupling is achieved with the new homonuclear decoupling scheme, an increased accuracy is achieved during the RDC extraction procedure.
Having established, that BIRD and perfectBIRD decoupling lead to notable advantages for RDC extraction, experiments are tested, with decoupling along the dimension of RDC coupling constant extraction with a real-time BIRD$^{(d)}$ homonuclear decoupling scheme **(submitted to RSC Advances)**. This decoupling method can be used to sample the fully homonuclear decoupled free Induction decay

with much reduced experiment duration, as compared to the cases before. Initially, the fast acquisition of F_2-real-time BIRD$^{(d)}$ CLIP-/CLAP-HSQC experiments had the disadvantage that a large price in the RDC extraction accuracy had to be accepted. Using phase-cycling during acquisition, a method is found, which restores much of the accuracy lost. From tests with a small molecule test sample, no direct penalty of the real-time decoupled experiment is observed in terms of RDC extraction precision, as compared to the reference experiment without homonuclear decoupling during acquisition.
In conclution **Project B** summarizes three BIRD-based pure shift techniques, which prove well suitable for heteronuclear one-bond coupling constant extraction.

Project C makes direct use of the perfectBIRD decoupling scheme derived in project B. A fully homo- and heteronuclear decoupled F_2-perfectBIRD HSQC experiment is presented, which is tailored for highest field strengths available. This experiment provides direct access to HSQC correlation information with notably good signal separation. Use of the perfectBIRD homonuclear decoupling technique hereby enables broadband decoupling which is achieved even for diastereotopic methylene protons.
This experiment is tested on an oligomeric urea-derivative, to illustrate the improved signal separation that comes through the combined use of on an increased effective duration of acquisition and the effect of homonuclear decoupling. Homonuclear decoupling hereby even is achieved for regions in the spectra containing pairs of coupling nuclei. The reduction of intensity of strong coupling artefacts by suitable data processing may be of particular interest, if the strategy proofs to be generally applicable.

The final **Project D** presents a practical solution to the long-standing problem of recording COSY-type correlation spectra with in-phase absorptive signal appearance. The CLIP-COSY **(published in ref. [328])** experiment presented achieves these desirable spectral features even with a single scan per t_1-increment and thus provides rapid access to COSY-type spectra with simple signal appearance along both spectral dimensions. It is demonstrated that the experiment enables very rapid acquisition of COSY-type spectra with full absorption mode, because the in-phase signals do not feature the strong signal loss anti-phase signals do, if only a low resolution is sampled in the indirect dimension. It is shown that, also as a consequence of the in-phase signal shape, the spectra are reasonably robust towards signal losses caused by exchange broadening - a situation where anti-phase COSY variants often feature severe signal loss. Additionally, the method presented closes a gap in the toolbox of pure shift NMR: Previously the application of pure shift techniques other than using a constant-time evolution was not possible for COSY due to their anti-phase signal appearance. The experiment presented in contrast opens up a wide variety of modifications with pure shift techniques.

To conclude, this work documents advances in the development of different NMR techniques, which add up to the pool of pure shift NMR methods and provide high quality structural information for solution state studies.

11. Zusammenfassung (Deutsch)

Die Dissertation „Entwicklung und Bewertung von Pure Shift Experimenten für die Magnetische Resonanzspektroskopie gelöster Moleküle“ (Lukas Kaltschnee, Technische Universität Darmstadt) beschreibt methodische Entwicklungen im Feld der hochauflösenden Kernresonanzspektroskopie an gelösten Substanzen. Die Arbeit trägt zu dem Arbeitsfeld der homonuklearen Breitbandentkopplung bei, welche in der letzten Zeit als „pure shift NMR“ erneut Aufmerksamkeit erregt. Die Arbeit ist in vier getrennte Projekte geteilt.

In **Projekt A** wird untersucht, ob es, durch das Einführen der homonuklearen Entkopplungsmethode, wie sie von ZANNGER und STERK vorgestellt wurde, zu Problemen bei der Messung von Signalintegralen in ^{1}H, 2D NOESY und gradientenselektierten NOE Spektren kommt. Aus den Untersuchungen der homonuklear entkoppelten ^{1}H Experimente wird geschlossen, dass die pure shift Aufnahmemethode tatsächlich zu einer Verzerrung der relativen Signalintegrale führen kann, welche für das untersuchte Testsystem aus Strychnin gelöst in $CDCl_3$ bis zu 25% beträgt.
Es wird gezeigt, dass die gewählte Homoentkopplungstechnik trotz dieser Abweichungen die NOE-basierten Distanzmessungen für Daten mit hohem Signal-zu-Rausch-Verhältnis nicht wesentlich stört. Für Daten mit niedrigem Signal-zu-Rausch-Verhältnis, welche mit homonuklearer Breitbandenkopplung erhalten werden, wird geschlossen, dass der Ansatz zur homonuklearen Entkopplung die obere Grenze der detektierbaren Distanzen begrenzt. Für Distanzen, welche unterhalb dieser inhärenten durch Sensitivität hervorgerufenen Grenze liegen liefern die homonuklear entkoppelten Methoden aber genaue NOE-basierte Distanzen aus pure shift Spektren. **(angenommenes Manuskript publiziert in Journal of Magnetic Resonance; DOI:** 10.1016/j.jmr.2016.08.007**)**

Projekt B beschreibt die Entwicklung und das Testen homonuklear entkoppelter HSQC Experimente, basierend auf den CLIP-/CLAP-HSQC Experimenten, welche für die exakte Messung von dipolaren Restkopplungen (RDCs) ausgelegt sind. Alle in diesem Kapitel beschriebenen Experimente ermöglichen die Extraktion der heteronuklearen Kopplungskonstanten in der hochaufgelösten Protonendimension der Experimente, welche teilweise oder volle Unterdrückung von homonuklearem Kopplungsmuster aufweist. Es wird in den aufeinander folgenden Arbeiten gezeigt, wie homonukleare Entkopplung entlang der spektralen Dimension der Kopplungskonstantenextraktion die Genauigkeit der experimentellen Bestimmung der RDCs verbessern kann.
Im ersten Teil des Projektes wird die Implementierung und Charakterisierung des F_2-BIRD CLIP-/CLAP-HSQC Experiments **(publiziert als Ref. [343])** beschrieben. Es wird gezeigt, dass die besagte experimentelle Technik qualitativ hochwertige Spektren mit deutlich reduzieren Signalweiten, sowohl bei Messung in isotroper Lösung als auch für schwach orientierte Proben, zeigt. Die Fähigkeit eines F_2-BIRD HSQCs mit vollständiger heteronuklearer Entkopplung qualitativ hochwertige homonukleare Korrelationsspektren zu liefern wird für ein kleines Molekül als Testsubstanz und für ein kleines Protein (55 Aminosäreeinheiten, *Penicillium* antifungal protein) gezeigt.
Anschließend wird ein Ansatz zur homonuklearen Entkopplung präsentiert, welcher ein grundsätzliches Problem der BIRD Entkopplungsmethode umgeht – um es zu benennen, dass diastereotope Methylenprotonen nicht entkoppelt werden können, sondern phasenverzerrte Signale aufweisen. Die perfectBIRD Entkopplungsmethode umgeht dieses Problem, was zu vollständig homonuklear entkoppelten Spektren führt. Es wird ein F_2-perfectBIRD CLIP-/CLAP-HSQC Experiment präsentiert **(publiziert als Ref. [213])**, erneut mit der Absicht der Vermessung heteronuklearer Kopplungskonstanten über eine Bindung im Kontext der RDC-Extraktion. Um die Leistungsfähigkeit des Experiments zu bewerten wird sowohl die Genauigkeit der Kopplungskonstantenextraktion, als auch deren Reproduzierbarkeit getestet. Es wird gezeigt, dass im Besonderen für die diastereotopen

Methylenprotonen, welche mit dem neuen homonuklearen Breitbandentkopplungselement nun vollständig entkoppelt werden, eine verbesserte Präzision der RDC Extraktion erzieht wird.
Nachdem gezeigt werden konnte, dass BIRD und perfectBIRD Entkopplung merkliche Vorteile für die RDC Extraktion liefern, werden Experimente getestet, welche BIRD Entkopplung in der Dimension der RDC Kopplungskonstantenextraktion mit einem real-time BIRD$^{(d)}$ Homoentkopplungsansatz erzielen. **(eingereicht bei RSC Advances)** Diese Entkopplungsmethode kann genutzt werden, um den vollen homonuklear entkoppelten freien Induktionszerfall in deutlich verkürzter Experimentdauer im Vergleich zu den vorher diskutierten Fällen zu messen. Die schnelle Aufnahme des F_2-real-time BIRD$^{(d)}$ CLIP-/CLAP-HSQCs hatte anfänglich leider den Nachteil, dass sie für sie deutliche Einbußen in der Genauigkeit der Kopplungskonstantenextraktion in Kauf genommen werden mussten. Durch die Nutzung von Phasenzyklen während der Aufnahme konnte eine Methode gefunden werden, welche einen großen Teil der zunächst verlorenen Genauigkeit wiederherstellt. In Tests an einem kleinen Molekül als Testsubstanz, konnte im Vergleich mit dem Referenzexperiment ohne homonukleare Entkopplung, kein direkter Nachteil der Methode real-time Homoentkopplungsmethode, bezogen auf die Genauigkeit der RDC Extraktion, festgestellt werden.
Zusammenfassend brerichtet **Projekt B** von drei BIRD-basierten pure shift Techniken, welche sich gut zur Extraktion von heteronuklearen Kopplungskonstanten über eine Bindung eignen.

Projekt C nutzt direkt das in Projekt B vorgestellte perfectBIRD Homoentkopplungselement. Ein vollständig homo- und heteronuklear entkoppeltes F_2-perfectBIRD HSQC Experiment wird präsentiert, welches für die Nutzung bei hohen Feldstärken ausgelegt ist. Das Experiment liefert direkten Zugang zur HSQC Korrelationsinformation mit bemerkenswert guter Signaltrennung. Die Nutzung der perfectBIRD Entkopplungsmethode ermöglicht hierbei eine Breitbandentkopplung, welche sogar für diastereotope Methylenprotonen erreicht wird.
Das Experiment wird an einem oligomeren Harnstoffderivat getestet, um die verbesserte Signaltrennung zu illustrieren. Diese wird durch eine kombinierte Erhöhung der effektiven Aufnahmedauer und durch den Effekt der homonuklearen Entkopplung erreicht. Homonukleare Entkopplung wird hierbei sogar für spektrale Regionen erreicht welche paare koppender Kerne enthalten. Eine Verringerung der Intensität von auftretenden Artefakten starker Kopplung durch die Verwendung von geeigneter Datenprozessierung könnte hierbei besonders interessant sein, falls sich herausstellt, dass das genutzte Konzept generell anwendbar ist.

Zuletzt präsentiert **Projekt D** eine praktische Lösung des lange vorhandenen Problems der Aufnahme von COSY-artigen Spektren mit in-phase artiger absorptiver Signalform. Das präsentierte CLIP-COSY Experiment **(publiziert als Ref. [328])** erreicht diese wünschenswerten spektralen Eigenschaften sogar mit einem einzigen Messdurchlauf pro t_1-Inkrement, und gibt so einen Zugang zu COSY-artigen Spektren mit einfacher Signalform in beiden spektralen Dimensionen. Es wird gezeigt, dass das Experiment die schnelle Aufnahme COSY-artiger Spektren mit vollständig absorptiven Signalen ermöglicht, da in-Phase Signale nicht den starken Sensitivitätsverlust aufweisen, der bei Antiphasensignalen auftritt, wenn nur eine geringe Auflösung in der indirekten Dimension verwendet wird. Es wird gezeigt, dass das Experiment einigermaßen robust gegen Signalverlust ist, welcher durch Austauschverbreiterung hervorgerufen wird – eine Situation, bei welcher anti-phasen Techniken oft ernsthaften Signalverlust aufweisen. Zusätzlich schließt die Technik eine Lücke in der Gruppe der pure shift Experimente: Zuvor war eine Anwendung von anderen pure shift Techniken als die der Nutzung einer konstanten Evolutionszeit, aufgrund der antiphasen-Form der Signale, nicht möglich. Im Vergleich dazu ermöglicht das vorgestellte Experiment die Möglichkeit einer vielfachen Modifikation mit pure shift Techniken.
Zusammenfassend dokumentiert diese Arbeit Fortschritte in der Entwicklung verschiedener NMR Techniken, welche hochqualitative Information für die Studien gelöster Moleküle liefern.

12. Literature

1. H. Kawamoto, *Proceedings of the IEEE*, 2002, **90**, 460-500.
2. W. S. Knowles, *Angew. Chem. Int. Ed.*, 2002, **41**, 1998-2007.
3. W. Braun, J. Kallen, V. Mikol, M. D. Walkinshaw and K. Wüthrich, *The FASEB Journal*, 1995, **9**, 63-72.
4. M. R. Jensen, M. Zweckstetter, J.-r. Huang and M. Blackledge, *Chem. Rev.*, 2014, **114**, 6632-6660.
5. K. Wüthrich, *Angew. Chem.*, 2003, **115**, 3462-3486.
6. H. Kessler, *Angew. Chem. Int. Ed.*, 1970, **9**, 219-235.
7. M. Blackledge, *Prog. Nucl. Magn. Reson. Spectrosc.*, 2005, **46**, 23-61.
8. K. Bingol and R. Brüschweiler, *Current Opinion in Clinical Nutrition & Metabolic Care*, 2015, **18**, 471-477.
9. B. Vögeli, J. Orts, D. Strotz, C. Chi, M. Minges, M. A. Wälti, P. Güntert and R. Riek, *J. Magn. Reson.*, 2014, **241**, 53-59.
10. B. Blümich, S. Haber-Pohlmeier and W. Zia, *Compact NMR*, De Gruyter, 2014.
11. T. D. W. Claridge, *High-Resolution NMR Techniques in Organic Chemistry*, ELSEVIER, New York, 2009.
12. R. W. Adams, in *eMagRes*, John Wiley & Sons, Ltd, 2014, vol. 3, ch. Pure Shift NMR Spectroscopy, pp. 295 - 309.
13. N. H. Meyer and K. Zangger, *Synlett*, 2014, **25**, 920-927.
14. L. Castañar and T. Parella, *Magn. Reson. Chem.*, 2015, **53**, 399-426.
15. K. Zangger, *Prog. Nucl. Magn. Reson. Spectrosc.*, 2015, **86–87**, 1-20.
16. G. B. Richard R. Ernst, Alexander Wokaun, *Principles of Nuclear Magnetic Resonance in One and Two Dimensions* Clarendon Press, Oxford, 1987.
17. M. H. Levitt, *spin dynamics*, John Wiley & Sons, Ltd, Chichester, second edition edn., 2008.
18. J. Keeler, *Understanding NMR spectroscopy*, John Wiley & Sons Ltd, Chirchester, UK, 2 edn., 2010.
19. J. A. J. P. J. Hore, S. Wimperis, *NMR: The Toolkit*, Oxford Science Publications, Oxford, 2000.
20. R. R. Ernst, *Angew. Chem. Int. Ed.*, 1992, **31**, 805-823.
21. C. A. de Lange and E. E. Burnell, *NMR of Ordered Liquids*, Kluwer Academic Publishers, Dortrecht, Netherlands, 2003.
22. W. S. Veeman, *Prog. Nucl. Magn. Reson. Spectrosc.*, 1984, **16**, 193-235.
23. L. Yao, A. Grishaev, G. Cornilescu and A. Bax, *J. Am. Chem. Soc.*, 2010, **132**, 4295-4309.
24. N. Nath, M. Schmidt, R. R. Gil, R. T. Williamson, G. E. Martin, A. Navarro-Vázquez, C. Griesinger and Y. Liu, *J. Am. Chem. Soc.*, 2016, **138**, 9548-9556.
25. K. Eichele, R. E. Wasylishen, J. F. Corrigan, N. J. Taylor, A. J. Carty, K. W. Feindel and G. M. Bernard, *J. Am. Chem. Soc.*, 2002, **124**, 1541-1552.
26. K. W. Waddell, E. Y. Chekmenev and R. J. Wittebort, *J. Am. Chem. Soc.*, 2005, **127**, 9030-9035.
27. G. Song, R. Kusumi, F. Kimura, T. Kimura, K. Deguchi, S. Ohki, T. Fujito and T. Simizu, *J. Magn. Reson.*, 2015, **255**, 28-33.
28. G. Kummerlöwe, S. L. Grage, C. M. Thiele, I. Kuprov, A. S. Ulrich and B. Luy, *J. Magn. Reson.*, 2011, **209**, 19-30.
29. N. Bloembergen, E. M. Purcell and R. V. Pound, *Phys. Rev.*, 1948, **73**, 679-712.
30. J. H. Prestegard, H. M. Al-Hashimi and J. R. Tolman, *Q. Rev. Biophys.*, 2000, **33**, 371-424.
31. I. Solomon, *Phys. Rev.*, 1955, **99**, 559-565.
32. R. Brückner, *Reaktionsmechanismen: Organische Reaktionen, Stereochemie, Moderne Synthesemethoden*, Spektrum Akademischer Verlag, 3 edn., 2009.
33. M. Hesse, H. Meier, B. Zeeh, S. Bienz, L. Bigler and T. Fox, *Spektroskopische Methoden in der organischen Chemie*, Georg Thieme Verlag KG, Stuttgart, Germany, 8 edn., 2012.
34. W. P. Aue, E. Bartholdi and R. R. Ernst, *J. Chem. Phys.*, 1976, **64**, 2229-2246.
35. H. Kessler, H. Oschkinat, C. Griesinger and W. Bermel, *J. Magn. Reson.*, 1986, **70**, 106-133.
36. A. Bax and R. Freeman, *J. Magn. Reson.*, 1981, **44**, 542-561.

37. L. Mueller, *J. Am. Chem. Soc.*, 1979, **101**, 4481-4484.
38. A. Bax, R. H. Griffey and B. L. Hawkins, *J. Magn. Reson.*, 1983, **55**, 301-315.
39. G. Bodenhausen and D. J. Ruben, *Chem. Phys. Lett.*, 1980, **69**, 185-189.
40. A. Bax and M. F. Summers, *J. Am. Chem. Soc.*, 1986, **108**, 2093-2094.
41. M. Rance, *J. Magn. Reson.*, 1987, **74**, 557-564.
42. S. P. Rucker and A. J. Shaka, *Mol. Phys.*, 1989, **68**, 509-517.
43. B. Reif, M. Köck, R. Kerssebaum, H. Kang, W. Fenical and C. Griesinger, *J. Magn. Reson. A*, 1996, **118**, 282-285.
44. J. Buddrus and H. Bauer, *Angew. Chem. Int. Ed.*, 1987, **26**, 625-642.
45. A. W. Overhauser, *Phys. Rev.*, 1953, **89**, 689-700.
46. D. Neuhaus and M. P. Williamson, *The Nuclear Overhauser Effect in Structural and Conformational Analysis*, John Wiley & Sons, New York, Second edn., 2000.
47. J. Jeener, B. H. Meier, P. Bachmann and R. R. Ernst, *J. Chem. Phys.*, 1979, **71**, 4546-4553.
48. B. H. Meier and R. R. Ernst, *J. Am. Chem. Soc.*, 1979, **101**, 6441-6442.
49. A. Kolmer, L. Kaltschnee, V. Schmidts, L. H. Peeck, H. Plenio and C. M. Thiele, *Magn. Reson. Chem.*, 2013, **51**, 695-700.
50. L. G. Xie, V. Bagutski, D. Audisio, L. M. Wolf, V. Schmidts, K. Hofmann, C. Wirtz, W. Thiel, C. M. Thiele and N. Maulide, *Chemical Science*, 2015, **6**, 5734-5739.
51. C. L. Perrin and T. J. Dwyer, *Chem. Rev.*, 1990, **90**, 935-967.
52. A. Kumar, R. R. Ernst and K. Wüthrich, *Biochem. Biophys. Res. Commun.*, 1980, **95**, 1-6.
53. S. Macura and R. R. Ernst, *Mol. Phys.*, 1980, **41**, 95-117.
54. A. Kumar, G. Wagner, R. R. Ernst and K. Wuethrich, *J. Am. Chem. Soc.*, 1981, **103**, 3654-3658.
55. A. A. Bothner-By, R. L. Stephens, J. Lee, C. D. Warren and R. W. Jeanloz, *J. Am. Chem. Soc.*, 1984, **106**, 811-813.
56. A. Bax and D. G. Davis, *J. Magn. Reson.*, 1985, **63**, 207-213.
57. M. Reggelin, H. Hoffmann, M. Koeck and D. F. Mierke, *J. Am. Chem. Soc.*, 1992, **114**, 3272-3277.
58. C. P. Butts, C. R. Jones and J. N. Harvey, *Chem. Commun.*, 2011, **47**, 1193-1195.
59. C. P. Butts, C. R. Jones, E. C. Towers, J. L. Flynn, L. Appleby and N. J. Barron, *Org. Biomol. Chem.*, 2011, **9**, 177-184.
60. B. Vögeli, *Prog. Nucl. Magn. Reson. Spectrosc.*, 2014, **78**, 1-46.
61. M. Karplus, *J. Chem. Phys.*, 1959, **30**, 11-15.
62. M. Karplus, *J. Am. Chem. Soc.*, 1963, **85**, 2870-2871.
63. P. E. Hansen, *Prog. Nucl. Magn. Reson. Spectrosc.*, 1981, **14**, 175-295.
64. G. Bifulco, P. Dambruoso, L. Gomez-Paloma and R. Riccio, *Chem. Rev.*, 2007, **107**, 3744-3779.
65. J. Schmidt, *J. Biomol. NMR*, 2007, **37**, 287-301.
66. C. M. Thiele, *Eur. J. Org. Chem.*, 2008, **2008**, 5673-5685.
67. R. M. Gschwind, *Angew. Chem. Int. Ed.*, 2005, **44**, 4666-4668.
68. A. Bax, *Protein Sci.*, 2003, **12**, 1-16.
69. B. Reif, M. Hennig and C. Griesinger, *Science*, 1997, **276**, 1230-1233.
70. J. Tropp, *J. Chem. Phys.*, 1980, **72**, 6035-6043.
71. P. F. Yip and D. A. Case, in *Computational Aspects of the Study of Biological Macromolecules by Nuclear Magnetic Resonance Spectroscopy*, eds. J. C. Hoch, F. M. Poulsen and C. Redfield, Plenium Press, New York, 1991, vol. 225, pp. 317 - 330.
72. P. Bernadó and M. Blackledge, *J. Am. Chem. Soc.*, 2004, **126**, 7760-7761.
73. P. Bernadó and M. Blackledge, *J. Am. Chem. Soc.*, 2004, **126**, 4907-4920.
74. O. F. Lange, N.-A. Lakomek, C. Farès, G. F. Schröder, K. F. A. Walter, S. Becker, J. Meiler, H. Grubmüller, C. Griesinger and B. L. de Groot, *Science*, 2008, **320**, 1471-1475.
75. L. Salmon, G. Bouvignies, P. Markwick, N. Lakomek, S. Showalter, D.-W. Li, K. Walter, C. Griesinger, R. Brüschweiler and M. Blackledge, *Angew. Chem. Int. Ed.*, 2009, **48**, 4154-4157.
76. C. M. Thiele, V. Schmidts, B. Böttcher, I. Louzao, R. Berger, A. Maliniak and B. Stevensson, *Angew. Chem.*, 2009, **121**, 6836-6840.

77. B. Böttcher, V. Schmidts, J. A. Raskatov and C. M. Thiele, *Angew. Chem. Int. Ed.*, 2010, **49**, 205-209.
78. G. Lipari and A. Szabo, *J. Am. Chem. Soc.*, 1982, **104**, 4546-4559.
79. G. Lipari and A. Szabo, *J. Am. Chem. Soc.*, 1982, **104**, 4559-4570.
80. G. Nodet, L. Salmon, V. Ozenne, S. Meier, M. R. Jensen and M. Blackledge, *J. Am. Chem. Soc.*, 2009, **131**, 17908-17918.
81. B. Vögeli, T. F. Segawa, D. Leitz, A. Sobol, A. Choutko, D. Trzesniak, W. van Gunsteren and R. Riek, *J. Am. Chem. Soc.*, 2009, **131**, 17215-17225.
82. P. Yip and D. A. Case, *J. Magn. Reson.*, 1989, **83**, 643-648.
83. G. P. Gippert, P. F. Yip, P. E. Wright and D. A. Case, *Biochem. Pharmacol.*, 1990, **40**, 15-22.
84. C. D. Schwieters, J. J. Kuszewski, N. Tjandra and G. Marius Clore, *J. Magn. Reson.*, 2003, **160**, 65-73.
85. C. D. Schwieters, J. J. Kuszewski and G. Marius Clore, *Prog. Nucl. Magn. Reson. Spectrosc.*, 2006, **48**, 47-62.
86. D. Acquotti, L. Poppe, J. Dabrowski, C. W. Von der Lieth, S. Sonnino and G. Tettamanti, *J. Am. Chem. Soc.*, 1990, **112**, 7772-7778.
87. J. Schleucher, J. Quant, S. J. Glaser and C. Griesinger, *J. Magn. Reson. A*, 1995, **112**, 144-151.
88. C. M. Thiele, K. Petzold and J. Schleucher, *Chem. Eur. J.*, 2009, **15**, 585-588.
89. M. P. W. David Neuhaus, *The Nuclear Overhauser Effekt in Structural and Conformational Analysis*, Wiley-VCH, New York, Second edn., 2000.
90. J. Keeler, *Understanding NMR Spectroscopy*, John Wiley & Sons, Ltd, Chirchester, UK, 2. edn., 2010.
91. W. A. Anderson and R. Freeman, *J. Chem. Phys.*, 1962, **37**, 85-103.
92. D. J. States, R. A. Haberkorn and D. J. Ruben, *J. Magn. Reson.*, 1982, **48**, 286-292.
93. N. Kuniaki, *J. Magn. Reson.*, 1986, **66**, 240-249.
94. O. W. Sørensen, M. Rance and R. R. Ernst, *J. Magn. Reson.*, 1984, **56**, 527-534.
95. M. J. Thrippleton and J. Keeler, *Angew. Chem. Int. Ed.*, 2003, **42**, 3938-3941.
96. K. E. Cano, M. J. Thrippleton, J. Keeler and A. J. Shaka, *J. Magn. Reson.*, 2004, **167**, 291-297.
97. C. Griesinger, O. W. Sørensen and R. R. Ernst, *J. Am. Chem. Soc.*, 1987, **109**, 7227-7228.
98. S. W. Fesik, R. T. Gampe and E. R. P. Zuiderweg, *J. Am. Chem. Soc.*, 1989, **111**, 770-772.
99. R. C. Crouch, R. B. McFadyen, S. M. Daluge and G. E. Martin, *Magn. Reson. Chem.*, 1990, **28**, 792-796.
100. J. Stonehouse, P. Adell, J. Keeler and A. J. Shaka, *J. Am. Chem. Soc.*, 1994, **116**, 6037-6038.
101. K. Stott, J. Stonehouse, J. Keeler, T.-L. Hwang and A. J. Shaka, *J. Am. Chem. Soc.*, 1995, **117**, 4199-4200.
102. K. Stott, J. Keeler, Q. N. Van and A. J. Shaka, *J. Magn. Reson.*, 1997, **125**, 302-324.
103. S. Macura, B. T. Farmer II and L. R. Brown, *J. Magn. Reson.*, 1986, **70**, 493-499.
104. H. Hu and K. Krishnamurthy, *J. Magn. Reson.*, 2006, **182**, 173-177.
105. N. H. Andersen, H. L. Eaton and X. Lai, *Magn. Reson. Chem.*, 1989, **27**, 515-528.
106. R. Boelens, T. M. G. Koning and R. Kaptein, *J. Mol. Struct.*, 1988, **173**, 299-311.
107. R. Boelens, T. M. G. Koning, G. A. van der Marel, J. H. van Boom and R. Kaptein, *J. Magn. Reson.*, 1989, **82**, 290-308.
108. M. Köck and C. Griesinger, *Angew. Chem.*, 1994, **106**, 338-340.
109. T. Geppert, M. Kock, M. Reggelin and C. Griesinger, *J. Magn. Reson. B*, 1995, **107**, 91-93.
110. G. E. Pake, *J. Chem. Phys.*, 1948, **16**, 327-336.
111. R. R. Gil, *Angew. Chem. Int. Ed.*, 2011, **50**, 7222-7224.
112. G. Kummerlöwe and B. Luy, in *Annu. Rep. NMR Spectrosc.*, ed. A. W. Graham, Academic Press, 2009, vol. Volume 68, pp. 193-232.
113. R. R. Gil, C. Griesinger, A. Navarro-Vázquez and H. Sun, in *Structure Elucidation in Organic Chemistry*, Wiley-VCH Verlag GmbH & Co. KGaA, 2015, DOI: 10.1002/9783527664610.ch8, pp. 279-324.

114. F. Kramer, M. V. Deshmukh, H. Kessler and S. J. Glaser, *Conc. Magn. Reson. A*, 2004, **21A**, 10-21.
115. A. O. Frank, J. C. Freudenberger, A. K. Shaytan, H. Kessler and B. Luy, *Magn. Reson. Chem.*, 2015, **53**, 213-217.
116. J. A. Losonczi, M. Andrec, M. W. F. Fischer and J. H. Prestegard, *J. Magn. Reson.*, 1999, **138**, 334-342.
117. E. Miclet, E. O'Neil-Cabello, E. P. Nikonowicz, D. Live and A. Bax, *J. Am. Chem. Soc.*, 2003, **125**, 15740-15741.
118. J. R. Tolman, J. M. Flanagan, M. A. Kennedy and J. H. Prestegard, *Proc. Natl. Acad. Sci.*, 1995, **92**, 9279-9283.
119. G. Cornilescu, J. L. Marquardt, M. Ottiger and A. Bax, *J. Am. Chem. Soc.*, 1998, **120**, 6836-6837.
120. C. M. Thiele, A. Maliniak and B. Stevensson, *J. Am. Chem. Soc.*, 2009, **131**, 12878-12879.
121. J. Meiler, J. J. Prompers, W. Peti, C. Griesinger and R. Brüschweiler, *J. Am. Chem. Soc.*, 2001, **123**, 6098-6107.
122. J. R. Tolman, *Curr. Opin. Struct. Biol.*, 2001, **11**, 532-539.
123. J. R. Tolman, H. M. Al-Hashimi, L. E. Kay and J. H. Prestegard, *J. Am. Chem. Soc.*, 2001, **123**, 1416-1424.
124. W. Peti, J. Meiler, R. Brüschweiler and C. Griesinger, *J. Am. Chem. Soc.*, 2002, **124**, 5822-5833.
125. T. S. Ulmer, B. E. Ramirez, F. Delaglio and A. Bax, *J. Am. Chem. Soc.*, 2003, **125**, 9179-9191.
126. F. Li, A. Grishaev, J. Ying and A. Bax, *J. Am. Chem. Soc.*, 2015, **137**, 14798-14811.
127. P. Bernado, L. Blanchard, P. Timmins, D. Marion, R. W. H. Ruigrok and M. Blackledge, *Proc. Natl. Acad. Sci.*, 2005, **102**, 17002 - 17007.
128. C. M. Thiele, V. Schmidts, B. Böttcher, I. Louzao, R. Berger, A. Maliniak and B. Stevensson, *Angew. Chem. Int. Ed.*, 2009, **48**, 6708-6712.
129. A. Krupp, Dr.-Ing., Helikal-chirale Poly(phenylacetylene) als Alignment-Medien zur Anwendung in der RDCbasierten Strukturanalytik, Technische Universität Darmstadt, 2015.
130. J. H. Prestegard, C. M. Bougault and A. I. Kishore, *Chem. Rev.*, 2004, **104**, 3519-3540.
131. A. Marx and C. Thiele, *Chem. Eur. J.*, 2009, **15**, 254-260.
132. C. M. Thiele, *Angew. Chem. Int. Ed.*, 2005, **44**, 2787-2790.
133. N. Tjandra and A. Bax, *Science*, 1997, **278**, 1111-1114.
134. M. Ottiger and A. Bax, *J. Biomol. NMR*, 1999, **13**, 187-191.
135. J. A. Losonczi and J. H. Prestegard, *J. Biomol. NMR*, 1998, **12**, 447-451.
136. M. R. Hansen, P. Hanson and A. Pardi, in *Methods Enzymol.*, Academic Press, 2000, vol. Volume 317, pp. 220-240.
137. M. R. Hansen, L. Mueller and A. Pardi, *Nat. Struct. Mol. Biol.*, 1998, **5**, 1065-1074.
138. M. Rückert and G. Otting, *J. Am. Chem. Soc.*, 2000, **122**, 7793-7797.
139. A. Meddour, I. Canet, A. Loewenstein, J. M. Pechine and J. Courtieu, *J. Am. Chem. Soc.*, 1994, **116**, 9652-9656.
140. A. Marx, V. Schmidts and C. M. Thiele, *Magn. Reson. Chem.*, 2009, **47**, 734-740.
141. C. Aroulanda, M. Sarfati, J. Courtieu and P. Lesot, *Enantiomer*, 2001, **6**, 281-287.
142. C. M. Thiele, *J. Org. Chem.*, 2004, **69**, 7403-7413.
143. N.-C. Meyer, A. Krupp, V. Schmidts, C. M. Thiele and M. Reggelin, *Angew. Chem. Int. Ed.*, 2012, **51**, 8334-8338.
144. X. Lei, Z. Xu, H. Sun, S. Wang, C. Griesinger, L. Peng, C. Gao and R. X. Tan, *J. Am. Chem. Soc.*, 2014, **136**, 11280-11283.
145. W. Zong, G. W. Li, J. M. Cao, X. Lei, M. L. Hu, H. Sun, C. Griesinger and R. X. Tan, *Angew. Chem. Int. Ed.*, 2016, **55**, 3690-3693.
146. B. Deloche and E. T. Samulski, *Macromolecules*, 1981, **14**, 575-581.
147. R. Tycko, F. J. Blanco and Y. Ishii, *J. Am. Chem. Soc.*, 2000, **122**, 9340-9341.
148. J. J. Chou, S. Gaemers, B. Howder, J. M. Louis and A. Bax, *J. Biomol. NMR*, 2001, **21**, 377-382.
149. P. W. Kuchel, B. E. Chapman, N. Müller, W. A. Bubb, D. J. Philp and A. M. Torres, *J. Magn. Reson.*, 2006, **180**, 256-265.

150. C. Gayathri, N. V. Tsarevsky and R. R. Gil, *Chem. Eur. J.*, 2010, **16**, 3622-3626.
151. K. Ruan and J. R. Tolman, *J. Am. Chem. Soc.*, 2005, **127**, 15032-15033.
152. T. Montag and C. M. Thiele, *Chem. Eur. J.*, 2013, **19**, 2271-2274.
153. H.-J. Sass, G. Musco, S. J. Stahl, P. T. Wingfield and S. Grzesiek, *J. Biomol. NMR*, 2000, **18**, 303-309.
154. Y. Ishii, M. A. Markus and R. Tycko, *J. Biomol. NMR*, 2001, **21**, 141-151.
155. S. Meier, D. Häussinger and S. Grzesiek, *J. Biomol. NMR*, 2002, **24**, 351-356.
156. K. Kobzar, H. Kessler and B. Luy, *Angew. Chem. Int. Ed.*, 2005, **44**, 3145-3147.
157. G. Kummerlöwe, J. Auernheimer, A. Lendlein and B. Luy, *J. Am. Chem. Soc.*, 2007, **129**, 6080-6081.
158. A.-C. Pöppler, H. Keil, D. Stalke and M. John, *Angew. Chem.*, 2012, **124**, 7963-7967.
159. M. Ottiger, F. Delaglio, J. L. Marquardt, N. Tjandra and A. Bax, *J. Magn. Reson.*, 1998, **134**, 365-369.
160. A. Bax and N. Tjandra, *J. Biomol. NMR*, 1997, **10**, 289-292.
161. J. R. Tolman and J. H. Prestegard, *J. Magn. Reson. B*, 1996, **112**, 269-274.
162. M. Ottiger, F. Delaglio and A. Bax, *J. Magn. Reson.*, 1998, **131**, 373-378.
163. K. Fehér, S. Berger and K. E. Kövér, *J. Magn. Reson.*, 2003, **163**, 340-346.
164. K. E. Kövér and K. Fehér, *J. Magn. Reson.*, 2004, **168**, 307-313.
165. C. M. Thiele and W. Bermel, *J. Magn. Reson.*, 2012, **216**, 134-143.
166. A. Enthart, J. C. Freudenberger, J. Furrer, H. Kessler and B. Luy, *J. Magn. Reson.*, 2008, **192**, 314-322.
167. L. Castañar, E. Sistaré, A. Virgili, R. T. Williamson and T. Parella, *Magn. Reson. Chem.*, 2015, **53**, 115-119.
168. L. Verdier, P. Sakhaii, M. Zweckstetter and C. Griesinger, *J. Magn. Reson.*, 2003, **163**, 353-359.
169. L. Jin and D. Uhrín, *Magn. Reson. Chem.*, 2007, **45**, 628-633.
170. K. E. Kövér and P. Forgó, *J. Magn. Reson.*, 2004, **166**, 47-52.
171. C. M. Thiele and W. Bermel, *Magn. Reson. Chem.*, 2007, **45**, 889-894.
172. M. Fredersdorf, R. Göstl, A. Kolmer, V. Schmidts, P. Monecke, S. Hecht and C. M. Thiele, *Chem. Eur. J.*, 2015, **21**, 14545-14554.
173. T. Carlomagno, W. Peti and C. Griesinger, *J. Biomol. NMR*, 2000, **17**, 99-109.
174. P. Tzvetkova, S. Simova and B. Luy, *J. Magn. Reson.*, 2007, **186**, 193-200.
175. A. Kaikkonen and G. Otting, *J. Am. Chem. Soc.*, 2001, **123**, 1770-1771.
176. C. Griesinger, O. W. Soerensen and R. R. Ernst, *J. Am. Chem. Soc.*, 1985, **107**, 6394-6396.
177. M. D. Sørensen, S. M. Kristensen, J. J. Led and O. W. Sørensen, *J. Magn. Reson. A*, 1993, **103**, 364-368.
178. A. Meissner and O. W. Sørensen, *Magn. Reson. Chem.*, 2001, **39**, 49-52.
179. P. Trigo-Mouriño, A. Navarro-Vázquez, J. Ying, R. R. Gil and A. Bax, *Angew. Chem. Int. Ed.*, 2011, **50**, 7576-7580.
180. Z. Wu and A. Bax, *J. Magn. Reson.*, 2001, **151**, 242-252.
181. T. Parella and J. F. Espinosa, *Prog. Nucl. Magn. Reson. Spectrosc.*, 2013, **73**, 17-55.
182. M. Kurz, P. Schmieder and H. Kessler, *Angew. Chem. Int. Ed.*, 1991, **30**, 1329-1331.
183. W. Koźmiński and D. Nanz, *J. Magn. Reson.*, 1997, **124**, 383-392.
184. J. Saurí and T. Parella, *Magn. Reson. Chem.*, 2012, **50**, 717-721.
185. J. Saurí, J. F. Espinosa and T. Parella, *Angew. Chem. Int. Ed.*, 2012, **51**, 3919-3922.
186. O. W. Sørensen, G. W. Eich, M. H. Levitt, G. Bodenhausen and R. R. Ernst, *Prog. Nucl. Magn. Reson. Spectrosc.*, 1984, **16**, 163-192.
187. M. H. Levitt and R. Freeman, *J. Magn. Reson.*, 1979, **33**, 473-476.
188. R. Freeman, *Prog. Nucl. Magn. Reson. Spectrosc.*, 1998, **32**, 59-106.
189. P. Hodgkinson and L. Emsley, *Prog. Nucl. Magn. Reson. Spectrosc.*, 2000, **36**, 201-239.
190. L. J. Edwards, D. V. Savostyanov, Z. T. Welderufael, D. Lee and I. Kuprov, *J. Magn. Reson.*, 2014, **243**, 107-113.
191. M. Elyashberg, *TrAC Trends Anal. Chem.*, 2015, **69**, 88-97.

192. N. H. Meyer and K. Zangger, *ChemPhysChem*, 2014, **15**, 49-55.
193. M. J. Duer, *Introduction to Solid-State NMR Spectroscopy*, Blackwell Publishing Ltd, Garsington, UK, 2004.
194. O. W. Soerensen, C. Griesinger and R. R. Ernst, *J. Am. Chem. Soc.*, 1985, **107**, 7778-7779.
195. K. Takegoshi, K. Ogura and K. Hikichi, *J. Magn. Reson.*, 1989, **84**, 611-615.
196. P. C. M. van Zijl, C. T. W. Moonen and M. von Kienlin, *J. Magn. Reson.*, 1990, **89**, 28-40.
197. R. V. Mulkern, J. L. Bowers, S. Peled, R. A. Kraft and D. S. Williamson, *Magn. Reson. Med.*, 1996, **36**, 775-780.
198. A. M. Torres, G. Zheng and W. S. Price, *Magn. Reson. Chem.*, 2010, **48**, 129-133.
199. J. A. Aguilar, M. Nilsson, G. Bodenhausen and G. A. Morris, *Chem. Commun.*, 2012, **48**, 811-813.
200. R. W. Adams, C. M. Holroyd, J. A. Aguilar, M. Nilsson and G. A. Morris, *Chem. Commun.*, 2013, **49**, 358-360.
201. B. Baishya, C. L. Khetrapal and K. K. Dey, *J. Magn. Reson.*, 2013, **234**, 67-74.
202. T. F. Segawa and G. Bodenhausen, *J. Magn. Reson.*, 2013, **237**, 139-146.
203. J. A. Aguilar, R. W. Adams, M. Nilsson and G. A. Morris, *J. Magn. Reson.*, 2014, **238**, 16-19.
204. D. Sinnaeve, *J. Magn. Reson.*, 2014, **245**, 24-30.
205. W. P. Aue, J. Karhan and R. Ernst, *J. Chem. Phys.*, 1976, **64**, 4226-4227.
206. K. Nagayama, P. Bachmann, K. Wuthrich and R. R. Ernst, *J. Magn. Reson.*, 1978, **31**, 133-148.
207. P. Sakhaii, B. Haase and W. Bermel, *J. Magn. Reson.*, 2013, **228**, 125-129.
208. R. Pendrill, O. W. Sørensen and G. Widmalm, *Magn. Reson. Chem.*, 2014, **52**, 82-86.
209. A. Bax, R. Freeman and G. A. Morris, *J. Magn. Reson.*, 1981, **43**, 333-338.
210. J. M. Fonville, A. D. Maher, M. Coen, E. Holmes, J. C. Lindon and J. K. Nicholson, *Anal. Chem.*, 2010, **82**, 1811-1821.
211. M. von Kienlin, C. T. W. Moonen, A. van der Toorn and P. C. M. van Zijl, *J. Magn. Reson.*, 1991, **93**, 423-429.
212. M. P. Williamson, *J. Magn. Reson.*, 1983, **55**, 471-474.
213. L. Kaltschnee, A. Kolmer, I. Timári, V. Schmidts, R. W. Adams, M. Nilsson, K. E. Kövér, G. A. Morris and C. M. Thiele, *Chem. Commun.*, 2014, **50**, 15702-15705.
214. A. J. Pell and J. Keeler, *J. Magn. Reson.*, 2007, **189**, 293-299.
215. P. Xu, X. L. Wu and R. Freeman, *J. Am. Chem. Soc.*, 1991, **113**, 3596-3597.
216. M. J. Thrippleton, R. A. E. Edden and J. Keeler, *J. Magn. Reson.*, 2005, **174**, 97-109.
217. B. Luy, *J. Magn. Reson.*, 2009, **201**, 18-24.
218. A. Verma and B. Baishya, *ChemPhysChem*, 2015, **16**, 2687-2691.
219. A. J. Shaka, J. Keeler and R. Freeman, *J. Magn. Reson.*, 1984, **56**, 294-313.
220. M. R. Wall and D. Neuhauser, *J. Chem. Phys.*, 1995, **102**, 8011-8022.
221. V. A. Mandelshtam and H. S. Taylor, *J. Chem. Phys.*, 1997, **107**, 6756-6769.
222. A. Martinez, F. Bourdreux, E. Riguet and J.-M. Nuzillard, *Magn. Reson. Chem.*, 2012, **50**, 28-32.
223. P. Sakhaii and W. Bermel, *J. Magn. Reson.*, 2014, **242**, 220-223.
224. A. Bax, A. F. Mehlkopf and J. Smidt, *J. Magn. Reson.*, 1979, **35**, 167-169.
225. M. Rance, G. Wagner, O. W. Sørensen, K. Wüthrich and R. R. Ernst, *J. Magn. Reson.*, 1984, **59**, 250-261.
226. M. E. Girvin, *J. Magn. Reson. A*, 1994, **108**, 99-102.
227. G. E. Martin and A. S. Zektzer, *Magn. Reson. Chem.*, 1988, **26**, 631-652.
228. M. Perpick-Dumont, W. F. Reynolds and R. G. Enriquez, *Magn. Reson. Chem.*, 1988, **26**, 358-361.
229. M. Perpick-Dumont, W. F. Reynolds and R. G. Enríquez, *Magn. Reson. Chem.*, 1988, **26**, 881-887.
230. W. F. Reynolds, D. W. Hughes, M. Perpick-Dumont and P. G. Enriquez, *J. Magn. Reson.*, 1985, **63**, 413-417.
231. W. F. Reynolds, S. McLean, M. Perpick-Dumont and R. G. Enríquez, *Magn. Reson. Chem.*, 1988, **26**, 1068-1074.
232. R. Powers, A. M. Gronenborn, G. Marius Clore and A. Bax, *J. Magn. Reson.*, 1991, **94**, 209-213.
233. R. Freeman, S. P. Kempsell and M. H. Levitt, *J. Magn. Reson.*, 1979, **35**, 447-450.
234. M. H. Levitt and R. Freeman, *J. Magn. Reson.*, 1981, **43**, 502-507.

235. A. J. Shaka, J. Keeler and R. Freeman, *J. Magn. Reson.*, 1983, **53**, 313-340.
236. A. J. Shaka, P. B. Barker and R. Freeman, *J. Magn. Reson.*, 1985, **64**, 547-552.
237. R. Fu and G. Bodenhausen, *Chem. Phys. Lett.*, 1995, **245**, 415-420.
238. Ē. Kupče and R. Freeman, *J. Magn. Reson. A*, 1995, **115**, 273-276.
239. Ē. Kupce, R. Freeman, G. Wider and K. Wüthrich, *J. Magn. Reson. A*, 1996, **122**, 81-84.
240. T. E. Skinner and M. R. Bendall, *J. Magn. Reson.*, 1997, **124**, 474-478.
241. F. Schilling, L. R. Warner, N. I. Gershenzon, T. E. Skinner, M. Sattler and S. J. Glaser, *Angew Chem Int Ed Engl*, 2014, **53**, 4475-4479.
242. R. Brüschweiler, C. Griesinger, O. W. Sørensen and R. R. Ernst, *J. Magn. Reson.*, 1988, **78**, 178-185.
243. G. Otting, L. P. M. Orbons and K. Wüthrich, *J. Magn. Reson.*, 1990, **89**, 423-430.
244. P. Berthault, H. Desvaux and B. Perly, *Magn. Reson. Chem.*, 1993, **31**, 259-265.
245. J. Huth, N. D. Kurur and G. Bodenhausen, *J. Magn. Reson. A*, 1996, **118**, 286-290.
246. V. V. Krishnamurthy, *Magn. Reson. Chem.*, 1997, **35**, 9-12.
247. A. Kaerner and D. L. Rabenstein, *Magn. Reson. Chem.*, 1998, **36**, 601-607.
248. J. P. Jesson, P. Meakin and G. Kneissel, *J. Am. Chem. Soc.*, 1973, **95**, 618-620.
249. A. Hammarstroem and G. Otting, *J. Am. Chem. Soc.*, 1994, **116**, 8847-8848.
250. J. Weigelt, A. Hammarström, W. Bermel and G. Otting, *J. Magn. Reson. B*, 1996, **110**, 219-224.
251. J. R. Garbow, D. P. Weitekamp and A. Pines, *Chem. Phys. Lett.*, 1982, **93**, 504-509.
252. K. Zangger and H. Sterk, *J. Magn. Reson.*, 1997, **124**, 486-489.
253. M. Nilsson and G. A. Morris, *Chem. Commun.*, 2007, 933-935.
254. P. Sakhaii, B. Haase and W. Bermel, *J. Magn. Reson.*, 2009, **199**, 192-198.
255. A. Cotte and D. Jeannerat, *Angew. Chem. Int. Ed.*, 2015, **54**, 6016-6018.
256. A. Lupulescu, G. L. Olsen and L. Frydman, *J. Magn. Reson.*, 2012, **218**, 141-146.
257. N. H. Meyer and K. Zangger, *Angew. Chem. Int. Ed.*, 2013, **52**, 7143-7146.
258. F. Bloch and A. Siegert, *Phys. Rev.*, 1940, **57**, 522-527.
259. H. Kessler, S. Mronga and G. Gemmecker, *Magn. Reson. Chem.*, 1991, **29**, 527-557.
260. S. J. Glaser, U. Boscain, T. Calarco, C. P. Koch, W. Köckenberger, R. Kosloff, I. Kuprov, B. Luy, S. Schirmer, T. Schulte-Herbrüggen, D. Sugny and F. K. Wilhelm, *The European Physical Journal D*, 2015, **69**, 1-24.
261. S. L. Patt, *J. Magn. Reson.*, 1992, **96**, 94-102.
262. M. Billeter, Y.-q. Qian, G. Otting, M. Müller, W. J. Gehring and K. Wüthrich, *J. Mol. Biol.*, 1990, **214**, 183-197.
263. A. J. Pell, R. A. E. Edden and J. Keeler, *Magn. Reson. Chem.*, 2007, **45**, 296-316.
264. M. Foroozandeh, R. W. Adams, N. J. Meharry, D. Jeannerat, M. Nilsson and G. A. Morris, *Angew. Chem. Int. Ed.*, 2014, **53**, 6990-6992.
265. J. A. Aguilar, S. Faulkner, M. Nilsson and G. A. Morris, *Angew. Chem. Int. Ed.*, 2010, **49**, 3901-3903.
266. G. A. Morris, J. A. Aguilar, R. Evans, S. Haiber and M. Nilsson, *J. Am. Chem. Soc.*, 2010, **132**, 12770-12772.
267. J. A. Aguilar, M. Nilsson and G. A. Morris, *Angew. Chem. Int. Ed.*, 2011, **50**, 9716-9717.
268. L. Castañar, P. Nolis, A. Virgili and T. Parella, *Chem. Eur. J.*, 2013, **19**, 15472-15475.
269. A. J. Kolkman, Ph.D. Thesis, NMR Spectroscopy in Drug Discovery - Application and Development of NMR Based Methodologies for P450BM3 Drug Metabolism, Metabolite Identification and Mixture Analysis, Radboud Universiteit Nijmegen, 2013.
270. P. Sakhaii, B. Haase, W. Bermel, R. Kerssebaum, G. E. Wagner and K. Zangger, *J. Magn. Reson.*, 2013, **233**, 92-95.
271. L. Castañar, P. Nolis, A. Virgili and T. Parella, *Chem. Eur. J.*, 2013, **19**, 17283-17286.
272. Lokesh and N. Suryaprakash, *Chem. Commun.*, 2014, **50**, 8550-8553.
273. K. J. Donovan and L. Frydman, *Angew. Chem. Int. Ed.*, 2015, **54**, 594-598.
274. J. Mauhart, S. Glanzer, P. Sakhaii, W. Bermel and K. Zangger, *J. Magn. Reson.*, 2015, **259**, 207-215.

275. B. O. Petersen, M. Nilsson, M. Bøjstrup, O. Hindsgaul and S. Meier, *Food Chem.*, 2014, **150**, 65-72.
276. D. Sinnaeve, M. Foroozandeh, M. Nilsson and G. A. Morris, *Angew. Chem. Int. Ed.*, 2016, **55**, 1090-1093.
277. S. Glanzer and K. Zangger, *ChemPhysChem*, 2015, **16**, 3313-3317.
278. S. Glanzer and K. Zangger, *J. Am. Chem. Soc.*, 2015, **137**, 5163-5169.
279. S. Glanzer, O. Kunert and K. Zangger, *J. Magn. Reson.*, 2016, **268**, 88-94.
280. T. Fäcke and S. Berger, *J. Magn. Reson. A*, 1995, **113**, 114-116.
281. J. Farjon, D. Merlet, P. Lesot and J. Courtieu, *J. Magn. Reson.*, 2002, **158**, 169-172.
282. L. Beguin, N. Giraud, J. M. Ouvrard, J. Courtieu and D. Merlet, *J. Magn. Reson.*, 2009, **199**, 41-47.
283. N. Gubensak, W. M. F. Fabian and K. Zangger, *Chem. Commun.*, 2014, **50**, 12254-12257.
284. S. R. Chaudhari and N. Suryaprakash, *ChemPhysChem*, 2015, **16**, 1079-1082.
285. N. Lokesh, S. R. Chaudhari and N. Suryaprakash, *Chem. Commun.*, 2014, **50**, 15597-15600.
286. R. T. Williamson, B. L. Márquez, W. H. Gerwick and K. E. Kövér, *Magn. Reson. Chem.*, 2000, **38**, 265-273.
287. L. Castañar, J. Saurí, P. Nolis, A. Virgili and T. Parella, *J. Magn. Reson.*, 2014, **238**, 63-69.
288. I. Timári, T. Z. Illyes, R. W. Adams, M. Nilsson, L. Szilagyi, G. A. Morris and K. E. Kövér, *Chemistry*, 2015, **21**, 3472-3479.
289. I. Timári, L. Szilágyi and K. E. Kövér, *Chem. Eur. J.*, 2015, **21**, 13939-13942.
290. N. Lokesh and N. Suryaprakash, *Chem. Phys. Lett.*, 2015, **625**, 10-13.
291. J. J. Koivisto, *Chem. Commun.*, 2013, **49**, 96-98.
292. J. A. Aguilar, J. Cassani, M. Delbianco, R. W. Adams, M. Nilsson and G. A. Morris, *Chem. Eur. J.*, 2015, **21**, 6623-6630.
293. D. Pitoux, Z. Hu, B. Plainchont, D. Merlet, J. Farjon, D. Bonnaffé and N. Giraud, *Magn. Reson. Chem.*, 2015, **53**, 836-844.
294. M. Foroozandeh, R. W. Adams, M. Nilsson and G. A. Morris, *J. Am. Chem. Soc.*, 2014, **136**, 11867-11869.
295. V. M. R. Kakita, S. P. B. Vemulapalli and J. Bharatam, *Magn. Reson. Chem.*, 2016, **54**, 308-314.
296. M. Jarenmark, G. Carlström, L. A. Fredin, J. Hedberg Wallenstein, I. Doverbratt, M. Abrahamsson and P. Persson, *Inorg. Chem.*, 2016, **55**, 3015-3022.
297. J. A. Aguilar, A. A. Colbourne, J. Cassani, M. Nilsson and G. A. Morris, *Angew. Chem. Int. Ed.*, 2012, **51**, 6460-6463.
298. J. Ying, J. Roche and A. Bax, *J. Magn. Reson.*, 2014, **241**, 97-102.
299. J. M. McKenna and J. A. Parkinson, *Magn. Reson. Chem.*, 2015, **53**, 249-255.
300. J. Wang, D. Borchardt and D. L. Rabenstein, *Magn. Reson. Chem.*, 2006, **44**, 744-752.
301. V. M. R. Kakita and J. Bharatam, *Magn. Reson. Chem.*, 2014, **52**, 389-394.
302. A. Bax, *J. Magn. Reson.*, 1983, **53**, 517-520.
303. V. Rutar, *Chem. Phys. Lett.*, 1984, **106**, 258-261.
304. D. Uhrín, T. Liptaj and K. E. Kövér, *J. Magn. Reson. A*, 1993, **101**, 41-46.
305. L. Paudel, R. W. Adams, P. Király, J. A. Aguilar, M. Foroozandeh, M. J. Cliff, M. Nilsson, P. Sándor, J. P. Waltho and G. A. Morris, *Angew. Chem. Int. Ed.*, 2013, **52**, 11616-11619.
306. J. A. Aguilar, P. Király, R. W. Adams, M. Bonneau, E. J. Grayson, M. Nilsson, A. M. Kenwright and G. A. Morris, *RSC Advances*, 2015, **5**, 52902-52906.
307. P. Király, R. W. Adams, L. Paudel, M. Foroozandeh, J. A. Aguilar, I. Timári, M. J. Cliff, M. Nilsson, P. Sandor, G. Batta, J. P. Waltho, K. E. Kövér and G. A. Morris, *J. Biomol. NMR*, 2015, **62**, 43-52.
308. C. Lorenc, J. Saurí, A. Moser, A. V. Buevich, A. J. Williams, R. T. Williamson, G. E. Martin and M. W. Peczuh, *ChemistryOpen*, 2015, **4**, 577-580.
309. J. Saurí, W. Bermel, A. V. Buevich, E. C. Sherer, L. A. Joyce, M. H. Sharaf, P. L. Schiff, Jr., T. Parella, R. T. Williamson and G. E. Martin, *Angew. Chem. Int. Ed.*, 2015, **54**, 10160-10164.
310. L. Castañar, R. Roldán, P. Clapés, A. Virgili and T. Parella, *Chem. Eur. J.*, 2015, **21**, 7682-7685.

311. J. Saurí, E. Sistaré, R. Thomas Williamson, G. E. Martin and T. Parella, *J. Magn. Reson.*, 2015, **252**, 170-175.
312. N. Helge Meyer and K. Zangger, *Chem. Commun.*, 2014, **50**, 1488-1490.
313. M. Foroozandeh, P. Giraudeau and D. Jeannerat, *Magn. Reson. Chem.*, 2013, **51**, 808-814.
314. A. Couffin, O. Thillaye du Boullay, M. Vedrenne, C. Navarro, B. Martin-Vaca and D. Bourissou, *Chem. Commun.*, 2014, **50**, 5997-6000.
315. G. Hamdoun, M. Sebban, E. Cossoul, A. Harrison-Marchand, J. Maddaluno and H. Oulyadi, *Chem. Commun.*, 2014, **50**, 4073-4075.
316. S. Islam, J. A. Aguilar, M. W. Powner, M. Nilsson, G. A. Morris and J. D. Sutherland, *Chem. Eur. J.*, 2013, **19**, 4586-4595.
317. S. Glanzer and K. Zangger, *Chem. Eur. J.*, 2014, **20**, 11171-11175.
318. L. Castañar, P. Nolis, A. Virgili and T. Parella, *J. Magn. Reson.*, 2014, **244**, 30-35.
319. R. W. Adams, L. Byrne, P. Király, M. Foroozandeh, L. Paudel, M. Nilsson, J. Clayden and G. A. Morris, *Chem. Commun.*, 2014, **50**, 2512-2514.
320. L. Byrne, J. Solà, T. Boddaert, T. Marcelli, R. W. Adams, G. A. Morris and J. Clayden, *Angew. Chem.*, 2014, **126**, 155-159.
321. M. A. McCoy and L. Mueller, *J. Am. Chem. Soc.*, 1992, **114**, 2108-2112.
322. A. Kolmer, L. J. Edwards, I. Kuprov and C. M. Thiele, *J. Magn. Reson.*, 2015, **261**, 101-109.
323. U. M. Reinscheid, J. Farjon, M. Radzom, P. Haberz, A. Zeeck, M. Blackledge and C. Griesinger, *ChemBioChem*, 2006, **7**, 287-296.
324. M. Fredersdorf, Ph.D. Thesis, NMR-Spektroskopische Strukturaufklärung eines neuen antituberkulotisch wirksamen Depsipeptids und weiterer kleiner Moleküle, Technische Universität, 2016.
325. K. Huben, M. Jewginski, A. Pabis, P. Paluch, B. Luy and S. Jankowski, *J. Pept. Sci.*, 2014, **20**, 901-907.
326. J. Klages, C. Neubauer, M. Coles, H. Kessler and B. Luy, *ChemBioChem*, 2005, **6**, 1672-1678.
327. H. M. Ge, H. Sun, N. Jiang, Y. H. Qin, H. Dou, T. Yan, Y. Y. Hou, C. Griesinger and R. X. Tan, *Chem. Eur. J.*, 2012, **18**, 5213-5221.
328. M. R. M. Koos, G. Kummerlöwe, L. Kaltschnee, C. M. Thiele and B. Luy, *Angew. Chem. Int. Ed.*, 2016, **55**, 7655-7659.
329. A. M. Gronenborn and G. M. Clore, *Prog. Nucl. Magn. Reson. Spectrosc.*, 1985, **17**, 1-32.
330. H. Kessler, M. Köck, T. Wein and M. Gehrke, *Helv. Chim. Acta*, 1990, **73**, 1818-1832.
331. Z. D. Pardo, G. L. Olsen, M. E. Fernández-Valle, L. Frydman, R. Martínez-Álvarez and A. Herrera, *J. Am. Chem. Soc.*, 2012, **134**, 2706-2715.
332. M. Mayzel, J. Rosenlöw, L. Isaksson and V. Orekhov, *J. Biomol. NMR*, 2014, **58**, 129-139.
333. R. Dass, W. Koźmiński and K. Kazimierczuk, *Anal. Chem.*, 2015, **87**, 1337-1343.
334. J. Bart, A. J. Kolkman, A. J. Oosthoek-de Vries, K. Koch, P. J. Nieuwland, H. Janssen, J. van Bentum, K. A. M. Ampt, F. P. J. T. Rutjes, S. S. Wijmenga, H. Gardeniers and A. P. M. Kentgens, *J. Am. Chem. Soc.*, 2009, **131**, 5014-5015.
335. V. M. Kakita and J. Bharatam, *Magn. Reson. Chem.*, 2014, **52**, 389-394.
336. Y. Q. Qian, M. Billeter, G. Otting, M. Müller, W. J. Gehring and K. Wüthrich, *Cell*, 1989, **59**, 573-580.
337. C. E. Müller, L. Wanka, K. Jewell and P. R. Schreiner, *Angew. Chem.*, 2008, **120**, 6275-6278.
338. K. Knoll, Bachelor Thesis, Untersuchungen der quantitativen Eigenschaften selektiver pure shift NOE Experimente, Technische Universität, 2014.
339. D. S. Stefan Berger, *Classics in Spectroscopy, Isolation and Structure Elucidation of Natural Products*, Wiley-VCH, Weinheim, 2009.
340. G. A. Morris, in *Encyclopedia of Magnetic Resonance*, John Wiley & Sons, Ltd, 2007, DOI: 10.1002/9780470034590.emrstm0579.pub2.
341. L. Kaltschnee, Master Thesis, Untersuchungen zur Quantifizierung 1H-entkoppelter protonendetektierter Experimente, Technische Universität Darmstadt, 2012.
342. T. Reinsperger and B. Luy, *J. Magn. Reson.*, 2014, **239**, 110-120.

343. I. Timári, L. Kaltschnee, A. Kolmer, R. W. Adams, M. Nilsson, C. M. Thiele, G. A. Morris and K. E. Kövér, *J. Magn. Reson.*, 2014, **239**, 130-138.
344. S. Loïc and B. Martin, *Reports on Progress in Physics*, 2015, **78**, 126601.
345. H.-R. Loosli, H. Kessler, H. Oschkinat, H.-P. Weber, T. J. Petcher and A. Widmer, *Helv. Chim. Acta*, 1985, **68**, 682-704.
346. B. L. Marquez, W. H. Gerwick and R. Thomas Williamson, *Magn. Reson. Chem.*, 2001, **39**, 499-530.
347. K. E. Kövér and G. Batta, *J. Magn. Reson.*, 2004, **170**, 184-190.
348. T. N. Pham, T. Liptaj, K. Bromek and D. Uhrín, *J. Magn. Reson.*, 2002, **157**, 200-209.
349. D. Uhrín, A. Mele, K. E. Kövér, J. Boyd and R. A. Dwek, *J. Magn. Reson. A*, 1994, **108**, 160-170.
350. B. Baishya and A. Verma, *J. Magn. Reson.*, 2015, **252**, 41-48.
351. A. L. Davis, J. Keeler, E. D. Laue and D. Moskau, *J. Magn. Reson.*, 1992, **98**, 207-216.
352. G. Kummerlöwe, S. Schmitt and B. Luy, *The Open Spectrosc. J.*, 2010, **4**, 16 - 27.
353. A. Kolmer, Ph.D. Thesis, Aufklärung von Struktur-Reaktivitäts-Beziehungen komplexer organischer Moleküle mit moderner NMR-Spektroskopie, Technische Universität, 2015.
354. L. Paudel, R. W. Adams, P. Király, J. A. Aguilar, M. Foroozandeh, M. J. Cliff, M. Nilsson, P. Sándor, J. P. Waltho and G. A. Morris, *Angew. Chem.*, 2013, **125**, 11830-11833.
355. N. H. Meyer and K. Zangger, *Angew. Chem.*, 2013, **125**, 7283-7286.
356. A. J. Shaka and J. Keeler, *Prog. Nucl. Magn. Reson. Spectrosc.*, 1987, **19**, 47-129.
357. W. A. Anderson, *Phys. Rev.*, 1956, **102**, 151-167.
358. M. Hübner, B. Rissom and L. Fitjer, *Helv. Chim. Acta*, 1997, **80**, 1972-1982.
359. D. Jeannerat, D. Ronan, Y. Baudry, A. Pinto, J.-P. Saulnier and S. Matile, *Helv. Chim. Acta*, 2004, **87**, 2190-2207.
360. K. Kazimierczuk, J. Stanek, A. Zawadzka-Kazimierczuk and W. Koźmiński, *Prog. Nucl. Magn. Reson. Spectrosc.*, 2010, **57**, 420-434.
361. M. Mobli and J. C. Hoch, *Prog. Nucl. Magn. Reson. Spectrosc.*, 2014, **83**, 21-41.
362. E. Kupče and R. Freeman, *Magn. Reson. Chem.*, 2007, **45**, 2-4.
363. D. Schulze-Sünninghausen, J. Becker and B. Luy, *J. Am. Chem. Soc.*, 2014, **136**, 1242-1245.
364. H. Kessler, H.-R. Loosli and H. Oschkinat, *Helv. Chim. Acta*, 1985, **68**, 661-681.
365. E. Kupče and R. Freeman, *J. Magn. Reson.*, 2007, **187**, 258-265.
366. H. Hu and K. Krishnamurthy, *Magn. Reson. Chem.*, 2008, **46**, 683-689.
367. P. W. A. Howe, *Magn. Reson. Chem.*, 2010, **48**, 837-841.
368. S. Ehni and B. Luy, *J. Magn. Reson.*, 2013, **232**, 7-17.
369. V. S. Manu and A. Kumar, *J. Magn. Reson.*, 2013, **234**, 106-111.
370. Y. C. Rodriguez, T. M. Duarte, Z. Szakonyi, E. Forró, F. Fülöp and T. J. Wenzel, *Chirality*, 2015, **27**, 708-715.
371. N. Giraud, M. Joos, J. Courtieu and D. Merlet, *Magn. Reson. Chem.*, 2009, **47**, 300-306.
372. K. Rachineni, V. M. R. Kakita, S. Dayaka, S. P. B. Vemulapalli and J. Bharatam, *Anal. Chem.*, 2015, **87**, 7258-7266.
373. B. O. Petersen, M. S. Motawie, B. L. Møller, O. Hindsgaul and S. Meier, *Carbohydr. Res.*, 2015, **403**, 149-156.
374. Y. E. Moskalenko, K. Pulka-Ziach and C. M. Thiele, presented at the 33rd European Peptide Symposium, Sofia (Bulgaria), 2014.
375. C. Hemmerlin, M. Marraud, D. Rognan, R. Graff, V. Semetey, J.-P. Briand and G. Guichard, *Helv. Chim. Acta*, 2002, **85**, 3692-3711.
376. V. Semetey, D. Rognan, C. Hemmerlin, R. Graff, J.-P. Briand, M. Marraud and G. Guichard, *Angew. Chem. Int. Ed.*, 2002, **41**, 1893-1895.
377. G. Guichard, A. Violette, G. Chassaing and E. Miclet, *Magn. Reson. Chem.*, 2008, **46**, 918-924.
378. T. Imhof, Bachelor Thesis, Untersuchung der Anwendbarkeit hochaufgelöster pure shift HSQC Experimente auf die Charakterisierung kleiner Moleküle, Technische Universität Darmstadt, 2015.
379. N. Marco, A. Fredi and T. Parella, *Chem. Commun.*, 2015, **51**, 3262-3265.

380. M. Foroozandeh, R. W. Adams, P. Király, M. Nilsson and G. A. Morris, *Chem. Commun.*, 2015, **51**, 15410-15413.
381. U. Piantini, O. W. Sørensen and R. R. Ernst, *J. Am. Chem. Soc.*, 1982, **104**, 6800-6801.
382. R. E. Hurd, *J. Magn. Reson.*, 1990, **87**, 422-428.
383. F. Tian, P. J. Bolon and J. H. Prestegard, *J. Am. Chem. Soc.*, 1999, **121**, 7712-7713.
384. M. R. M. Koos and B. Luy, presented at the EUROMAR 2015, Prague (Czech Republic), 2015, *poster P185*.
385. Y. Xia, G. Legge, K.-Y. Jun, Y. Qi, H. Lee and X. Gao, *Magn. Reson. Chem.*, 2005, **43**, 372-379.
386. A. L. Davis, E. D. Laue, J. Keeler, D. Moskau and J. Lohman, *J. Magn. Reson.*, 1991, **94**, 637-644.
387. C. Y. Chen and R. J. W. Le Fèvre, *Tetrahedron Lett.*, 1965, **6**, 4057-4063.
388. T. A. Crabb and A. R. Katritzky, in *Adv. Heterocycl. Chem.*, ed. R. K. Alan, Academic Press, 1984, vol. Volume 36, pp. 1-173.
389. C. Griesinger, O. W. Sørensen and R. R. Ernst, *J. Chem. Phys.*, 1986, **85**, 6837-6852.
390. C. Griesinger, O. W. Sørensen and R. R. Ernst, *J. Magn. Reson.*, 1987, **75**, 474-492.
391. S. Talluri and H. A. Scheraga, *J. Magn. Reson.*, 1990, **86**, 1-10.
392. D. Marion and A. Bax, *J. Magn. Reson.*, 1988, **80**, 528-533.
393. K. Kazimierczuk and V. Y. Orekhov, *Angew. Chem. Int. Ed.*, 2011, **50**, 5556-5559.
394. V. Y. Orekhov and V. A. Jaravine, *Prog. Nucl. Magn. Reson. Spectrosc.*, 2011, **59**, 271-292.
395. T. Luan, V. Jaravine, A. Yee, C. Arrowsmith and V. Orekhov, *J. Biomol. NMR*, 2005, **33**, 1-14.
396. R. Bruschweiler, *J. Chem. Phys.*, 2004, **121**, 409-414.
397. D. A. Snyder and R. Brüschweiler, in *Encyclopedia of Magnetic Resonance*, John Wiley & Sons, Ltd, 2007, DOI: 10.1002/9780470034590.emrstm1098.
398. C. Griesinger, O. W. Sørensen and R. R. Ernst, *J. Magn. Reson.*, 1989, **84**, 14-63.
399. C. S. Johnson Jr, *Prog. Nucl. Magn. Reson. Spectrosc.*, 1999, **34**, 203-256.
400. R. Tycko, A. Pines and J. Guckenheimer, *J. Chem. Phys.*, 1985, **83**, 2775-2802.
401. J. M. Bohlen and G. Bodenhausen, *J. Magn. Reson. A*, 1993, **102**, 293-301.
402. D. Marion, M. Ikura, R. Tschudin and A. Bax, *J. Magn. Reson.*, 1989, **85**, 393-399.
403. W. E. Steinmetz and A. Lin, *Carbohydr. Res.*, 2009, **344**, 2533-2538.

13. List of Figures

14. Appendices

14.1. Experimental sections not included in publications or manuscripts

14.1.1. Project A, Figure 6.1: Comparison between sections from NOESY spectra with normal acquisition and Zangger-Sterk homodecoupling in the F_2-dimension

A sample containing the tetrapeptide Boc-L-(π-Me)-His-^{A}Gly-L-Cha-L-Phe-OMe used by the SCHREINER-Group[337] was used for acquisition. The sample contained 29.1 mg of the peptide dissolved in 0.7 ml of toluene-d_8. The spectra were acquired with a gradient-selected NOESY with zero-quantum-filtration during mixing. The F_2-Zangger-Sterk NOESY spectrum (same as used in the manuscript) was collected with an effective spectral width covering roughly 1.5 ppm, as limited by the slice selection gradient. Further experimental parameters are available from the author upon request.

14.1.2. Project B, Figure 7.5: Perfect echo homonuclear decoupling

2,3-Dibromothiophene was purchased from Sigma Aldrich and used without any further purification. A 0.85 M sample was prepared in CD_2Cl_2 (5 mm tube, no sample sealing) and stored in the dark (fridge). NMR-experiments were performed on an Avance III spectrometer operating a 11.4 T magnet, equipped with a TBI probe (1H, 2H, 31P, BB) with z-gradient The sample temperature was regulated at 300K. The proton spectrum without homonuclear decoupling shown was recorded in a single scan. 2.66 s of acquisition were used. The proton spectrum with homonuclear decoupling was recorded as a pseudo-2D dataset with 128 t_1-increments of each 21.3 ms resulting in an FID length of 2.66 s. The pulse sequence "Jref_no_2dw.lk" was used. A single scan was used for each t_1-increment with an inter scan delay of 80 s. The 1D dataset was constructed from the interferogram acquired using a predecessor of the "pshift"-AU (see: electronic material). For both spectra, time domain data was 2x zero filled and exponential apodization (line broadening of 0.3 Hz) was applied before FT

14.1.3. Project B, Figure 7.8: F_2-perfectBIRD CLIP-HSQC with States encoding

The sample contained 145.4 mg (+)-IPC (purchased from Sigma Aldrich) and 664.2 mg CD_2Cl_2 (purchased from Euriso-Top). The spectrum was acquired on a DRX-II spectrometer operating a 9.4 T magnet (400 MHz proton frequency), equipped with a 5 mm QNP probe (1H, 2H, ^{13}C/^{19}F/^{31}P) equipped with z-gradient. The pulse program "hsqcCLIP_2D_PerfectBIRD.v1.0.lk" was used in its DRX-implementation (ZGOPTNS: "-DLABEL_DRX"). Spectral widths were 10.4 ppm for ^{1}H and 70 ppm for ^{13}C, with the transmitter placed at 2.5 ppm and 45 ppm, respectively. Two scans per t_1-increment and four dummy scans were used. In F_1, 64 points were sampled which were 2x zero-filled and subject to a squared cosine apodization before FT. In the pseudo-direct dimension, 16 data chunks of each 30.72 ms were concatenated to provide a resulting FID containing 4192 data points. 4x zero-filling and no apodization was applied in the direct dimension.

14.1.4. Project B, Figure 7.9: F_2-traces of F_2-perfectBIRD CLIP-HSQC spectra with differing data chunk lengths

The anisotropic sample was the one used in ref. [213] was used. F_2-traces collected at the carbon chemical shift of carbon 7 for different lengths of the acquisition chunk are shown. The 1D traces were extracted from a series of F_2-perfectBIRD CLAP-HSQC spectra collected at 400HMz proton frequency (pulse program "hsqcCLAP_2D_PerfectBIRD.v1.0.lk"). The spectral width was 10.4 ppm in F_2 and 70 ppm in

F_1. 64 data points were collected in the F_1 dimension and the number of data chunks acquired in the broadband decoupling dimension was adjusted in order to sample the FID for at least 268.8 ms (2048 complex data points at a dwell time of 120 μs). The constructed FID was truncated to 2048 complex points if more data points were sampled. The data was collected using 16 dummy scans and a four step phase cycle. INEPT and BIRD delays were optimized for $^1J_{CH}$ = 145 Hz. During the CLAP-HSQC-block of all experiments smoothed chirp pulses were used for inversion (Crp60,0.5,20.1; 60 kHz bandwidth, 500 μs length) and refocusing (Crp60comp.4, 60 kHz bandwidth, 2 ms length) on ^{13}C. All gradients were of 1 ms length (smoothed chirp, SMSQ10.100) followed by a 200 μs gradient recovery delay. The gradients are G1 = 15%, G2 = 80%, G3 = 11%, G4 = 20.1%, G5 = 8 %, G7 = 100% of the maximum gradient strength of 53.1 G/cm.

14.1.5. Project C, Figure 8.3, Cyclosporine A spectra acquired at 400 MHz ^{1}H frequency

A 25 mM sample of Cyclosporine A dissolved in benzene-d_6 in a 5 mm tube was used (supplied by Bruker BioSpin GmbH, filling height: 6 cm). The spectra were acquired on a DRX-II spectrometer operating a 9.4 T magnet (400 MHz proton base frequency, Bruker Biospin Karlsruhe), equipped with a 5 mm QNP probe (^{1}H, ^{2}H, ^{13}C/^{19}F/^{31}P) equipped with z-gradient. The system was operated by TopSpin™ 1.3, patchlevel 10. Temperature was regulated at 300 K with a BCU 05 chiller. All spectra were acquired with 12.5 ppm and 166 ppm spectral width in the proton and carbon dimension respectively (spectral widths are represented as rounded values, the dwell time in the proton dimension used is 200 μs). Transmitters were placed at 5 ppm for ^{1}H and at 74.58 ppm for ^{13}C. 16 dummy scans, 4 scans per increment and a relaxation delay of 1.5 s were used in all cases. In the ^{13}C-dimension, 256 complex data points were sampled. Hard 90°-pulses used were 10.68 μs for ^{1}H and 8 μs for ^{13}C. INEPT and BIRD delays were adjusted for a one-bond coupling of 145 Hz in all cases. Adiabatic pulses used for inversion and refocusing of ^{13}C were linear sweeps over 60 kHz with 500 μs and 2000 μs duration, respectively. The amplitude profile was shaped at the outmost 20% of each side of the sweep by quarter-sine ramps (Crp60,0.5,20.1 and Crp60comp.4). The amplitude was calibrated for an adiabaticity factor Q = 5. GARP decoupling was used during acquisition (power adjusted for an equivalent 100 μs 90° ^{13}C-pulse). In F_1 Echo-Antiecho-TPPI encoding was used in all cases with an encoding gradient of 80% and a decoding gradient of 20.1% of the maximum gradient strength. All gradients were of 1 ms length and were followed by a 200 μs recovery delay. All time-domain data was subject to a squared cosine apodization (QSINE, SSB = 2) and was zero-filled to 4192 x 512 complex data points. No baseline correction was applied.

The spectrum with conventional acquisition without homodecoupling (102.4 ms acquisition; shown in black) was acquired with the pulse program “hsqcetgpsp.2” from the standard pulse-program library. In the proton dimension 512 complex data points were sampled (102.4 ms acquisition). No trim pulse was used (power and length set to small values). Gradients were half-sine shaped (SINE.100).

The spectrum with pseudo-3D acquisition without homodecoupling (409.6 ms cumulated acquisition; shown in purple) was acquired with the pulse program “hsqcetgpsp.2_3D.lk”, which, apart from not being compatible with Avance III systems, is equivalent to “hsqcetgpsp.2_3D_r1.4.lk” used for measurements at 11.4 T (see Figure 8.5 & Figure 8.9). In the proton dimension, four data chunks each containing 512 complex data points were sampled (409.6 ms cumulated acquisition). No trim pulse was used (power and length set to small values). Gradients were smoothed-squared shaped (SMSQ10.100). The final 2D dataset was obtained by concatenating FIDs with the pshift-AU.

The spectrum with perfectBIRD decoupling (409.6 ms cumulated acquisition; shown in red) was acquired with the pulse program “hsqcCLIP_EA_pBIRD_CPD.v2.0.lk” (ZGOPTNS: “-DLABEL_DRX”), which for NS ≤ 4 is equivalent to “hsqcCLIP_EA_pBIRD_CPD.r1.4.lk” (only changes in the comments) for which the pulse sequence is shown in Figure 8.1. In the proton dimension, 16 data chunks each

containing 128 complex data points were sampled (409.6 ms cumulated acquisition). Gradients were smoothed-squared shaped (SMSQ10.100). Gradient amplitudes as fractions of the maximum strength were $G_1 = 15\%$, $G_2 = 80\%$, $G_3 = 11\%$, $G_4 = 20.1\%$, $G_5 = 17\%$, $G_6 = 8\%$ and $G_7 = 100\%$ (numbering of gradients according to Figure 8.1 a)). The final 2D dataset was obtained by concatenating FIDs with the pshift-AU.

14.1.6. Project C, Figure 8.5, Cyclosporine A spectra acquired at 600 MHz ^{1}H frequency (pure shift experiment acquired with pulse program shown in Figure 8.1 a))

A 25 mM sample of Cyclosporine A dissolved in benzene-d_6 in a 5 mm tube was used (supplied by Bruker BioSpin GmbH, filling height: 6 cm). The spectra were acquired on an Avance III narrow bore system operating a 11.4 T magnet (600 MHz proton base frequency, Bruker Biospin, Karlsruhe) equipped with a 5 mm triple-band inverse probe (^{1}H, ^{2}H, ^{31}P, BB) with z-gradient. The system was operated by TopSpin™ 3.1, patchlevel 5. Temperature was regulated at 300 K with a BCU-Xtreme chiller. All spectra were acquired with 10.4 ppm and 166 ppm spectral width in the proton and carbon dimension respectively (spectral widths are represented as rounded values, the dwell time in the proton dimension used is 160 μs). Transmitters were placed at 4.75 ppm for ^{1}H and at 74.58 ppm for ^{13}C. 64 dummy scans, 4 scans per increment and a relaxation delay of 1 s were used in all cases. In the ^{13}C-dimension, 192 t_1-increments were sampled. Hard 90°-pulses used were 9.13 μs for ^{1}H and 13 μs for ^{13}C. INEPT and BIRD delays were adjusted for a one-bond coupling of 145 Hz in all cases. Adiabatic pulses used for inversion and refocusing of ^{13}C were linear sweeps over 60 kHz with 500 μs and 2000 μs duration, respectively. The amplitude profile was shaped at the outmost 20% of each side of the sweep by quarter-sine ramps (Crp60,0.5,20.1 and Crp60comp.4). The amplitude was calibrated for an adiabaticity factor $Q = 5$. GARP decoupling was used during acquisition (power adjusted for an equivalent 60 μs 90° ^{13}C-pulse). In F_1 Echo-Antiecho-TPPI encoding was used in all cases with an encoding gradient of 80% and a decoding gradient of 20.1% of the maximum gradient strength. All gradients had a smoothed squared shape (SMSQ10.100), were of 1 ms length and were followed by a 200 μs recovery delay. All time-domain data was subject to a squared cosine apodization (QSINE, SSB = 2) and was zero-filled to 4192 x 256 complex data points. No baseline correction was applied.
The spectrum shown in black was acquired with the pulse program “hsqcetgpsp.2” from the standard pulse-program library. In the proton dimension 625 complex data points were sampled (100 ms acquisition). No trim pulse was used (length set to zero).
The spectrum shown in purple was acquired with the pulse program “hsqcetgpsp.2_3D_r1.4.lk”. In the proton dimension, four data chunks each containing 550 complex data points were sampled (352 ms cumulated acquisition). No trim pulse was used (length set to zero). The final 2D dataset was obtained by concatenating FIDs with the pshift-AU.
The spectrum shown in red was acquired with the pulse program “hsqcCLIP_EA_pBIRD_CPD.r1.4.lk”. In the proton dimension, 20 data chunks each containing 125 complex data points were sampled (400 ms cumulated acquisition), but for processing only the first 352 ms of the resulting FID were used. Gradient amplitudes as fractions of the maximum strength were $G_1 = 15\%$, $G_2 = 80\%$, $G_3 = 11\%$, $G_4 = 20.1\%$, $G_5 = 17\%$, $G_6 = 8\%$ and $G_7 = 50\%$ (numbering of gradients according to Figure 8.1 a)). The final 2D dataset was obtained by concatenating FIDs with the pshift-AU.

14.1.7. Project C, Figure 8.6, Comparison of the signal shape of two representative methyl groups, obtained with the different implementations of the F_2-perfectBIRD HSQC

Experimental parameters equal those for Figure 8.5 (see paragraph 14.1.6), with the following exceptions:

- Hard 90° pulse lengths for ^{13}C were reduced to 12.77 μs in all cases.

- A reduced chunk duration of 17.6 ms (110 complex data points) was used, resulting in 352 ms of total acquisition (2200 complex data points) from the 20 data chunks used per F_1-increment.

Further experimental parameters applying only to the traces shown in red:

- The spectrum from which the traces shown are extracted was collected with the pulse sequence shown in Figure 8.1 b) (hsqcCLIP_EA_pBIRD_CPD.r2.1.lk).
- For the 2D dataset, only 96 complex points were collected in F1.

Further experimental parameters applying only to the traces shown in green:

- The spectrum from which the traces shown are extracted was collected with the pulse sequence shown in Figure 8.1 b) (hsqcCLIP_EA_pBIRD_CPD.r2.1.lk).
- Adiabatic bi-level decoupling[239] was used during acquisition (bi_p5m4sp_4sp.2) with inversion pulses that were swept over a 42 kHz range (Crp42,1.5,20.2) over a 1.5 ms length. For the high-power decoupling period the power level was adjusted for an adiabaticity factor of $Q = 12$ and in the low-power decoupling period $Q = 3$ was used.

Further experimental parameters applying only to the traces shown in blue:

- The spectrum from which the traces shown are extracted was collected with the pulse sequence shown in Figure 8.1 b) (hsqcCLIP_EA_pBIRD_CPD.r2.2.lk).
- Adiabatic bi-level decoupling[239] was used during acquisition (bi_p5m4sp_4sp.2) with inversion pulses that were swept over a 42 kHz range (Crp42,1.5,20.2) over a 1.5 ms length. For the high-power decoupling period the power level was adjusted for an adiabaticity factor of $Q = 12$ and in the low-power decoupling period $Q = 3$ was used.

14.1.8. Project C, Figure 8.7, Tests of the pulse sequence shown in Figure 8.1 b) with a $CHCl_3$-sample at a 11.4 T instrument (600 MHz on protons)

A sample containing 95 mg $CHCl_3$ in 810 mg $CDCl_3$ was prepared (no sealing, T_1 of ^{13}C-sattelite proton signal: 9.9 s). The $^1J_{CH}$ coupling was read from ^{13}C-satellites in a ^{1}H spectrum. Proton T_1-values were estimated from a two-point inversion-recovery measurement (9.9 s for $^{13}CHCl_3$). The spectra were acquired on an Avance III narrow bore system operating a 11.4 T magnet (600 MHz proton base frequency, Bruker Biospin, Karlsruhe) equipped with a 5 mm triple-band inverse probe (1H, 2H, 31P, BB) with z-gradient. The system was operated by TopSpin™ 3.2, patchlevel 5. Temperature was regulated at 300 K with a BCU-Xtreme chiller.

All spectra were acquired with the pulse program "hsqcCLIP_EA_pBIRD_CPD.r2.1.lk" (see Figure 8.1 b)). All spectra were acquired with 10.4 ppm spectral width in the proton dimension respectively (the dwell time in the proton dimension used is 160 μs). A single t_1 time-point was measured at the minimum t_1 value and a 1D-spectrum was extracted from the single t_2-t_3-plane measured. Transmitters were placed on resonance, unless otherwise stated. 4 dummy scans, 2 scans per increment and a relaxation delay of 15 s were used in all cases. In the proton dimension, 20 data chunks each containing 125 complex data points were sampled (400 ms cumulated acquisition).

Hard 90°-pulses used were previously calibrated for the sample used (9.18 μs for ^{1}H and 12.88 μs for ^{13}C). INEPT and BIRD delays were adjusted for a one-bond coupling of CNST2 = 209 Hz unless otherwise stated. Adiabatic pulses used for inversion and refocusing of ^{13}C were linear sweeps over 60 kHz with 500 μs and 2000 μs duration, respectively. The amplitude profile was shaped at the outmost 20% of each side of the sweep by quarter-sine ramps (Crp60,0.5,20.1 and Crp60comp.4). The amplitude was calibrated for an adiabaticity factor $Q = 5$. GARP decoupling was used during acquisition (power adjusted for an equivalent 60 μs 90° ^{13}C-pulse). All gradients had a smoothed squared shape (SMSQ10.100), were of 0.9 ms length and were followed by a 200 μs recovery delay. Gradient amplitudes as fractions of the maximum strength were $G_1 = 15\%$, $G_2 = 80\%$, $G_3 = 11\%$, $G_4 = 20.1\%$,

G_5 = 17%, G_6 = 8% and G_7 = 90% (numbering of gradients according to Figure 8.1 b)). The final 1D dataset was obtained by first extracting the first 2D-plane out of the 3D dataset (using rser2d) and subsequently concatenating FIDs with the pshift-AU.
All time-domain data was subject to exponential apodization (EM, LB = 1 Hz) and was zero-filled to 4192 complex data points. Manual phasing was used only to 0th order. No baseline correction was applied.

14.1.9. Project C, Figure 8.8, Test of ^{13}C offset tolerance of the experiment shown in Figure 8.1 c) with a $CHCl_3$-sample at a 9.4 T instrument (400 MHz on protons)

The $CHCl_3$ sample described in section 14.1.8 was used. The spectra were acquired on an Avance III HD narrow bore system operating a 9.4 T magnet (400 MHz proton base frequency, Bruker Biospin, Karlsruhe) equipped with a 5 mm broadband-direct probe (BB, ^{19}F/^{1}H/^{2}H) with z-gradient. The system was operated by TopSpin™ 3.2, patchlevel 5. Temperature was regulated at 300 K with a BCU II – 80/60 chiller. Hard 90°-pulses used on this machine are 10.25 μs for ^{1}H and 10.0 μs for ^{13}C.the pulse program "hsqcCLIP_EA_pBIRD_CPD.r2.2.lk" (see Figure 8.1 c)), with the exception of the spectrum shown without homonuclear decoupling. The latter used the same implementation of the HSQC-part of the experiment, but with normal F_2-acquisition directly following time-point II (pulse program "hsqcetgpipsp.2.lk", provided in the electronic supplements).A single t_1 time-point was measured at the minimum t_1 value and a 1D-spectrum was extracted from the single t_2-t_3-plane measured. Transmitters were placed on resonance, unless otherwise stated. 4 dummy scans, 2 scans per increment and a relaxation delay of 15 s were used in all cases. In the proton dimension, spectra were acquired with 12.5 ppm spectral width (the dwell time in the proton dimension used is 200 μs). For homonuclear decoupled spectra, 20 data chunks each containing 100 complex data points were sampled (400 ms cumulated acquisition). In the experiment without homonuclear decoupling, a total of 512 complex points were sampled (102.4 ms acquisition)INEPT and BIRD delays were adjusted for a one-bond coupling of CNST2 = 209 Hz. Adiabatic pulses used for inversion and refocusing of ^{13}C were linear sweeps over 80 kHz with 500 μs and 2000 μs duration, respectively. The amplitude profile was shaped at the outmost 20% of each side of the sweep by quarter-sine ramps (Crp80,0.5,20.1 and Crp80comp.4). The amplitude was calibrated for an adiabaticity factor Q = 5. For heteronuclear decoupling, adiabatic single-level decoupling[237, 238] with p5m4-cycling[400] was used (p5m4sp180.2) with inversion pulses that were swept over a 60 kHz range (Crp60,1.5,20.1000.lk) over a 1.5 ms length. The amplitude profile was ramped at the outmost 20% of the pulses using a quarter-sine profile[401]. The power level for broadband decoupling was adjusted for an adiabaticity factor of Q = 3.
All gradients had a smoothed squared shape (SMSQ10.100), were of 0.9 ms length for the F_2-perfectBIRD HSQC experiments and 0.7 ms for the experiment without homonuclear decoupling, and were followed by a 200 μs recovery delay. Gradient amplitudes as fractions of the maximum strength were G_1 = 15%, G_2 = 80%, G_3 = 11%, G_4 = 20.1%, G_5 = 17%, G_6 = 8% and G_7 = 50% (numbering of gradients according to Figure 8.1 c)). The final 1D dataset was obtained by first extracting the first 2D-plane out of the 3D dataset (using rser2d) and subsequently concatenating FIDs with the pshift-AU.For the homonuclear decoupled experiments, time-domain data was subject to exponential apodization (EM, LB = 1 Hz) and was zero-filled to 4192 complex data points. Manual phasing was used only to 0th order. No baseline correction was applied.
For the experiment without homonuclear decoupling, time-domain data was subject to exponential apodization (EM, LB = 4 Hz) and was linear-forward predicted to 4192 complex data points (Me_mod: "LPfc", NCOEF: 64). Manual phasing was used only to 0th order. No baseline correction was applied.

14.1.10. Project C, Figure 8.9, Cyclosporine A spectra acquired at 600 MHz ^{1}H frequency (pure shift experiment acquired with pulse program shown in Figure 9.1 c))

Experimental parameters equal those for Figure 8.5 (see paragraph 14.1.6), with the following exceptions:

- Hard 90° pulse lengths for ^{13}C were reduced to 12.77 μs in all cases.
- The F_2-perfeectBIRD HSQC was collected with the pulse sequence shown in Figure 8.1 c) (hsqcCLIP_EA_pBIRD_CPD.r2.2.lk), with a reduced chunk duration of 17.6 ms (110 complex data points) was used, resulting in 352 ms of total acquisition (2200 complex data points) from the 20 data chunks used per F_1-increment.
- For the F_2-perfectBIRD HSQC experiment and for the experiment without homonuclear decoupling and standard acquisition (shown in black), the proton transmitter was moved to 3.0 ppm and a ^{1}H 90° hard pulse length of 9.25 μs was used. In these experiments, adiabatic pulses for inversion and refocusing were swept over 80 kHz over the same time periods (shapes Crp80,0.5,20.1 and Crp80comp.4), but with the power level adjusted. For heteronuclear decoupling, adiabatic single-level decoupling[237, 238] with p5m4-cycling[400] was used (p5m4sp180.2) with inversion pulses that were swept over a 60 kHz range (Crp60,1.5,20.1000.lk) over a 1.5 ms length. The power level for broadband decoupling was adjusted for an adiabaticity factor of Q = 3.
- The homocoupled HSQC with improved F_2-resolution was acquired using adiabatic bi-level decoupling[239] during acquisition (bi_p5m4sp_4sp.2) with inversion pulses that were swept over a 42 kHz range (Crp42,1.5,20.2) over a 1.5 ms length. For the high-power decoupling period the power level was adjusted for an adiabaticity factor of Q = 12 and in the low-power decoupling period Q = 3 was used.

14.1.11. Projejct C, Figure 8.11, Comparison of ^{1}H-^{13}C-HSQC spectra collected for oligourea 8 (1.9 mM) in pyridine-d_5, acquired at 320 K.

Oligourea **8** was donated by KAROLINA PULKA-ZIACH (University of Warshaw) and used as obtained. 1.6 mg of the substance was dissolved in 0.6145 ml pyridine-d_5 (as determined by weight; 99.8% deuteration, Merck KGaA) inside a 5 mm NMR-tube. After initial measurements, the sample content was transferred to another NMR-tube, where it was degassed by several freeze-pump-thaw cycles, prior to sample sealing under reduced pressure.

The spectra were acquired on an Avance III HD narrow bore system operating a 16.45 T magnet (700 MHz proton base frequency, Bruker Biospin, Karlsruhe) equipped with a cryogenically cooled 5 mm inverse probe (^{1}H/^{19}F – ^{31}P/^{13}C/^{15}N/D) with z-gradient. The system was operated by TopSpin™ 3.2, patchlevel 6. Temperature was regulated at 320 K with a BCU II – 80/60 chiller. Hard 90°-pulses used are 6.7 μs for ^{1}H and 9.3 μs for ^{13}C.Figure 8.1 c) with Δ = 0, as implemented by WOLFGANG BERMEL (the pulse program is provided in the electronic supplements).

Both spectra were acquired with a spectral width of 165 ppm in the ^{13}C-dimension. In both cases 64 dummy scans and a four-step phase-cycle were used and 180 complex data points were collected in the ^{13}C dimension. Each transient was followed by a 1 s relaxation delay. ^{1}H and ^{13}C transmitter frequencies were placed at 4.4 ppm and 80 ppm respectively. INEPT and BIRD delays were optimized for a 145 Hz one-bond coupling.

The experiment without homonuclear decoupling was acquired with 14.28 ppm spectral width in the ^{1}H dimension (100 μs dwell-time) and 102.4 ms of acquisition (1024 complex data points). For the homodecoupled experiment a 8.925 ppm ^{1}H spectral width (160 μs dwell-time) was used. 32 transients in the homonuclear decoupling dimension were measured with incrementation of t_2 in 5.12 ms steps. Each transient was acquired with 99.48 ms of continued acquisition (624 complex data points). After

data reassembly (without FID-averaging) an FID of 163.84 ms length (1024 complex data points) resulted in the pseudo-direct dimension.
In both cases shaped adiabatic pulses swept over a 60 kHz frequency range were used for inversion and refocusing on ^{13}C. For inversion, a 500 μs single sweep (Crp60,0.5,20.1 from the standard pulse library) and for inversion a composite sweep pulse of 2 ms length was used (Crp60comp.4 from the standard pulse library). Both pulse amplitudes were calculated for an adiabaticity factor of Q = 5. For broadband heteronuclear decoupling both experiments used adiabatic bi-level decoupling[239] (bi_p5m4sp_4sp.2 as implemented in TopSpin 3.2 pl 6) with pulses that were adiabatically frequency swept over a 42 kHz band. A 1.5 ms pulse length and a shaped profile (Crp42,1.5,20.2) were used. During the high-power decoupling period, the pulse power was adjusted for an adiabaticity factor of $Q = 12$, during the low-power decoupling period $Q = 3$ was used.
All gradient pulses used were of 900 μs length and used a shaped amplitude profile (SMSQ10.100). Gradient strengths are reported as fractions of the nominal maximum gradient strength of 53.5 G/cm. For coherence selection and Echo/Antiecho-encoding gradient pulses of 80 % (G_2) and 20.1% (G_4) were used in both cases. Additional gradient pulses $G_1 = 23\%$, $G_3 = 11\%$, $G_5 = 17\%$, $G_6 = 7\%$ and $G_7 = 90\%$ (numbering of gradients according to Figure 8.1 c)) were used for the homodecoupled experiment.
In both cases, the FID was zero-filled to 2048 complex data points in the direct dimension and in the indirect dimension forward linear prediction with 32 coefficients was used to obtain a total of 256 complex data points. In both cases a squared cosine function was used for apodization (QSINE; SSB: 2) before Fourier transformation. Data was manually phased and no baseline correction was applied.

14.1.12. Project C, Experiments used for signal assignment in oligourea 8

The experiments were performed using the same sample and spectrometer and pulse lengths as described in section 14.1.11. Further ^{1}H-^{13}C-HSQC experiments were used as described in that section. An additional ^{1}H-^{13}C-HSQC without homonuclear decoupling was collected with 6144 complex data points in the carbon-dimension (16.7 h of acquisition; 4.7 Hz resolution in F_1, 16384 complex data points for processing), with settings otherwise identical to the experiment described.
TOCSY, EASY ROESY, DQF-COSY, ^{1}H-^{15}N-HSQC and HMBC experiments used the pulse programs contained in the TopSpin 3.2 patchlevel 6 pulse program library (*dipsi2esgpph*, *roesyadjsphpr*, *cosydfph*, *hsqcetgpsi* and *hmbcetgpl3nd* respectively). TOCSY, EASY ROESY and DQF-COSY were measured with 11 ppm spectral width in both dimensions with the transmitter placed at 5 ppm. 1024 x 256 (TOCSY), 1024 x 128 (EASY ROESY) and 8192 x 256 (DQF-COSY) complex data points were collected using 8, 24 and 24 steps in the phase cycle respectively. All experiments were preceded by 32 dummy scans and a relaxation delay of 1.5 s (TOCSY) or 2 s (EASY ROESY and DQF-COSY) was used. TOCSY and EASY ROESY used gradients for coherence selection, set as recommended by the manufacturer. The TOCSY experiment used a 100 ms DIPSI-2 mixing element[42]. The EASY ROESY used adiabatically ramped low- and high-filed spin lock periods with a total of 200 ms spin locking at 6.4 kHz. The requested spin-lock tilt-angle was set to 45°.
The ^{1}H-^{15}N-HSQC was acquired with spectral widths of 14.3 ppm on ^{1}H and 120 ppm on ^{15}N with the transmitters set to 4.7 ppm and 100 ppm respectively. 1024 x 128 complex data points were sampled with 32 scans, preceded by 64 dummy scans. INEPT-delays were adjusted to a 90Hz coupling constant. No trim pulse was used. Gradient-based Echo-Antiecho-encoding was used. GARP-4 decoupling (240 μs pulse length) was used during acquisition.
The ^{1}H-^{13}C-HMBC was acquired with widths of 12.0 ppm on ^{1}H and 160 ppm on ^{15}N with the transmitters set to 4.7 ppm and 95 ppm respectively. 2048 x 256 complex data points were sampled with 16 scans, preceded by 32 dummy scans. The timing was optimized for a heteronuclear long-range coupling of 8 Hz. The three-step J-low-pass filter used was optimized to span a range of one-bond couplings between

120 Hz and 170 Hz. Gradient filtration was used as recommended by the manufacturer. A 2 ms composite adiabatic chirp pulse was used for refocusing on ^{13}C. 2048 x 2048 complex data points were used for processing. In the ^{1}H dimension an unshifted sine function was used for apodization, in the ^{13}C dimension a squared cosine function was used after forward linear prediction with 32 coefficients.
2x zero-filling and apodization with a squared cosine function was applied for all spectra but the HMBC. All chemical shifts reported were referenced to the solvent signal appearing at 8.71 ppm in a proton spectrum and calibration was transferred to all 2D spectra.

14.1.13. Project C, Figure 8.12, Chemical shift extraction by spin-system simulation

The reference ^{1}H-spectrum was collected for the sample and using the experimental setup described in section 14.1.11. The sample temperature was regulated at 320 K. A single scan ^{1}H-experiment was performed using a spectral width of 20.1 ppm and 2.34 s of acquisition. A 6.7 μs 90° excitation pulse was used. An exponential apodization (LB: 0.3 Hz) was applied before Fourier transformation.
Spectrum simulation was performed using the Bruker TopSpin™ NMR-Sim™ experiment simulator version 5.6. The option "File -> Experiment setup -> Load from TopSpin Dataset" was used to transfer the settings from ^{1}H-spectrum. Relaxation effects were turned off during the simulation. The pulse amplitude for the 6.7 µs hard pulse was set to 37313.4 Hz. All simulated data was subject to 2x zero-filling (to 65536 complex data points) and to an exponential apodization (LB: 2 Hz) prior to Fourier transformation. The phase correction was calculated from the pulse length used during the simulation.
A four-spin system was defined for simulation. Three spins were coupled to each other, a fourth spin not coupled to the others was positioned at 4.4 ppm to facilitate validation of the spectrum phasing. In different simulations, the settings for chemical shifts and coupling constants of the three coupling spins were adjusted until good agreement between the simulated and the measured data was achieved, as judged by visual inspection. This was achieved by setting ν_1 = 3268.1 Hz (4.667 ppm), ν_2 = 3327.2 Hz (4.751 ppm), ν_3 = 5069 Hz, $J_{1,2}$ = 15.38 Hz, $J_{1,3}$ = 5.6 Hz and $J_{2,3}$ = 6.0 Hz.
It should be noted that the third spin is not resolved in the proton spectrum, so its frequency was fixed at 5069 Hz, according to the chemical shift extracted from 2D spectra.

14.1.14. Project D, Figure 9.2, a) gradient selected magnitude COSY and b) CLIP-COSY, measured for a strychnine (267 mM) in $CDCl_3$

A strychnine sample 267 mM (89 mg/ml) in $CDCl_3$, was used. The sample has been degassed by several freeze-pump-thaw cycles before sealing in a 5 mm tube. Rates for longitudinal relaxation $(T_1)^{-1}$ range from $(4.8\ s)^{-1}$ to $(0.54\ s)^{-1}$ for this sample as reported in (Chapter 2 of the Supporting information of the manuscript inserted into chapter 6 (Project A))
Spectra were acquired on an Avance III narrow bore system operating a 11.4 T magnet (600.3 MHz proton base frequency, Bruker Biospin GmbH, Karlsruhe) equipped with a 5 mm triple-band inverse probe (^{1}H, ^{2}H, ^{31}P, BB) with z-gradient. The system was operated by TopSpin™ 3.2, patchlevel 5. Temperature was regulated at 300 K with a BCU-Xtreme chiller.
The gradient-selected magnitude COSY was acquired with the pulse sequence reported in ref. [211], as implemented in the TopSpin™ 3.2 pl. 5 pulse program library (*cosygpqf*). The CLIP-COSY used the pulse sequence shown in Figure 9.1 b), which is provided in the electronic supplements as *cope2dgp.t1.6.lk* (compiled with ZGOPTNS: "*-DLABEL_ZQF -DLABEL_ZF*").
Spectra were collected with 10.41 ppm spectral width in both dimensions, with the transmitter placed at 5 ppm in the ^{1}H-spectrum. Data matrices of 8192 x 128 real data points were sampled after 16 dummy scans with a single scan per t_1-increment. The gradient-selected COSY is processed in magnitude mode,

while the CLIP-COSY is processed in phase-sensitive mode using complex encoding[402] in the indirect dimension.

Hard 90° ^{1}H-pulses of 9.38 μs duration were used. Pulsed field gradients, with exception of G_1 in the CLIP-COSY (for numbering see Figure 9.2 b)), were of smoothed square shape (*SMSQ10.100*) with an duration of 1 ms and followed by a 200 μs recovery delay. The gradient-selected COSY used 10% of the maximum gradient strength ($\sim$ 50 G/cm), and the CLIP-COSY used G_2 = 10% and G_3 = 33%.

For Thrippleton-Keeler-filtration, the CLIP-COSY experiment used adiabatically frequency swept pulses with a 60 kHz sweep over 20 ms length. An amplitude profile with quarter-sine ramps at the outer 10% of the pulse was used (*Crp60,20,20.10*). The pulse amplitude was adjusted for an adiabaticity factor Q = 5 in the middle of the sweep.

Time domain signals were zero-filled to 16384 real data points in t_2 and linear forward prediction to 1024 real data points was applied in t_1 using 32 adjustable coefficients. For the gradient-selected COSY unshifted squared sine functions were used for apodization. The CLIP-COSY used exponential apodization in F_2 (*LB*: 1 Hz) and a squared cosine function (*SSB*: 2) in the indirect dimension. The CLIP-COSY was manually phased and subjected to automatic baseline correction in F_1.

14.2. Project C, Signal assignment for oligourea 8

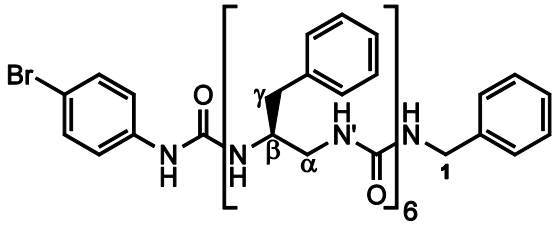

8

Figure 14.1: Structure of oligourea **8**, as also shown in Figure 8.10.

Table 14.1: Signal assignment for oligourea **8**. Values reported in bold letters were added to the signal assignment reported in the Bachelor thesis of Timo Imhof[378]. ^{15}N chemical shifts are reported using liquid ammonia as the reference. *J*-coupling values were extracted from a ^{1}H-spectrum. Only $^{3}J_{HH}$ values are reported, which involve one nitrogen-bound proton and one carbon bound proton. Values that could only be roughly be determined are marked with an asterisk.

position		^{1}H NMR, δ [ppm]	^{15}N NMR, δ [ppm]	^{13}C NMR δ [ppm]	$^{3}J_{NH,\ H\alpha\ or\ H\beta}$ [Hz]
Bn-cap	1A	**4.751**		44.09	**6.0**
	1B	**4.667**		44.09	**5.6**
	NH	7.25	82.65		
	C_q			**141.8**	
	ortho	**7.62**		**127.7**	
	meta	**7.35**		**128.52**	
	para	**7.22**		**126.63**	
residue 1	C=O			**159.6**	
	NH'	7.05	77.09		
	α pro(S)	4.385		44.695	8.6
	α pro(R)	3.161		44.695	3.1
	β	4.847		51.235	9.24
	γA	2.831		40.45	
	γB	2.831		40.45	
	δ			**139.33**	
	ε	**7.345**		**129.5**	
	ζ	**7.228**		**128.3**	
	η	**7.13**		**126.05**	
	NH	6.524	91.47		
residue 2	C=O				
	NH'	6.91	75.92		
	α pro(S)	4.307		46.32	9.2*
	α pro(R)	2.65		46.32	2.7
	β	4.86		50.48	10.2
	γA	2.744		39.735	
	γB	2.65		39.735	
	δ			**138.9**	
	ε	**7.207**		**129.3**	

	ζ	**7.181**		**128.31**	
	η	**7.098**		**126.04**	
	NH	6.4	92.73		
residue 3	C=O				
	NH'	6.92	77.28		
	α pro(S)	3.98		46.395	9.4*
	α pro(R)	2.53		46.395	3.1
	β	4.692		50.98	10.35
	γA	2.79		39.16	
	γB	2.596		39.16	
	δ			**138.95**	
	ε	**7.45**		**129.52**	
	ζ	**7.353**		**128.48**	
	η	**7.202**		**126.31**	
	NH	6.38	92.26		
residue 4	C=O				
	NH'	6.97	77.75		
	α pro(S)	4.12		45.955	9.6
	α pro(R)	2.635		45.955	2.8
	β	4.5		51.17	10.15
	γA	2.81		39.05	
	γB	2.635		39.05	
	δ			**138.7**	
	ε	**7.35**		**129.45**	
	ζ	**7.333**		**128.52**	
	η	**7.235**		**126.48**	
	NH	6.44	92.37		
residue 5	C=O				
	NH'	6.61	77.71		
	α pro(S)	3.94		46.03	9.9
	α pro(R)	2.47		46.03	3.6
	β	4.46		51.015	10
	γA	2.73		38.725	
	γB	2.61		38.725	
	δ			**138.6**	
	ε	**7.27**		**129.21 or 129.23**	
	ζ	**7.296**		**128.56 or 128.72**	
	η	**7.23 or 7.25**		**126.57 or 126.75**	
	NH	6.7	91.95		
residue 6	C=O			**160.1**	
	NH'	7	77.75		
	α pro(S)	3.882		45.81	9*
	α pro(R)	2.76		45.815	3.5*

	β	4.663		55.84	9.65
	γA	2.85		38.99	
	γB	2.76		38.99	
	δ			**138.1**	
	ε	**7.27**		**129.21 or 129.23**	
	ζ	**7.295**		**128.56 or 128.72**	
	η	**7.23 or 7.25**		**126.57 or 126.75**	
	NH	6.628	96.09		
(pBr)Ph-cap	C=O			**157.1**	
	NH	9.512	105.25		
	Cq-(N)			**139.7**	
	Ar-ortho-(N)	**7.503**		**121**	
	Ar-meta-(N)	**7.511**		**132.2**	
	Cq-(Br)			**114.8**	

14.3. Project D, Product operator analysis for perfect echo mixing in the case of an arbitrarily large weakly coupled spin system

The analysis is carried out for the pulse sequence element enclosed in Figure 9.1 b) between time points I and V. The effect of N weakly coupling partners on the initial transverse component on spin 1 is analysed, without considering chemical shift evolution. This is sufficient to compute the final state of the weakly coupled spin system at time point V, if all pulses are considered to be perfect instantaneous flips.

Initial coherence generated directly prior to time point I first evolves during 2τ:

$$
\begin{aligned}
&-I_{1,y} \xrightarrow{180^\circ_x} I_{1,y} \xrightarrow{\text{for all n: } \pi J_{1,n} 2\tau} \\
&I_{1,y} \prod_n \cos(\pi J_{1,n} 2\tau) \\
&- \sum_j 2 I_{1,x} I_{j,z} \sin(\pi J_{1,j} 2\tau) \prod_{n \neq j} \cos(\pi J_{1,n} 2\tau) \\
&- \sum_j \sum_{k \neq j} 4 I_{1,y} I_{j,z} I_{k,z} \sin(\pi J_{1,j} 2\tau) \sin(\pi J_{1,k} 2\tau) \prod_{n \neq j,k} \cos(\pi J_{1,n} 2\tau) \\
&+ \sum_j \sum_{k \neq j} \sum_{l \neq j,k} 8 I_{1,x} I_{j,z} I_{k,z} I_{l,z} \sin(\pi J_{1,j} 2\tau) \sin(\pi J_{1,k} 2\tau) \sin(\pi J_{1,l} 2\tau) \prod_{n \neq j,k,l} \cos(\pi J_{1,n} 2\tau) \\
&+ \ldots
\end{aligned}
\tag{14.1}
$$

The number of terms obtained hereby is determined by the size of the spin system. Note that none of the indices used in this formula or used later shall run over spin 1. The $90°_y$ pulse introduces the mixing desired.

$$
\begin{aligned}
&(14.1) \xrightarrow{90^\circ_y} \\
&I_{1,y} \prod_n \cos(\pi J_{1,n} 2\tau) \\
&+ \sum_j 2 I_{1,z} I_{j,x} \sin(\pi J_{1,j} 2\tau) \prod_{n \neq j} \cos(\pi J_{1,n} 2\tau) \\
&- \sum_j \sum_{k \neq j} 4 I_{1,y} I_{j,x} I_{k,x} \sin(\pi J_{1,j} 2\tau) \sin(\pi J_{1,k} 2\tau) \prod_{n \neq j,k} \cos(\pi J_{1,n} 2\tau) \\
&- \sum_j \sum_{k \neq j} \sum_{l \neq j,k} 8 I_{1,z} I_{j,x} I_{k,x} I_{l,x} \sin(\pi J_{1,j} 2\tau) \sin(\pi J_{1,k} 2\tau) \sin(\pi J_{1,l} 2\tau) \prod_{n \neq j,k,l} \cos(\pi J_{1,n} 2\tau) \\
&+ \ldots
\end{aligned}
\tag{14.2}
$$

Each of the terms is now analysed separately, for convenience. We start with the simples one:

$$
\begin{aligned}
&(14.1) \xrightarrow{\text{for all n: } \pi J_{1,n} 2\tau} \\
&\prod_n \cos(\pi J_{1,n} 2\tau) \Bigg\{ I_{1,y} \prod_p \cos(\pi J_{1,p} 2\tau) \\
&- \sum_q 2 I_{1,x} I_{q,z} \sin(\pi J_{1,q} 2\tau) \prod_{p \neq q} \cos(\pi J_{1,p} 2\tau) \\
&- \sum_q \sum_{r \neq q} 4 I_{1,y} I_{q,z} I_{r,z} \sin(\pi J_{1,q} 2\tau) \sin(\pi J_{1,r} 2\tau) \prod_{p \neq q,r} \cos(\pi J_{1,p} 2\tau) \\
&+ \sum_q \sum_{r \neq q} \sum_{s \neq q,r} 8 I_{1,x} I_{q,z} I_{r,z} I_{s,z} \sin(\pi J_{1,q} 2\tau) \sin(\pi J_{1,r} 2\tau) \sin(\pi J_{1,s} 2\tau) \prod_{p \neq q,r,s} \cos(\pi J_{1,p} 2\tau) \\
&+ \ldots \Bigg\}
\end{aligned}
\tag{14.3}
$$

Under the assumption of ideal z-filtration, the only term that will not be suppressed and thus will contribute to the final result is

$$
(14.3) \xrightarrow{180^\circ_x} \xrightarrow{90^\circ_x} \xrightarrow{\text{z-filter}} \xrightarrow{90^\circ_{-x}} - \prod_n \cos(\pi J_{1,n} 2\tau)\, I_{1,y} \prod_p \cos(\pi J_{1,p} 2\tau) = -I_{1,y} \prod_n \cos^2(\pi J_{1,n} 2\tau), \tag{14.4}
$$

because all other terms contain transverse components during the z-Filter.

Next we analyse the sum of two-spin coherences. We first analyse the evolution under coupling with spin 1,

$$
(14.1) \xrightarrow{\pi J_{1,j} 2\tau} \sum_j \sin(\pi J_{1,j} 2\tau) \prod_{n \neq j} \cos(\pi J_{1,n} 2\tau) \{ 2 I_{1,z} I_{j,x} \cos(\pi J_{1,j} 2\tau) + I_{j,y} \sin(\pi J_{1,j} 2\tau) \}, \tag{14.5}
$$

And subsequently with all other spins

$$(14.5) \xrightarrow{\text{for all p}\neq\text{j: } \pi J_{1,n}2\tau}$$

$$\sum_j \sin(\pi J_{1,j}2\tau)\cos(\pi J_{1,j}2\tau)\prod_{n\neq j}\cos(\pi J_{1,n}2\tau)\Bigg\{2I_{1,z}I_{j,x}\prod_{p\neq j}\cos(\pi J_{j,p}2\tau)$$
$$+\sum_{q\neq j}4I_{1,z}I_{j,y}I_{q,z}\sin(\pi J_{j,q}2\tau)\prod_{p\neq j,q}\cos(\pi J_{j,p}2\tau)$$
$$-\sum_{q\neq j}\sum_{r\neq j,q}8I_{1,z}I_{j,y}I_{q,z}I_{r,z}\sin(\pi J_{j,q}2\tau)\sin(\pi J_{j,r}2\tau)\prod_{p\neq q,r,s}\cos(\pi J_{j,p}2\tau)+\ldots\Bigg\} \qquad (14.6)$$
$$\sum_j \sin^2(\pi J_{1,j}2\tau)\prod_{n\neq j}\cos(\pi J_{1,n}2\tau)\Bigg\{I_{j,y}\prod_{p\neq j}\cos(\pi J_{j,p}2\tau)$$
$$-\sum_{q\neq j}2I_{j,x}I_{q,z}\sin(\pi J_{j,q}2\tau)\prod_{p\neq j,q}\cos(\pi J_{j,p}2\tau)$$
$$-\sum_{q\neq j}\sum_{r\neq j,q}4I_{j,y}I_{q,z}I_{r,z}\sin(\pi J_{j,q}2\tau)\sin(\pi J_{j,r}2\tau)\prod_{p\neq j,q,r}\cos(\pi J_{1,p}2\tau)+\ldots\Bigg\}$$

Again, analysing which of these terms contributes to final signal (assuming a perfect z-filter) the number of terms reduces to the ones containing a single spin operator:

$$(14.6)(14.3) \xrightarrow{180^\circ_x} \xrightarrow{90^\circ_x} \xrightarrow{\text{z-Filter}} \xrightarrow{90^\circ_{-x}} -\sum_j I_{j,y}\sin^2(\pi J_{1,j}2\tau)\prod_{n\neq j}\cos(\pi J_{1,n}2\tau)\prod_{p\neq j}\cos(\pi J_{j,p}2\tau). \qquad (14.7)$$

For all terms in (14.2) containing products of three-, four- or more single-spin operators, i.e.

$$-\sum_j\sum_{k\neq j}4I_{1,y}I_{j,x}I_{k,x}\sin(\pi J_{1,j}2\tau)\sin(\pi J_{1,k}2\tau)\prod_{n\neq j,k}\cos(\pi J_{1,n}2\tau)$$
$$-\sum_j\sum_{k\neq j}\sum_{l\neq j,k}8I_{1,z}I_{j,x}I_{k,x}I_{l,x}\sin(\pi J_{1,j}2\tau)\sin(\pi J_{1,k}2\tau)\sin(\pi J_{1,l}2\tau)\prod_{n\neq j,k,l}\cos(\pi J_{1,n}2\tau) \qquad (14.8)$$
$$+\ldots$$

we can rule out, that these contribute to the final signal detected (again assuming ideal z-filtration), by a simple argument:
All of these terms contain products of two or more transverse single-spin operators with direction x. Throughout the second spin echo period (time points III to V in Figure 9.1b)), this does not change as a result of weak *J*-coupling, as described in equations (94) in ref. [186], while chemical shift evolution is refocused at time point V. As however, in the ideal case the $90°_x$ – z-filter – $90°_{-x}$ sandwich supresses all coherences but products of single-spin with direction y (i.e.: $I_{a,y}$, $2I_{a,y}I_{b,y}$, $4I_{a,y}I_{b,y}I_{c,y}$, …), all terms in (14.2) containing the product $I_{j,x}I_{k,x}$ will be suppressed. In (14.2), all terms with three-, four- or more single-spin operators contain this product.

At the start of acquisition, the only terms therefore remaining are those in (14.4) and in (14.7). At this instant, we therefore obtain:

$$-I_{1,y} \xrightarrow{\text{I through V}} \xrightarrow{90^\circ_x} \xrightarrow{\text{z-filter}} \xrightarrow{90^\circ_{-x}}$$
$$-I_{1,y}\prod_n\cos^2(\pi J_{1,n}2\tau) - \sum_j I_{j,y}\sin^2(\pi J_{1,j}2\tau)\prod_{n\neq j}\cos(\pi J_{1,n}2\tau)\prod_{p\neq j}\cos(\pi J_{j,p}2\tau) \qquad (14.9)$$

The term containing $I_{1,y}$ generates the diagonal peaks, while all terms containing $I_{j,y}$-operators lead to cross-peaks. If relative peak amplitudes were to be determined by this formula, it would also be required to consider contributions from relaxation.

14.4. Project D, Signal assignment for Rebaudisoide A in DMSO-d_6

Signal assignment for rebaudioside A, dissolved in DMSO-d_6 (11.6 mM) was based on ^{1}H, HSQC, DQF-COSY, ^{13}C, HMBC, NOESY, ROESY and TOCSY spectra, measured at 300K at 700 MHz proton resonance frequency. Chemical shifts reported were referenced using the solvent residual signal in the proton spectrum.

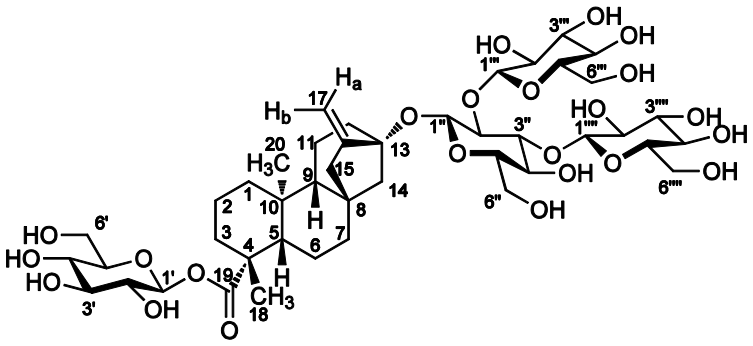

Figure 14.2: Structure of rebaudisoide A with numbering used below. For assignment in pyridine-d_5 see ref. [403].

No	δ(^{13}C)	δ(^{1}H)	No	δ(^{13}C)	δ(^{1}H)
1	40.53*	0.78 1.78			
2	19.1	1.80 1.35	1”	97.1	4.465
3	37.9	2.06 0.99	2”	79.3	3.488
4	43.60		3”	86.7	3.54
5	56.9	1.04	4”	69.4	3.16
6	21.7	1.93 1.71	4”-OH		4.50
7	41.5	1.48 1.35	5”	76.5	3.12
8	42.3		6”	61.4	3.68 3.41
9	53.7	0.91	6”-OH		4.65
10	39.4				
11	20.3	1.69 1.49	1”’	102.9	4.63
12	36.7	1.86 1.45	2”’	75.0	2.98
13	85.7		2”’-OH		5.12
14	43.65*	1.44 2.10	3”’	76.9	3.14
15	47.5	2.04 1.98	3”’-OH		4.95
16	153.6		4”’	70.7	3.05
17	104.4	a:5.05 b:4.74	4”’-OH		4.88
18	28.6	1.14	5”’	77.1	3.05
19	176.0		6”’	61.7	3.61 3.42
20	15.5	0.87	6”’-OH		4.07
1’	94.6	5.27	1””	103.5	4.42
2’	73.0	3.15	2””	74.2	3.04
2’-OH		5.20	2””-OH		5.60
3’	77.37*	3.25	3””	77.0	3.16
3’-OH		4.96	3””-OH		5.07
4’	70.0	3.14	4””	70.5	3.06
4’-OH		4.95	4””-OH		5.00
5’	78.1	3.19	5””	77.4	3.19
6’	61.0	3.46 3.63	6””	61.4	3.70 3.40
6’-OH		4.47	6””-OH		4.58

15. Curriculum Vitae

Lukas Kaltschnee
Born in Frankfurt am Main, Germany

Education

08/92 – 07/96	Elementary school, Frankfurt a. M. and Friedrichsdorf
08/96 – 07/05	Secondary school, *Philipp-Reis-Schule*, Friedrichsdorf
09/05 – 05/06	Civilian service, *Frankfurter Verein für soziale Heimstätten e.V.*
10/06 – 03/10	Study of Chemistry B. Sc., *Technische Universität Darmstadt*, Darmstadt
09/08 – 07/09	Studies abroad (ERASMUS exchange program), *École Polytechnique Fédérale de Lausanne*, Lausanne (Switzerland)
04/10 – 04/12	Study of Chemistry M. Sc., *Technische Universität Darmstadt*, Darmstadt Major field of study: Physical Chemistry
06/11 – 09/11	External research project, *Max-Planck-Institut für Polymerforschung*, Mainz Research group Dr. F. Laquai
10/11 – 04/12	Master thesis, *Technische Universität Darmstadt*, Darmstadt
06/12 – 08/16	Ph. D. studies, *Technische Universität Darmstadt*, Darmstadt
07/14 – 09/14	Visiting scientist, *University of Manchester*, UK, Research group Prof. Ph. D. G. A. Morris

Bachelor thesis

Title	Effect of Coadsorbents on the Performance of Dye Sensitized Solar Cells
Group	Prof. Dr. M. Grätzel
Place	Faculté des Sciences de Base, École Polytechnique Fédérale de Lausanne; handed in at the Eduard-Zintl-Institut für Anorganische und Physikalische Chemie, Technische Universität Darmstadt

Master thesis

Title	Untersuchungen zur Quantifizierung 1H-entkoppelter protonendetektierter Experimente
Group	Prof. Dr. C. M. Thiele
Place	Department of Chemistry, Technical University Darmstadt

Prizes and awards

01/13 – 12/14	Ph. D. fellowship of the Merck'sche Gesellschaft für Kunst und Wissenschaft e.V.

Talks

1 Improving Signal Separation for Oligomeric Structures in Pure Shift HSQC Spectra
GDCh FGMR 37th Annual Discussion Meeting, Darmstadt, 09/15. (upgraded Poster)

Lukas Kaltschnee
Am Ziehgraben 43
60488 Frankfurt am Main

Erklärung

Ich erkläre hiermit, dass ich meine Dissertation selbstständig und nur mit den angegebenen Hilfsmitteln angefertigt habe.

Darmstadt, den 28. Juni 2016

(Lukas Kaltschnee)

Lukas Kaltschnee
Am Ziehgraben 43
60488 Frankfurt am Main

Erklärung

Ich erkläre hiermit, noch keinen Promotionsversuch unternommen zu haben.

Darmstadt, den 28. Juni 2016

(Lukas Kaltschnee)